

Analysis of Coupled Seals, Secondary and Powerstream Flow Fields in Aircraft and Aerospace Turbomachines

M.M. Athavale, Y.H. Ho, and A.J. Przekwas
CFD Research Corporation, Huntsville, Alabama

The NASA STI Program Office . . . in Profile

Since its founding, NASA has been dedicated to the advancement of aeronautics and space science. The NASA Scientific and Technical Information (STI) Program Office plays a key part in helping NASA maintain this important role.

The NASA STI Program Office is operated by Langley Research Center, the Lead Center for NASA's scientific and technical information. The NASA STI Program Office provides access to the NASA STI Database, the largest collection of aeronautical and space science STI in the world. The Program Office is also NASA's institutional mechanism for disseminating the results of its research and development activities. These results are published by NASA in the NASA STI Report Series, which includes the following report types:

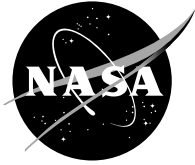
- **TECHNICAL PUBLICATION.** Reports of completed research or a major significant phase of research that present the results of NASA programs and include extensive data or theoretical analysis. Includes compilations of significant scientific and technical data and information deemed to be of continuing reference value. NASA's counterpart of peer-reviewed formal professional papers but has less stringent limitations on manuscript length and extent of graphic presentations.
- **TECHNICAL MEMORANDUM.** Scientific and technical findings that are preliminary or of specialized interest, e.g., quick release reports, working papers, and bibliographies that contain minimal annotation. Does not contain extensive analysis.
- **CONTRACTOR REPORT.** Scientific and technical findings by NASA-sponsored contractors and grantees.

- **CONFERENCE PUBLICATION.** Collected papers from scientific and technical conferences, symposia, seminars, or other meetings sponsored or cosponsored by NASA.
- **SPECIAL PUBLICATION.** Scientific, technical, or historical information from NASA programs, projects, and missions, often concerned with subjects having substantial public interest.
- **TECHNICAL TRANSLATION.** English-language translations of foreign scientific and technical material pertinent to NASA's mission.

Specialized services that complement the STI Program Office's diverse offerings include creating custom thesauri, building customized databases, organizing and publishing research results . . . even providing videos.

For more information about the NASA STI Program Office, see the following:

- Access the NASA STI Program Home Page at <http://www.sti.nasa.gov>
- E-mail your question via the Internet to help@sti.nasa.gov
- Fax your question to the NASA Access Help Desk at 301-621-0134
- Telephone the NASA Access Help Desk at 301-621-0390
- Write to:
NASA Access Help Desk
NASA Center for Aerospace Information
7121 Standard Drive
Hanover, MD 21076



Analysis of Coupled Seals, Secondary and Powerstream Flow Fields in Aircraft and Aerospace Turbomachines

M.M. Athavale, Y.H. Ho, and A.J. Przekwas
CFD Research Corporation, Huntsville, Alabama

Prepared under Contract NAS3-27392

National Aeronautics and
Space Administration

Glenn Research Center

Acknowledgments

During the course of this project, the authors had to draw on the expertise, experience and help from a number of individuals which was essential in the successful completion of the project. Bob Hendricks and Bruce Steinetz, NASA Glenn Research Center, provided continuous encouragement, guidance, help and patience, which were vital for this effort. The authors have had occasion to draw on the expertise on a number of individuals from CFD Research Corporation. Thanks are due to Ashok Singhal, President, CFDRC, for guidance and encouragement during the course of the project. Thanks are due to S. Bayyuk, M.Z. Pindera, N. Vaidya, H.Q. Yang, Y. Jiang, and R.K. Avva, for technical advice and discussions at various stages of this work. Thanks are due to John Munson and Jim Forry, Allison Engine Co., for providing the geometries and data for the T-56 turbine calculations. Work on the G.E. aspirating seal needed help from Mr. Shapiro, Shapiro Associates, Alan McNickle, Stein Seal, and Norm Turnquist, Bharat Bagepalli, and Tom Tseng, GE CR&D and GEAE. Finally, thanks are due to Jennifer Swann for preparation of this manuscript as well as the numerous publications attached in this report.

Available from

NASA Center for Aerospace Information
7121 Standard Drive
Hanover, MD 21076

National Technical Information Service
5285 Port Royal Road
Springfield, VA 22100

Available electronically at <http://gltrs.grc.nasa.gov>

Contents

Abstract.....	1
1. Introduction.....	2
2. Flow and Heat Transfer Simulations in T-56 Turbine Drum.....	3
2.1 Simulations on Individual Disk Cavity Pairs.....	4
2.2 Complete Turbine Drum Flow and Conjugate Heat Transfer Simulations.....	10
2.3 Summary.....	16
3. Aspirating Face Seal Modeling.....	16
3.1 Aspirating Seal Geometry and Operation.....	17
3.2 Simulations Performed.....	18
3.3 2-D Simulations.....	19
3.4 3-D Simulations.....	20
3.5 Summary.....	26
4. Flow and Heat Transfer in Disk Cavities.....	26
4.1 Flow in Contra-Rotating Disk Cavity.....	27
4.2 Simulation of Heat Transfer in Rotating Cavities.....	37
5. 3-D Secondary and Power Stream Coupling Methodology.....	41
5.1 Flow Codes.....	43
5.2 Functions of Interface Routines.....	44
5.3 Issues in Formulation of Interface Methodology.....	47
5.4 Flow Treatment at the Interface.....	48
5.5 Interface Data Interpolation Methodology.....	50
5.6 Summary.....	53
6. Coupled, Transient Analyses of Power Stream-Secondary Flows.....	53
6.1 Bladeless Rotor+Stator+Cavity in Turbine Section.....	53
6.2 UTRC High-Pressure Rig Simulations.....	56
6.3 NASA Low-Speed-Air Compressor (LSAC) Rig.....	64
6.4 Summary.....	66
7. Summary and Recommendations for Future Work.....	68
7.1 Recommendations for Future Work.....	69
8. References.....	69
Appendix A—Selected Publications.....	71
Appendix B—An Algorithm for Interpolation Between Computational Interfaces with Arbitrary Grid Matching.....	141
Appendix C—Users’ Manual for Coupled, Time-Accurate, Three-Dimensional Computations of Primary-Secondary Flow Interactions at Rim Seals With SCISEAL-MS–TURBO Codes.....	151

Analysis of Coupled Seals, Secondary and Powerstream Flow Fields in Aircraft and Aerospace Turbomachines

Mahesh M. Athavale, Y.H. Ho, and Andrzej J. Przekwas
CFD Research Corporation
Huntsville, Alabama 35805

Abstract

This project was established with rather broad goals of 1. application of the present-day computational fluid dynamics (CFD) tools to the complex flow and heat transfer phenomena in the secondary flow system elements in gas turbine engines, 2. application to specific OEM problems, and 3. coupling of two computational tools to treat the complex, time-unsteady interaction of the primary and secondary flow streams in a gas turbine engine.

All of the above objectives were met successfully during the course of this project. Some of the specific achievements from this work are:

1. Flow and thermal analysis of the secondary flow system in an actual turbine section. The T-56 turbine section data was provided by Allison Engine Co of Rolls Royce Aerospace Group. Flow and conjugate heat transfer calculations in the three inner disc-cavity pairs + associated mainpath were completed. Results in terms of rim seal flows at various locations, gas temperatures, temperatures in the rotor disks were compared with data from Allison. Other numerical experiments included effects of reduction of coolant flows, changes in seal clearances, and changes in the mainpath flow conditions on the cavity flow fields.
2. Flow analysis of the GE/NASA aspirated face seal. This seal is being developed as a candidate for the GE90 balance piston replacement for an existing labyrinth seal. Flow and load characteristics of the seal were calculated using 2-D analyses and compared with experiments and other calculations during the design stages. Subsequently a test rig for the seal was built, and it was found to show different operational characteristics. Full 3-D CFD analysis was then performed on the face seal. Flow details showed interference of flow streams from the two major components of the seal that prevented the proper operation. A fix for this was suggested and implemented in the seal. After the modification, the seal performance was close to the design specifications.
3. SCISEAL code was coupled with MS-TURBO, a CFD code developed at Mississippi State University for the treatment of the multi-stage rotor-stator and rimseal-cavity flow interaction in gas turbines. Both codes were appropriately modified, and an interface algorithm was developed to link the two codes during parallel execution. The interface treatment allows for the relative motion generated by the rotor stages, interpolated fluxes and flow variables from one code to another and ensures flux conservation across the interface. This coupled algorithm has been successfully used to simulate the interaction of the disc cavity and primary flow in the UTRC H.P. Rig. Additional simulations may be undertaken to assist the ongoing experimental efforts on this rig.

In addition to these major tasks, several additional tasks were accomplished. These include validation of the CFD codes on the flow and heat-transfer processes in typical disc cavities, assessment of the flow in planar honeycomb seals and comparison with experiments, and support to NASA as well as others for dissemination and utilization of NASA seals code SCISEAL.

1. Introduction

With the increasing importance on improvements of gas turbine engine performance in terms of efficiency and power output, all of the major subsystems of a typical gas turbine are under scrutiny. The secondary flow system in a turbine engine, which includes the coolant air circuits as well as the leakage flows in seals and the disk cavity flows is one of the areas that has shown promise of substantial gains in the overall engine efficiency through optimization of coolant flows and improvements in seal performance [1]. Impact of such changes, however, on the overall engine performance must be thoroughly evaluated before the changes are implemented. The secondary flow system is intimately tied with the other major flow stream in an engine, namely the power or mainpath flow stream. The power stream essentially is the flow above the blade platforms, and generates the engine power.

The above-blade platform flows have received considerable attention in the past and present and is a fairly mature technology. Computational fluid dynamics (CFD) codes for multi-stage flow calculations of the power stream are available and are routinely used in design calculations [2]. The power-stream calculations and designs typically have included the effects of the secondary flow streams (coolant leakage in turbine section and the seal leakage in the compressor) using simplified models of the leakage/coolant flows entering into the power stream at the rim seal locations.

The power-stream flow is inherently time-transient because of the relative motion between successive rotor and stator stages that exist in typical multi-stage compressor and turbine sections. There has been interest in performing such time-accurate interactions in the power stream flows during the design stages of a machine. Effects of this time-transient nature on the interaction of the power stream with the secondary stream flows therefore need to be investigated as well and is the logical next step in calculations of the primary and secondary flow interaction.

In a typical multi-stage turbine section the coolant flows serve to cool the rotor disks and other support structures and protect these from the hot power-stream gases. The coolant flow typically is high-pressure air from the compressor section, and hence it is 'expensive' and represents a net parasitic loss in terms of lost power and efficiency; at the same time, it is essential for cooling of the structural parts. For these reasons, optimum coolant flow rates need to be found that would provide adequate cooling performance at the lowest coolant flow rates to minimize the parasitic losses. Under these requirements, the interaction between the power stream and the secondary stream at and around the rim seals becomes of extreme importance. The transient nature of the power-stream flows must be taken into consideration when evaluating the rim seal flows.

The main objectives of the present work were several fold:

1. Develop a coupled, transient simulation methodology for calculations of the interaction between the powerstream and the secondary flow in a typical gas turbine engine turbine and compressor sections.
2. Apply the coupled simulation methodology to typical multi-stage turbine and compressor problems. Validate the codes against available experimental data;
3. Apply the 3-D CFD code SCISEAL to different secondary flow and/or seal turbomachinery seal problems. To provide relevance to the simulation results, the problem definitions were obtained from different gas turbine manufacturers, namely Rolls Royce Allison Engine Co. and GE CR&D. Results of the simulations for GE were found to be of importance in their face seal design improvements.
4. Further validate the CFD codes on cavity flow and heat-transfer problems using quality published experimental and numerical data.

All of these objectives were successfully met during the course of this work. The following chapters in this report present the details of the work. The work done on the Allison T-56 turbine cavities and interaction with the mainpath is presented in Chapter 2. Chapter 3 deals with the work that was performed on a novel aspirated face seal design from GE. 3-D simulations of the flow in the face seal were done to

provide crucial flow insight for a successful seal design. Results of a validation study performed on disk cavity flow and heat transfer are presented in Chapter 4.

Description of the methodology for coupled transient powerstream and secondary flow is presented in Chapter 5 where the CFD codes, interface strategy, and treatment is described. Some sample validation results for the interface are also presented. The coupled codes were then applied to the coupled power-secondary flow streams in the UTRC High-Pressure Turbine Stage Rig. This rig was built to provide such data for code validations. Details of the calculations, simulation results and some comparisons with the experimental data are presented in Chapter 6. A brief summary and recommendations for future work are outlined in Chapter 7.

2. Flow and Heat Transfer Simulations in T-56 Turbine Drum

The typical multi-stage turbine section in a gas turbine engine presents a very complex flow and heat-transfer problem. The power stream consists of fast moving hot gas from the combustor that is expanded through the stator and rotor rows to generate work. The disk cavities usually have compressed air as purge flow introduced at one or more locations, which serve to cool the rotor disks as well as supporting structures for the labyrinth seals. The purpose of the purge flow is twofold: to cool the rotor disks, and also to prevent the powerstream gases from entering the disk cavities through the rim seals.

The advanced CFD code, SCISEAL [3] is ideally suited to analyze these complex flow and heat-transfer problems in the turbine disk cavities and associated labyrinth seals. As a demonstration/validation problem, the turbine section disk cavities of the T-56 gas turbine engine were considered. These engines are currently installed on C-130 Military transport planes. The characteristics of the engine are: pressure ratio of 14.1, mass flow rate 15.7 kg/s, engine speed of 14240 rpm and a power rating of 5250 h.p. at sea-level takeoff conditions. Geometries of the disc cavities and flow conditions were obtained from Allison Engine Company, Rolls Royce Aerospace Group (RRAE). A cross-section through the turbine section of this engine is shown in figure 2-1. The turbine section consists of four rotor stages and three intermediate stator vanes. There are three inter-stage disk cavity pairs (Stage 1-2, 2-3 and 3-4 cavities) and a single disk cavity ahead of the first rotor and aft of the fourth rotor.

The present work was focused on the three pairs of the interstage cavities. Simulations were first carried out on the individual disk cavity pairs for flow and heat transfer, with particular focus on the stage 1-2 cavity, where the flow conditions are most severe (highest pressures and temperatures with multiple

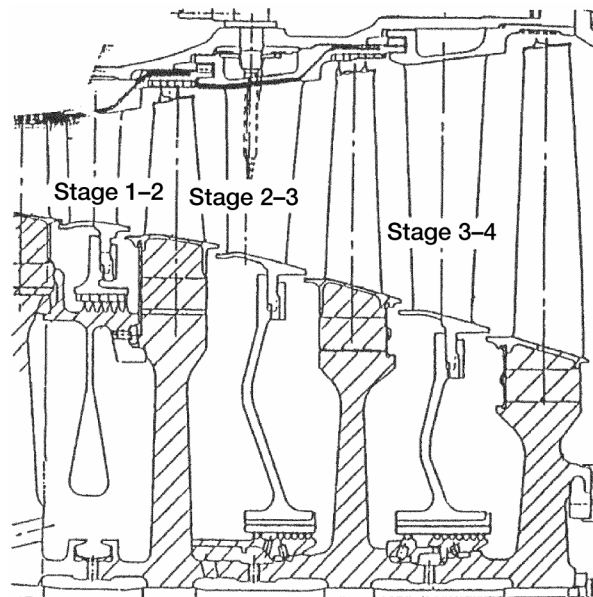


Figure 2-1.—Turbine section of T-56 gas turbine engine.

coolant injection and exhaust paths). Variations in the labyrinth seal clearances, and effects of coolant flow reduction on the flow field were studied. Baseline flow and heat transfer calculations on the other two individual pairs (Stage 2-3 and 3-4) were also performed. Flow information obtained from RRAE design codes was made available for comparison with present results, and included pressure and temperatures in the cavities as well as seal mass flow rates and total temperatures.

One of the problems faced during the heat transfer calculations in the individual cavity simulations was the thermal boundary condition to be imposed on the cavity walls. Typically, the rotor disks as well as labyrinth seal supports conduct heat across and in this sense all the inner cavity pairs are ‘connected’ to each other. Due to this reason, the wall temperatures and/or heat fluxes are dependent on the flow and thermal conditions in the cavities, and so are not known a-priori. The only way to properly treat these wall conditions is to include the solid parts in the solution domain together with the flow in the cavities. This necessitates solution of a conjugate heat transfer problem where the energy equation in the solid parts is coupled with the fluid energy equation, with appropriate treatment at the solid-fluid interfaces. To perform this calculation properly, however, the calculation domain has to extend to cover all of the solid and fluid domains that are likely to participate in the conjugate heat transfer.

The second set of calculations thus focused on the conjugate heat transfer problem in the turbine drum. In the present case, all of the inner cavity pairs as well as solid parts of all four rotors were included in the calculations.

All of the calculations presented in this chapter assumed that there were no circumferential variations in the flow and heat-transfer in the cavities and power-stream flows. This allows the use of a 2-D axisymmetric computational domain as well as steady-state treatment of the flow. This treatment simplifies the problem and reduces the computational requirements, and for these reasons has been used widely. It generally will account for all of the important flow features in disk cavity flows in a time-averaged sense. The flow in the power stream, however, is inherently time-dependent due to rotor blade motion and can generate dynamic flow conditions near the rim seal, which will affect the cavity-powerstream flow interaction. Solution methodology and results for such calculations are presented in later chapters of this report.

Following subsections discuss the two sets of simulations and additional details are found in two publications [4,5], copies of which are attached in appendix A.

2.1 Simulations on Individual Disk Cavity Pairs

As outlined above, the three inner cavity pairs in the turbine section of T-56 engine were considered in this work, with all the appropriate coolant injection in each of the pair. Of the three pairs, the first pair (Stage 1-2) is relatively small in radial extent, while the second and third pairs are large in radial direction which provide axial thrust balancing forces for the turbine shaft. The Stage 1-2 pair was also used to perform some parametric studies, namely effects of change in the labyrinth seal clearance and effects of reduction in the coolant flow injection in the cavity.

2.1.1 Geometry and Grids.—Geometries of the three disk cavity pairs were obtained from RRAE in the form of drawings. Also obtained from RRAE were the flow conditions for the power streams and the purge flow inlets in the different cavity sets. Multi-domain, structured grids were built on each of the pairs. All of the major details in the geometry were accurately reproduced in the grids, including the clearance gaps in the labyrinth seals. The labyrinth seals have honeycomb surfaces on the stator side, which can be represented by increasing the surface friction factors, but in the present case such data was unavailable, and hence a smooth stator surface in the labyrinths seals was assumed. A very limited amount of grid refinement studies were performed on these complex geometries. The final configurations were:

Stage 1-2 Cavity: 34 domains, 8700 computational cells.

Stage 2-3 Cavity: 37 domains, 45000 computational cells.

Stage 3-4 Cavity: 44 domains, 29000 computational cells.

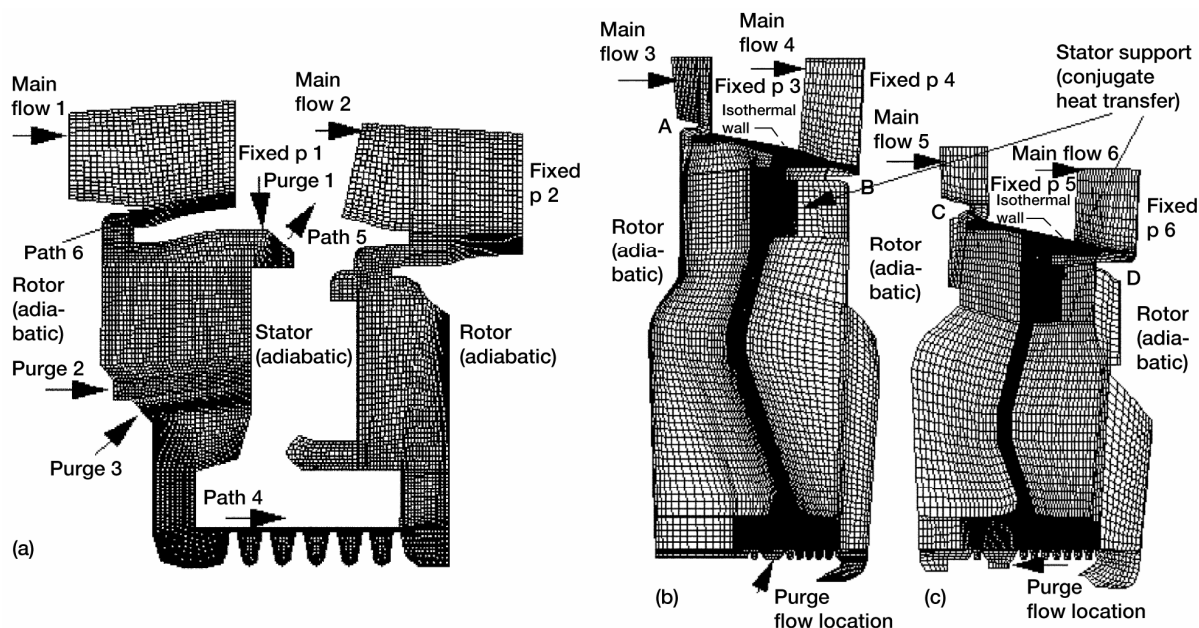


Figure 2-2.—Computational grids for the T-56 turbine cavities (stages 1-2 cavities are not the same scale as stages 2-3 and 3-4). (a) Stage 1-2 (no conjugate heat transfer calculation). (b), (c) Stages 2-3 and 3-4 (every third line is shown for the flow domain).

Figure 2-2 a, b, and c show the computational grids for the three cavity pairs. The grid sizes for the Stage 2-3 and 3-4 cavities are much higher than Stage 1-2 cavities due to their larger physical sizes as well as more complicated labyrinth seals.

2.1.2 Flow and Boundary Conditions.—The flow in the cavities and power stream was assumed compressible with air as the working fluid with variable properties, with the viscosity variation governed by Sutherland's law. The standard k- ϵ model of turbulence was used to treat the turbulent flow. No slip walls with appropriate tangential/rotational velocities were assumed on the solid walls. For this series of runs, all walls were assumed to be adiabatic. The conditions at takeoff were assumed with an engine rotational speed of 14200 rpm.

The powerstream conditions were specified on separate domains attached at each individual rim seal location. Each of the powerstream block was defined with appropriate boundary conditions: an inlet boundary with specified mass flow, an exit boundary with a specified static pressure, stationary walls on the outer wall/casing and rotating or stationary walls on the rotor/stator. The powerstream flow was thus split in six separate streams with individual sets of boundary conditions that were held fixed with no connection between the successive power stream domains. The values of the boundary conditions for the powerstream were obtained from the RRAE design codes.

The coolant/purge flows were specified as inlet boundaries at the appropriate locations. Appropriate temperature, pressure and mass flow conditions were specified at these coolant injection locations.

Several different runs were completed on the individual pair configurations:

1. Baseline/design condition steady state runs: where the boundary conditions and geometry of the cavities were at the nominal design values. The flow rates and gas temperatures at the different rim seal locations were calculated and compared with the data from RRAE design codes.
2. Study of change on the labyrinth seal clearance on the flow field: Stage 1-2 cavities were used to perform this study, where the effects of doubling the labyrinth seal clearance was studied and results compared with design data.
3. Effects of reduction in the coolant flowrates: Again the Stage 1-2 cavity pair was used at nominal geometry, and the coolant flow rates were successively decreased to evaluate the effects on the cavity flow field and the interaction between the powerstream and cavity flow.

2.1.3 Results and Discussion.—For all the baseline studies, the flow conditions were held at a nominal design point. The results in terms of streamlines, static pressure fields, and temperature fields are presented in figures 2-3 through 2-5.

In the Stage 2-3 and 3-4 cavities, the purge flow enters in the labyrinth seal at one or more intermediate points and then is carried over to the cavities on either side (figures 2-3a and b). Both pairs have ‘upstream’ (left of the labyrinth seal) cavities that are relatively narrow in the axial direction; these cavities interface with a powerstream domain that has a higher pressure. The “downstream” cavities both have relatively “squarer” cross-sections which show stronger recirculation zones as compared to the recirculation zones in the upstream cavities. The design of all rim seals is such that the powerstream flow sees a backward facing step at each rim seal. This generates a recirculation zone at the rim seal and the purge flow has to work around it, typically entering the powerstream near the upstream edge of the back step. In all four rim seals, in the present case, the net flow direction is from the cavity to the powerstream, i.e., there is no ingestion of the hot powerstream gas in the cavities. The flow rates and average gas temperatures at each rim seal are of importance and the values from present calculations are compared with the values from RRAE design data in table 2-1. As seen from these results the calculated flow splits show a higher flow rate through the downstream rim seal while the design calculations show an opposite trend. The calculated rim seal temperature and the average cavity pressure values however are fairly close to the design data.

TABLE 2-1.—COMPARISON BETWEEN THE DESIGN DATA AND THE PREDICTION FOR STAGES 2-3 AND 3-4 CAVITIES (SEE FIGURE 2-2A FOR PATH NO. NOTATION)

Location	Design			Predicted (without conjugate heat transfer)		
	Mass (kg/s)	Pressure (Pa)* $\times 10^5$	Temperature (k)	Mass (kg/s)	Pressure (Pa)* $\times 10^5$	Temperature (K)
A	0.0567	3.309	741	0.0376	3.275	786
B	0.0376	2.137	698	0.0540	2.068	716
C	0.0340	1.724	705	0.0240	1.689	700
D	0.0209	1.103	703	0.0272	1.069	666

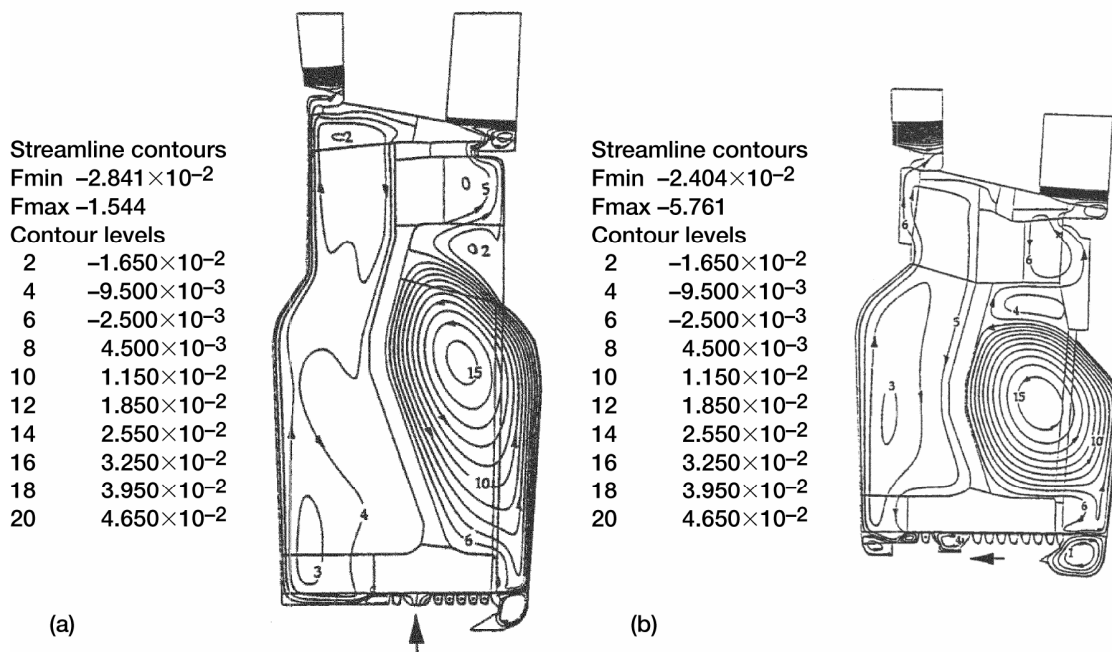


Figure 2-3.—(a) Streamline plot for stage 2-3 cavities. (b) Streamline plot for stage 3-4 cavities. (Arrow indicates the location of purge flow injection).

Streamline contours
 Fmin -7.796×10^{-2}
 Fmax -1.073
 Contour levels
 2 -6.346×10^{-2}
 4 -5.038×10^{-2}
 6 -3.731×10^{-2}
 8 -2.423×10^{-2}
 10 -1.115×10^{-2}
 12 1.923×10^{-3}
 14 1.500×10^{-2}
 16 2.808×10^{-2}
 18 4.115×10^{-2}
 20 5.423×10^{-2}
 22 6.731×10^{-2}
 24 8.038×10^{-2}
 26 9.346×10^{-2}

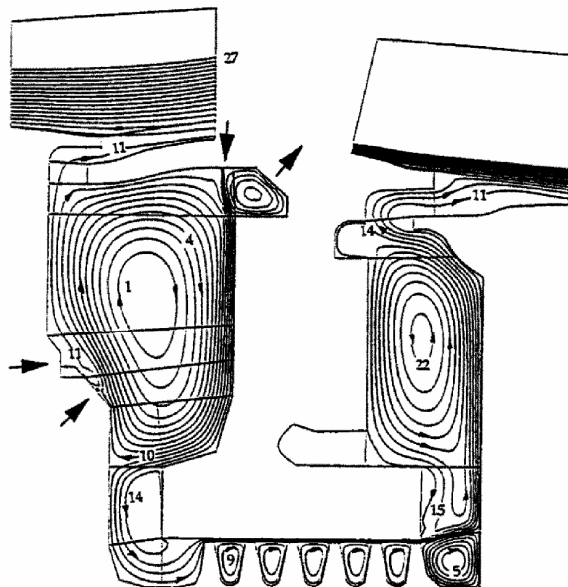


Figure 2-4.—Streamline plot for stage 1-2 cavities, labyrinth seal clearance = 0.012 in. (arrows indicate locations of the purge flow injection).

TABLE 2-2.—COMPARISON BETWEEN THE DESIGN DATA AND THE PREDICTION FOR STAGE 1-2 CAVITIES (SEE FIGURE 2-2A FOR PATH NO. NOTATION; LABYRINTH SEAL CLEARANCE = 0.012 IN)

Path No.	Design	Temp (°F)	Prediction	Temp (°F)
	Massflow (lb/s)		Massflow (lb/s)	
4	0.249	1058	0.308	1032
5	0.041	1058	0.030	1029
6	0.099	1058	0.095	1100

The Stage 1-2 cavity is much more compact in radial direction and has multiple coolant flow injection points, with different coolant flow properties at each injection location. The baseline calculation shows a main recirculation zone in each of the cavities (figure 2-4). The coolant injection points are marked in this figure and effects of the coolant on the streamline pattern can be seen. As indicated in figure 2-4, the coolant injection points are all in the upstream cavity. Part of the coolant flow then enters the power stream flow through the upstream rim seal. The remaining flow goes in the downstream cavity through the labyrinth seal and then exits into the powerstream at the downstream rim seal. Both the rim seals have the backward facing step structure. The powerstream flow generates recirculation zones near the rim seals, and the purge flow has to exit around these zones. As before, flow rates and temperatures of the air at the rim seals as well as through the labyrinth seal are of interest and the calculated values are shown in table 2-2 (see figure 2-2a for location of measurement locations); also presented are the values from RRAE design data. As seen, the two sets show good correlation. The temperature contours in the cavities are shown in figure 2-5, and the effects of coolant injection on the upstream cavity flow are apparent. The gas temperatures near the rim seals also show absence of powerstream gas ingestion.

As outlined earlier, one parametric study on Stage 1-2 cavities involved increasing the labyrinth seal clearance by a factor of two while maintaining all other conditions constant. During engine operation, rotor excursions are common, and typically the labyrinth teeth contact the stator and increase the effective seal clearance. The effects of such clearance changes need to be understood during the design stage and this parametric study was an attempt to see how sensitive the cavity flow is to changes in the labyrinth seal.

Temperature contours
Contour levels

	K
2	794.8
4	834.4
6	874.0
8	913.5
10	953.1
12	992.7
14	1032
16	1072
18	1111
20	1151
22	1191
24	1230

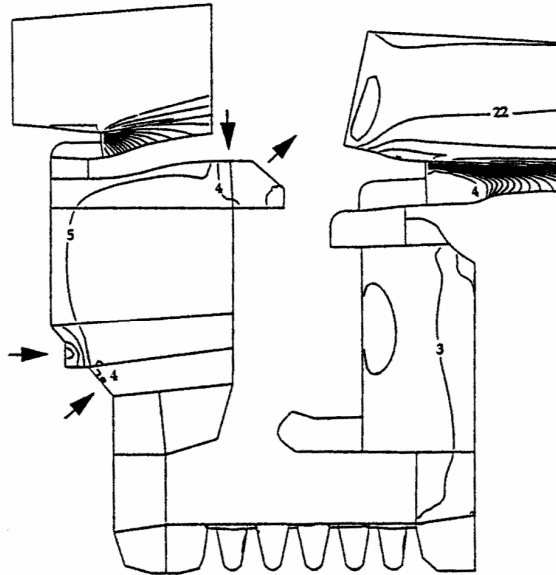


Figure 2-5.—Temperature contours for stage 1-2 cavities, labyrinth seal clearance = 0.012 in. (arrows indicate locations of the purge flow injection).

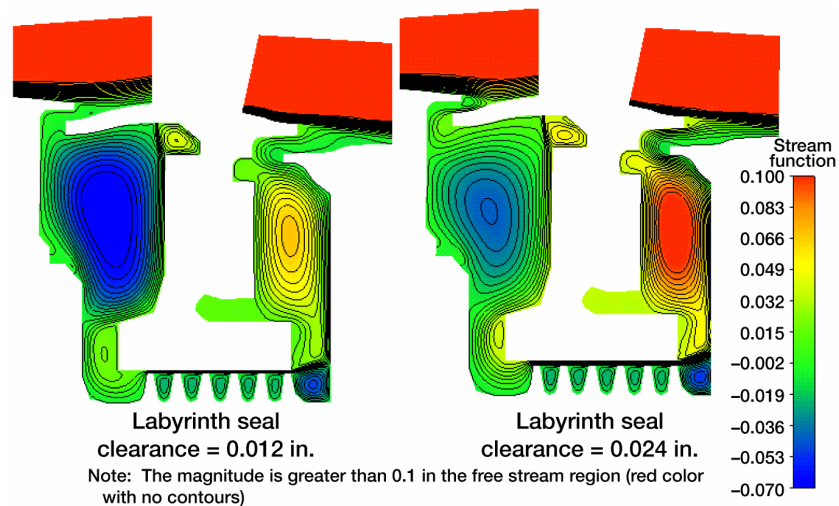


Figure 2-6.—Streamline patterns in stage 1-2 cavities at two labyrinth seal clearances.

A simulation was performed on the Stage 1-2 cavity with the labyrinth seal clearance enlarged to 0.024 inches from the nominal value of approx. 0.5 mm (0.012 inches). All of the other parameters, including coolant injection rates were kept fixed. The calculated streamline pattern in the cavities for larger labyrinth clearance is shown in figure 2-6, along with the streamline pattern for the baseline case for comparison. Dramatic changes in the flow pattern in the upstream cavity and the upstream rim seal are seen as a result of the clearance increase. The large recirculation bubble in the upstream cavity is pushed down and there is clear evidence of powerstream flow ingestion, as indicated by the streamline pattern at the upstream rim seal. This ingested flow then mixes with the coolant flow injected in the upstream cavity, passes through the labyrinth seal into the downstream cavity, and finally exits in the powerstream at the downstream rim seal. As a result of the powerstream gas ingestion in the upstream cavity, the average temperatures in the cavities as well as the temperatures of the air through the rim seals are higher (see fig. 2-7). This is seen in table 2-3 (figure 2-2a for location of measurement locations), where the rim seal flow data for the Stage 1-2 cavities at the higher labyrinth seal clearance are given along with the design data from RRAE. The computed results show fair-good correlation with the design numbers, including the flow rate and gas temperature at the upstream rim seal, where a negative flow rate indicates ingestion in the cavity.

TABLE 2-3. COMPARISON BETWEEN THE DESIGN DATA AND THE PREDICTION FOR STAGE 1-2 CAVITIES (SEE FIGURE 2-2A FOR PATH NO. NOTATION; LABYRINTH SEAL CLEARANCE = 0.024 IN)

Path No.	Design		Prediction	
	Massflow (lb/s)	Temp (°F)	Massflow (lb/s)	Temp (°F)
4	0.510	1223	0.610	1315
5	0.038	1223	0.041	1148
6	-0.153	1691	-0.220	1830

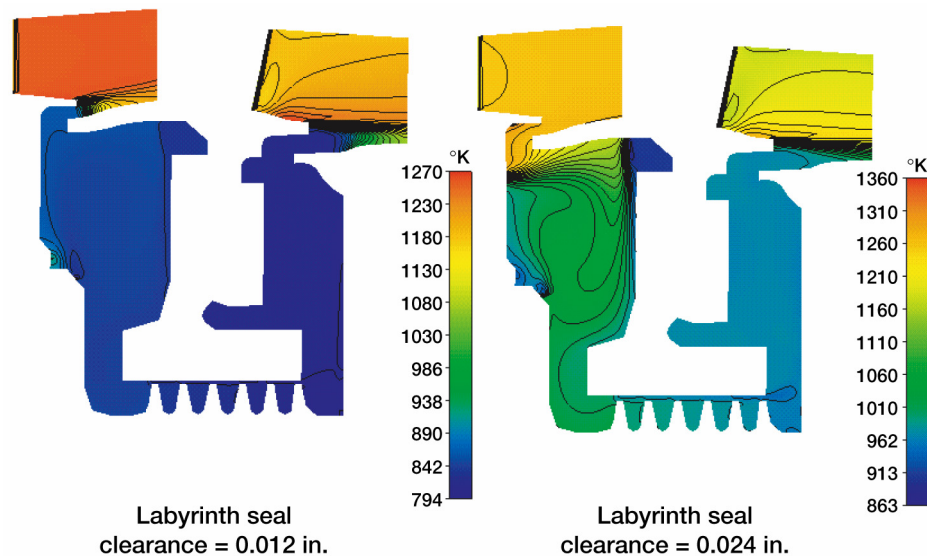


Figure 2-7.—Temperature field in stage 1-2 cavities at two labyrinth seal clearances.

The second parametric study on the Stage 1-2 cavities involved flow simulations under decreasing coolant flow rates. During these parametric runs, the coolant flow rates were reduced progressively for all of the coolant injection sites by the same percentage. Simulation runs at 100, 75, 65, and 50 percent of the nominal coolant flow rates were performed with fixed powerstream conditions. The temperature plots for these runs are shown in figures 2-8A through 2.8D. The temperature field plots reveal that there is no powerstream gas ingestion at 75 percent coolant flow rate. At 65 percent coolant flow, gas temperatures at the upstream rim seal show substantial increase, indicating possible ingestion. The overall cavity temperatures are still similar to 75 percent case, indicating that the ingestion, if any, is at a fairly small rate. The overall temperature levels in the cavities rise slightly with reduction in coolant flow rates as expected. At 50 percent of the design coolant flow, the upstream rim seal temperatures as well as the upstream cavity temperatures are substantially higher, indicating gas ingestion at large flow rates. These simulations indicate that the cavity designs have some margin of safety built in for the coolant flow rates. Clearly, if one was willing to sacrifice some or this safety margin, perhaps the coolant flow rates could be reduced by some percentage without affecting the disk cooling substantially. Obviously if such a reduction is envisaged, much more detailed 2-D and 3-D simulations and experiments need to be done to ensure that adequate cooling is indeed still available even after the reduction in the coolant flow rates. The high-pressure, coolant air is expensive and represents a loss in engine power and efficiency. Hence the possibility in coolant flow reductions is one of the major considerations behind engine performance enhancement via secondary flow stream optimization.

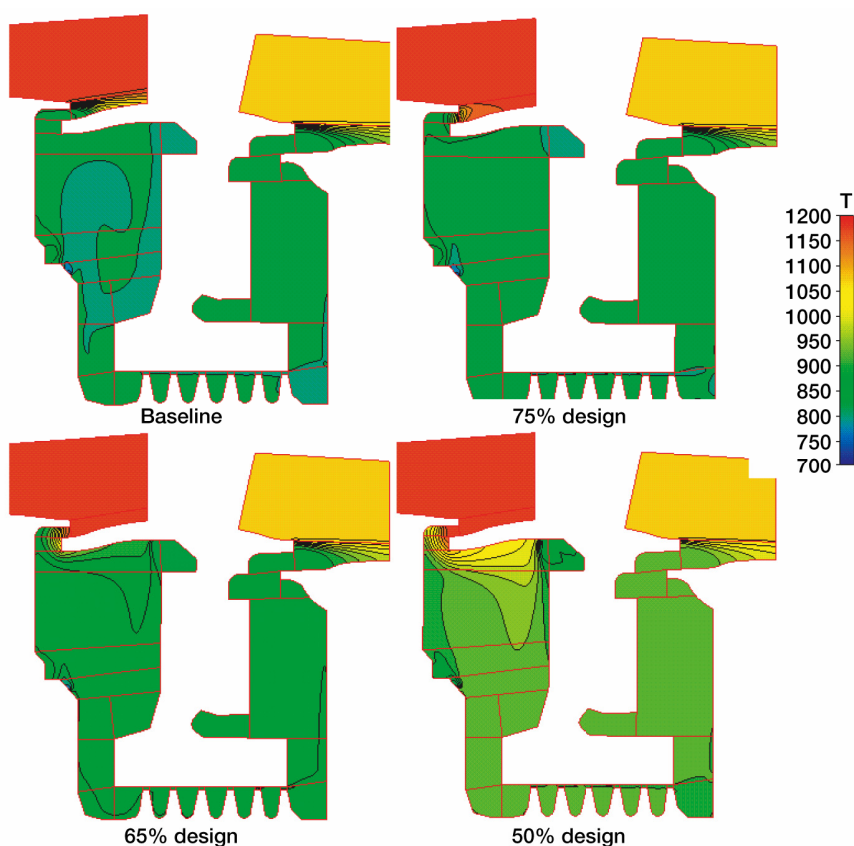


Figure 2-8.—Effects of reduction in purge flow rates on the temperature fields in stage 1-2 cavities.

Another parametric study on the Stage 1-2 cavity involved calculations of the cavity flows under the influence of a sudden change in the powerstream conditions, such as would take place during the change of an engine power setting, e.g., from fast idle to take-off power and takeoff-power to cruise. Steady state simulations for the initial condition (e.g., fast idle) were first obtained, then the powerstream conditions changed/ramped to the another set (e.g., takeoff) and the effects of the change on the cavity flow were calculated. Details of the computation are given in [6]. The simulations showed that under both these power setting changes, the cavity flows remained fairly stable, and did not ingest powerstream gas, even when switching from fast idle (low pressures in powerstream) to takeoff (maximum temperature and pressure conditions in powerstream).

2.2 Complete Turbine Drum Flow and Conjugate Heat Transfer Simulations

As remarked in the previous section, the walls of the rotors and stators were assumed to be adiabatic in the earlier calculation. Clearly this is not a correct boundary condition, and in the absence of temperature/heat flux profile data, can lead to thermal field solutions that may contain discrepancies. In order to estimate such differences, the entire turbine drum was considered in the next set of calculations. All of the solid parts under the blade platform, including all four rotor disks and the supports of the honeycomb stators were included in the solution domain. The computational model of the entire turbine drum is shown in figure 2-9, where the fluid and solid parts are marked, as well as the flow and thermal boundary conditions. As seen in this figure, the computational domain, which contains fluid as well as solid parts, is very complex. A multi-domain grid with 140 domains and 91K cells was built for these

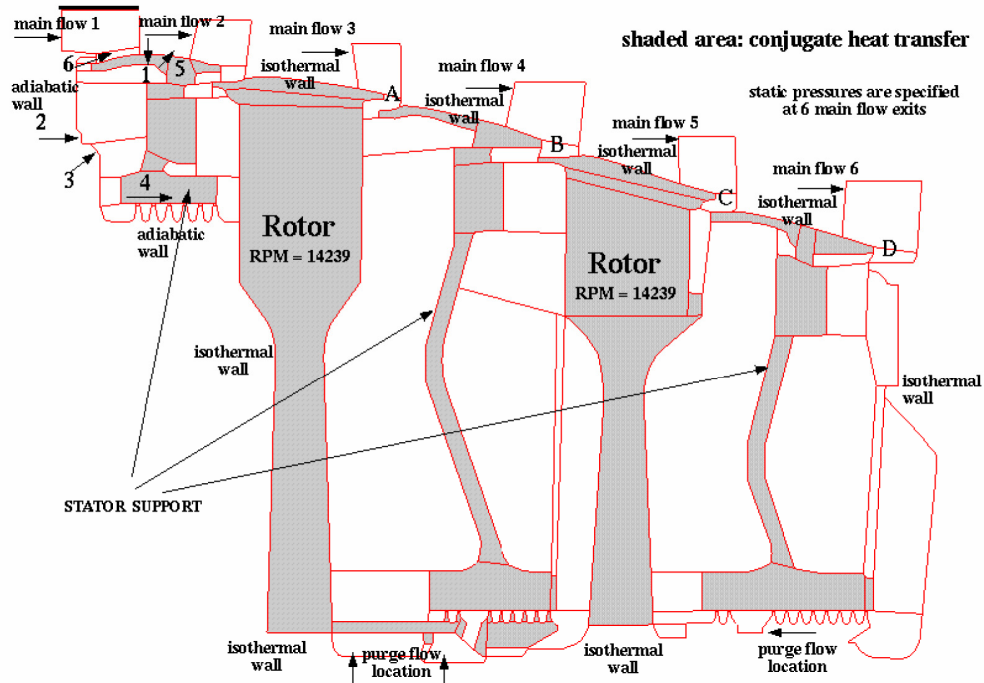


Figure 2-9.—Flow domain and conditions for the conjugate heat transfer calculations of all inner disk cavity pairs.

simulations. A small-scale grid independence study showed that changes in the grid sizes showed small effects on the flow solutions.

Working fluid for this calculation was also taken as air with variable properties. The six powerstream domains with the associated inlet and exit boundary conditions as well as all the cavity purge flow locations and the flow rates were also kept the same as for the individual cavity pair calculations. The main difference here was the use of implicit, conjugate heat transfer conditions at all of the walls that were in contact with the working fluid in the disk cavities. Isothermal conditions were imposed at the blade platform walls that are in contact with the powerstream, with temperature values that corresponded to the local powerstream fluid temperatures. Boundary conditions at the bases of the rotor disks as well as the outer walls of rotor 1 and rotor 4, and the walls of the labyrinth teeth also were boundaries where external thermal conditions were needed. In the present calculations, these walls were assumed isothermal, with the wall temperatures set at the coolant temperature. The reasoning for this was that these solid parts are in contact with the coolant flow, and hence at or near the coolant temperature. The standard k- ϵ model was used to treat turbulence.

The results of the simulations are shown in terms of field plots of streamlines, temperatures and pressures in the computational domain. Figures 2-10 through 2-12 show these plots for the entire drum. The radial extents of Stage 1-2 cavity-pair are much different from the other two pairs, and plots of Stage 1-2 pair are shown separately in subsequent plots for clarity.

Results for the Stage 1-2 cavity pair are shown in figure 2-13a (streamlines) and 2-13b (temperature). The basic streamline/flow pattern is very similar to that shown in figure 2-4. An egress of cavity fluid in the powerstream is seen at both rim seals (path No. 4 and 6). The temperature plot in figure 2-13a also shows the distribution in the solid parts of the computational domain (seal support, rotor disk). Compared to figure 2-5, the cavity temperatures are generally higher. The temperatures in the rotor disk and the labyrinth seal supports show highest temperatures near the upper side where the solids are in contact with the powerstream gases. The temperatures then decrease as one moves towards lower radii, indicating that there is conductive transfer of heat in the solid parts from the hot powerstream gases to the cavity flow.

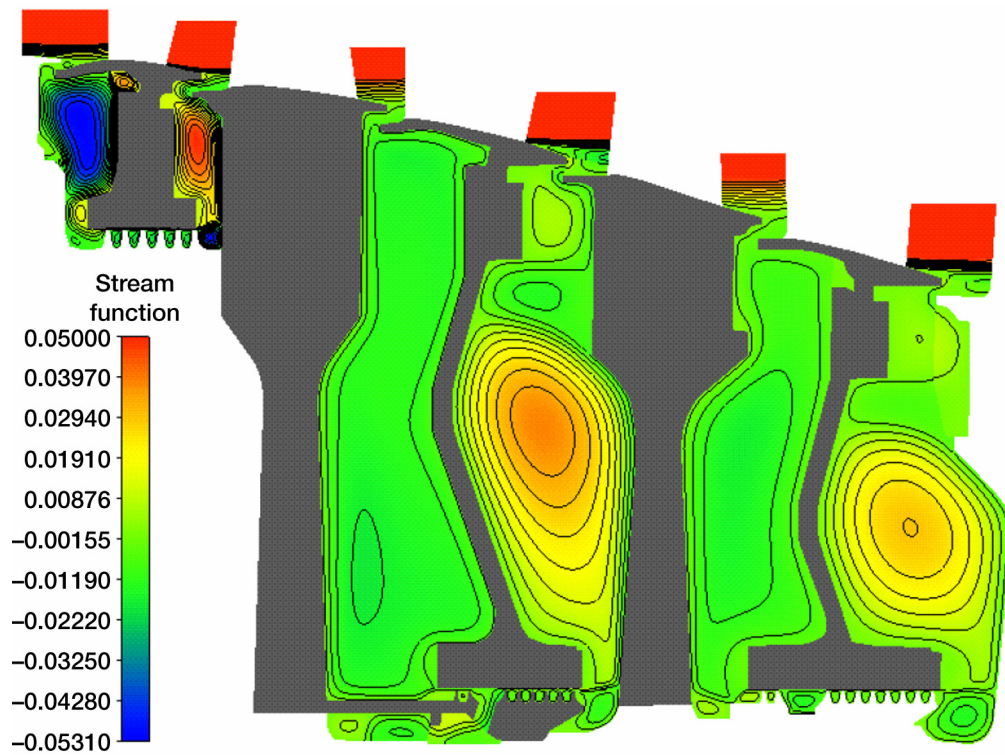


Figure 2-10.—Stream function plot for all inner disk cavity pairs in the turbine drum.

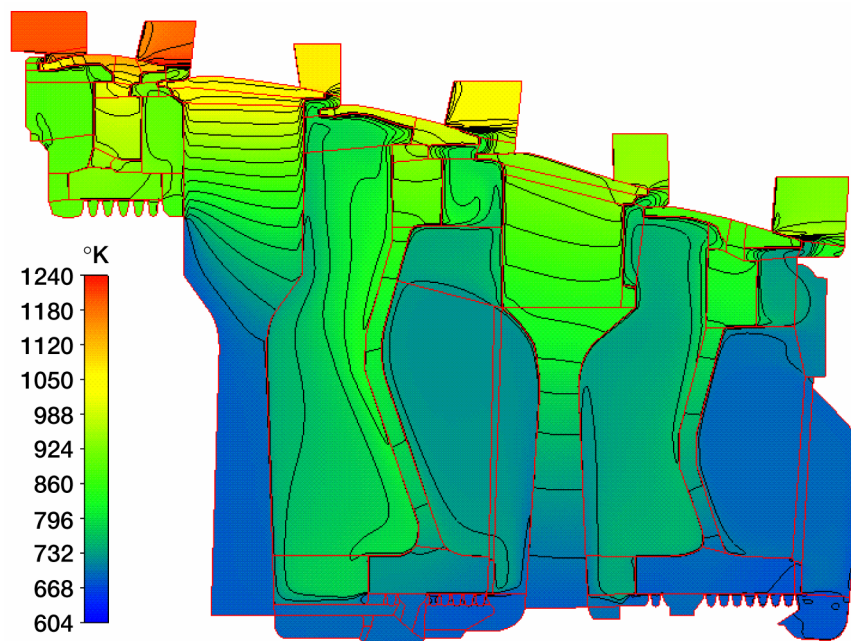


Figure 2-11.—Temperature field in fluid and solid parts of the turbine cavities.

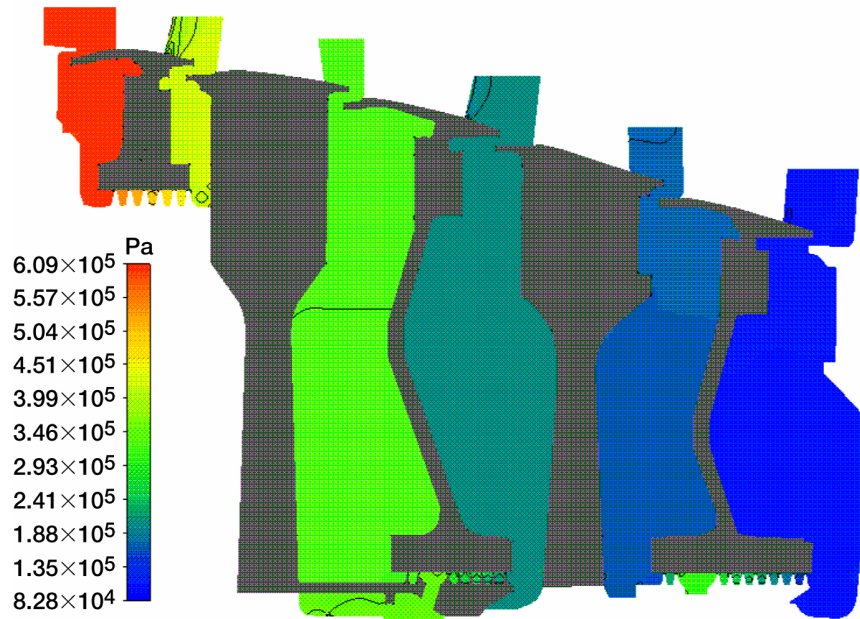


Figure 2-12.—Static pressures in the inner disk cavity flow fields for the turbine drum.

This heat transfer represents additional heat load on the coolant flow supplied in the cavity, and this is reflected in an increase in the cavity flow temperature levels.

Corresponding streamline and temperature plots for the Stage 2-3 and 3-4 cavities are shown in figure 2-14a and 2-14b. Again, the cavity streamline pattern is similar to the pattern obtained with isolated cavity calculations (see figs. 2-3a and 2-3b), with an elongated, weak recirculation zone in the upstream cavity in each pair, and a strong zone in the downstream cavity. Flow patterns at all rim seals (Paths marked A – D in figure 2-9) show cavity fluid egress into the powerstream flow. Temperature contour plots show strong temperature gradients in the rotor disks, with highest temperatures near the blade platforms, and decreasing towards smaller radii. This temperature gradient generates additional thermal load on the coolant flows with a consequent increase in cavity flow temperature, similar to the Stage 1-2 cavity flow.

The additional thermal loads imposed on the cavity flow by the conduction in the rotor disks and labyrinth seal supports can be assessed by considering the gas temperatures at the rim seals. These results are shown in tables 2-4 and 2-5, together with the RRAE design numbers. Also shown in the tables are the results of the earlier calculations, where the conduction in solids was not considered. As seen from these tables, the calculated mass flux rates through the various rim seals show minimal changes as a result of the inclusion of the conjugate heat transfer in the solid parts. The gas temperatures through the rim seals, however, show an increase from the earlier solutions which varies from 4 K to 70 K for the Stage 2-3 and 3-4 cavity pairs and the increase is about 30 K at the upstream rim seal, path 6, in the Stage 1-2 cavity pair. This increase represents the thermal load placed on the cavity flow by conduction in the solid parts. The temperatures are generally higher than the RRAE design numbers, where the heat transfer through the solid parts was not included. The temperature increases in the rim seal gas flows are fairly substantial and indicate that the conjugate heat transfer problem with conduction in the solid parts has to be considered when performing these calculations. The usual way of calculations with adiabatic walls will generate gas temperatures that will be cooler than actual, and thus overpredict the cooling performance. This can lead to inadequate cooling performance in an actual engine, especially as the coolant flow rates get optimized.

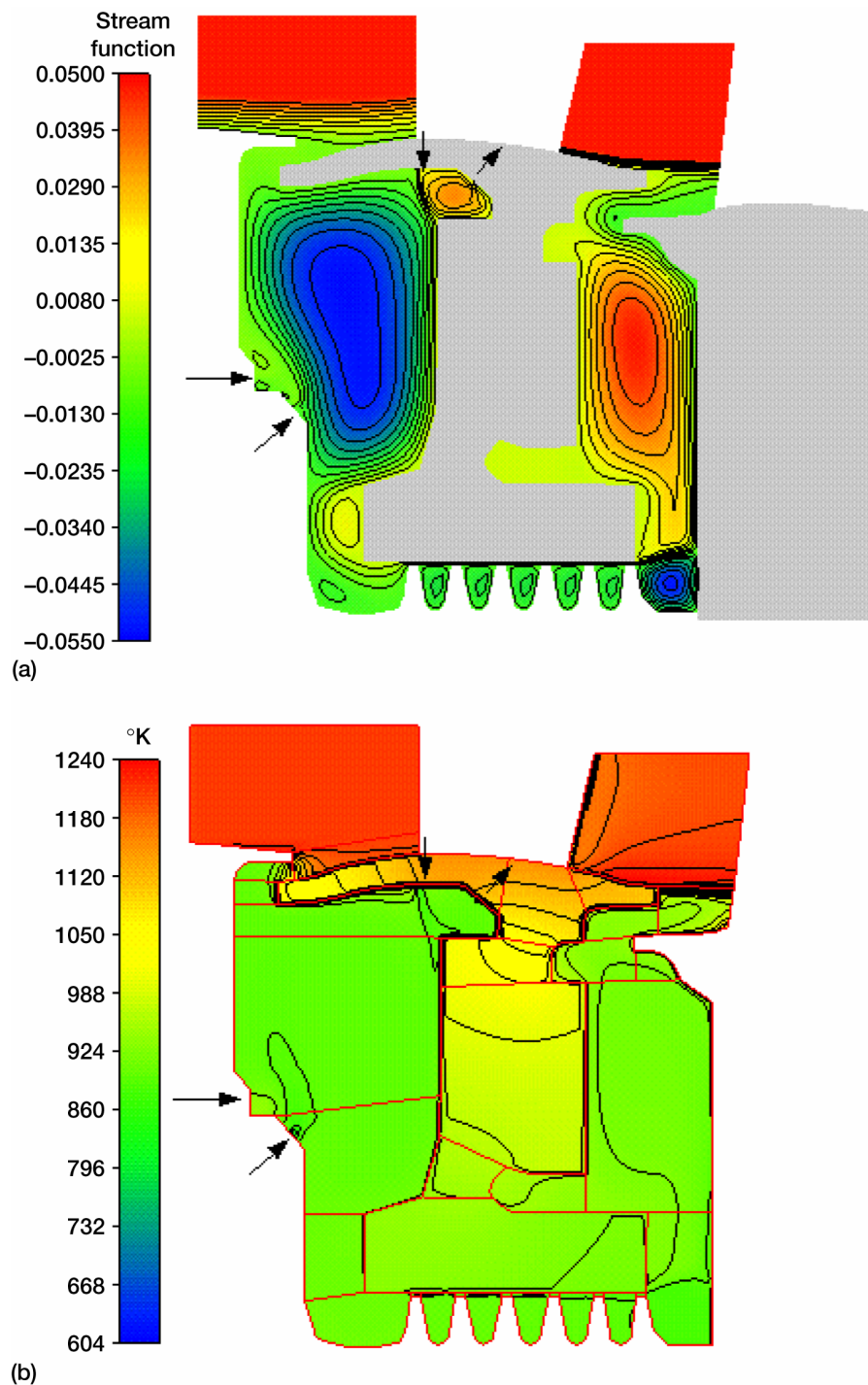


Figure 2-13.—Details of streamlines and temperatures in stage 1-2 cavities with conjugate heat transfer. (a) Stream function distribution inside the stage 1-2 cavities. (b) Static temperature distribution inside the stage 1-2 cavities and the central support wall.

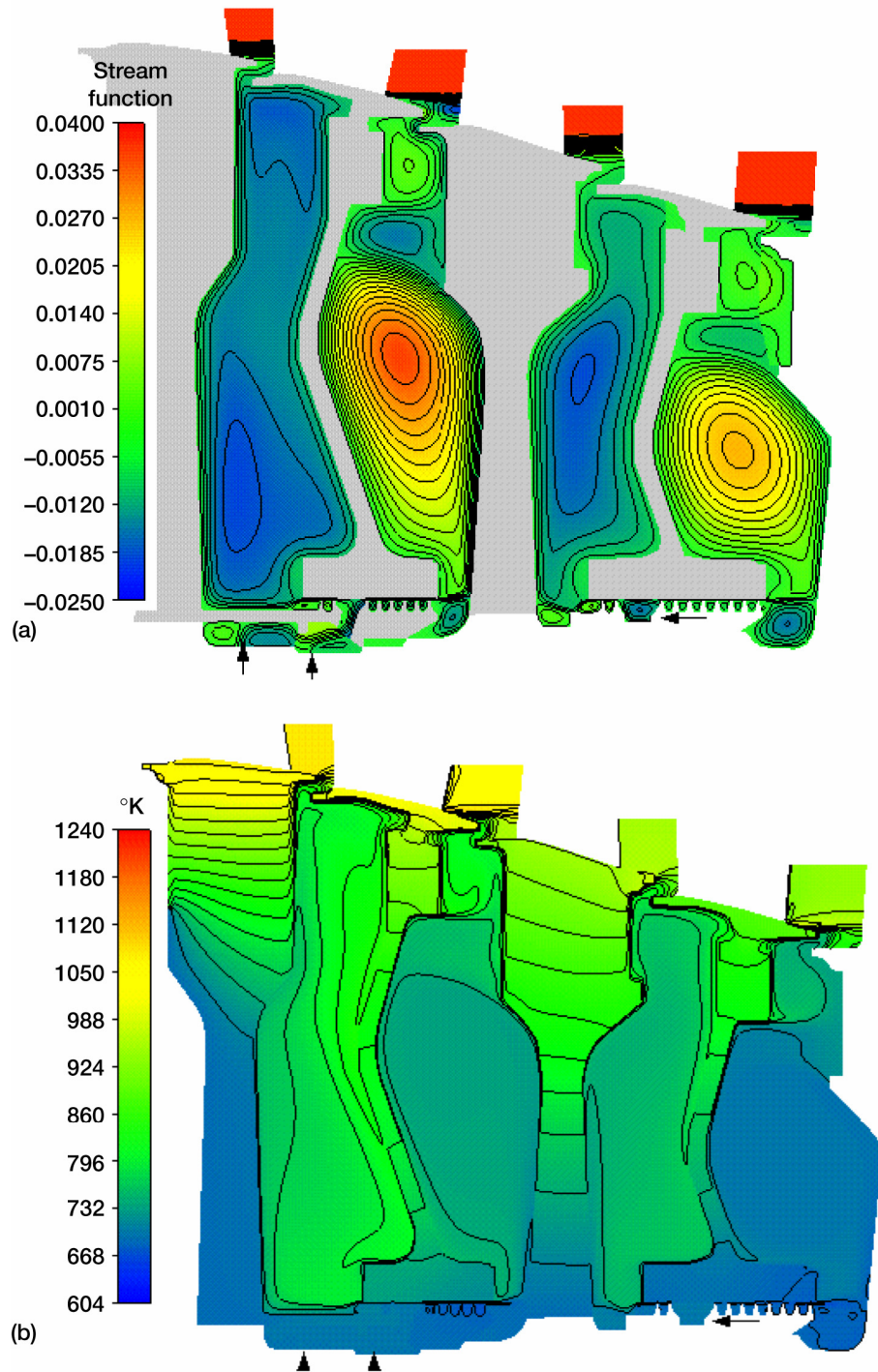


Figure 2-14.—Stream function and temperature fields in stage 2-3 and 3-4 cavities (conjugate heat transfer included). (a) Stream function distribution inside the stages 2-3 and 3-4 cavities. (b) Static temperature distribution inside the stages 2-3 and 3-4 cavities, the central support walls, and the rotor support walls.

TABLE 2-4.—COMPARISON BETWEEN THE DESIGN DATA AND THE PREDICTION FOR STAGE 1-2 CAVITIES (SEE FIGURE 2-2A FOR PATH NO. NOTATION)

Path No.	Design		Prediction (include conjugate heat transfer for solid parts)		Prediction (without conjugate heat transfer)	
	Massflow (kg/s)	Temperature (K)	Massflow (kg/s)	Temperature (K)	Massflow (kg/s)	Temperature (K)
4	0.1129	843	0.1284	870	0.1397	829
5	0.0186	843	0.0249	984	0.0136	827
6	0.0449	843	0.0481	893	0.0431	866

TABLE 2-5.—COMPARISON BETWEEN THE DESIGN DATA AND THE PREDICTION FOR STAGES 2-3 AND 3-4 CAVITIES (SEE FIGURE 2-2A FOR LOCATIONS NOTATION)

Location	Design			Prediction (include conjugate heat transfer for all solid parts)			Prediction (without conjugate heat transfer)		
	Mass (kg/s)	Pressure (Pa)*x10 ⁵	Temp. (K)	Mass (kg/s)	Pressure (Pa)*x10 ⁵	Temp. (K)	Mass (kg/s)	Pressure (Pa)*x10 ⁵	Temp. (K)
A	0.0567	3.309	741	0.0390	3.282	790	0.0376	3.275	786
B	0.0376	2.137	698	0.0522	2.089	794	0.0540	2.068	716
C	0.0340	1.724	705	0.0249	1.6823	769	0.0240	1.689	700
D	0.0309	1.103	703	0.0263	1.082	732	0.0272	1.069	666

*Values at the center of the cavities

2.3 Summary

To summarize this chapter, the flow and heat transfer processes in the turbine section of the RRAE T-56 engine were simulated. Three pairs of inner disk cavities in the turbine section were first individually considered at the design operating point and simulations showed flow egress into the powerstream at all rim seals. The rim seal temperatures correlate well with RRAE design data. Stage 2-3 and 3-4 flow splits in the two cavities, however, showed discrepancies from the design data, which may have been due to coolant flow injection location mismatch and/or grid refinements. Stage 1-2 cavity flows showed good agreement with design data. Dramatic effects on the Stage 1-2 cavity were seen with increase in the labyrinth seal clearance, and demonstrated the sensitivity of the cavity flows to this parameter. Simulations on Stage 1-2 cavity pair with varying coolant flow rates also indicated that powerstream gas ingestion did not occur till the coolant flows were reduced to 50 percent of the design values. Such information will be of significant use when designing the cavities with optimized coolant flow rates.

The complete turbine drum calculation including heat-transfer in solid parts indicated that heat conduction in the solids provided another path for the hot powerstream gas to transfer thermal energy to the cavity flows. This thermal load resulted in increase in the overall temperature levels in all inner cavities. These effects can be substantial and need to be included when assessing the effectiveness of the coolant in the disk cavity flows. Additional studies are needed to further explore some of the differences found in the calculated results and RRAE design data.

3. Aspirating Face Seal Modeling

An enhanced aspirating face seal is being evaluated by GE Aero Engine Co. (GEAE), GE Corporate Research and Development Center (GE CR&D)[7-9] and NASA Glenn Research Center. The seal is being considered as a replacement for labyrinth seals in aircraft engines for reduced leakage and improved engine efficiency. This chapter deals with the simulation work that was performed during the design stages of this seal as well as the full scale testing in a test rig during which a performance problem

design stages of this seal as well as the full scale testing in a test rig during which a performance problem was discovered. Using 3-D simulations of the face seal flow, the reason for the performance problem was identified and a fix suggested. This fix was tried out successfully in the test rig and the seal performance with the fix was found to be very close to the original design specifications. Following sections describe the seal configuration, the simulation work that was performed during the initial design stages as well as during the rig-testing phase.

3.1 Aspirating Seal Geometry and Operation

The aspirating face seal is being considered as a replacement for the conventional labyrinth seal, especially at larger diameters. The labyrinth seal typically has larger clearances with increasing diameters, with consequent increased leakage, and hence the aspirating face seal design is expected to be very attractive in large diameter seals. The seal is non-contacting type, with a typical working clearance of 0.0015 to 0.003 inches. Unlike the conventional face seals, the aspirated face seal design has a clearance that is dynamically adjusted depending on the seal operating conditions. The seal relies on a hydrodynamic air-bearing to provide a stiff air film that generates the film loads to maintain the working clearances to prevent rubbing and thus provide long operational life.

A schematic of the seal is shown in figure 3-1 (also table 3-1). The high-pressure air is located on the seal inner diameter and the low-pressure air is on the outer diameter side. The L-shaped component is the primary seal. A secondary piston ring is provided on the primary seal to allow the primary seal to translate axially in response to air pressure changes and rotor motion. A garter spring and a set of axial compression springs keep the piston ring seal in its housing and provide sealing force.

The primary seal is mounted on the seal housing on rotation locks. A number of retraction springs located at the outer circumference of the primary seal provide the force needed to retract the seal away from the rotor when there is no air pressurization. The primary seal has two load bearing surfaces that face the smooth surfaced rotor: a primary seal dam and the hydrostatic bearing, which are separated by a circumferential vent slot. The air bearing has a number bearing feed holes located circumferentially, which are connected to the high-pressure side and deliver high-pressure air to the bearing to create a load-bearing film.

The leakage air going radially outward from the dam and inward from the bearing is collected in a vent slot/trench and vented to the low-pressure region through several axial and radial slots, also placed at several circumferential locations. A labyrinth tooth (called as aspirating tooth) controls the flow rate through the seal dam when the seal is in open position. At equilibrium, the various forces that act on the seal are shown in figure 3-2. Forces F_1 and F_2 are generated in the hydrostatic bearing and the dam respectively and the two forces act to open the seal. The high-pressure air at P_{high} generates a force F_b on the seal that tries to close the seal gap. The retraction spring force, F_s , acts to open the seal as well. The sliding friction at the secondary piston seal provides a frictional force that opposes any axial motion of the primary seal.

TABLE 3-1.—ASPIRATING FACE SEAL COMPONENTS

1	Primary face seal ring
2	Secondary piston ring
3	Radial garter spring
4	Axial compression springs
5	Seal housing
6	Primary seal dam
7	Vent groove
8	Hydrostatic gas bearing surface
9	Vent slots
10	Aspirator tooth
11	Retraction coil springs
12	Flow deflector (enhanced seal only)

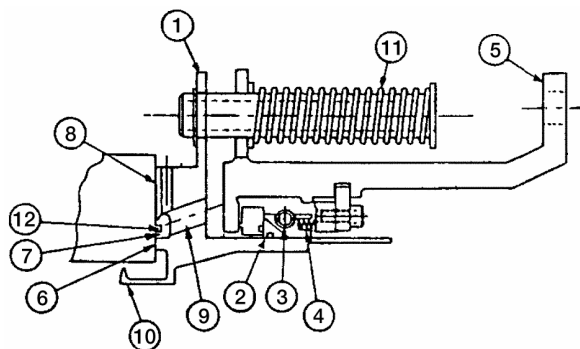


Figure 3-1.—Cross-section of the enhanced 36 in. diameter face seal.

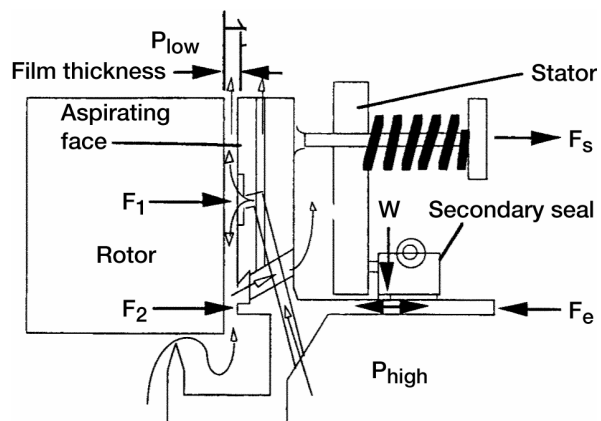


Figure 3-2.—Various forces acting on the aspirating seal.

In the 'open' position, the air pressures are same on the high pressure and low pressure side, and the retraction spring force F_s (see figure 3-2) keeps the primary seal away from the rotor surface at maximum clearance. Once the seal is pressurized, i.e., $P_{high} > P_{low}$, the flow through the labyrinth tooth creates a lower pressure in the lower cavity and a closing force, F_c , is generated due to P_{high} acting on the seal outer surfaces. When the seal closely approaches the rotor, pressure drop now is across the seal dam rather than the aspirating tooth. The hydrostatic bearing, also fed with the high-pressure air, starts providing an opening force that opposes the closing force F_c . The bearing opening force increases rapidly as the seal clearance reduces, and thus the air bearing provides a very stiff air film that provides sufficient balancing force to counteract F_c and F_s and maintain the seal in equilibrium at a design clearance of 0.0015 to 0.003 inches. Any changes in the film thickness are discouraged because of the restoring changes in the bearing servo forces that restore the force equilibrium. The seal will track changes in P_{high} as well as any changes in the rotor position by sliding on the piston ring till the equilibrium position is achieved. The seal can be operated at very tight clearances over the entire range of operating conditions and maintains low leakage rates.

3.2 Simulations Performed

The simulations that were performed on this seal were at two different levels during the seal design and testing program. The first series of simulations were performed during the design stages. 2-D axisymmetric simulations on the overall seal geometry were performed to corroborate the film stiffness and load calculations performed with simpler design codes. These calculations covered a large range of clearance and seal pressurization values. Another of the aim of this study was to assess the seal loads at relatively larger clearances (> 0.01 inches), which are outside the valid range for the design codes. Results for two different aspirated face seals were considered: one was a test seal with a smaller diameter, built to test the validity of the concept. The second seal was the full-size seal that was to be used in the test rig.

The second set of simulations was performed during the testing phase of the full sized rig. This set involved full 3-D simulations of the full-sized seal as well as the smaller test seal. These simulations were performed to analyze the flow field in the seal and to explain anomalous behavior that was observed during the testing of the full-size seal. Details of the two sets of results follow:

3.3 2-D Simulations

These simulations were performed using a 2-D axisymmetric seal configuration. The actual seal has a finite number of radial and axial slots as well as bearing holes that feed high-pressure air to the hydrostatic bearing. For the 2-D results these were converted to channels and the channel widths were adjusted to maintain the flow areas in the 2-D configuration. An 8 domain 2-D grid with 16000 computational cells was built for these simulations and is shown in figure 3-3 along with the boundary conditions.

The working fluid was air and was treated as compressible and with variable properties. The flow in parts of the seal is turbulent and in parts it is near-laminar (e.g., hydrostatic bearings at small clearances). The low-Re $k-\epsilon$ model was used in this case to treat the turbulence, because this model can handle laminarization of flow in the bearing. Total pressure and temperature conditions were specified at the aspirating tooth inlet as well as the inlet to the bearing feed holes. Exit pressure conditions were specified at the radial and axial slot exits as well as at the outer boundary of the bearing.

A representative streamline and pressure plots for the seal flow are shown in figures 3-4 and 3-5. The streamlines show the fluid movement through the seal. The flow from the aspirating tooth enters the dam, accelerates and is dumped into the circumferential vent slot and eventually exits through the axial and radial slots. Nearly half of the bearing flow, fed from the high-pressure air through the bearing feed holes, exits radially outwards. The remaining flow enters the circumferential vent slot, mixes with the flow from the dam and exits through the axial slot.

The seal total leakage and the bearing and dam loads are several different clearance and pressure conditions were calculated, and compared with the design code calculations. In general, the comparison with the design code results was good at small clearances (below 0.004 inches). At large clearances the design code results become somewhat inaccurate. The seal showed very high film stiffness at small clearances. As designed, the pressurized air bearing provided a large fraction of the seal restoring force at

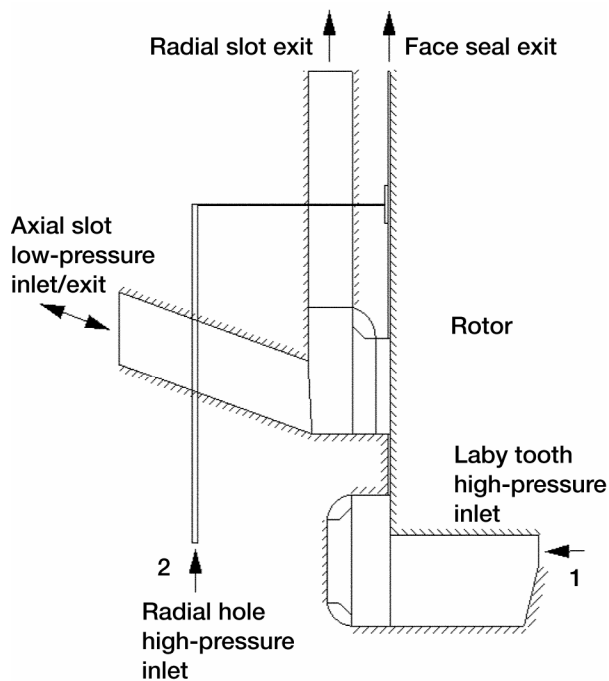


Figure 3-3.—Flow domain and boundary conditions for GE aspirating face seal, 2D representation.

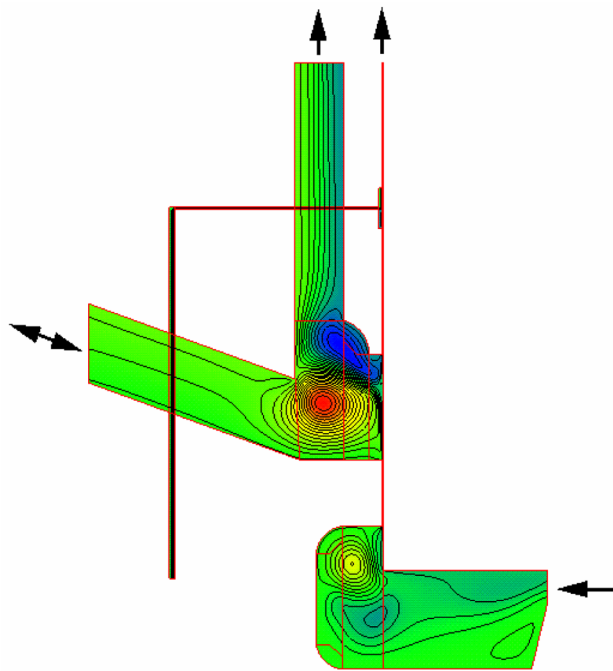


Figure 3-4.—Streamline pattern, 2D simulation of aspirating face seal.

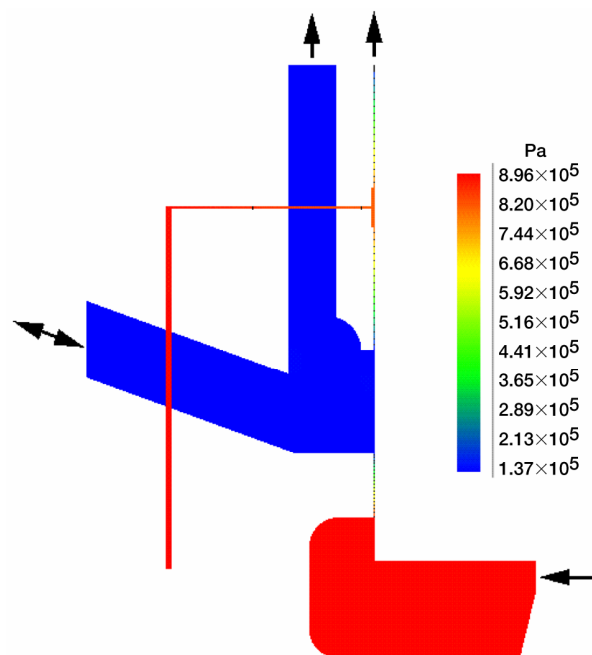


Figure 3-5.—Static pressure distribution in aspirating face seal, 2D simulation.

Wireframe of the CFD model
Bearing open 100%,
2.5 degree sector,
16 mil clearance

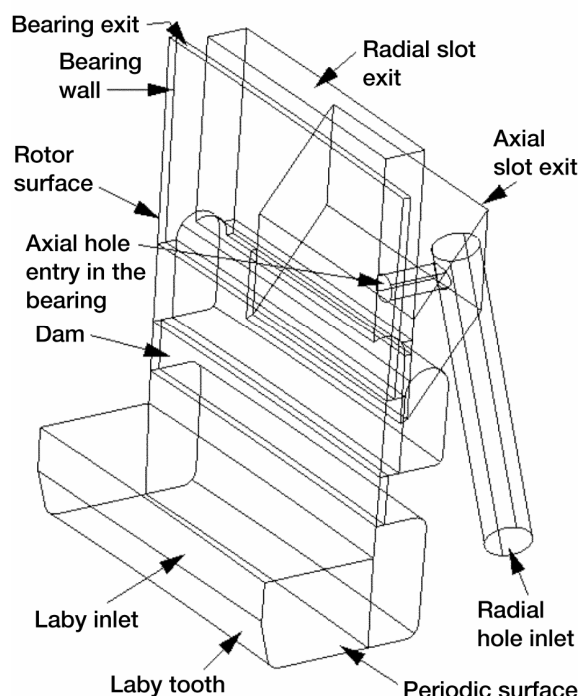


Figure 3-6.—Wireframe model of the GE aspirating face seal.

these small clearances. At larger clearances, the bearing film stiffness dropped rather sharply with much smaller load capacity generated by the bearing. This exercise proved that the scientific code SCISEAL could be successfully applied to complex seal geometries without any special treatment and produce reasonable results.

3.4 3-D Simulations

3-D simulations on the seal were performed during the testing phase of a full-scale model. It was observed during testing that the test seal showed a very stable, repeatable operating clearance of 0.016 inches (at a seal pressurization of 7 psid) as against 0.0015 inches, the design value. In the absence of any empirical or analytical data from the design codes that explained this behavior, the only possible solution was to simulate the flow in the seal in full configuration using 3-D CFD codes, and then to identify the possible causes for the observed behavior. Earlier results on this seal with the SCISEAL code had provided sufficient confidence in the code capabilities, and SCISEAL was again used to simulate the full 3-D seal flow at the observed test rig condition in order to analyze the flow.

3.4.1 Geometry and Flow Conditions.—In order to reproduce the actual flow phenomena as accurately as possible, the actual test seal dimensions were used (as against the design geometry) to build a 21 domain structured grid on the aspirating face seal. The test seal geometry has a large number of radial and axial vent slots that connect to the vent trench, and a representative PI sector of the seal was used to perform the simulations. In the present case, a PI angle of 2.5 degrees was used which included one set of axial and radial vent slots and one bearing feed hole. All other features in the seal are axisymmetric (aspirating tooth, vent trench, rotor, labyrinth cavity). A wire frame model of the computational domain is shown in figure 3-6; also shown in this figure are the flow boundary conditions. A solids model of the seal with all of the working surfaces is shown in figure 3-7.

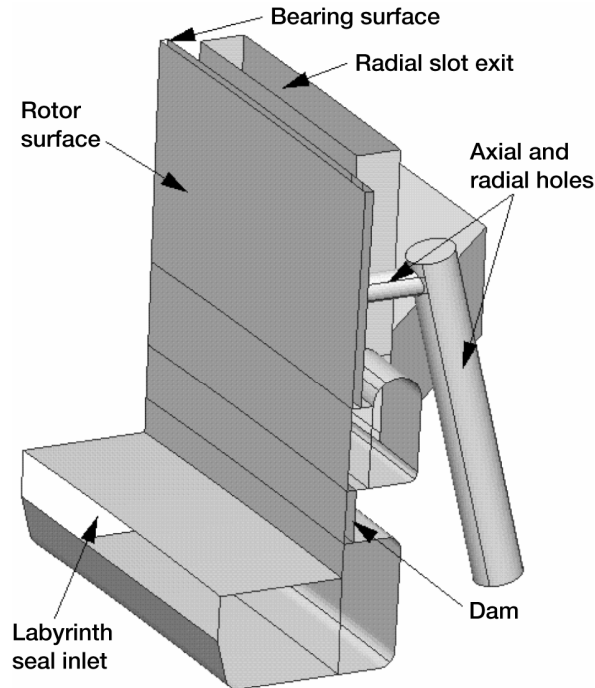


Figure 3-7.—Solids model of the aspirating face seal showing all solid surfaces.

Steady-state simulations were performed at a number of different seal clearance values and pressurizations that were either tried out in the seal rig or were planned for testing. The rotor was kept stationary for both the experiments and simulations. One possible way to simulate the seal is to fix the seal pressure and let the seal clearance change using a force balance model. The other approach was to fix the seal clearance and pressurization at different values and calculate the seal balancing forces to assess the tendency of the seal at that point (closing, opening or in equilibrium). The second approach was used in the present calculations. Similar to the 2-D runs, air was used as the compressible working fluid with variable properties. The standard k- ϵ model, however, was used for turbulence to keep the grid sizes small and economical. All of the walls were assumed adiabatic for these runs.

3.4.2 Simulation Results.—The first simulation run was performed for a seal gap of 0.016 inches and an inlet pressure of 7.1 psid, which was the experimentally observed stable seal configuration. The reaction force values F_1 and F_2 on the dam and the bearing portions of the seal were evaluated by integrating the computed pressure forces on the respective surfaces. The seal opening forces ($F_1 + F_2 + F_s$) were then compared with the seal closing force F_c . The computed values of F_1 and F_2 showed that the seal closing and opening forces were balanced well at the 0.0016 inch setting. This was the exactly the behavior seen in the experiments. The calculated seal leakage rate of 0.98 lb/s also compared well with the experimental value of 1.01 lb/s. This case thus provided a measure of validation and confidence in the computational model. Additional runs then were taken at different clearance values, above and below the stable 0.0016 inch gap. At higher seal gaps, the bearing force (opening) was found to be too small to counteract the closing force F_c and seal showed a tendency to close. At smaller clearances, the seal opening forces $F_1 + F_2$ were found to be higher than the seal closing force, and hence the seal had a tendency to open. This corroborates very well the experimental observations that the seal had a very stable operating point at 0.016 inches gap, and would return to this position when perturbed to higher as well as lower seal gaps.

Flow-field details at the stable configuration are shown in figures 3-8 through 3-11. Velocity vectors in the r-X plane containing the centerline of the bearing feed hole are shown in figure 3-8. Distinct flow

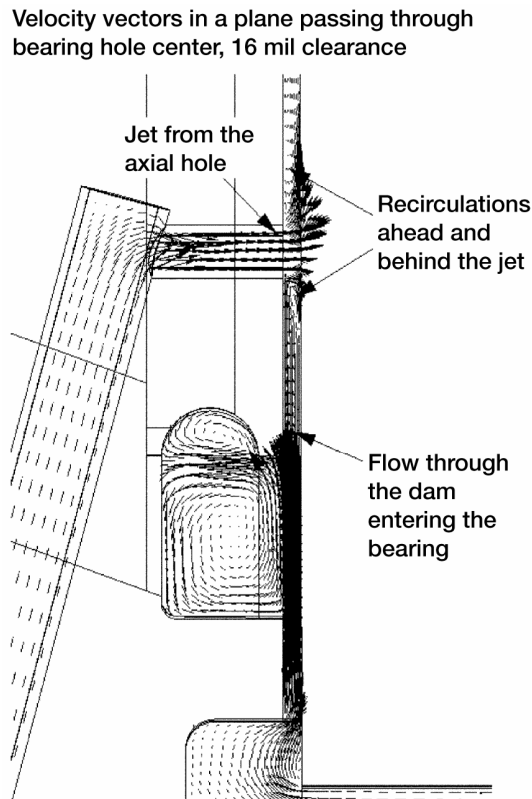


Figure 3-8.—Velocity vectors in the aspirating seal, r-X cutting plane passing through the bearing feed hole centerline.

threads are clearly seen in the plot. High-pressure air enters the aspirating tooth cavity and then the dam, while the feed holes also supply the high-pressure air to the bearing. The flow exiting the dam into the circumferential vent slot/trench has a high velocity, and this air enters into the lower exit of the bearing instead of going out to the low-pressure region through the axial and radial slots. The air coming into the bearing from the feed hole is also swept up by the flow from the dam. A similar r-z section, but midway between the bearing feed holes (figure 3-9) shows that the fast flow from the dam enters the lower bearing exit, and continues uninterrupted till it goes out the outer exit of the bearing. A view of the velocities in the r- θ plane, placed near the seal surface is shown in figure 3-10 and shows the flow from the dam entering the bearing, and interfering with the flow from the bearing feed hole. The characteristic pattern of the interaction between the bearing feed flow and dam flow was also confirmed by oil trace patterns observed on the rotor surface during seal testing. (Personal communication from Mr. Turnquist, GE CR&D)

A pressure plot in the seal gap is shown in figure 3-11 and indicates that the overall pressure level in the bearing is higher than the exit pressure (lower seal pressure), as a result of the dam flow coming into the bearing. This bearing pressurization from the dam flow generated sufficient pressure load in the bearing seal to equilibrate at a gap of 0.016 inches rather than the design value of 0.0015 to 0.002 inches. During the seal design stages, all of the design calculations were performed under two assumptions: (1) The flow from the bearing and the seal dam do not interfere with each other, and these two elements essentially operate independently, and (2) The seal calculations were done at a given clearance, without consideration to the process of bringing the seal to this gap from a 'wide open' initial seal gap. *It is the interaction between the dam flow and the bearing at relatively larger clearances that was found to be the cause of the anomalous seal behavior.*

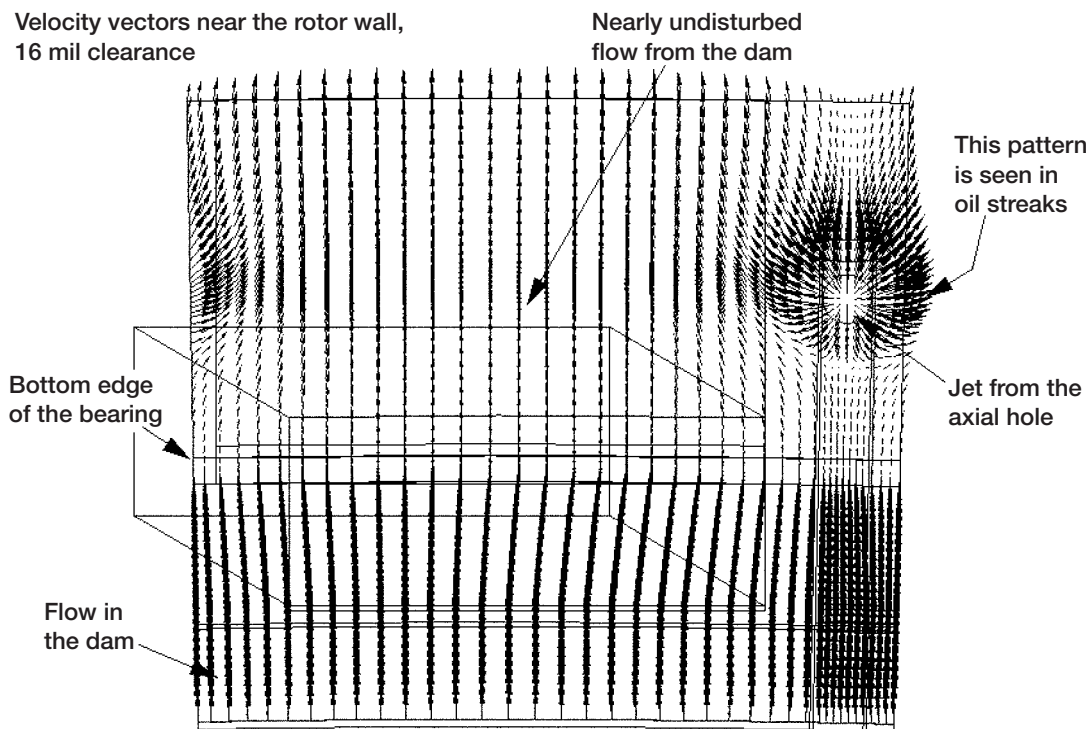


Figure 3-10.—Velocity vectors in a r - θ plane near the rotor wall.

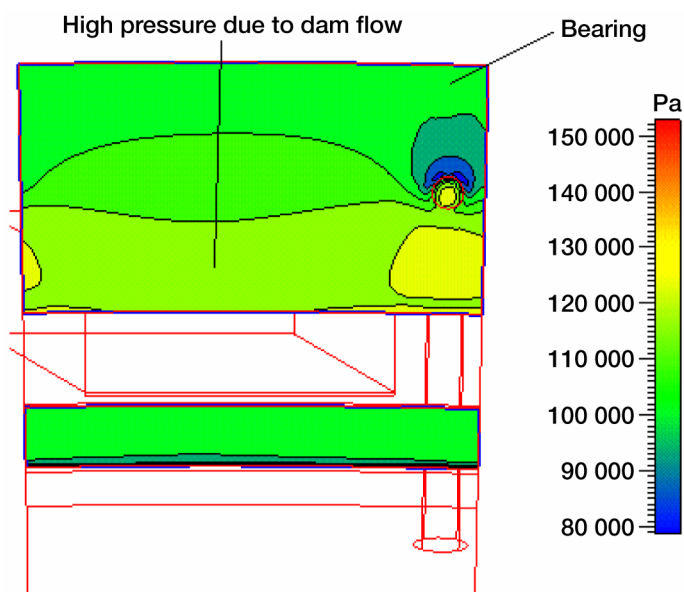


Figure 3-11.—Static pressure plot in the r - θ plane on the seal face, original design.

To test the interference hypothesis, ways to prevent the dam flow from entering the bearing were considered. The simplest was to consider a small ledge wall on the rotor surface located such that it protruded in the circumferential vent slot/trench, at the radial midpoint of the trench. Since the ledge was only to act as a flow diverter, the axial extent of the ledge/protrusion was not thought to be critical, and a small axial width (3 mm) was assumed. A solids model showing the placement and extent of the ledge in the seal model is shown in figure 3-12. Simulations were then performed for a seal clearance of 0.016 inches. This ledge/flow diverter was found to be very effective in diverting the dam flow away from the bearing. This is clearly seen from the velocity plots in figures 3-13, 3-14 and 3-15. The cutting planes for these plots are the same as used in figures 3-8 through 3-10 respectively. The dam flow is seen to make a near 90 degree turn at the ledge (figure 3-13, 3-14) and exit via the axial slot to the seal low pressure region. As a consequence of the flow diversion, the static pressure at the inner radius of the bearing is much lower than before, and the flow from the bearing feed hole now exits both at the inner and outer radii. This is clearly seen in figure 3-15, where the flow velocities at the feed hole are symmetric (compare with figure 3-10). The pressure plot in the seal gap, figure 3-16, shows dramatic changes in bearing static pressures which are now much closer to the vent pressure. This reduction in the computed bearing pressure levels results in a much smaller bearing film force F_2 , and eventually produces a force balance on the seal that closes the seal gap at this setting.

Subsequent to this analysis the test seal was modified to build a small ledge on the rotor and was tested for stationary and spinning rotor and the initial closing performance of the seal now followed the design predictions exactly. This test seal has also been tested at different speeds and pressurization levels and stable, predictable performance has been obtained from the seal over the entire operating envelope. For details, see [8,9] also included in appendix B.

Partial 'solids' model with some of the walls removed to show details of the deflector plate
Viewed from the slot side

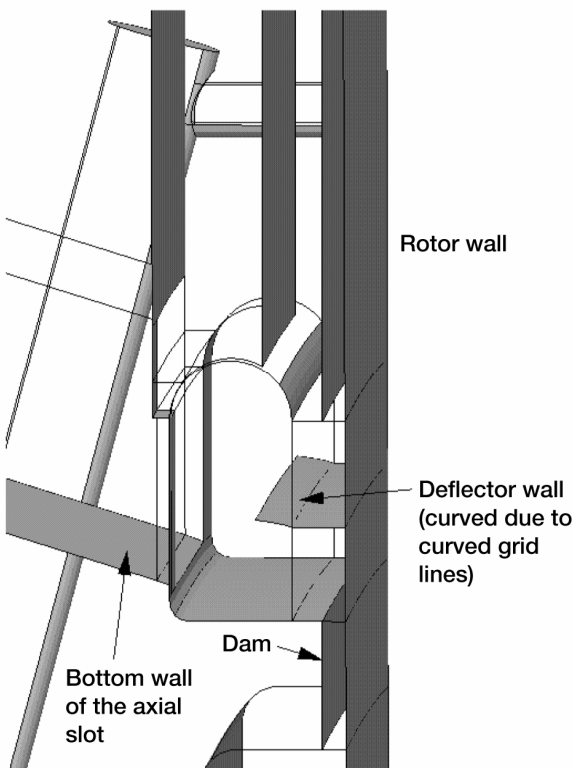


Figure 3-12.—Solids model of the seal with the proposed deflector wall in the circumferential vent.

Velocity vectors in the plane of bearing hole centers, 16 mil, with wall in between the dam and the bearing

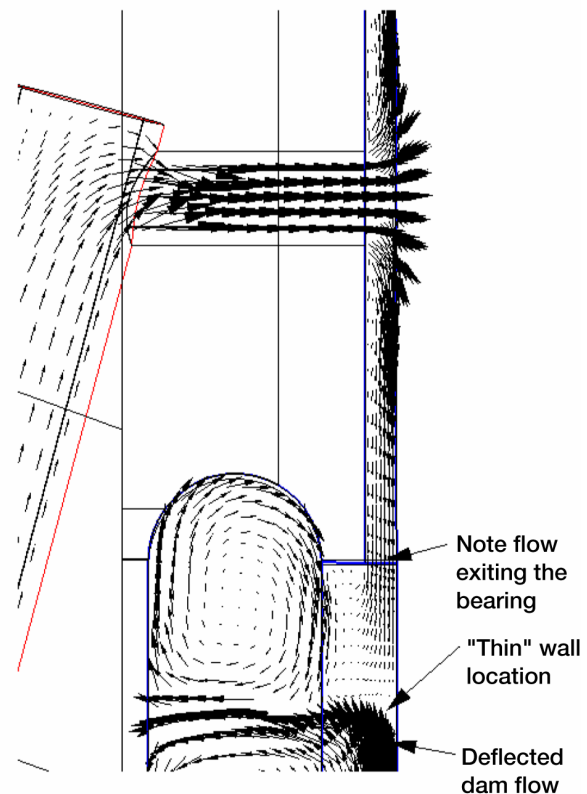


Figure 3-13.—Velocity vectors in r-X plane through bearing hole center for modified seal. Note bearing flow exit at both ends.

Velocity vectors in the midplane of the bearing,
16 mil, with deflector

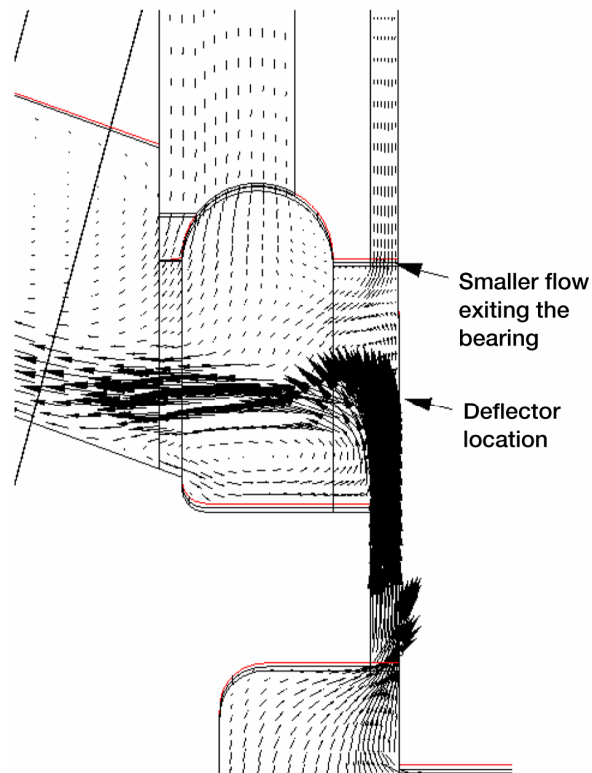


Figure 3-14.—Velocity plot in r-X plane, boundary between bearing holes, modified seal. Note complete deflection of dam flow.

Velocity vectors near the rotor wall,
16 mil, with deflector

Velocity pattern is now similar to the 3 mil case

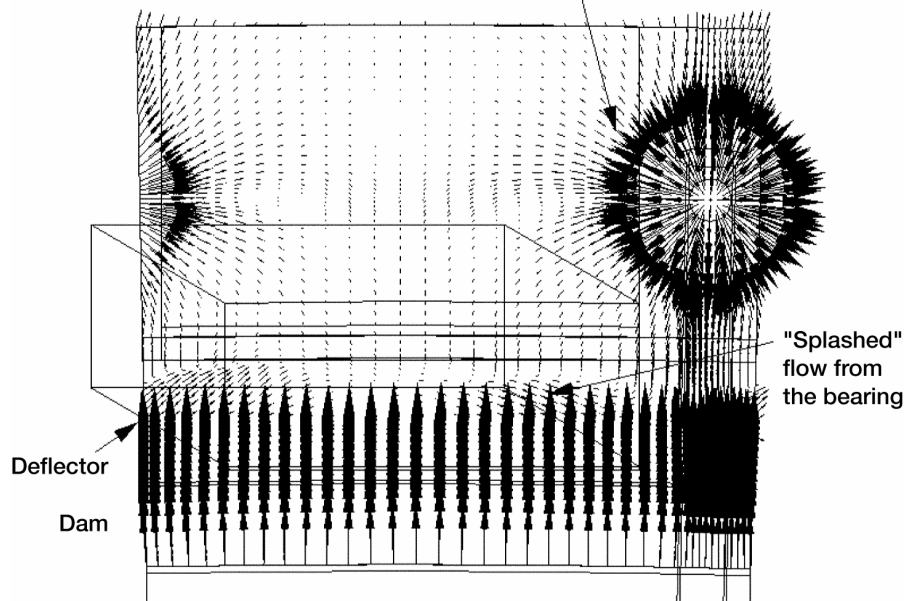


Figure 3-15.—Velocities near rotor wall in r-θ plane, modified seal. Note symmetrical bearing flow.

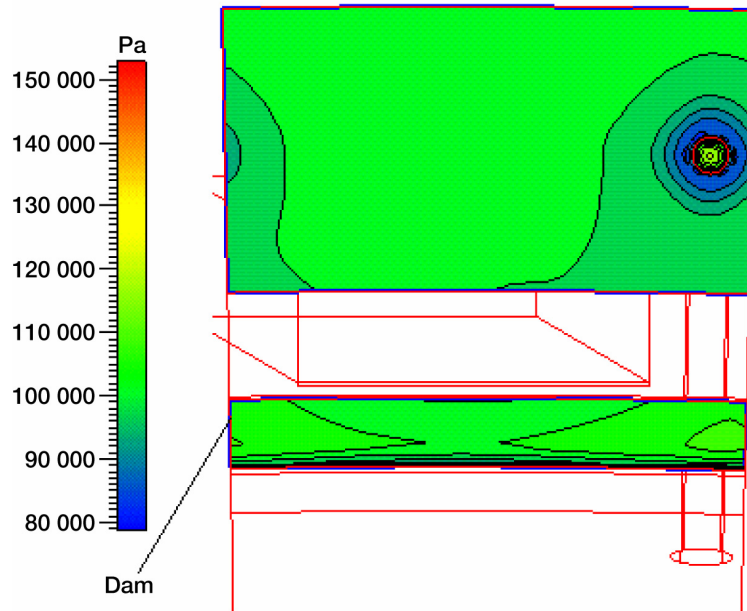


Figure 3-16.—Static pressure in r - θ plane on seal face, modified seal.
Note low bearing pressure levels.

3.5 Summary

The complex flow field in an aspirated face seal was computed both in 2-D and 3-D configurations. The 2-D simulations matched well with the design calculations. However, the 3-D simulations proved of significance in analyzing a test seal that showed considerable deviations in behavior from the designed values. 3-D flow analyses showed the interference of flows in two different components of the seal at large gaps, and pointed to a possible fix. The design codes could not consider these interactions at larger clearances and hence could not predict the anomalous behavior.

This example illustrates the utility of the full 3-D CFD calculations with SCISEAL on this complex problem. The details of the flow field and pressures were reproduced accurately by the code, and provided first the cause of the anomalous behavior, and then suggested a fix which could be tried out in computations to assess its effectiveness. Although the 3-D calculations take much longer to perform than the design calculations with simpler codes, the design codes often can not account for all of the flow phenomena that may take place in a seal. As new and more complex shaped seals are designed and tested, the 3-D CFD calculations definitely have a place in the design procedures. These calculations can provide details of the flow fields as well as seal component performance, point out problem areas and reasons, and aid in the design process to ensure a successful design.

4. Flow and Heat Transfer in Disk Cavities

Rotating cavities with or without throughflow occur in a number of different places in a typical engine. A number of different configurations are possible depending on the location of the cavity. Cavities near the rim seal typically have a combination of a rotating and stationary walls, while the cavities nearer the centerline can have all rotating walls. In the turbine section, the cavity throughflow is typically the coolant air that purges the cavity and cools the rotor disk temperatures. To effectively estimate the cooling performance in the disk cavities one needs to assess the accuracy of the numerical codes that are being used. This chapter deals with two studies of flow and flow+heat transfer in typical disk cavities found in the turbine sections. Experimental data was available for the two studies, and the

SCISEAL code was used to simulate the flow problems at different operating conditions and the numerical results compared with the experiments to assess the accuracy of the predictions.

Of the different turbulence models that are available in SCISEAL, the standard k- ϵ model and the low-Re k- ϵ models are two models that are widely used. Part of the efforts in this task were devoted to assess the results from these two models on the same flow problems, in order to evaluate the accuracy of the predictions and to assess the efficacy of using these models to handle the typical disk-cavity problems encountered in gas turbines.

Of the two sets of calculations considered here, one dealt with the flow in a cavity formed by two contra-rotating walls and the experimental details and data are presented by Kilic et al,[10] and Gan et al [11]. The cavity flows were run at different relative disk speeds and throughflow rates. This type of cavities are encountered in turbines with contra-rotating shafts.

The second set of calculations included flow and heat transfer in a cavity with co-rotating walls, with a coolant throughflow. The experimental details and data are given by Northrop et al [12]. Heat transfer characteristics on the cavity walls were compared with experimental data.

Details of the calculations and computations are given in the following sections.

4.1 Flow in Contra-Rotating Disk Cavity

This Section summarizes the flow simulations performed in a cavity formed by a pair of rotating disks. A schematic of this configuration is shown in figure 4-1.

As shown in the figure, the cavity is formed of two disks with outer radii R of 391 mm. Each of the disks carries a shroud along the outer periphery which rotates with the disk. A gap of width s_c exists between the two shrouds which allows radial egress of air as shown. When a 'purge' air flow is used, it is introduced through a central hole of radius a in the left disk, and then passes up radially through the two 'gauze' tubes shown which are attached to the two disks and rotate with them. The tubes even out the variation in the radial velocity as the flow enters the cavity, but only partially, especially at higher purge flow rates. The overall geometry is described in terms of three aspect ratios whose values are: the gap ratio $G = s/R = 0.12$, the clearance ratio $G_c = s_c/R = 0.016$ and the inner-to-outer radius ratio $a/R = 0.128$.

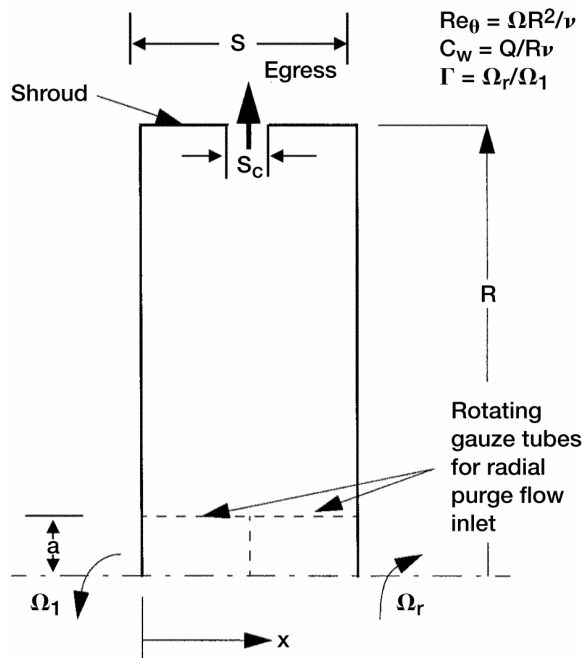


Figure 4-1.—Schematic of contra-rotating cavity.

Two series of experiments were reported in Kilick et al.[10] and Gan et al..[11]. In one case the disk speeds were varied with no purge flow, and in the second series, the disk speeds were fixed, and purge flow rates were varied. In both cases, velocity measurements were taken at different radial locations, and the radial and tangential velocities were measured across the gap in the disks along the X direction. The two velocity components were normalized with the local wall swirl velocity $W_1 = \Omega_1 r$ and plotted as a function of the axial distance normalized with the cavity gap X_{\max} . Details of the two computational series are described below.

4.1.1 No Purge Flow, Varying Disk Speeds.—In the first series, the left disk was rotated at a constant angular speed at a nominal $Re_0 = 1.25e6$. The right side disk was rotated in the opposite direction at varying speeds, to get different angular speed ratio ($\Gamma = \Omega_r/\Omega_l$) values from 0 to -1.0 . No purge flow was used in this series. Simulations were carried out for five Γ values of 0.0, -0.4 , -0.6 , -0.8 and -1.0 . Of these, shown in this note are results for $\Gamma = 0.0$, -0.4 and -0.8 .

A 2-D axisymmetric grid with 67 cells in the axial direction and 110 cells in the radial direction was generated for this series. The flow domain covered the entire cavity from $r = 0$ to $r = R$. The shroud gap was blocked with a linear imposed tangential velocity to account for the variation from one shroud to the other. The flow was taken as constant property and incompressible, with no-slip walls on disk and shroud surfaces with the appropriate angular speeds. The low-Re k- ϵ model was used for turbulence treatment and the grid spacing near the walls was close enough to get nondimensional wall distances $y^+ < 0.3$ in most cases.

As mentioned above, the experimental results were in the form of plots of normalized velocity components Vs. axial distance, plotted at normalized radial distances of $r/R = 0.6, 0.7, 0.8$ and 0.85 and at $\Gamma = 0.0, -0.4$ and -0.8 . These are shown in figures 4-2 through 4-4. Also shown in the plots are the experimental data for comparison. In general the comparison between the numerical and experimental data is good to very good, and the changes in the flow due to the varying right-disk-rotation are picked up correctly. A description of the flow structure changes (in terms of the streamlines) with the right-hand disk speed is given in [10] and the streamline patterns calculated in the present simulations match well with the computations reported in [10].

4.1.2 Constant Disk Speeds, Varying Purge Flow Rates.—The disk rotation speeds ratio was fixed at $\Gamma = -1.0$, and the radial throughflow rate was varied (see Gan et al.. [11]). The purge flow rate was specified in terms of a flow coefficient C_w , defined as $C_w = Q/Rv$ where Q was the volume flow rate and v the kinematic viscosity. Four flow coefficient values were analyzed: $C_w = 0.0, 2320, 6310$ and 9280 . For the zero purge case (Case 1), the grid used was similar to that used in previous Section. For the nonzero purge flow cases, the computational domain was changed from Case 1 by moving up the lower boundary to coincide with the gauze tubes. A uniform radial velocity was imposed at the inlet boundary to generate the purge flow, and a tangential velocity corresponding to the surface speed of the gauze tube was also imposed.

The nonzero purge flow cases were simulated using both the low-Re turbulence model as well as the standard k- ϵ model to assess the differences in the solutions obtained with these models. The grids used in the low-Re case had 67 and 95 cells in the axial and radial directions respectively, and yielded a nondimensional wall distance y^+ of < 0.3 at all cells near the walls. For the standard k- ϵ model, the grid size was reduced to 47 and 88 cells in the axial and radial directions, to ensure that the first cell away from the wall stayed in the proper y^+ range ($y^+ > 11.5$ for the first cell) for the wall functions.

As in the previous series, the tangential and radial velocities were measured in the experiments at several radial locations across the cavity gap. Plots of the calculated normalized velocities (with the low-Re k- ϵ turbulence model) as a function of the axial distance at different radial heights are shown in figures 4-5 through 4-8. Also shown are the experimental data for comparison. As in the previous Section, the agreement between the two data sets is good to very good. Computations presented in Gan et al. [11] also show similar agreement with the experimental data, albeit their treatment of the inlet boundary condition for the nonzero purge flow cases is somewhat arbitrary. Under the conditions described, the inflow condition used in the present study appears to be more reasonable. In actuality, the

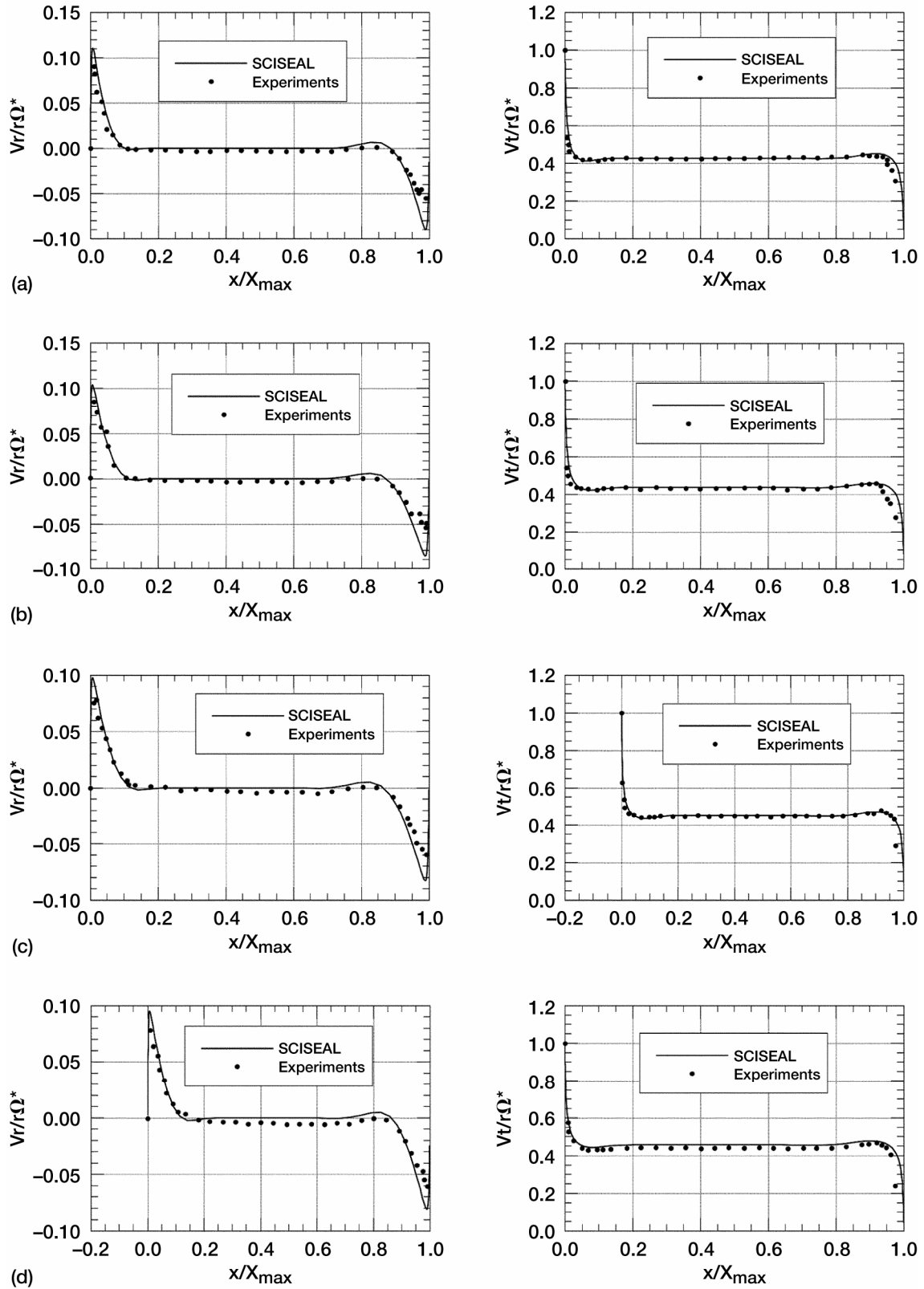


Figure 4-2.—Normalized radial (left column) and tangential (right column) velocities, no purge, $\Gamma = 0.0$, $Re_\phi = 1.25 \times 10^6$. (a) $r/R = 0.6$. (b) $r/R = 0.7$. (c) $r/R = 0.8$. (d) $r/R = 0.85$.

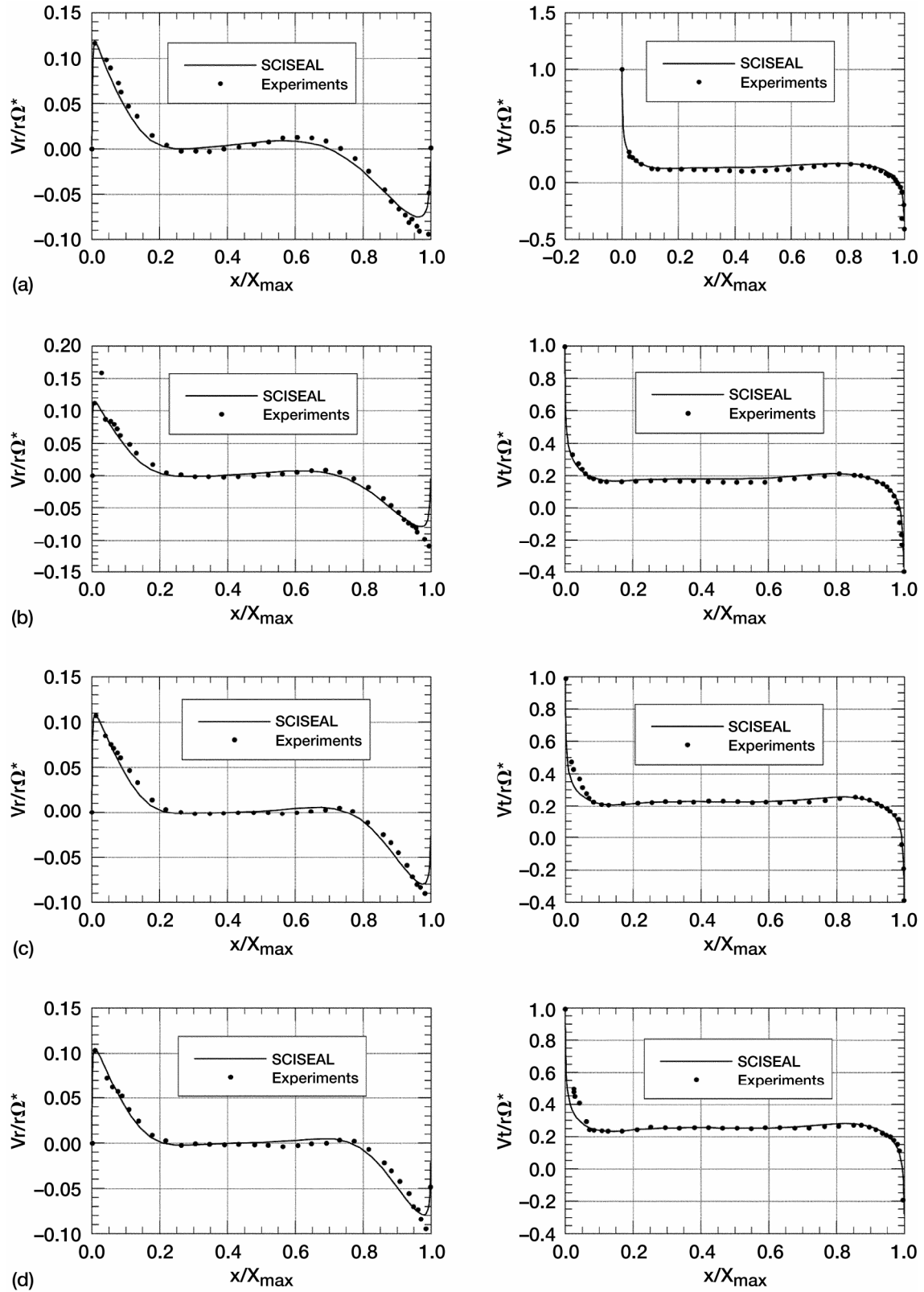


Figure 4-3.—Normalized radial (left column) and tangential (right column) velocities, no purge, $\Gamma = -0.4$, $\text{Re}_\phi = 1.25 \times 10^6$. (a) $r/R = 0.6$. (b) $r/R = 0.7$. (c) $r/R = 0.8$. (d) $r/R = 0.85$.

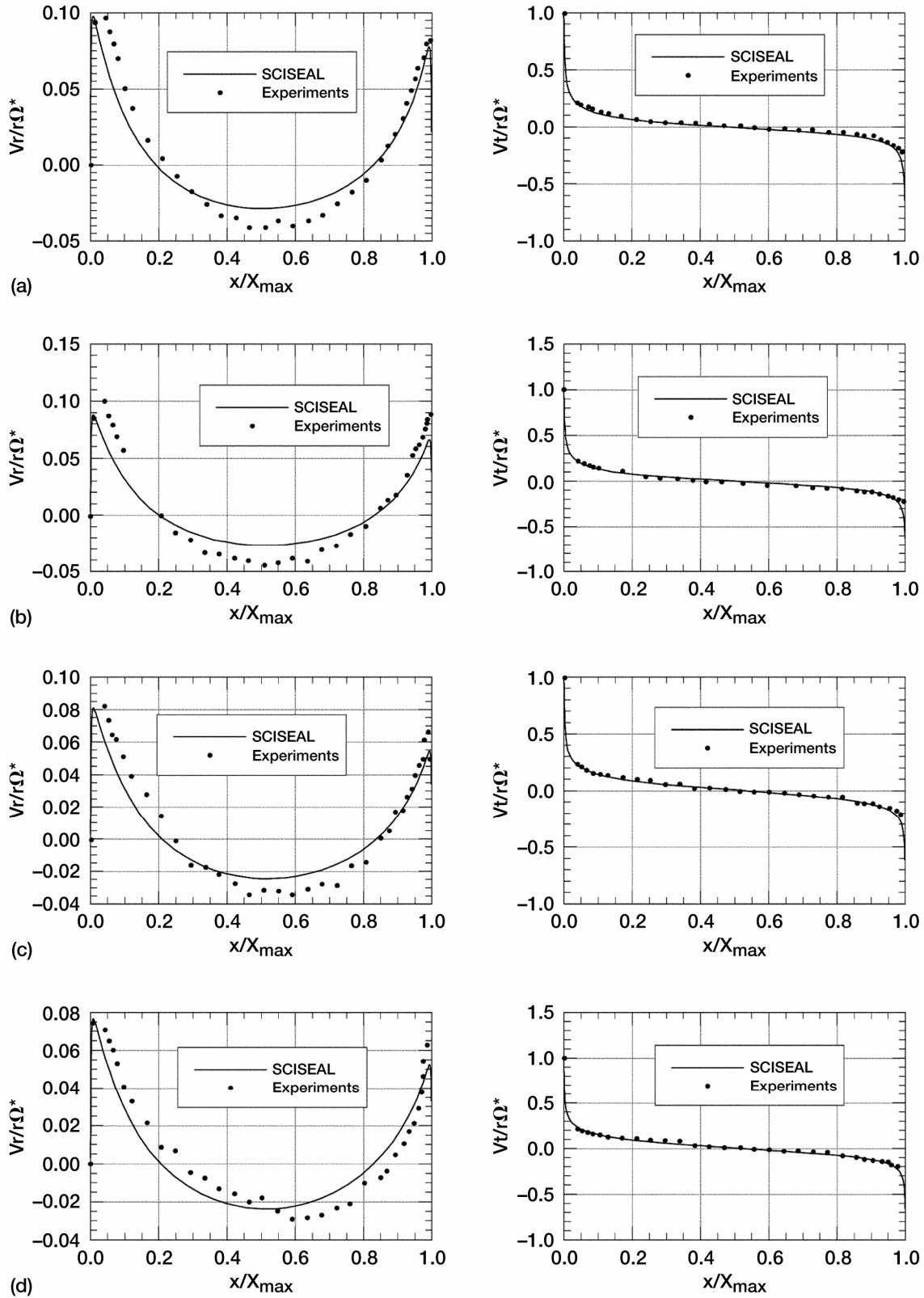


Figure 4-4.—Normalized radial (left column) and tangential (right column) velocities, no purge, $\Gamma = -0.8$, $\text{Re}_\phi = 1.25 \times 10^6$. (a) $r/R = 0.6$. (b) $r/R = 0.7$. (c) $r/R = 0.8$. (d) $r/R = 0.85$.

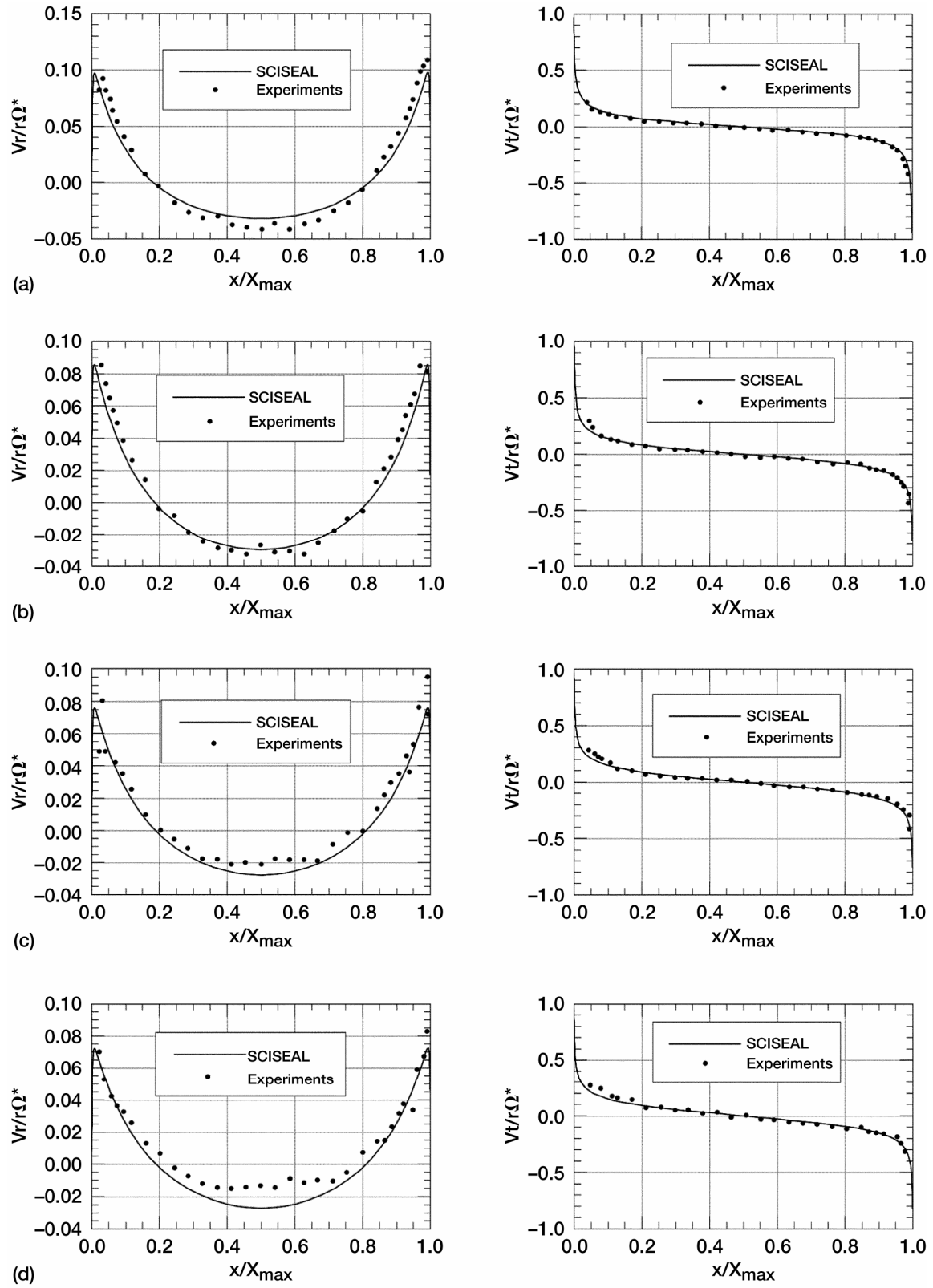


Figure 4-5.—Normalized radial (left column) and tangential (right column) velocities for $C_w = 0.0$, $Re_\phi = 1.17 \times 10^6$. (a) $r/R = 0.6$. (b) $r/R = 0.7$. (c) $r/R = 0.8$. (d) $r/R = 0.85$.

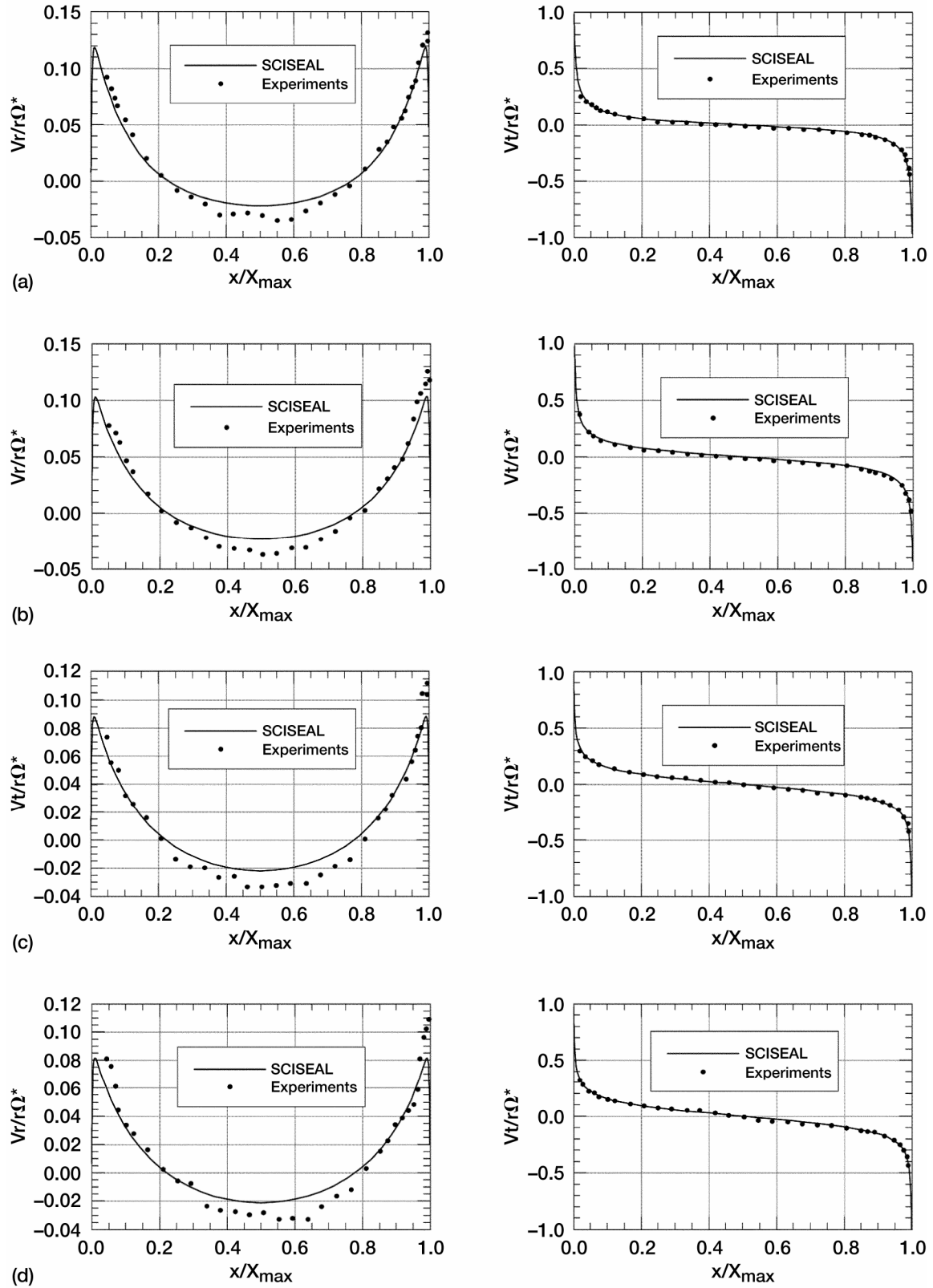


Figure 4-6.—Normalized radial (left column) and tangential (right column) velocities for $C_w = 2310$, $Re_\phi = 6.66 \times 10^5$. (a) $r/R = 0.6$. (b) $r/R = 0.7$. (c) $r/R = 0.8$. (d) $r/R = 0.85$.

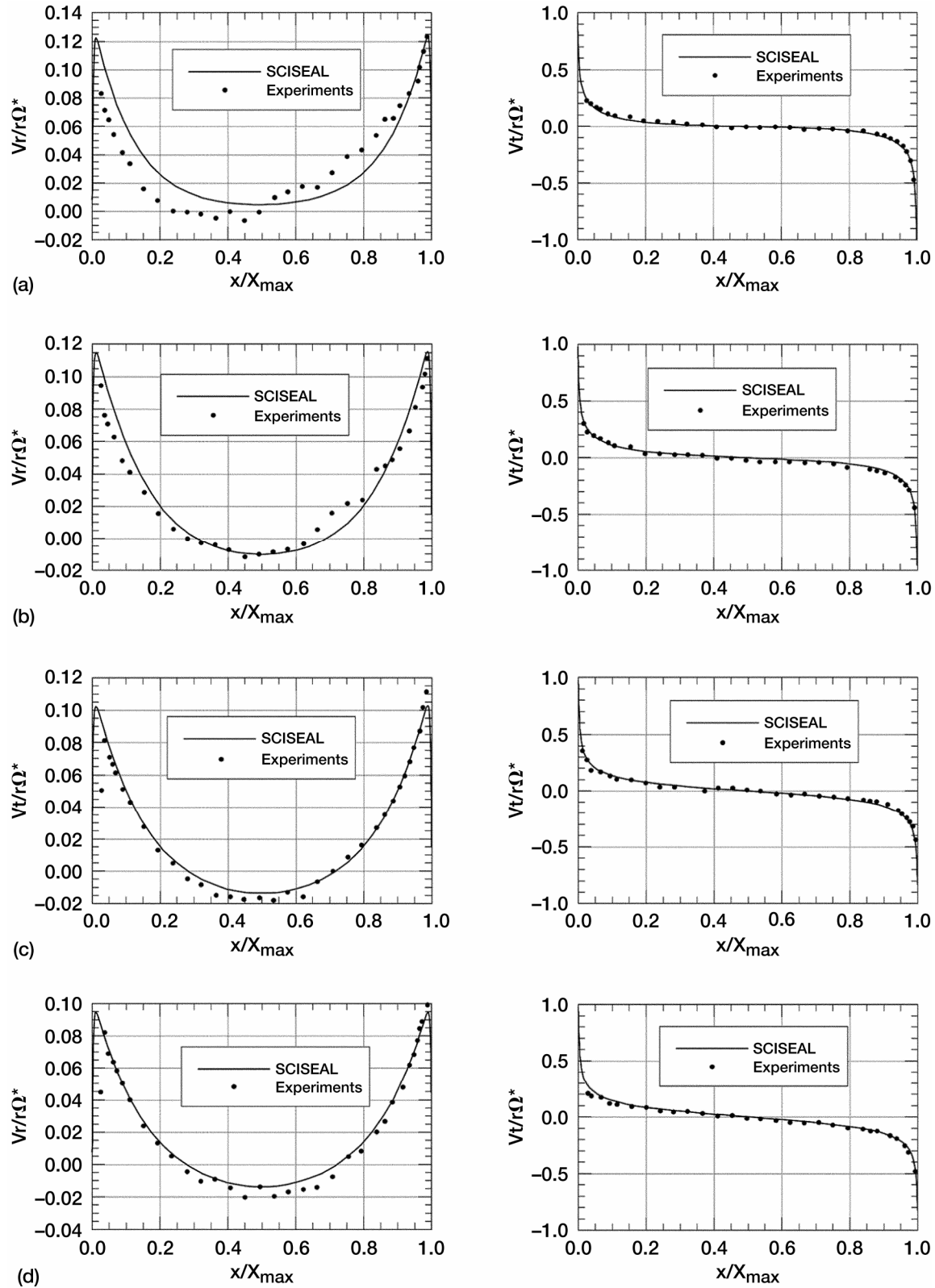


Figure 4-7.—Normalized radial (left column) and tangential (right column) velocities for $C_w = 6320$, $Re_\phi = 7.08 \times 10^5$. (a) $r/R = 0.6$. (b) $r/R = 0.7$. (c) $r/R = 0.8$. (d) $r/R = 0.85$.

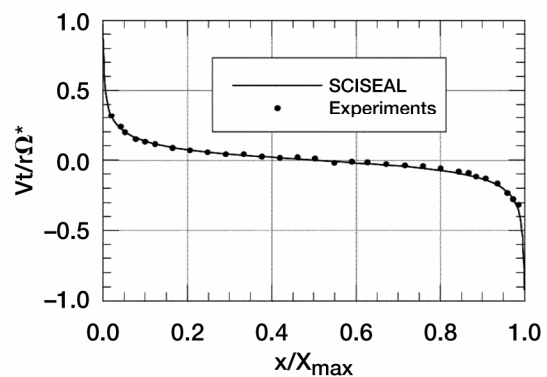
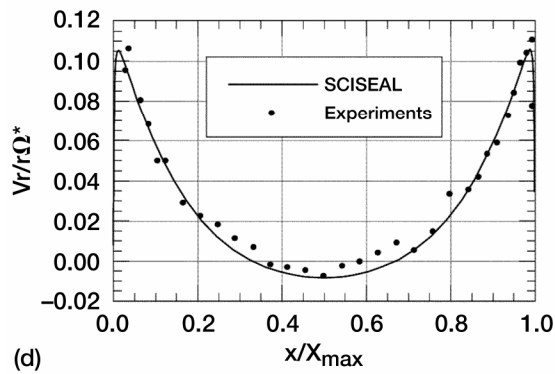
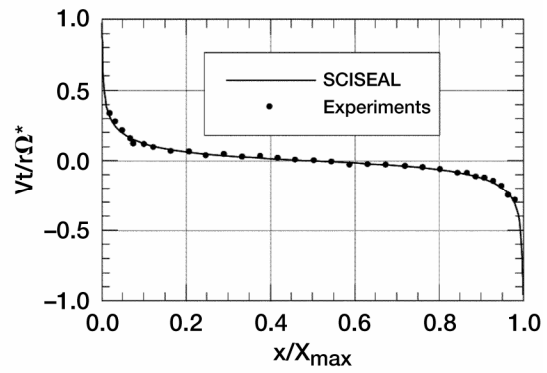
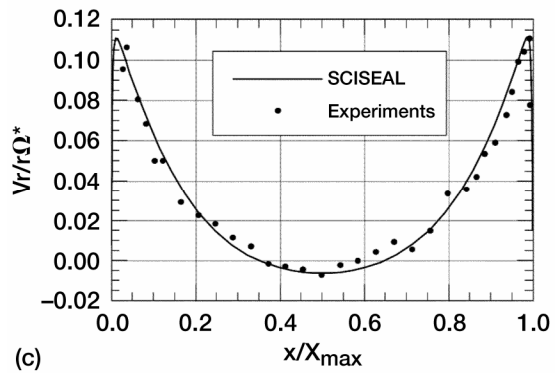
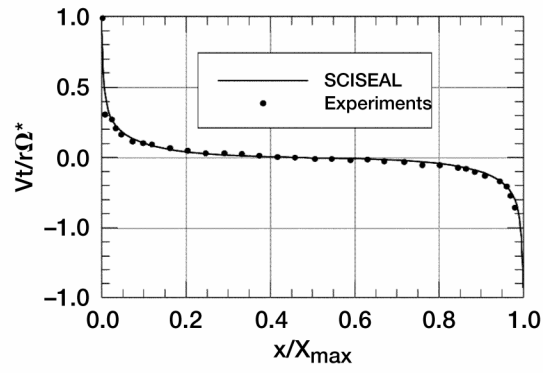
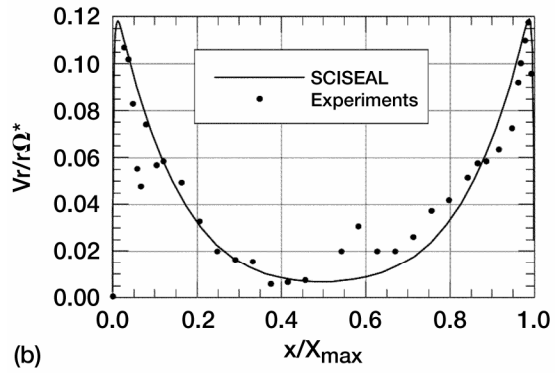
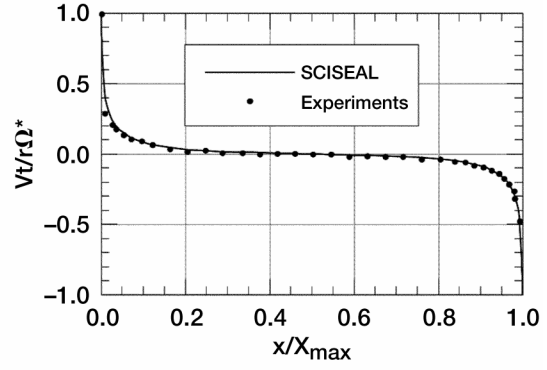
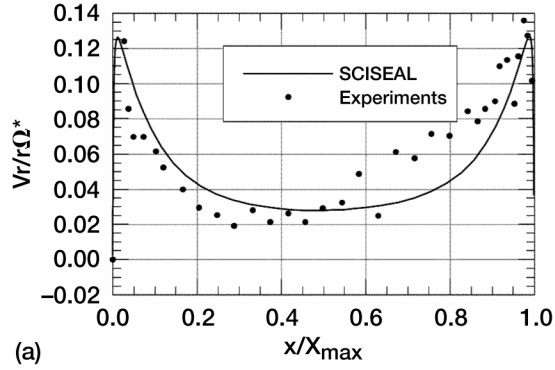


Figure 4–8.—Normalized radial (left column) and tangential (right column) velocities for $C_w = 9280$, $Re_\phi = 6.84 \times 10^5$. (a) $r/R = 0.6$. (b) $r/R = 0.7$. (c) $r/R = 0.8$. (d) $r/R = 0.85$.

axially entering flow impinges on the right side disk, and then moves along the radial direction, and this creates a stronger radial flow near the right side, especially for smaller radii as seen in figures 4-8a and 4-8b. As expected, the discrepancy is larger at lower radii and higher purge flows, but towards the shroud regions, the flow tends to even out.

These runs were also repeated with the standard k- ϵ model and the results compared with experimental data as well as the low-Re k- ϵ model results. As an example, the velocity profiles for $C_w = 6320$ at various radial stations for the two turbulence models and experimental data are shown in figure 4-9. As seen in these plots, the results from the standard and low-Re k- ϵ (Chien, 1982, [21]) models are very close to each other, and agree well with the experimental data. Similar agreement between the two turbulence models was seen at all other purge flow rates.

Finally, the changes in the flow structure with increasing purge flow rates is illustrated in figure 4-10 where the streamlines of the flow at $C_w=2310$ and 6320 are plotted. As described in Gan et al. [11], the flow structure consists of a source region exists near the inlet where the radial velocity is positive, boundary layers on the rotating walls with radially outward flow and a pair of contrarotating vortices from the boundary layers to the central midplane. The flow at the axial midplane is radially inwards due to the counterrotating vortices. At the lower purge flow rates, a secondary contrarotating pair of vortices near the inlet plane is seen, and this is a results of the lower purge velocities. At higher purge flow rates the inlet radial momentum is sufficiently large to eliminate the secondary vortex pair.

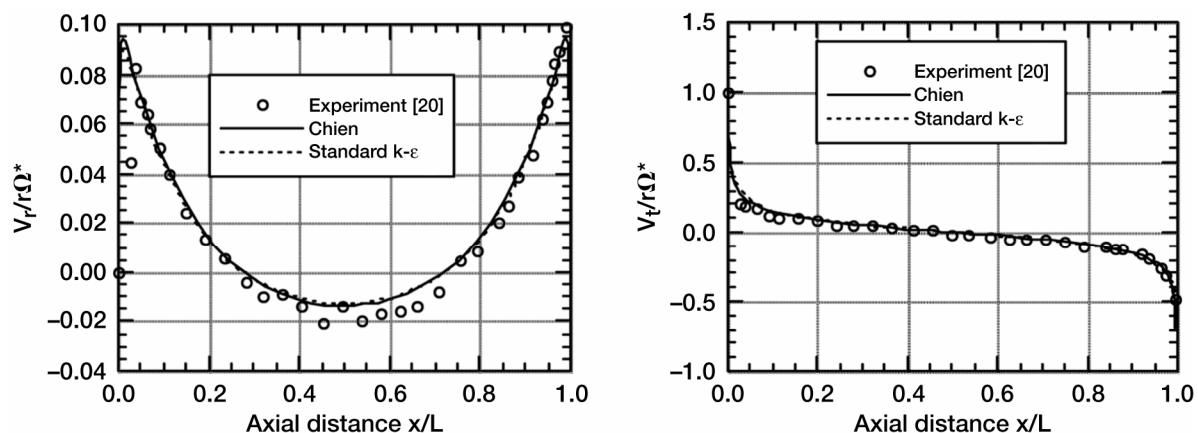


Figure 4-9.—Radial and tangential velocity distribution at $r/b = 0.85$, $C_w = 6320$, standard k- ϵ model.

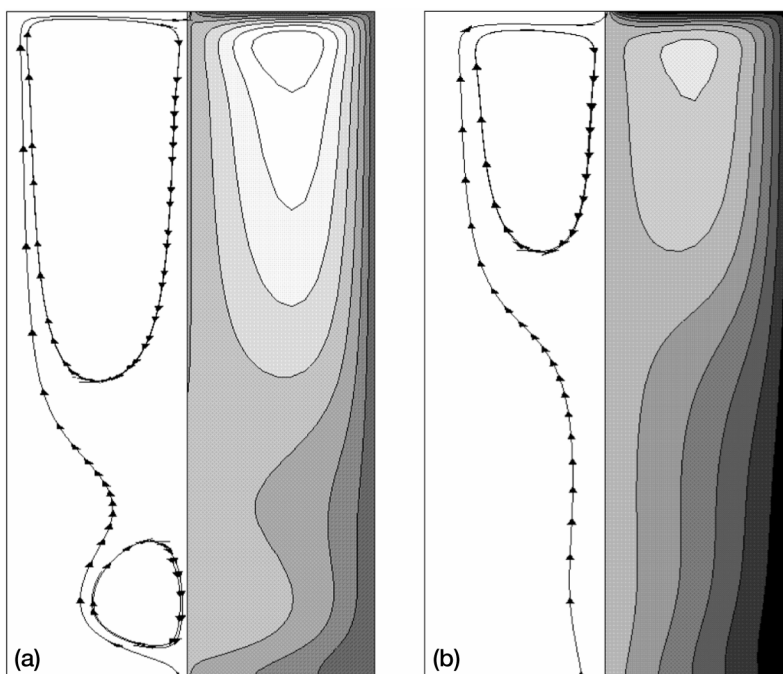


Figure 4-10.—Computed streamlines for contra-rotating cavity.
(a) $C_w = 2310$. (b) $C_w = 6320$.

4.2 Simulation of Heat-Transfer in Rotating Cavities

This series of runs involved the flow and heat-transfer calculations in a cavity with co-rotating walls at fixed, equal wall rotational speeds. The flow configuration is shown in figure 4-11. Experiments were carried out and reported by Northrop and Owen [12]. The flow domain consists of two rotating disks 0.428 m in diameter with a separation of 0.059 m. The disks are joined at the top with an insulated rim that has several holes along the centerline on the periphery that act as the flow exit passage. Cooling air flow was introduced through a central hole in one of the disks (called as upstream disk) and exits through the holes in the rim. Both the disks were heated using electric heaters, and the disks have thermocouples and flux meters for temperature and heat flux measurements. The experiments involved heating the disks to get different radial distributions of wall temperatures and to measure the local Nusselt numbers at different flow and disk rotation conditions.

The simulations assumed the flow to be 2-D axisymmetric, and incompressible. The flow was assumed to enter radially at inner radius $r/R = 0.1$, and a uniform radial velocity was assumed. For the present range of temperature variations, constant fluid properties were assumed. Measured profiles of wall temperatures were used as thermal boundary conditions on the walls. Three different types of temperature profiles were considered in the experiments: increasing, constant or decreasing as a function of the radial distance. Such temperature data for one coolant flow rate and three rotational Reynolds numbers was presented in the paper and these correspond to a total of nine different flow cases (3 rotational speeds X 3 types of temperature profiles). The temperature plots from the paper were scanned to generate the profiles which then were used for wallboundary values. Some extrapolation was needed for the smaller radial distances ($r/R < 0.3$) where data was not available, and a linear extension based on the last two points was used. The experimental profiles of the wall temperatures are shown in figure 4-12 for a non-dimensional coolant flow of $C_w = 7000$.

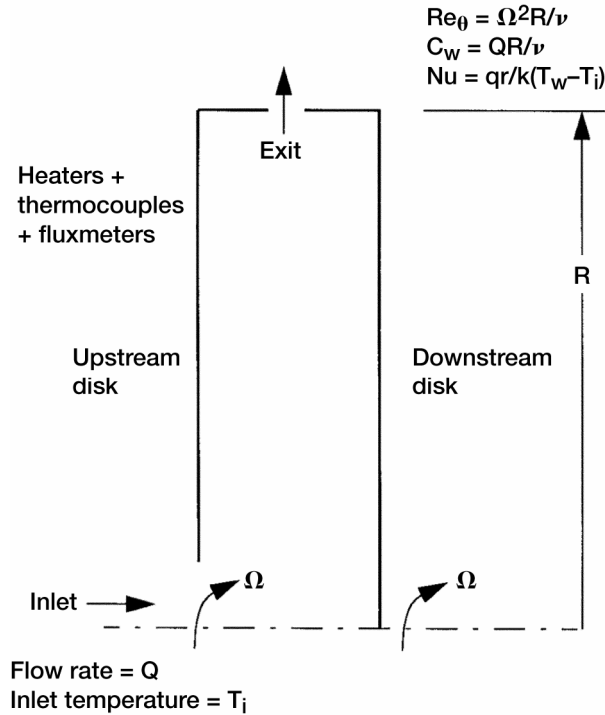


Figure 4-11.—Schematic of the rotating cavity.

Simulations were carried out using two different turbulence models: 1) standard k - ϵ model with wall functions, and 2) low-Re k - ϵ model. Two different computational grids were generated for the two models to satisfy the wall y^+ conditions. For the low-Re model, a grid with 84 cells in the axial direction and 137 in the radial direction was used. The computed y^+ distances were < 0.3 at all walls. For the standard k - ϵ model the first-cell wall distances are much larger, and a grid with 52 cells in the axial direction and 120 in the radial direction was used (with y^+ values at the first cell ranging from approx. 13 to 100).

Flow and heat-transfer solutions were obtained at one nondimensional coolant flow rate $C_w = 7000$, for which the measured wall temperatures were published (see figure 4-12). Three rotational Reynolds numbers Re_θ were considered: 6.6×10^5 , 2.0×10^6 and 3.3×10^6 . Calculated wall heat fluxes were converted into local Nusselt numbers using the local wall and gas inlet temperatures, and the distribution of the Nusselt numbers as a function of normalized radial distance r/R for different flow conditions are plotted in figures 4-13 through 4-21. In general the comparison is fair to good except the results for the “positive” wall temperature profile at $Re_\theta = 3.3 \times 10^6$. Some discrepancy in the results for the positive wall temperature profile at $Re_\theta = 2.0 \times 10^6$ is also noted. Further studies for the source of this discrepancy are needed.

Results of these series of numerical simulations and the comparison with experimental as well as published numerical results clearly indicate that the presently available flow and turbulence models (standard and low-Re k - ϵ models) in SCISEAL provide flow and heat-transfer solutions in disk cavity flows that are of adequate accuracy [see also ref. 13]. A number of different turbulence models have been used for cavity flows including the k - ω model, and k - ϵ models with corrections for the rotational effects near the wall. This aspect has not been explored in the present work. A comparative study of the standard k - ϵ and low-Re k - ϵ models with the ‘improved’ models in terms of accuracy, ease of use, convergence characteristics should be performed to assess the relative merits of these models and to come arrive at the ‘best’ model that describes the rotating cavity flow and heat transfer phenomena optimally.

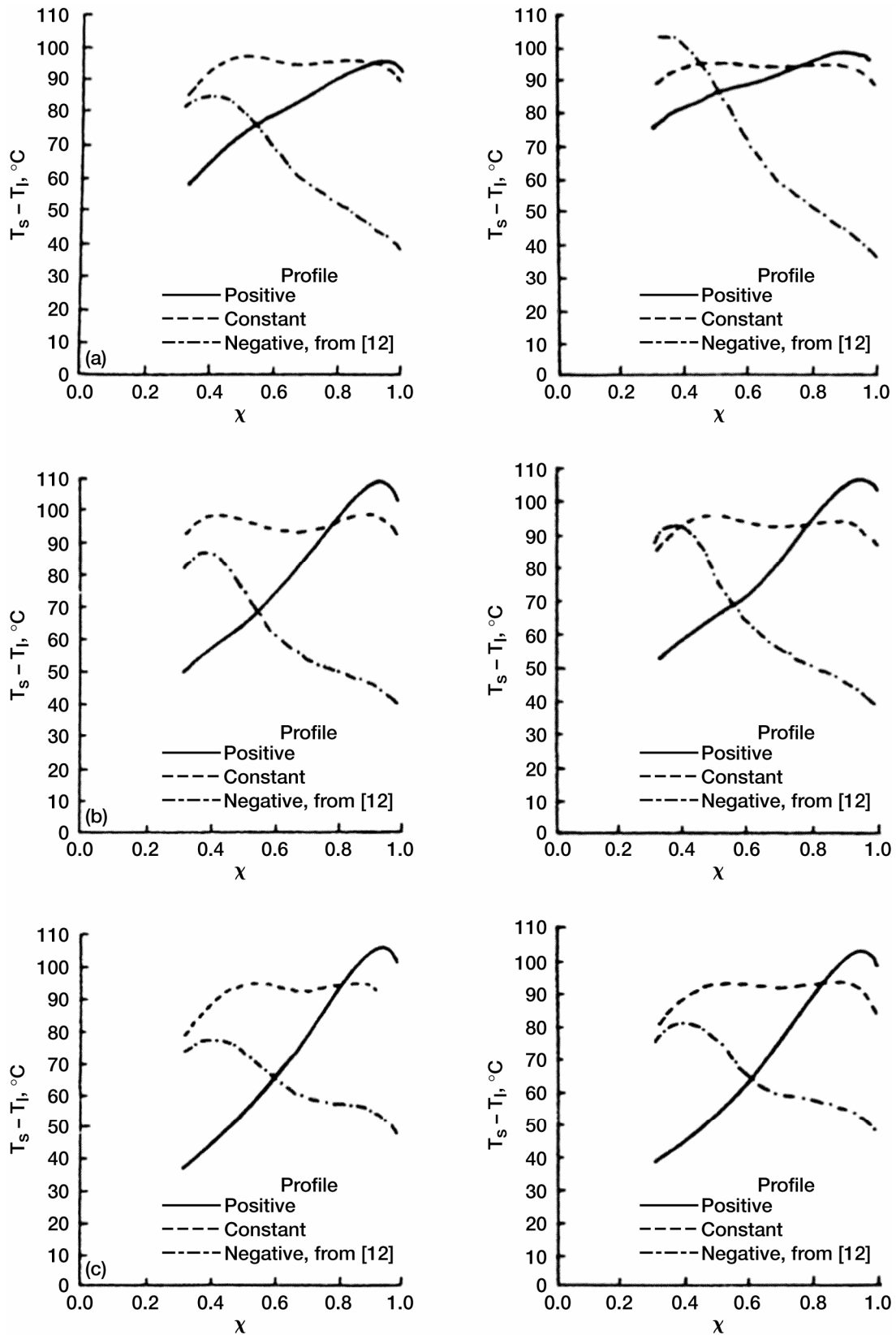


Figure 4-12.—Typical radial temperature profiles for $C_w = 7000$. Downstream disc (left column) and upstream disc (right column). (a) $Re_\phi = 0.66 \times 10^6$. (b) $Re_\phi = 2.0 \times 10^6$. (c) $Re_\phi = 3.3 \times 10^6$.

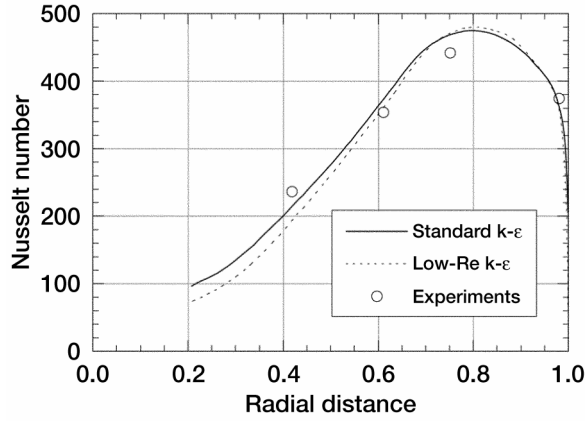


Figure 4-13.—'Constant' wall temperature profile, $Re_\phi = 6.6 \times 10^5$.

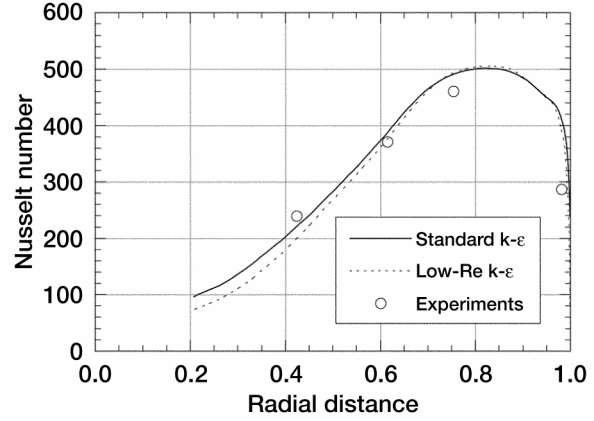


Figure 4-14.—'Positive' wall temperature profile, $Re_\phi = 6.6 \times 10^5$.

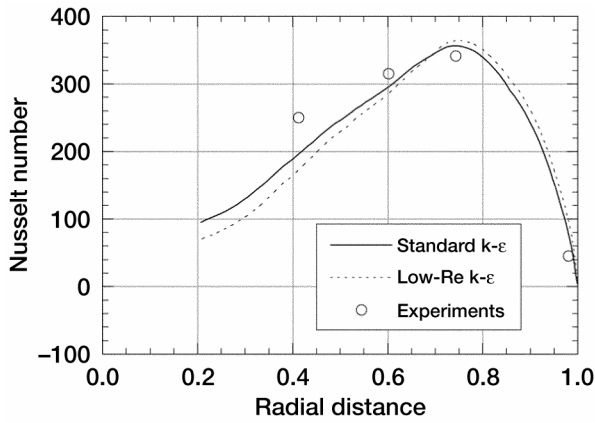


Figure 4-15.—'Negative' wall temperature profile, $Re_\phi = 6.6 \times 10^5$.

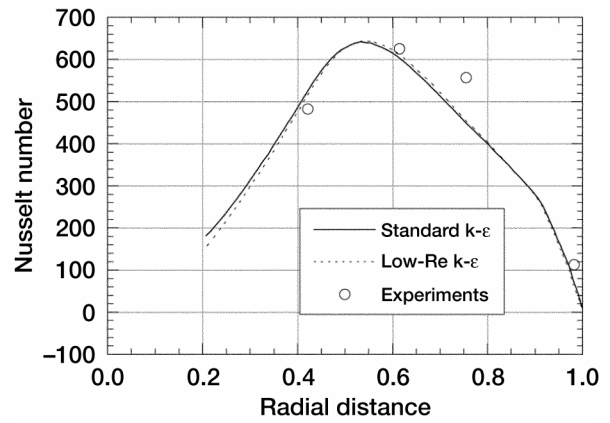


Figure 4-16.—'Constant' wall temperature profile, $Re_\phi = 2.0 \times 10^6$.

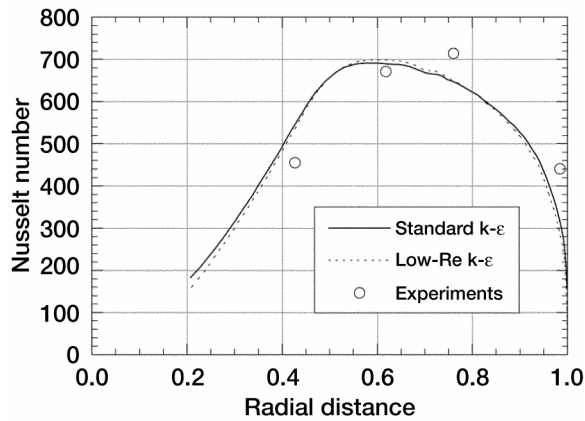


Figure 4-17.—'Positive' wall temperature profile, $Re_\phi = 2.0 \times 10^6$.

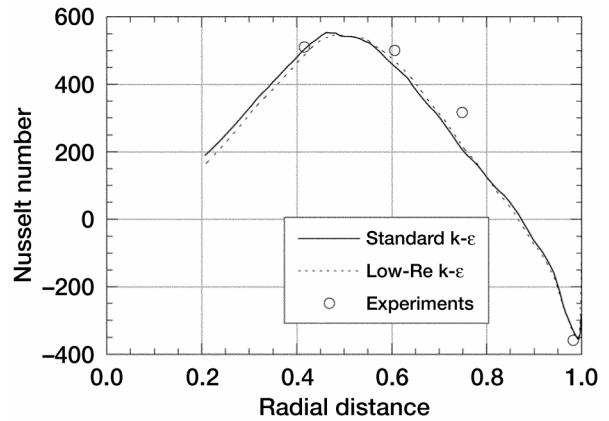


Figure 4-18.—'Negative' wall temperature profile, $Re_\phi = 2.0 \times 10^6$.

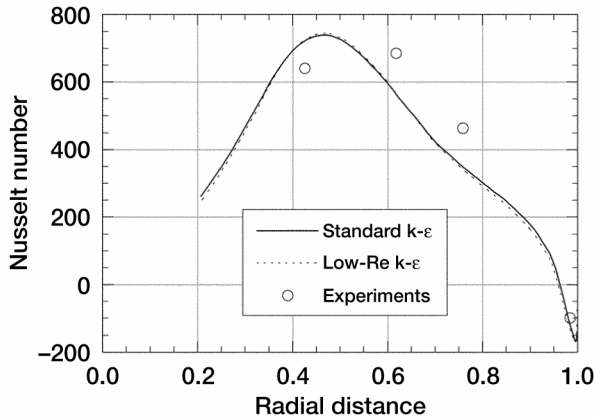


Figure 4-19.—'Constant' wall temperature profile, $Re_\phi = 3.3 \times 10^6$.

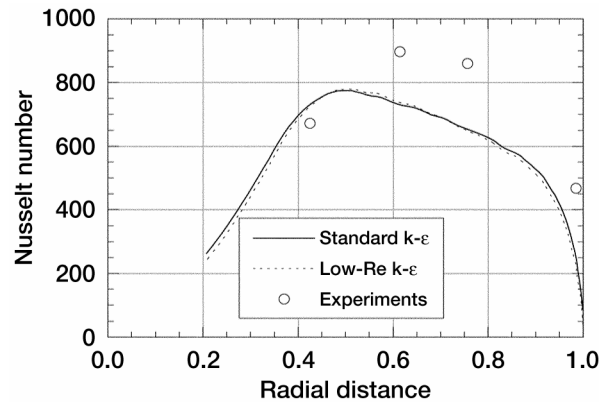


Figure 4-20.—'Positive' wall temperature profile, $Re_\phi = 3.3 \times 10^6$.

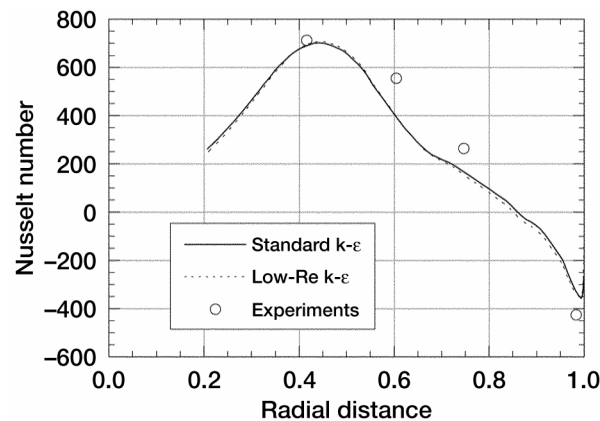


Figure 4-21.—'Negative' wall temperature profile, $Re_\phi = 3.3 \times 10^6$.

5. 3-D Secondary and Power Stream Coupling Methodology

The 2-D, axisymmetric solutions of coupled primary and secondary flows in turbine section were presented in Chapter 2. They provided a great deal of important information and insight into the flow and heat transfer processes in the secondary flow elements as well as the interaction between the two flow streams. Such an analysis capability is essential, and provides relatively fast and detailed solutions. These solutions assume steady-state interaction and no circumferential variations in the flow fields. In reality the rotor and stator blade wakes produce circumferential variations in the powerstream flow and consequently can affect the rim seal flows. In addition, motion of the rotor blades makes the flow inherently unsteady due to interaction of the blade wakes from one stage with the flow in the next stage. This also produces a transient flow field near the rim seal, which can affect the secondary flow in the cavity. With the current drive for optimization of the coolant flow rates, this time-unsteadiness of the powerstream and its interaction with the secondary flow stream also may need to be resolved in much more detail. Such an analysis ensures a much more detailed picture of the flow at the rim seals, and the interaction between the powerstream and the cavity flow.

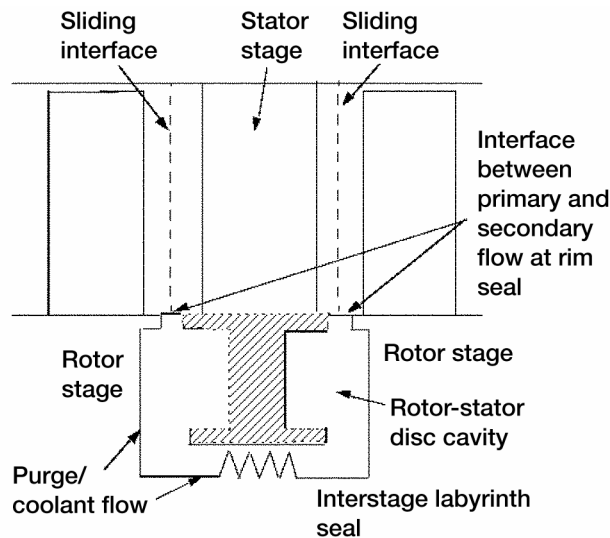


Figure 5-1.—Schematic of a typical interstage cavity in a turbine section with interfaces of interest.

The effects of the interaction are present in both the compressor section and the turbine section of a typical gas turbine engine. Figure 5.1 shows a schematic of a typical disk cavity pair that is used in the inner rows of a multi-stage compressor/turbine. Different requirements and considerations go with disk cavity flows in a compressor section and a turbine section, as outlined below:

Compressor Section: In a compressor section, the ‘downstream’ rim seal is at a higher pressure than the upstream rim seal. This drives a flow in the cavity pair such that there is ingress of flow in the downstream rim seal and cavity. This flow moves to the upstream cavity through the labyrinth seal, and exhausts in the powerstream at the upstream rim seal. The leakage flow affects the engine performance in two ways. It represents a net loss because a portion of the compressed air is being expanded through the cavity/labyrinth seal and the flow energy eventually is converted to heat. Secondly, the flow coming out of the upstream rim seal has tangential velocities that are different than the powerstream flow near the rim seal [2]. This changes the inlet velocity vectors near the stator row hub and can affect the stator row efficiency. In a compressor section, such alterations in the flow can also impact the stall performance. Of interest in a compressor section is the time variation of the leakage flows, the velocity distribution of the leakage flow as it gets injected in the powerstream and the resulting interaction with powerstream flow.

Turbine Section: Flow dynamics in the turbine section is different, with the upstream cavity/rim seal at a higher pressure (and temperature) than the downstream cavity/rim seal. This would, normally, result in flow ingestion at the upstream rim seal, and exhaust at the downstream rim seal. However, ingestion of the hot powerstream gas into the cavities will increase component temperatures and will adversely affect life. For this reason, hot gas ingestion into the cavities is usually avoided. This is achieved by injecting high-pressure compressor air into the cavities and using it to prevent hot gas ingestion as well as providing cooling for the components. Since the coolant flow represents a parasitic loss, current focus is on optimization of the coolant flow rates, which would provide adequate cooling capacity at the minimum possible flowrates. Of particular interest in the turbine section is the flow dynamics at the rim seal, effects of circumferential pressure variations (due to blade wakes) on rim seal flow and the cooling of components as the coolant flow is optimized.

When selecting the numerical tools to attack this very complex problem several issues need to be resolved, in order to assure that the flow physics is treated properly and physically plausible solutions are generated for the powerstream, disk cavity flow and the interaction between the two. A number of issues

related to the computational and physical aspects of the solution procedure were considered during the development of the coupled code methodology. These were:

1. Flow codes and solver selection
2. Methodology for coupling the codes: Physics and numerics, type of data transfer, level of coupling
3. Interface interpolation routines, changes in the flow solvers
4. Synchronization of the codes

Description of these issues and the methods adopted in each are described in the following subsections. The flowcharts for the overall execution procedure as well as other related procedures are also discussed. It should be noted here that there are now, possibly, 'better' methods to treat some of these issues; the methods adopted and used herein were the best available at the time this work was performed and represented the state-of-the-art at that time. Obviously, as flow solvers evolve, other methods may become attractive for solutions of this type of flows.

5.1 Flow Codes

Flow physics in the two flow streams are widely different. The powerstream flow is compressible, transonic and inertia dominated, while the cavity/seal flow is slower, with narrow flow passages, has dominant heat-transfer, turbulence and viscous effects. The powerstream flows are usually handled using the density-based codes, while the slower flows can be better handled using the pressure-based methodology. At a minimum, the solver capabilities needed for treatment of the two flow streams are:

1. Powerstream: transonic flow, turbulence, resolution of time-accurate interaction between successive blade rows in a multi-row machine.
2. Secondary flow stream: solution of slower compressible flows, turbulence modeling, conjugate heat transfer, complex geometry handling.

Although it may be possible to use a single code to treat both flow regimes, the code performance in terms of speed and accuracy may not be optimal. In addition, any single code developed specifically for one flow regime could need extensive modifications and validation efforts to be able to handle the coupled flows. For these reasons, we decided to use two separate codes, specifically developed for the two flow streams, in the project. One can then select mature codes that have been validated and demonstrated on the respective flow streams, and the thrust of the research would then be on development of the coupling interface only. The codes selected were: **MS-TURBO** for the powerstream solutions and **SCISEAL** for the secondary flows. Both these codes were developed under different NASA contracts, and have been validated and applied to a variety of problems. A brief description of the codes and the salient features that are relevant to the present research are given below:

5.1.1 SCISEAL Code.—This code was developed for flow+heat transfer+dynamics simulations in turbomachinery seals and secondary flow elements [3]. It uses a finite-volume formulation for integrating Navier-Stokes equations. The velocity-pressure coupling is done through a modified SIMPLEC algorithm. Structured multi-block grids are used to discretize the computational domain. Details of the governing equations, flux calculations, boundary condition treatment and physical models are given elsewhere [3]. Presented here are the salient features of the code:

1. Treatment of incompressible and compressible flows due to pressure-based formulation, time-dependent and steady-state solutions
2. High order spatial and temporal discretization, body-fitted coordinate (BFC) grids
3. A variety of turbulence models, including Baldwin Lomax, standard and low-Re k - ϵ models, k - ω model, and a 2-layer model.
4. Implicit multi-media conjugate heat transfer
5. Stationary and rotating coordinate frames, moving/deforming grid treatment
6. A comprehensive set of boundary condition types, for treatment of all secondary flow conditions.
7. Procedures for calculation of rotordynamic coefficients.

SCISEAL has been validated and demonstrated on a number of benchmark and demonstration problems in turbomachinery seals, disk cavities and secondary flow systems. The solutions presented in Chapters 2-4 in this report were calculated using this code, and amply prove the capabilities and accuracy of the code on relevant disk cavity problems.

5.1.2 MS-TURBO Code.—MS-TURBO was developed at Mississippi State University for the computations of time-accurate flows in multi-row turbomachines [14-17]. It uses a density-based formulation to integrate 3-D unsteady Euler/N-S equations on structured, multi-block grids. The flow equations are non-dimensionalized and written in generalized coordinates to be able to treat body-fitted grids. The convective fluxes are discretized using flux difference splitting and up to third order accuracy are possible using Osher-Chakravarthy method. The first-order convective fluxes at a cell face $\left(i + \frac{1}{2}\right)$ are written as:

$$\tilde{F}_{i+\frac{1}{2}} = \frac{1}{2} \left[\tilde{F}_i + \tilde{F}_{i+\frac{1}{2}} - \Delta \tilde{F}_{i+\frac{1}{2}}^+ + \Delta \tilde{F}_{i+\frac{1}{2}}^- \right] \quad (5.1)$$

where $\Delta F_{i+\frac{1}{2}}^\pm$ are the flux differences along the right and left running characteristics. Higher order

differencing is achieved by adding correction terms to the first-order fluxes. Diffusive terms are discretized using central differencing. Fluxes near sharp gradients are limited using Van-Leer flux limiting method. Typical turbomachine flows are inertia dominated, and viscous effects in flow-wise direction are small and are ignored in MS-TURBO (thin layer N-S equations). An eddy-viscosity based turbulence model is available for treatment of turbulent flows. Boundary condition formulation is characteristics-based for robustness and accuracy. [14,16]

For handing time-accurate solutions in multiple rows with relative motion, an algorithm is needed to resolve the sliding interfaces between successive rows. In MS-TURBO, a grid deformation/clicking algorithm is used to treat the relative motion. Each blade row has structured multiblock grids, and successive rows are connected through the sliding/clicking interface. A one-to-one match is maintained between the grids at the interface. A deformation zone is associated with each interface. As one blade row moves with respect to the next one, the relative motion is in the circumferential direction, and the cells in the deformation zone are allowed to distort up to a point and then are snapped/clicked to the next cell in tangential direction. The number of time-steps for grid clicking is controlled from outside. When the grid coordinates on the end faces of the deformation zone are known, a linear interpolation scheme is used to regenerate the grids inside the deformation zone. Grid distortion and clicking implies moving/ deforming grids, and a space-conserving moving grid algorithm is used where the grid motion is included in the convective fluxes through a coordinate transformation. *All of the blade rows are treated in absolute frame of reference.*

Each blade row can be separated into several radial zones as needed. The code treats one blade row at a time, so that the in-core storage requirement is for one blade row only. This reduces the working memory size, and allows treatment of a large number of blade rows. The data related to blade rows other than the working row are stored on disk and loaded into the core as needed.

5.2 Functions of the Interface Routines

During a typical run, the two codes will run in parallel, each working on separate flow streams, and exchanging data at certain times to keep the powerstream and secondary flow linked. The overall flowchart for the coupled, transient simulation procedure is shown in figure 5-2. The schematic of the

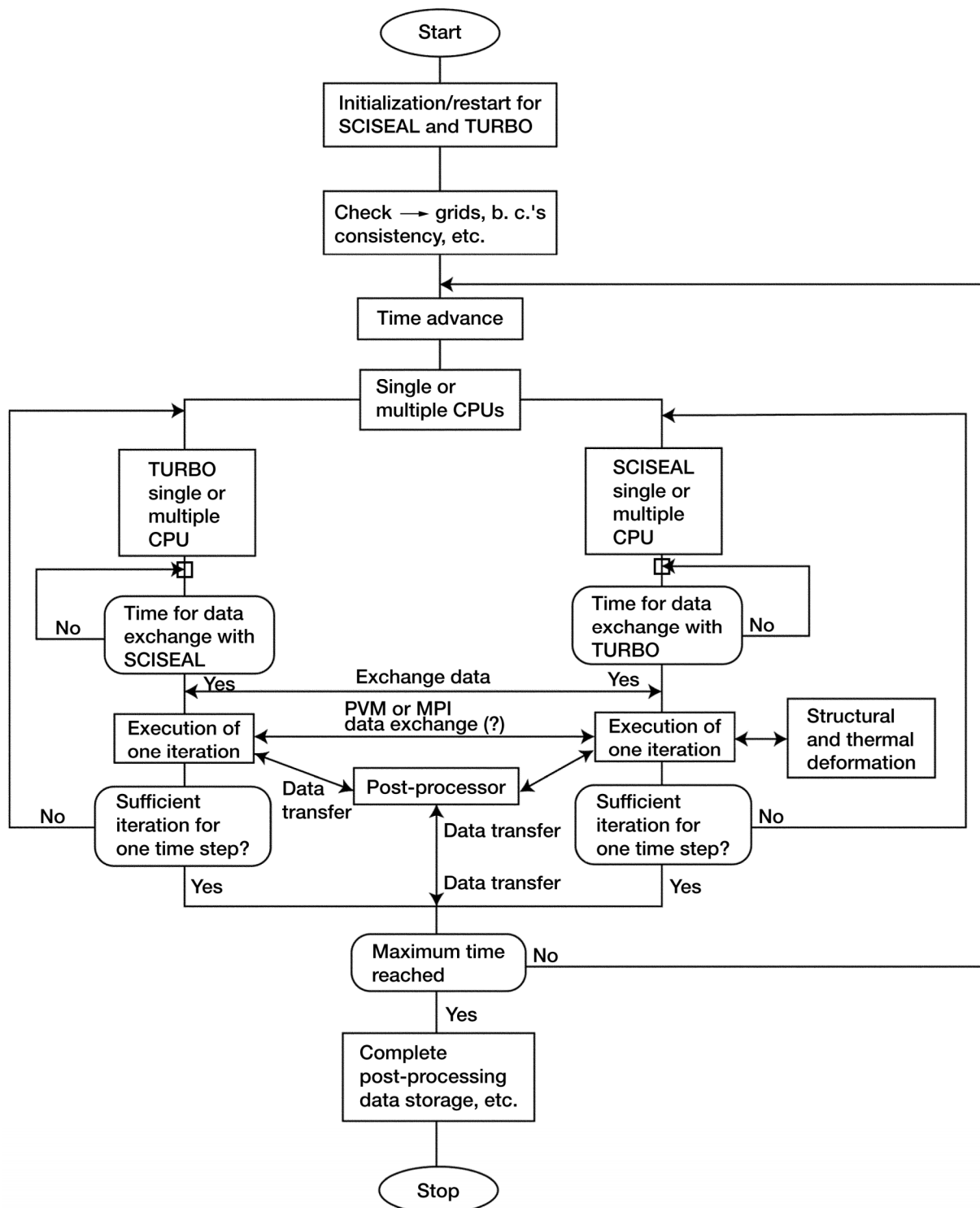


Figure 5-2.—Flowchart for the coupled execution of SCISEAL and MS-TURBO codes.

typical powerstream-secondary flow cavity shown in figure 5-1 is also modified and shown in figure 5-3 to denote the various codes and expected interface placements which are used in the coupled codes. The interface algorithm between the two codes is invoked frequently during the execution, and has to perform different functions. Some of the capabilities that were considered during this development are:

1. Initial data preparation for each code: this involves identification of the interface boundaries, check on the location, size of the domains and initial flow variables and flux preparation.
2. Code run status: Interface routines check the execution status of each code during a coupled run to determine whether the codes are at a proper point for data exchange
3. Data preparation for exchange: appropriate data from each of the codes at all interfaces is collected, sorted and stored for interpolation procedure.
4. Interpolation of data from one code to another: This is a key step in the interface linking and requires a lot of careful attention. Due to the motion of the rotor stages, the interface grids are at different physical locations. The data on these have to be 'rotated' to match the grid locations prior to interpolation. Interpolation scheme is general enough to treat any type of grids (structured, unstructured).
5. Exchange of data: After interpolation of appropriate data from one code to another, the data is made available to the other code. Currently the interface data sets are written out to disk files, which are accessed by both codes. Appropriate interlocking mechanisms are provided in each code to synchronize the data input/output processes in the two codes.
6. Placement of the data: The data read in from the disk files and placed into appropriate locations in each code for use in subsequent iterations/time steps. Different boundary data structures are used in the two codes, and this has to be taken into account.

The interface at present consists of three sets of routines in addition to the modifications made to the individual flow solvers. One set is in SCISEAL for data collection, exchange and transfer. The second set is in MS-TURBO for similar functions. The third set is outside of the two flow solvers, and is used to perform the interpolation of data from one code to another and this set of routines is called from both codes.

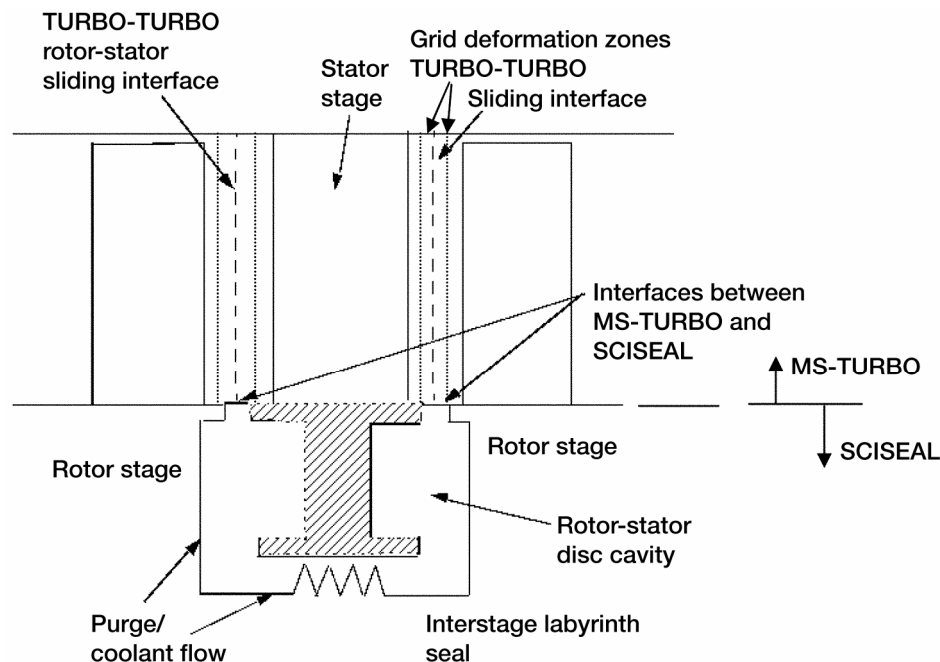


Figure 5-3.—Flow domain and interface placements in the coupled execution procedure.

5.3 Issues in Formulation of Interface Methodology

The basis for interface algorithm is discussed in this section. Several different items were taken into account during the interface development. Specifically, the items that impacted the coupling procedure and methods used to resolve these are described below.

Code solution methodologies: The two codes, SCISEAL and MS-TURBO, although solve the same N-S equations, their solution procedures are very different. The so-called density based formulation used in MS-TURBO uses a time-dependent form of compressible flow equations. MS-TURBO uses an implicit coupled equation solution method that is geared for time-accurate solutions. It does allow for Newton subiterations within each time step, which may not be necessary when the code is running singly. SCISEAL, on the other hand, uses a sequential method for solution of N-S equations, and needs several subiterations at each time-step. This has bearing on code synchronization as well as the level at which the data transfer can take place during execution.

Flow variables: The primitive variables in MS-TURBO, [density, momentum, total internal energy] (ρ , u , v , w , e), are nondimensionalized as compared to those used in SCISEAL [pressure, velocity, total enthalpy] (p , u , v , w , H). This means additional data inputs are needed for reference values used in MS-TURBO, and additional operations are needed to convert data sets from non-dimensional to dimensional form. Conversions such as from total internal energy e used in MS-TURBO to total enthalpy H in SCISEAL need to be considered. MS-TURBO uses the ideal gas law for the working fluid, with constant specific heats, and a similar specification was used in SCISEAL.

Flux calculations: Both codes use a finite volume treatment, and evaluation of fluxes at the interface is a key consideration when transferring data across this interface. MS-TURBO uses a flux-difference splitting method with the density-based, coupled form of N-S equations (conservative form), while SCISEAL uses products of convective fluxes and primary variables (strong-conservative form) to evaluate the fluxes. The interface algorithm should be worked in such a way that the interface fluxes from the two codes match, so that conservation of fluxes across the interface is ensured.

Boundary condition treatment: The methodology used to treat boundaries and to calculate boundary fluxes has direct relevance to the interface treatment. Characteristics-based boundary condition treatment is used in MS-TURBO. A phantom layer of cells is stored next to each boundary, and this information is used for boundary flux calculations. SCISEAL code uses local flow conditions at a boundary and the type of boundary condition to come up with a treatment for flux computations. In SCISEAL, a phantom cell layer is assumed, but never used explicitly. Instead, equivalent expressions for boundary values of variables are calculated and directly used.

Placement of interface: This can affect the solution accuracy as well as the stability of the solution procedure. A number of different constraints on the location and shape of the interface can be considered based on code methodologies and flow. The location should be compatible with the requirements for the sliding/clicking interface needed for MS-TURBO; local geometry features at the rim seal need to be considered, and the location should be in relatively benign flow regions, e.g., avoid recirculation zones as much as possible. The typical rim seal geometry has the upstream blade platform lip overlapping the lip of the next row blade platform as shown in figure 5-3. This geometry, coupled with the powerstream flow generates a recirculation zone at the rim seal (backward-face-step type flow).

The obvious location of the interface is shown in figure 5-4a. This allows simpler domain geometry definitions and cleaner shapes for sliding interfaces. The interface, however, is almost certain to intersect the recirculation zone expected in the rim seal. The interface could be moved back in the neck of the rim seal as shown in figure 5-4b, which will probably avoid the rim recirculation, but this now poses problems with geometry definition and the placement of the clicking interface for MS-TURBO. Such a placement would require treatment of different of boundary types at different $i/j/k$ planes. The MS-TURBO code had a limited range of boundary type and $i/j/k$ face combinations and placement of the interface in the rim seal neck would have required implementation of several additional boundary types. For example, on a 'west' or 'east' face boundary in MS-TURBO, currently only an inlet boundary is

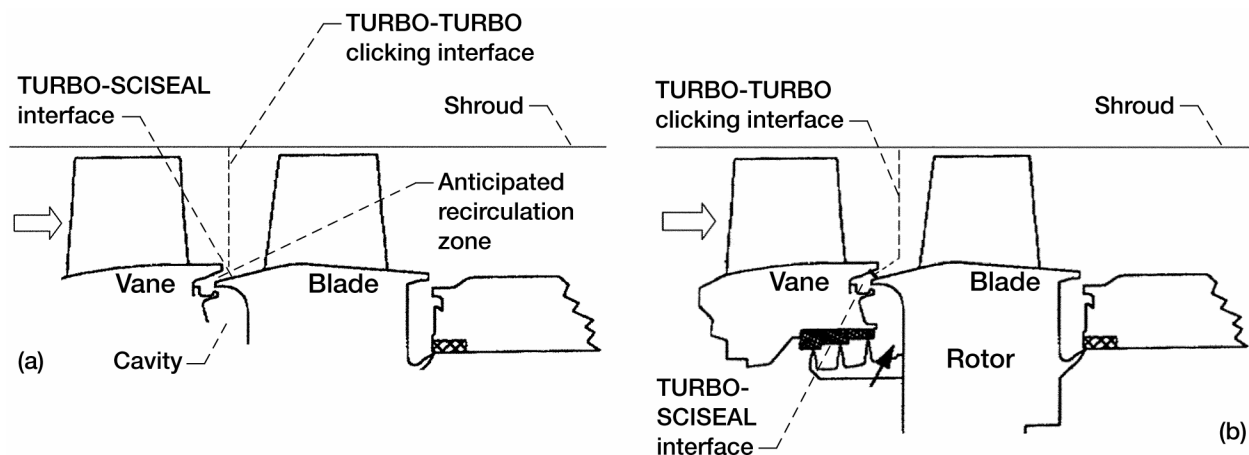


Figure 5-4.—(a) Interface strategy used in the simulations. (b) Alternative interface placement.

supported, while a wall boundary specification would be needed if we decide to extend the interface into the rim seal gap. For these reasons, the interface location as shown in figure 5-4a was finalized.

Interface shape: The interface strategy should be independent of the geometry of the interface. Two geometrical constraints were placed on the interface shapes due to the type of the flow and ease of grid generation. The edges of the interfaces in θ direction have to be circular arcs and this restriction comes from sliding interface (the circumferential boundary lines can not be wavy). The interface should be generated by revolving a curve in the r - x plane, and this curve should preferably be a straight line in the r - x plane whenever possible, where x is the axial coordinate.

5.4 Flow Treatment at the Interface

All of the items mentioned in the previous section were taken into account during the building of the flow solution methodology at the interfaces. The actual steps and methods that were used to resolve these issues are discussed below.

Conservation of fluxes at interface: As remarked above, MS-TURBO uses a phantom layer of cells next to a boundary surface to calculate the fluxes at the boundary, while a specified flux value at a boundary can be used directly in SCISEAL. This allowed a way to calculate the fluxes, which would ensure conservation at the interface. The basic methodology is:

- (a) Primitive flow variable values from the cell layer next to the interface in SCISEAL are interpolated from SCISEAL to MS-TURBO interface grid. This step accounts for the differences in relative locations of the individual surface grid sets for each code. The interpolated primitive variables are nondimensionalized and used directly in the phantom layer of cells next to the interface boundaries in MS-TURBO code. The boundary fluxes are then calculated in MS-TURBO using the normally used flux-difference splitting algorithm.
- (b) The boundary fluxes in MS-TURBO are then transferred to the interface routines, dimensionalized, rotated appropriately, and then interpolated from the MS-TURBO to SCISEAL interface grid. Care is taken to ensure flux conservation during the interpolation procedure.
- (c) The interpolated fluxes are used to enforce boundary conditions in SCISEAL at the interface. Since the flux direction can be into or out of the boundary, care is taken during boundary condition implementation.
- (d) The fluxes for k and ϵ equations from SCISEAL at present can not be calculated from the MS-TURBO code version used in this project. Instead, values of k and ϵ are calculated locally at each interface boundary cell in SCISEAL and then mass fluxes at the interface are used to calculate the convective flux of k and ϵ at the interface boundary.

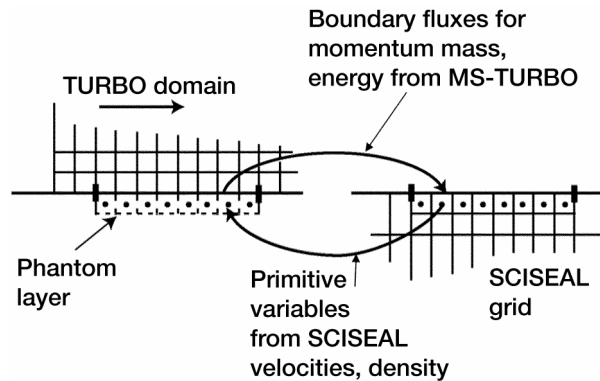


Figure 5-5.—Schematic of data transfer between the two codes and the types of data transferred.

A schematic of this variable/flux transfer methodology is shown in figure 5-5.

The above procedure ensures that both codes use the same fluxes at the interface, and thus flux conservation is enforced. The approach uses existing code methodologies at boundaries and provides a consistent way to handle this important and difficult step. This approach has been coded and tried out and performs very well as will be shown in the next chapter.

Level of linking of the two codes: This refers to the how frequently the two codes exchange data during execution, and at which level the exchanged data is used. One possibility was to exchange the data at the end of each time step. This would make the procedure completely explicit, reduce the algorithm stability, and put restrictions on the size of a stable time step. The next level was to exchange data several times during a time step. This method requires that the codes perform subiterations during each time step. SCISEAL code performs subiterations due to the pressure-based formulation. The equivalent in MS-TURBO was the Newton subiterations, where this capability is typically used for enhancing the temporal accuracy of the solution. However, in the present case, it was also used for allowing a much tighter coupling between the two codes. Typically the number of iterations needed for SCISEAL were much higher than the Newton iterations needed in MS-TURBO. The number of subiterations between each data transfer for each code is flexible, and is a part of the input data. With this tighter coupling, the stability of the coupled execution procedure was enhanced. This was tested on simple problems where the data exchange was done once a time step, and several times during a time step, and the stability of the solution procedure was seen to be better with multiple data transfers.

Synchronization of the codes: The two codes use different solution methodologies and also will operate on different flow domain sizes. For these reasons, the execution times per time step/subiteration for the two codes usually are quite different. Synchronization of the execution of the two codes and data exchange at appropriate times can become a problem. In the present algorithm the data exchange is done through data files that are written to a disk. The readiness check of each code for data exchange is done through two sets of files. A flag marker file is written out by each code when it writes out a data set to the disk. The other code then checks for the existence of the flag file and reads in the data set from the other code. After the reading is complete, the flag file and the data file are deleted from the disk. When writing out data sets, the existence of this flag and data files is checked, and if they exist, the codes go into a timed sleep mode and check the files periodically. To avoid indefinite execution of one code in case if the other code stops execution for some reason, an upper limit on the total wait time is enforced. If the other code does not read the older data sets in this time span, then the execution of the first code is stopped with an error message.

The data exchange can be done through more sophisticated methods such as MPI or internet sockets. However, three reasons are found compelling for using data transfer through disk files:

1. Interface data sets are not expected to be very large because the sizes of interfaces are usually not very large, and file data transfer is acceptably fast.
2. During execution, one can look at the data sets if they are written out in ASCII format to check on the time stamps, values etc. This can give an indication of the state of health of the coupled execution run.
3. In case of abnormal termination of any one of the codes, the last data sets will stay on the disk and perhaps provide clues to the reasons for termination, and provide an intermediate point for restarting the run.

5.5 Interface Data Interpolation Methodology

One of the key issues in the interface treatment is the way the data are interpolated from one code to another. The complexity of this procedure naturally depends on the complexity of the interface geometries, computational grid topology at the interface, relative locations of the interface and the degree of accuracy needed (in terms of conservative properties). Additionally, the procedure for collecting the interface data before interpolation is also a consideration. Multiple steady/stationary powerstream blade stages interacting with stationary cavities/rim seals present a very challenging problem at the interface of the two flow streams, and given below are some details of the strategy used to handle this. The important considerations are: interface geometry and location; grids used on the interfaces; collection of needed data at the interface from the two codes; methods used for interpolation of data across the interfaces; placing the interpolated data back to the two codes for use in computations.

Interface geometry and location: In a typical coupled powerstream-secondary stream problem, the flow domains associated with the disk cavities are completely stationary in time. Grids associated with the stator rows are stationary in the main, except the deforming zones at sliding interfaces. The domains associated with the rotor stage(s), however, move with the rotor blades and also change shapes in the deforming zones. The interface patches between MS-TURBO and SCISEAL, thus can be physically located far apart from each other, or may be partially overlapping. A typical example of this is shown in figure 5-6, where interfaces for the three components from a rotor-stator-cavity combination are shown. In order to interpolate and transfer the data across the interfaces, the procedure established was:

1. Angular locations of a reference point on each interface are tracked in time, to get the relative positions of the interface pairs.
2. Before the interpolation procedure, the data donor surface/patch from SCISEAL or MS-TURBO is imaged to the data receiver surface/patch of the other code. Two consecutive images of the donor surface are generated, in order to ensure that the receiver surface is completely 'covered' by the donor surface images (figure 5-6).

The interpolation subroutines are now fed the geometrical details of the double-imaged donor surface and the single receiver surface for data processing.

The interpolation subroutines are now fed the geometrical details of the double-imaged donor surface and the single receiver surface for data processing.

Surface grids on interface boundaries: The grids associated with SCISEAL flow domains are stationary in time and the surface grids usually consist of structured quadrilaterals. The grids on the MS-TURBO interfaces will also be structured quads. However, the interface boundary shapes as well as the grids change shapes at each time step. The reason for this is the deforming zones associated with the deforming/clicking algorithm. The interpolation algorithm thus needs to account for the geometry and grid changes at each time step.

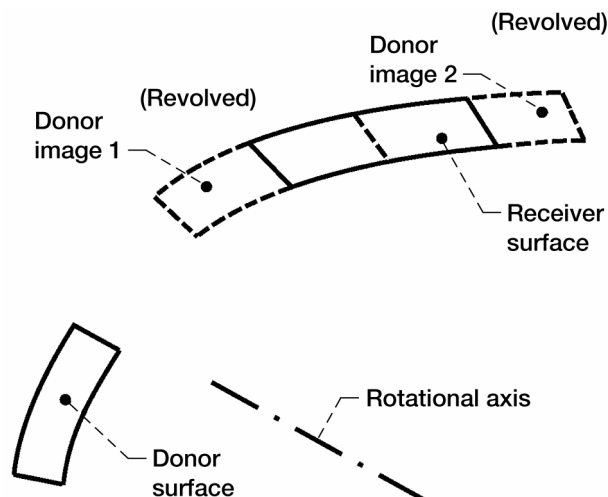


Figure 5-6.—Schematic of imaging of donor surfaces to the receiver surface prior to interpolation.

Collection of interface data: Has to follow the solution methodology of each code and the type of data to be transferred across. The primary flow variables are transferred from SCISEAL. These are updated at the end of each iteration, and are available easily from their respective storage locations. The data from MS-TURBO are the boundary fluxes for the five governing equations (continuity, 3 momentum equations, and energy,) and retrieving this information is more involved. As remarked in a previous section, MS-TURBO accesses information one blade row at a time. The linear implicit set of discretized flow equations is inverted at each Newton subiteration, and the flux information is overwritten during the inversion procedure. For this reason, the fluxes have to be stored during the ‘forward sweep’ of the solution algorithm, one blade row at a time. The MS-TURBO code needed modifications at a much deeper level in the algorithm than the SCISEAL code. Both convective and diffusive fluxes are collected in MS-TURBO.

Data preparation for interpolation: This is a two step process. In the first step the raw data from each code is first brought into dimensional form. SCISEAL code works on dimensional flow variables, and thus the first step is not required. MS-TURBO code, however, uses nondimensional flow equations, and both the convective and diffusive fluxes have to be dimensionalized separately before transfer to the interpolation algorithm.

The second step involves conversion of this data for rotation/imaging needed during interface match. Both codes use Cartesian velocity components as the primary variables and body-fitted generalized coordinate systems. For interface rotation, however, the fluxes and the variables in the flow equations in Cartesian system can not be used directly. Instead these are first converted locally into the equivalent r - θ - x coordinates, (i.e., a cylindrical coordinate system). This is accomplished by using a simple transformation of the type:

$$\begin{bmatrix} \phi_r \\ \phi_\theta \end{bmatrix} = \begin{bmatrix} \cos \theta & + \sin \theta \\ -\sin \theta & \cos \theta \end{bmatrix} \begin{bmatrix} \phi_j \\ \phi_k \end{bmatrix} \quad (5.2)$$

for the radial and tangential velocities, u_r and u_θ as well as for the fluxes along the radial and tangential grid lines. Imaging this converted data set now essentially means keeping the same flux/variable values, but changing the θ coordinate appropriately. The values of the new θ coordinates for each interface data set are determined from the relative locations of the interfaces. Once the new θ values are known, the fluxes/variables in the r - θ - x coordinate system are converted back to the Cartesian system via a reverse transformation:

$$\begin{bmatrix} \phi_j \\ \phi_k \end{bmatrix} = \begin{bmatrix} \cos \theta & -\sin \theta \\ +\sin \theta & \cos \theta \end{bmatrix} \begin{bmatrix} \phi_r \\ \phi_\theta \end{bmatrix} \quad (5.3)$$

The fluxes/variables are then ready for interpolation from the donor face sets to the receiver face sets.

Interpolation procedure: This is another key aspect of the interface methodology. It is a very complex problem due to:

- (a) cylindrical interface shapes;
- (b) surface grids which change continually and are usually skewed;
- (c) partially overlapping surface sets, where the receiver surfaces will cover only 50 percent of the area of the donor surface image pair;
- (d) need for fast procedures because the interpolation routines will be used a number of times by both codes during each single time step.

Note is also made of the fact that the donor data of fluxes/variables are not available at the grid nodes, but at the centroids of the faces or cells, and these values have to be interpolated to the centroids of the receiver surface.

An algorithm was developed at CFDRC to treat such a problem of interpolation and the method is very briefly described here. Additional formulation is given in appendix B. The method uses the following key steps:

1. Normal vectors at each grid face on the donor surface are calculated first. Any type of surface element can be treated, including triangles, quads and arbitrary polyhedra. For faces with more than three sides, the normal direction may not be unique, and a weighted average procedure is then used.
2. The face-center data (fluxes, variables) available on the donor grid is then transferred to the face corners using a Laplacian interpolation algorithm.
3. Gradients of the variable data at the face centers of donor grid are calculated using the corner values found in step 2.
4. For each of the face centroid from the receiver grid, the closest face centroid from the donor grid is found next. This is needed for the final interpolation procedure
5. Each receiver face centroid is projected in the face-normal plane of the closest face/centroid in the donor face. Variable value at the receiver centroid is then found by using the corresponding value at the donor face centroid, gradient at the donor face centroid and the distance between the donor and receiver face centers.

The interpolation procedure is used several times during a typical time step and speeding up the process is of help. Some speedup was achieved by storing the information related with donor face normals and the centroid neighbors in step 4. This information is calculated once at the beginning of each time step and used subsequently. Steps 2, 3, and 5 deal with variables to be interpolated, and have to be repeated at each data exchange.

The procedure described above is not guaranteed to be flux conserving in the global sense, i.e., if the variables/fluxes were integrated over the donor and receiver surfaces, the two may not match. This is not very crucial for variable transfer from SCISEAL to MS-TURBO, but the reverse transfer of fluxes from MS-TURBO to SCISEAL must be conservative. To achieve this, an additional integration step was added in MS-TURBO. The fluxes from the donor and receiver surfaces are integrated and the two values compared. The interpolated fluxes on the receiver surface are then adjusted using a simple constant multiplication factor to equalize the integrated/global values from the donor and receiver.

One further improvement to the interpolation procedure could involve the use of a flux conserving methodology where the faces from receiver grids are projected into the donor faces. A surface cutting

algorithm is then used to find out the intersection and overlaps of the donor and receiver surfaces. The fluxes are then interpolated from the donor surface to receiver surface grids using weighted area averages of the overlapping areas, and finally the contributions to each of the receiver grid faces are summed up. Such a procedure can be exactly flux conserving for donor-receiver surfaces which are planar. For cylindrical donor-receiver surface pairs, however, the accuracy of flux conservation will depend on the grid distribution, grid coarseness and other factors, and the overall effort may be only as accurate as the method currently being used.

Placement of interpolated data: This is the last step in the interface treatment procedure. As mentioned above, the interpolated data is written out to disk files for the other code to read in. On the MS-TURBO side, the input data consists of the variable values for the phantom layer. The input variable data is nondimensionalized first, and then stored at the appropriate boundary region phantom layer for use. On the SCISEAL side, the input data are fluxes from MS-TURBO. These are stored in the appropriate boundary storage array associated with the SCISEAL boundaries.

5.6 Summary

The methodology for a coupled, transient, 3-D solution procedure using two different codes for two different flow streams in a turbomachine, e.g., gas turbine engine, was described in this chapter. The rationale for the procedures and choice of the codes used, SCISEAL and MS-TURBO was described, followed by the various issues associated with the coupling procedure and the methods used in the present work to address these issues. The procedure for interpolation of data needed for coupled execution was described next to complete all aspects of the coupled execution. This methodology has been coded, debugged, and used on two test problems, a turbine rig problem and to a compressor rig. Description of these cases, solution methodology and sample results are described in the next Chapter.

6. Coupled, Transient Analyses of Power Stream-Secondary Flows

The codes and methodology described in the previous chapter was utilized to compute several 3-D, coupled, powerstream and secondary flows in gas turbines. Specifically, the codes were tried out on a simple case to validate/checkout the codes and coupling procedure. Second case was the high-pressure turbine rig developed by UTRC to test a high-work turbine stage. Third case that was attempted was a section from the NASA Glenn Research Center's Large Low-speed Compressor Rig (LSAC) that was built for generating flow data for code validation. These simulations comprised the validation and demonstrations problems. Details of these simulations are presented in this Chapter.

6.1 Bladeless Rotor+Stator+Cavity in a Turbine Section

This was the first case tried out and also served to debug the codes as well as validate the numerical models and the interface treatment. As would be appreciated, testing the time-accurate, coupled code methodology is not very easy for lack of suitable benchmark problems. A simplified case was therefore developed that could be solved by one of the two codes (SCISEAL or MS-TURBO) on its own, and this solution taken as the benchmark. The coupled codes were then tried next and the simulation results compared with the single-code simulations for validation and sanity checks. The MS-TURBO code was hardwired to handle only the powerstream flow and could not be used to treat the cavity portion as well. SCISEAL did have the flexibility to handle both flow streams, except the sliding interface between the stator and the rotor stages. The one way out was to consider a rotor+stator+cavity problem where the blades in the powerstream were taken out. This reduced the problem to a steady-state, axisymmetric flow

which could be handled by SCISEAL alone. A number of variations on this bladeless powerstream problem were tried and duplicated with the single code as well as the coupled codes.

6.1.1 Flow Geometry and Boundary Conditions.—The flow geometry consisted of a bladeless rotor stage followed by a bladeless stator stage, with an intermediate rim seal attached to a disk cavity with a very simple geometry. A solids model (solid surfaces with computational grids) is shown in figure 6-1 along with the boundary conditions and flow conditions that were used. The powerstream flow inlet boundary was at 300K, Mach 0.25 and the exit pressure was set at 100 kPa. The upstream stage was the rotor, and the hub wall was rotating at 1000 rpm. The rim seal gap was attached to an L shaped disk cavity, and the pressure conditions at the disk cavity inlet were specified as a boundary condition. All disk cavity walls attached to the rotor section were also treated as rotating walls. The powerstream conditions were held fixed, while the cavity inlet pressure were varied. With a sufficiently low inlet pressure the powerstream flow could be ingested into the cavity and by raising it the cavity flow could be forced into the powerstream at the rim seal. These cases were tried out with both cavity flow ingress and egress at the rim seal and the coupled code methodology checked out under both conditions.

The steady-state simulations were carried out with SCISEAL on a multi-block (1 block in powerstream and 2 blocks in the disk cavity) structured grid that was also used in the coupled code simulations. The grid was kept fairly coarse for fast execution and debugging. Two main cases were considered: one with definite flow ingress into the cavity and the other with a clear flow egress into the powerstream. Simulations and results of these cases are described next.

6.1.2 Flow Ingress in Cavity.—The cavity pressures were set to a low value of 98 kPa and the SCISEAL code was first used to obtain the steady-state simulations of the coupled powerstream-cavity flows. The same problem was then run in time-transient mode with the coupled codes and this was continued till a time-invariant solution was obtained. The mass flow rates at the cavity inlet/outlet plane were compared from the two sets of simulations and these were: 1.92×10^{-3} kg/s for the run with SCISEAL code alone and 1.83×10^{-3} kg/s for the coupled code run, and the two sets correlate well.

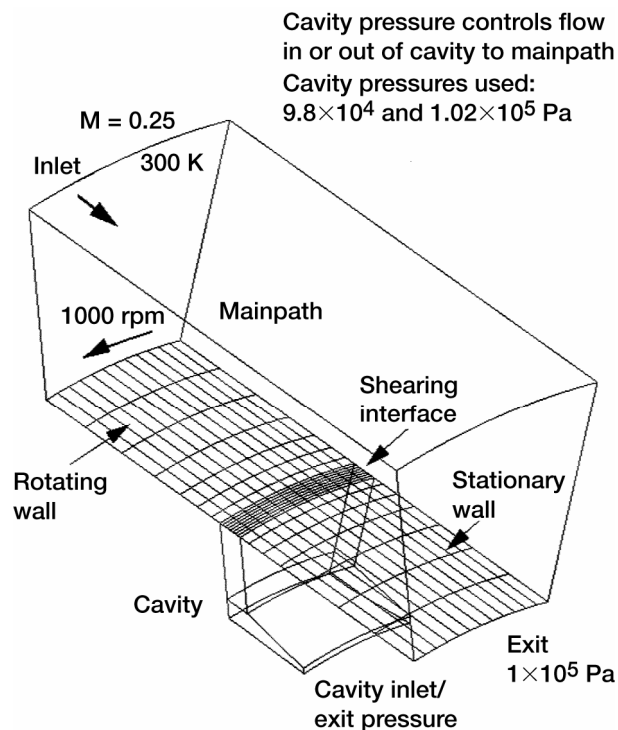


Figure 6-1.—Flow geometry and boundary condition for the annular rotor + stator + cavity test case.

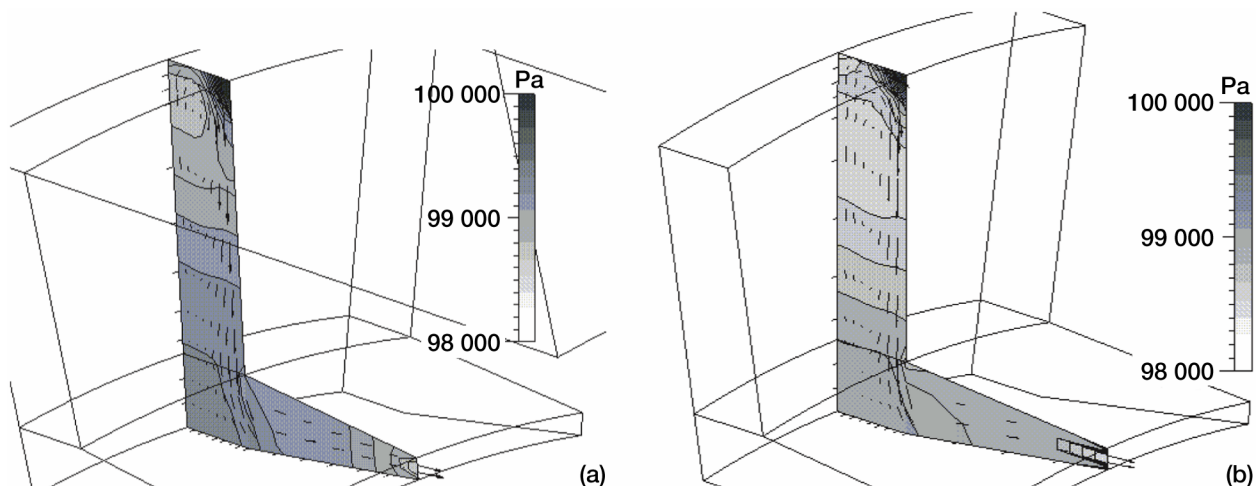


Figure 6-2.—Velocity and pressure field in the cavity with ingestion in the cavity. (a) Single code, SCISEAL. (b) Coupled codes, SCISEAL + MS – TURBO.

The structure of the flow near the rim seal is of interest and was checked for major flow features as well as pressure field. Combined velocity + pressure field plots from the single code run and the coupled code run are shown in figure 6-2a and 6-2b. Plotted here are the flowfields below the rim seal, i.e., the region handled by SCISEAL in the coupled runs.

Due to the fast powerstream flow, a recirculation zone is created at the rim seal interface. The cavity wall attached to the rotor spins and produces disk-pumping action, so that the flow near this wall always moves up radially. This flow gets turned at the rim seal interface, and again at the opposite stationary wall of the disk cavity. Due to the recirculation zone at the seal, the ingested powerstream flow enters the rim seal near the stationary wall of the cavity. As seen from the plots in Figs 6-2a and b, the velocity pattern associated with the recirculation zone as well as the stagnation pressure near the rim seal on the stationary side is very similar in both runs. This shows that in this case, when there is a net ingress into the cavity the coupled codes produce similar results to the single code run.

6.1.3 Flow Egress from the Cavity.—For this run, the cavity inlet pressure was set to 102 kPa with the powerstream conditions left unchanged. The single code results from SCISEAL produce a net flow into the cavity (and out of the rim seal to powerstream) of 2.388326×10^{-3} kg/s, and this compares very well with a computed flow egress from the rim seal of 2.256348×10^{-3} kg/s for the coupled code run.

The velocity + pressure field plots for an r-x plane for the single code and coupled code runs are shown in figures 6-3a and 6-3a. As before, the gross flow features as well as the pressure field distribution is very similar in the two runs.

Due to the flow egress condition at the rim seal, the flow features are different from the earlier case, with the rim seal region showing almost no recirculation. The disk pumping on the rotor wall augments the exiting flow and the radial momentum of this flow carries it in the powerstream in a near-radial direction. However, away from the rotor side cavity wall, the rim seal velocity shows the effects of the axial momentum of the powerstream flow, which tends to force the rim seal flow in the axial direction. A recirculation bubble forms near the cavity stator wall in this case, and the two sets of results show very similar velocity distribution near this recirculation zone.

This example served to show that the mass and momentum flux calculation as well as the data exchange at the interface is taking place properly, including the geometry manipulation and interpolation algorithm. Relative pressures in the cavity and powerstream decide the flow direction at the rim seal, and this example showed that the pressure information in the individual flow domains as well as across the interface is being transmitted properly. Although not shown here, the pressures are continuous across the interface, as will be shown in the next example where the two flow streams were plotted together.

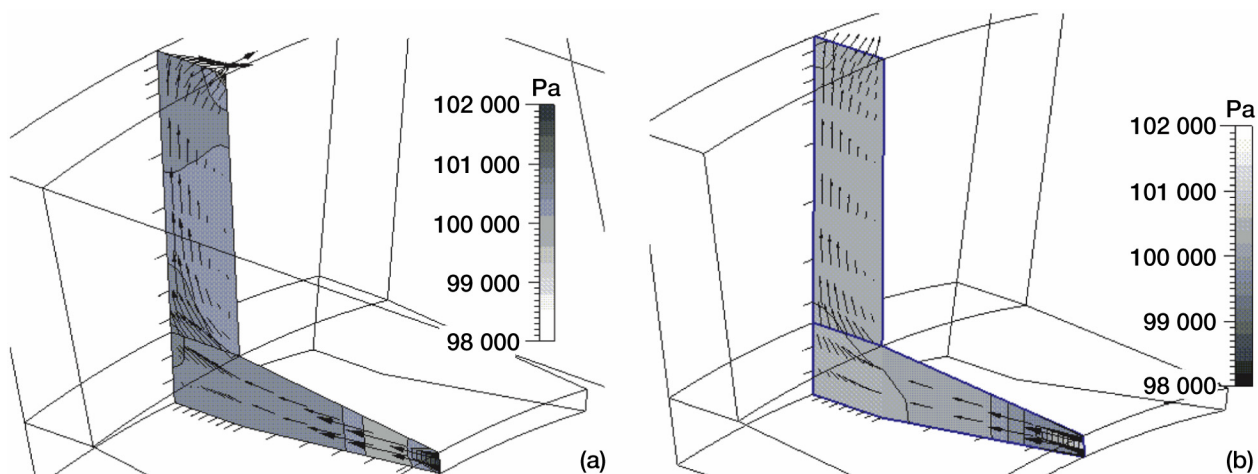


Figure 6-3.—Velocity and pressure field in the cavity with flow egress from the cavity. (a) Single code, SCISEAL. (b) Coupled codes, SCISEAL + MS – TURBO.

6.2 UTRC High-Pressure Rig Simulations

A test rig was built at UTRC to test a single rotor+stator+cavity configuration of a high-work turbine stage. Although not run at the actual engine conditions, the rig was built to provide detailed pressure, temperature and velocity information in all regions in time-averaged form and more importantly, in unsteady form. With this data the understanding of the dynamics between the powerstream flow and the disk cavity flows would be enhanced, and the unsteady data generated by the rig could be used for CFD code validation. This flow problem was simulated using the coupled code methodology developed here. The time-accurate results generated in the simulations are to be validated against the data from the H.P. Rig, and also provide flow details to UTRC for better instrumentation in the rig [19].

6.2.1 Geometry and Flow Information.—A cross section of the H.P. Rig is shown in figure 6-4 and shows the major components and flow directions. The circled area is the flow domain of interest and details of the geometry in this area is shown in figure 6-5. The powerstream flow domain consists of a stator vane that guides the incoming flow, followed by a single rotor stage. Two disk cavities are present on either side of the rotor stage, and the disk cavity upstream of the rotor stage is the cavity of interest. This interstage cavity interfaces with the powerstream at the rim seal. As shown, the rim seal has a ‘tongue and groove’ form and the overlap of the stator platform over rotor platform generates a backward facing step configuration. The powerstream flow will generate a recirculation zone at the rim seal as a result of this overlap. A three knife stepped labyrinth seal is present at the entrance of the cavity.

Blade counts on the stator vane and rotor stages were 48 and 58 respectively. If treated exactly, the representative PI sector would be 180 degrees, and would lead to a very large computational grid. For this reason, the blade count ratio was adjusted to 48 and 60 blades in the stator and rotor stage respectively, and the rotor blade thickness was adjusted to maintain the blocking factor. With this adjustment, the representative PI sector was set at 30 degrees, with 4 blades in the stator stage and 5 blades in the rotor included in the calculation domain.

Multi-domain structured grids were built in the powerstream domains, with one domain in each blade-to-blade block of the stator and rotor stages. Grids in the radial directions were matched exactly at the rotor-stator sliding/clicking interface. Grids in the θ direction were also matched one-to-one at the rotor-stator clicking interface. In θ direction, however, this match is over the entire flow problem, and this puts some restrictions on how the θ direction grid can be distributed in the individual blade-to-blade blocks (the θ direction cell counts in stator and rotor blade-to-blade blocks must be in inverse ratio to the blade count ratio). In the present case, the grids in each of the blade-to-blade block in the stator vane had

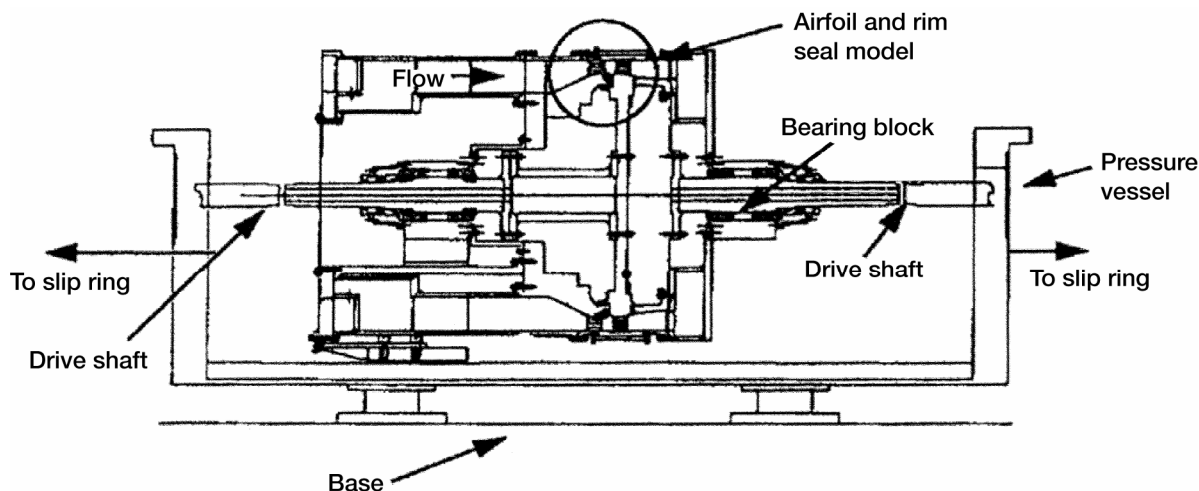


Figure 6-4.—Schematic of the UTRC HP turbine test rig.

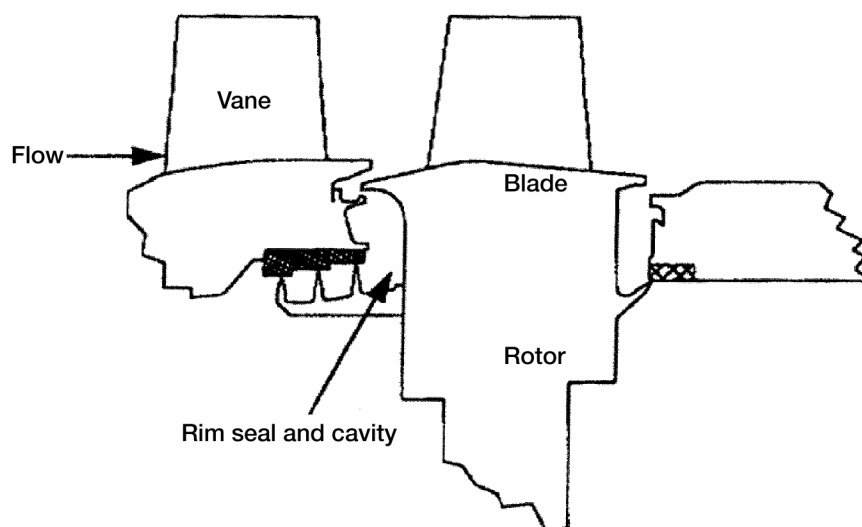


Figure 6-5.—Detail of the flow domain in the UTRC HP rig.

49 by 12 by 15 cells in the axial, radial and θ direction. The corresponding distribution in the rotor stage was 36 by 12 by 12 cells in each blade-to-blade block. This yielded a total of 61200 cells in the powerstream. The deformation zones ahead and after the rotor-stator clicking interface each had 4 cells in the axial direction. This is a relatively coarse grid, and should be refined. The tip clearance for the rotor stage was ignored for this computation. For the disk cavity and the labyrinth seal (SCISEAL flow domain), a multiblock, structured grid with 16 blocks was built and was generated by revolving a set of faces that define the r - x cross-section of the cavity. The computational grid for cavity+rim seal had approximately 33000 cells and used 30 cells in the θ direction to interface with 60 cells from the powerstream grid. figure 6-6 shows a solids model of the cavity and rim seal grids. The grids in the powerstream blocks were relatively straightforward, with H grid topology in each blade-to-blade block.

The grids in the rotor move with the rotating blades, and could be physically located anywhere in the circle. These have to be rotated and imaged for interpolation to the stationary grids, as was outlined in the previous chapter. Figure 6-7 shows the relative locations of the three grids at a given time during the computations.

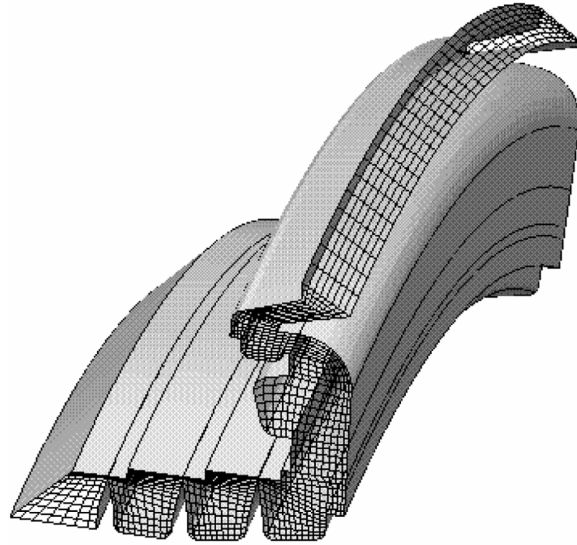


Figure 6-6.—Solids model of the 16 domain computational grid in the cavity and rim seal.

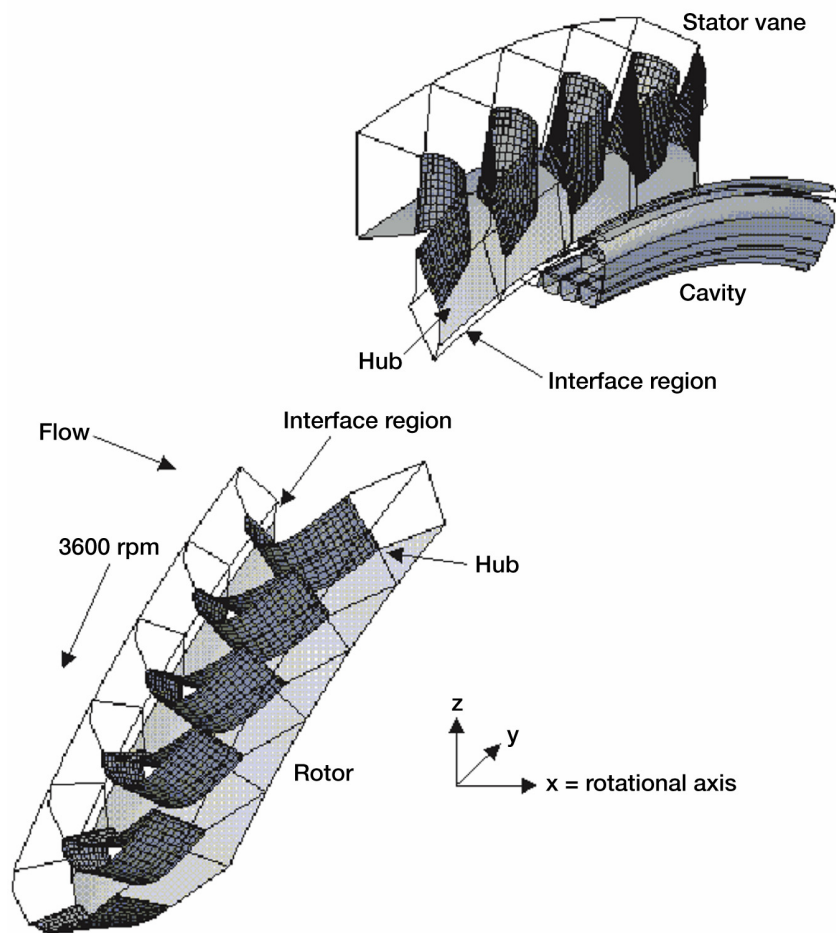


Figure 6-7.—Relative locations of flow domains at a specified time instant.

Air was used as the working fluid. In the powerstream, it was treated as a constant viscosity fluid and an eddy viscosity based model was used to treat turbulence. The upstream boundary for the stator row is an inlet Mach number and stagnation quantities (pressure and temperature). The incoming flow was taken as axial. The inlet Mach numbers is rather low at 0.09. At the exit of the rotor stage, static pressure with inertial radial correction was specified (the radial pressure gradient is matched to the centrifugal gradient generated by the tangential/swirl velocity at the exit). The shroud was a stationary wall. All the walls on the stator stage were stationary adiabatic walls, and the rotating, adiabatic walls were imposed on the rotor surfaces. The rotor speed was 3600 rpm. The inlet flow temperature was at room condition, 302.6 K. The powerstream inlet total pressure was set at 155 kPa/22.4 psia and the nominal exit pressure was 122 kPa/17.8 psia. The nominal exit pressure was imposed at the shroud of the powerstream exit, with decreasing pressure towards the hub as a result of the radial inertial balance.

The cavity and rim seal flow was treated as a compressible, variable property flow and the turbulence was handled with the standard $k-\epsilon$ model. The cavity inlet condition was specified in terms of the stagnation pressure and temperature. The stagnation temperature was set at room conditions/ 302.6 K and the stagnation inlet pressure was specified in terms of a fraction of the powerstream inlet total pressure. Several runs at different inlet pressure ratios (cavity total pressure/powerstream inlet total pressure) were completed: 0.97, 0.88 and 0.8.

Time step to be used in the coupled execution is determined by the powerstream code, MS-TURBO. The time step is specified in terms of the number of distortion steps to be taken before the grids in θ direction are clicked to the next grid. Once the circumferential grid-count in the powerstream and the rotor speed are known, the physical time step size is fixed. In the present solutions, the time step was set so that 16 deformation steps were taken in-between each grid click. This yielded 640 time steps per 30 degrees of rotor travel. The corresponding maximum CFL in MS-TURBO was approx. 8. For the present runs, first order time and space discretization in powerstream were used, while first-order time and second order central differencing were used in the cavity flow.

6.2.2 Results and Discussion.—Steady-state simulations of the cavity and powerstream were also performed to quantify the rim seal flow rates, which provided an anchoring point for the flow in a 2-D axisymmetric mode, where the blade wakes are ignored. Once the time-accurate simulations were done, these could than be compared and contrasted with the 2-D runs to assess the size of changes caused by the axisymmetric flow assumption. Representative 2-D velocity vectors in the cavity for an inlet pressure ratio of 0.97 are shown in figure 6-8 and clearly show the recirculation dominated cavity flow, as well as the recirculation zone at the rim seal. Location of the interface for the coupled MS-TURBO and SCISEAL run is also shown in this figure for reference and the interface could be expected to intersect the rim seal recirculation zone. The mass flow rate in the rim seal for this configuration was 0.278×10^{-3} kg/sec for a 30 degree PI sector.

The time-accurate, coupled solution runs were started with initial runs on both TURBO and SCISEAL codes, with the interaction turned off. The disk cavity solution was obtained with SCISEAL, and for this run constant flux values were specified at the interface boundary at the rim seal; the 2-D solution data was used to estimate these flux values. The initial run on the powerstream flow was done with MS-TURBO running in single code mode, with wall conditions in place of the rim seal interface. All of the other flow and boundary conditions were maintained at the desired values. Since the aim of the initial run was to wash out the initial condition, the time step in TURBO run was increased to 4 times the coupled execution time step, and the code was run for 600 time steps.

After the initial runs were completed, the parallel execution was started, and at a preset time step, the interface boundaries in both were 'opened' by starting the data exchange; this was similar to breaking open a membrane in-between the two codes. The exchanged data was underrelaxed for a prespecified number of initial time steps and then the underrelaxation was removed. The coupled execution procedure was continued for at least two PI sector rotations, i.e., for at least 60 degrees of rotor turn. At this point the flow was nearly time-periodic and then the solutions for the next 30 degrees of rotor turn were collected for processing.

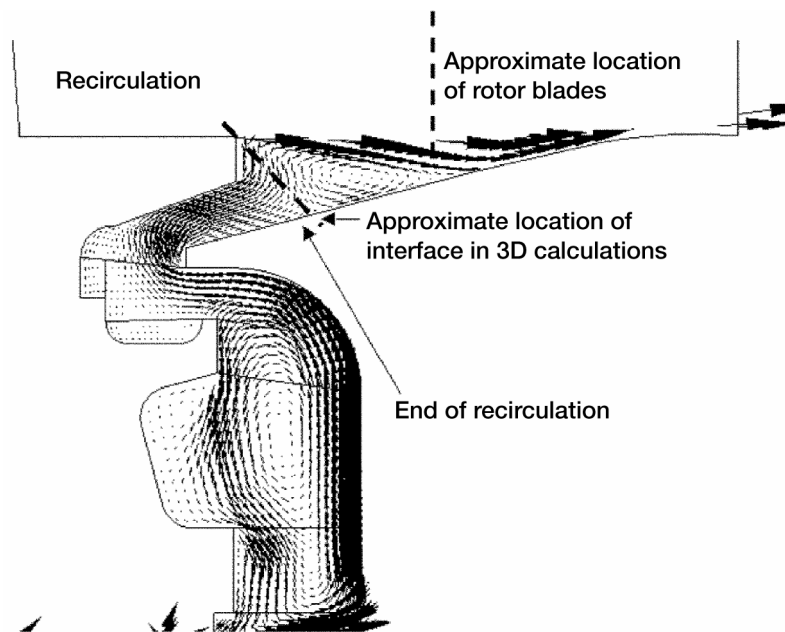


Figure 6-8.—Velocity vectors for 2D axisymmetric solution of the HP rig cavity.

As remarked earlier, three runs with cavity inlet stagnation pressure at 0.97, 0.88 and 0.8 times the powerstream inlet stagnation pressure were completed. 3-D time accurate solutions generate voluminous data and it is difficult to show it in detail. Only representative plots are shown here and discussed. The results have also been used to prepare slides of results at different times steps and these have been combined to produce animated plots. See CD attached to this report.

A representative pressure surface plot in the powerstream domain (MS-TURBO solution) is shown in figure 6-9, showing the pressure distribution along the hub surface which also contains the interface between MS-TURBO and SCISEAL. The stator blade wakes are clearly visible (although not very dramatic for the test rig conditions). The wakes then interact with the cavity flow and affect the interface pressure distribution, and exert some influence near the entrance of the rotor blade row. The flow is expanding along the powerstream and the continually decreasing pressure along the powerstream flow direction reflects this.

One of the assumptions in the powerstream-cavity flow interaction was that the blade-wake interaction in such problems could be strong, providing substantial changes in the rim seal flow field. In the present case, however, such changes were not seen. In fact, the serpentine passage in the rim seal and cavity seemed to produce a large amount of flow damping, so that the flows near the labyrinth seal were perturbed to a very small degree.

Two representative velocity plots are shown here to explain the calculated flow fields. The location of the cutting planes was fixed based on the location of the rim seal with respect to the stator blade wakes. Figure 6-10 shows the “wake” cross-section and “midplane” cross-sections used in the plots. Figure 6-11 shows the “complete” cross-sectional surface that includes the cavity and the powerstream and illustrates the complexity of the flow domain. All of the vector plots shown here used combined cutting planes as shown in figure 6-11.

Two velocity vector plots in the r - x cross section of the cavity+powerstream are shown in figures 6-12a and b. The rim seal in figure 6-12a is in the blade wake, and it is midway between two wakes for figures 6-12b. The recirculation zone in the rim seal area is clearly seen. When the cutting plane is in the wake region this recirculation zone is somewhat weaker than for the cutting plane in midway plane where the pressure levels are lower. There are also some differences in the velocity plots and pressure values in the neck region and cavity below, but it is too small to be seen in these plots. Some

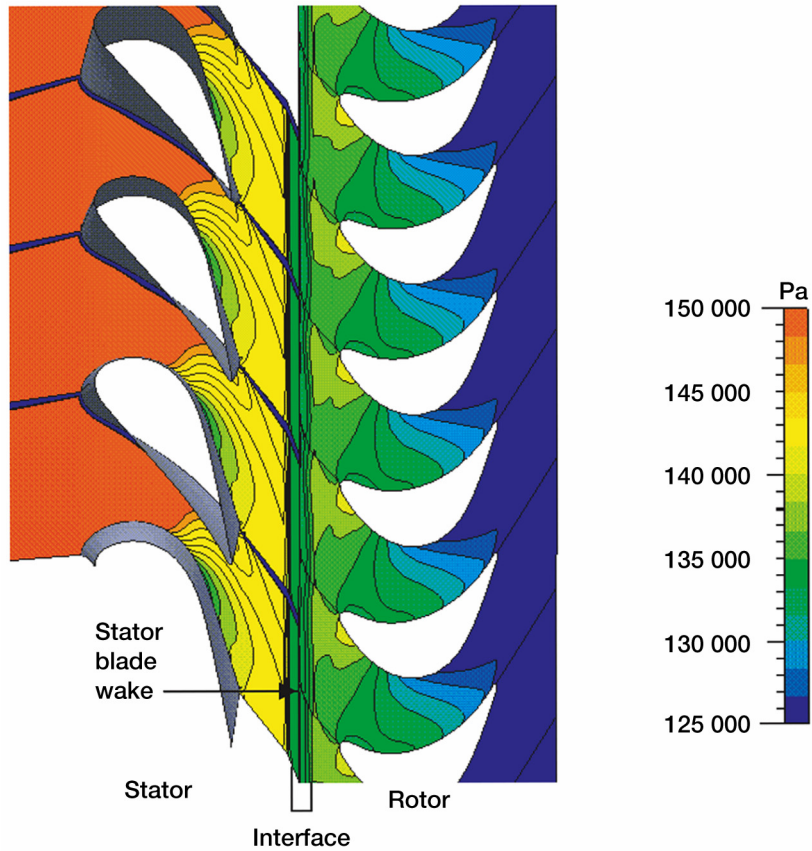


Figure 6-9.—Representative surface pressure plot in the powerstream at the hub.

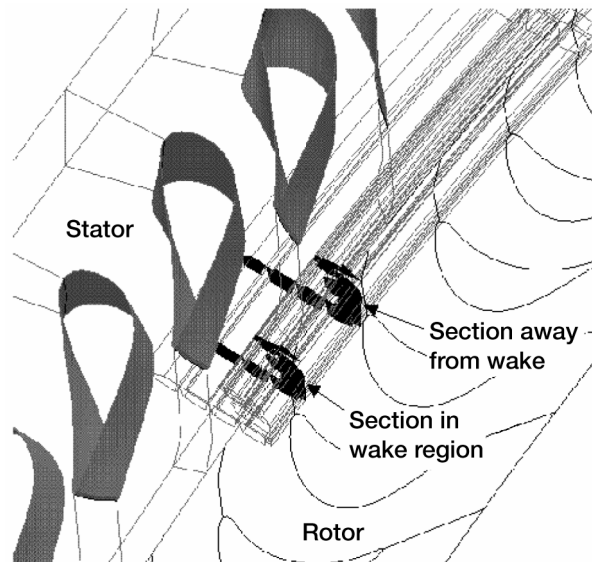


Figure 6-10.—Relative locations of the cross-sectional planes in the cavity for velocity plots.

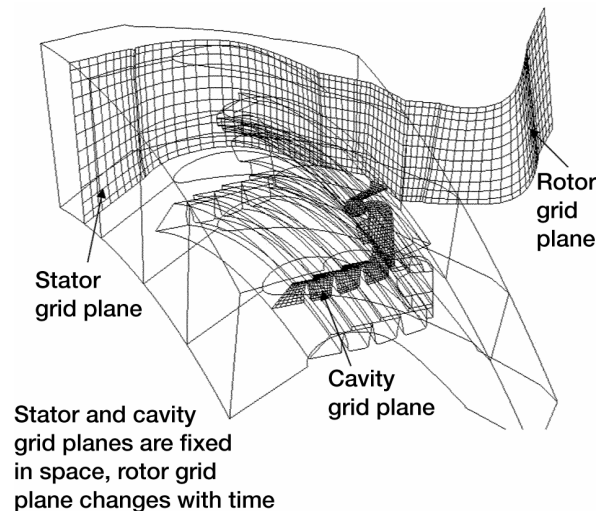


Figure 6-11.—Relative locations and shapes of the plotting planes cavity plane in mid-passage.

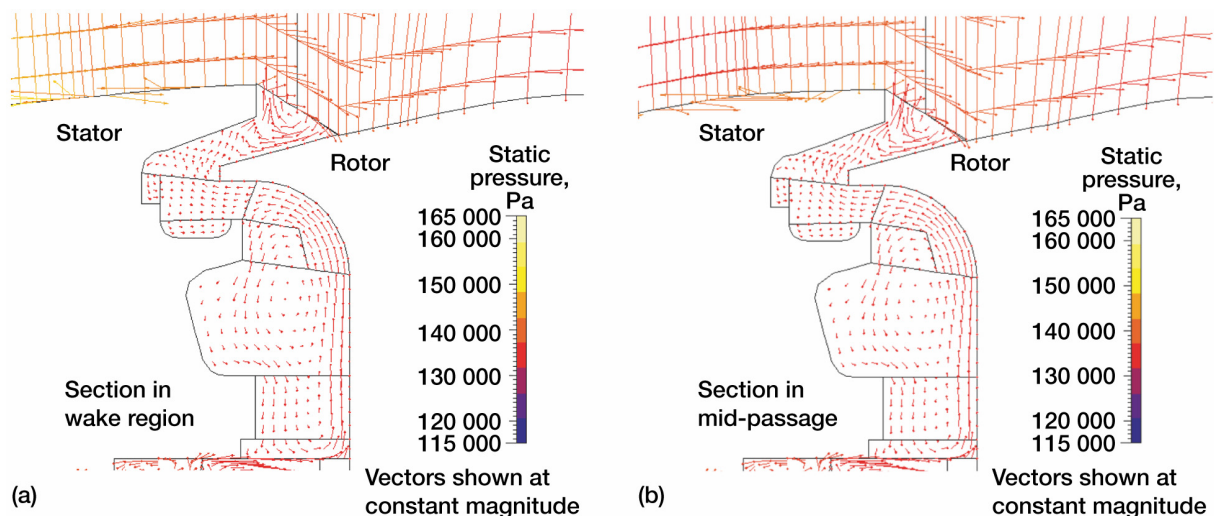


Figure 6-12.—Velocity vectors and pressure field for the HP rig at pressure ratio of 0.98. Cutting planes as shown. (a) Cutting plane in wake region. (b) Cutting plane in mid-wake region.

preliminary experimental data from the rig suggests that the pressure changes in the cavity, induced by the blade passing, are very small, of the order of a few percent of the powerstream pressures, and this correlates well with the plots shown here.

The velocities in the cavity cross section show a torturous flow path, flow threads and numerous recirculation zones. The right side wall and bottom labyrinth wall are rotating. This produces pumping action along all vertical walls and generates a large recirculation zone in the vertical open area of the cavity. The flow moves into the rim seal neck along the top surface, goes around the rotor ledge and then is slung out towards the stator ledge. The recirculation zone near the rim seal also helps this motion. The cavity flow then moves along under the stator ledge till it mixes in the mainpath flow. The stepped labyrinth seal shows the usual recirculation zones, the main one in the labyrinth cavity and another in the step region.

The velocity plots in figure 6-12a or b can also be compared with the 2-D solution shown in figure 6-8. The main flow features are similar except the recirculation zone in the rim seal area, which is much flatter in the 2-D solutions as compared to the coupled run. One reason is that the blades in the

rotor stage were ignored in the 2-D run, and these produce flow disturbances which would tend to reduce the recirculation zone in axial direction. The mass flow through the rim seal in the 3-D run varied from 0.22–0.26 kg/s as compared to 0.278 kg/s seen in the 2-D run, which are in fairly good agreement. Such comparisons in flow structure and flow rates will be ultimately useful in assessing the 2-D results with the ‘correct’ 3-D time accurate solutions as more flow cases are analyzed.

Reducing the cavity inlet pressure ratio from 0.97 to 0.88 reduced the rim flow into the powerstream, but the flow structures remained essentially the same. A large reduction to a pressure ratio of 0.8, however, produced results that were substantially different in terms of the flowrates at the rim seal which went from approx. 0.0146 kg/s into the powerstream at pressure ratio 0.88 to a flowrate of 0.0165 kg/s into the cavity at a pressure ratio of 0.8, indicating that the zero flow rate at the rim seal could be inferred to be at approx. a pressure ratio of 0.85. UTRC had some experimental data for the average flow rates into and out of the cavities and the data indicated that the zero flow rate condition was seen at a pressure ratio of 0.84. Thus, good correlation was seen between the numerical and experimental data.

A representative velocity plot in the midway plane for pressure ratio of 0.8 is shown in figure 6-13a to illustrate the changes in the cavity flow when the rim seal ingests the powerstream flow. For comparison, the corresponding vector plot for pressure ratio of 0.88 is shown in figure 6-13b. The obvious differences are in the labyrinth seal area where the flow vectors on top of the teeth have reversed direction in figure 6-13a (flow from right to left). The flow before the rim seal and near the blade platform ledges also shows dramatic changes. The recirculation at the interface is still similar, but in figure 6-13a, the flow near the rotor ledge is stronger, and a part of this continues on into the gap between the rotor-stator ledges. The recirculation neat the rotor ledge tip has reversed direction and this flow then gets added to the downward leg of the recirculation in the vertical block of the cavity. Differences are also seen at the lower end of the recirculation zone, where a large part of the downward leg of the recirculation flow goes into the labyrinth seal in figure 6-13a, while in figure 6-13b it is turned away from the labyrinth seal and absorbed in the upward leg of the recirculation zone.

These runs and representative plots show the detailed information that can be generated using the coupled codes. The limited amount of comparison with 2-D runs as well as experimental data has shown that to this extent, the physics and numerics in the coupled execution procedure has been done properly and produces reasonable results. UTRC is in the process of additional, time-accurate data generation from the H.P. Rig and this data will be invaluable into validating and anchoring the coupled code execution procedure.

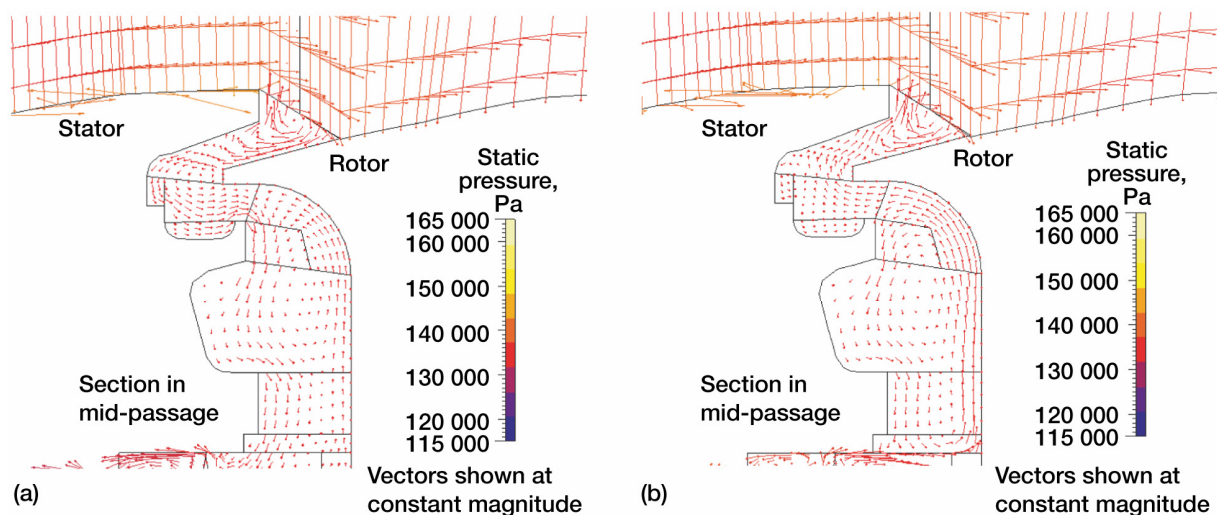


Figure 6-13.—Velocity and pressure plot for HP rig at two different cavity pressure ratios. Cutting plane in the mid-wake region. (a) $P_{ratio} = 0.8$, ingress into cavity. (b) $P_{ratio} = 0.88$, egress from cavity.

As remarked earlier, the time step size corresponded to a CFL number of around 8. Some testing has shown that CFL numbers of up to 12 can be used. The time step size is determined by the blade motion criterion, and so offers a limited amount of control on the possible CFL values. Time dependent runs are in general expensive, and the present methodology was no exception. The codes were run on two Silicon Graphics R10000 processors, and together, the two codes needed approximately 10 minutes of clock time per time step. The total number of time steps usually ran about 2000-2200 for periodic solutions. This translates a total clock time of about 360 hours. With the advent of faster machines with clock speeds of 1 GHz and more, these computational times will reduce substantially, making even the time-accurate runs a possibility for design simulations.

6.3 NASA Low-Speed Air Compressor (LSAC) Rig

A low-speed air compressor facility was built at NASA Glenn Research Center and used to generate flow data in a multi-stage machine, for code validation as one of the purposes. The rig has four rotor stages, inlet and exit guide vanes and three intermediate stator rows, see figure 6-14. The interstage cavities can be altered to some extent to change labyrinth seal shapes etc. to evaluate their effects on the cavity flows. A description of the rig and blade geometries etc. is given in [20]. The authors, Wellborn and Okiishi, conducted experiments on the rotor 3-4 interstage cavity and rim seals to analyze the coupled, time dependent flow fields. The powerstream flow in their configuration had 3 blade rows: rotor No. 3, stator No. 3 and rotor No. 4. The interstage cavity is relatively simple in shape, and the labyrinth seal had a single tooth. The experimental data includes velocity profiles in the powerstream, rim seals, and partway into the cavities. A schematic of the experimental configuration is shown in figure 6-15.

6.3.1 Geometry and Flow Conditions.—The blade rows have simpler blade ratios: 39 blades on each rotor and 52 blades on the stator vane. This allows the use of 3 blades each in the two rotor stages and 4 blades in the stator stage, with a PI angle of $360/13$ degrees. The operational conditions for the rig are: 960 rpm, flow rate of 12.3 kg/s and a pressure ratio of 1.04 over the entire rig. The disk cavities in the compressor sections typically are not cooled with purge flow. The flow in the two disk cavities and the labyrinth seal is driven by the pressure differential between the rim seal after the stator blade and the rim seal before the stator.

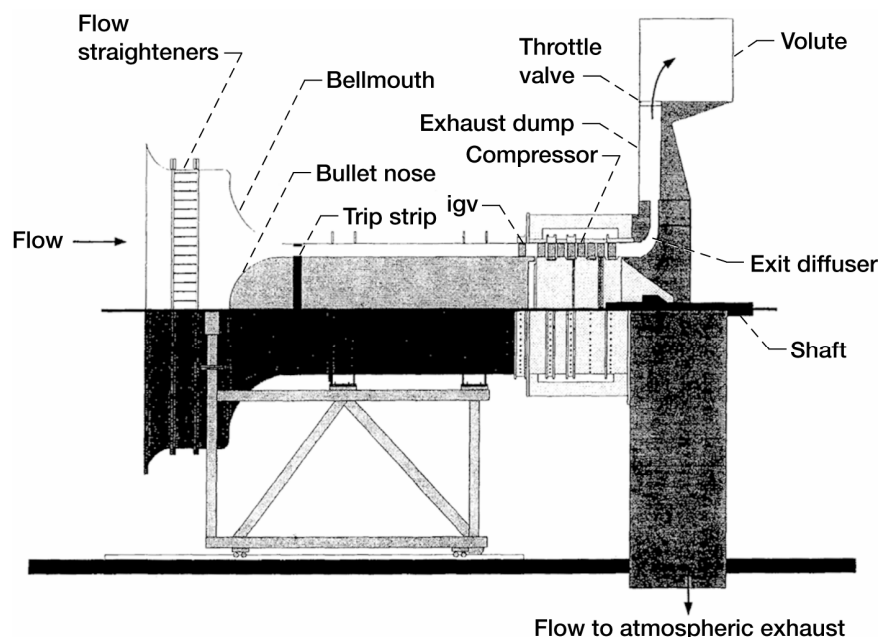


Figure 6-14.—NASA Lewis low-speed axial-flow compressor (LSAC).

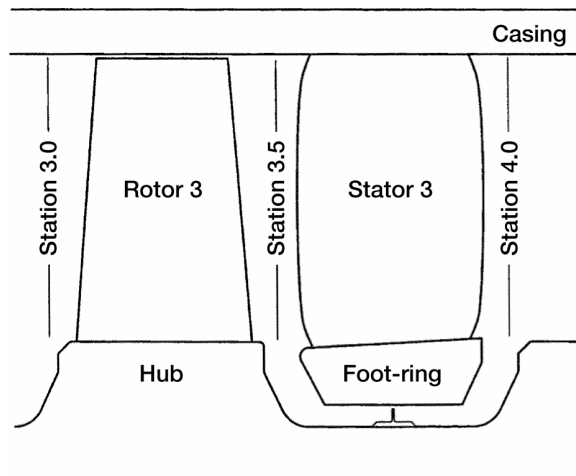


Figure 6-15.—Schematic of third stage of LSAC and the interstage disk cavity.

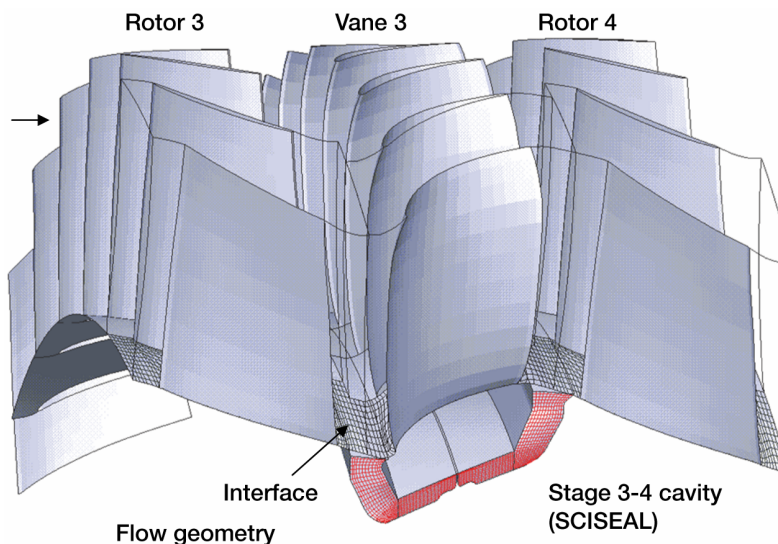


Figure 6-16.—Solids model of the LSAC rig flow domain.

A multi-domain grid was built for the powerstream with one block in each of the blade-to-blade passages. This yielded 3 blocks each in the two rotor stages and four domains in the stator. The grid sizes used were 29 by 12 by 12 cells in the axial, radial and tangential directions in each block of the rotor stages and 40 by 12 by 9 cells in each block of the stator stage. This yielded a total of approximately 130K cells in the powerstream flow. A 7-domain, 28K cell grid was generated for the secondary flow circuit. A solids view of the flow domains showing the powerstream blades and the disk cavities is shown in figure 6-16.

The external flow boundary conditions are needed only in the powerstream for this configuration since the cavity flow is entirely driven by the powerstream. At the inlet of the first rotor stage the inlet Mach number, swirl conditions and the total pressure and temperature were available. At the rotor exit a static pressure with radial balance condition was imposed.

6.3.2 Results and Discussion.—As for the H.P. rig, the solutions were started with a steady-state run for the cavity flow with some reasonable flux conditions at the inlet of the two rim seals. The TURBO code was run on the powerstream with walls at the rim seal interface. At a predetermined time, both the rim seal interfaces were then allowed to exchange data. The time step was determined by the grid clicking frequency at the stator-rotor interfaces. The circumferential grid count in the powerstream passage was 36 and 16 time steps were used per grid click to yield 576 steps per PI sector.

A number of different simulation runs were attempted. Initially, the exact rig conditions were used, but the simulations tended to diverge relatively quickly. Changes in the time step size as well as the number of subiterations per time step in the two codes usually would change the number of time steps before code divergence.

In consultation with NASA personnel, the rpm of the rotor stages was doubled to 1920 rpm, in order to achieve higher flow speeds in the powerstream in an attempt to bring the Mach numbers in the applicable range for the MS-TURBO code. However, the pressure ratio across the machine was kept as before, *which should also have been scaled up*. With this reduced pressure increase at a given flow rate, the powerstream flow rate was much smaller than that which would correspond to the lower pressure rise. A run was completed with these conditions, and revealed that the lower flow rate generated low velocities near the hub, and in some places produced reverse flow near the hub (consistent with incipient stall). Typical velocity and pressure plots from the coupled procedure are shown in figure 6-17a, where the cavity section was placed in the wake of the stator blade and 6-17b where the section was placed halfway between the stator blade wakes. As seen, the gross features of the cavity flow include recirculation zones in both the rim seals as well as in the vertical sections of both cavities. The expected jetting of flow on top of the labyrinth tooth is also seen. Although the main flow features were clearly captured in the simulated solution, quantitative comparisons with experimental results could not be performed at the flow conditions used in these simulations. An additional run at the proper pressure ratio was started but could not be completed because of time and resource limitations.

6.4 Summary

The results presented in this chapter indicate that the coupled execution procedure can be successfully used to handle the powerstream and cavity flow interaction in the time-accurate mode. The validation test case, although simple, served to show that the basic physical and numerical arguments used in the algorithm development are correct and coded properly. The H.P. rig simulations showed that the coupled codes can handle complex shaped cavity and powerstream flows. Results from the coupled codes matched with the 2-D simulations and experiments, and the predicted cavity inlet pressure ratio for a zero rim seal flow matched well with the UTRC experimental value. One of the concerns during the simulations was the relatively small perturbations seen in the cavity flow as a result of the powerstream disturbances. Part of the reason may be that the wakes upstream of the rim seal were fixed in space while rotor blades that were downstream of the rim seal produced perturbations in the powerstream. These disturbances are small compared to those one would get if the upstream blade wakes were moving. These small disturbances were then further damped out in the rim seal. Additional experiments in the H.P. rig, with better instrumentation for transient measurements are in progress and results from these tests will be valuable in further validation of the codes. The LSAC runs were somewhat less successful, and part of the reason may have been the extremely slow powerstream flow that had to be handled by MS-TURBO. The compressor cavity simulations are more difficult because the success of the coupled codes will depend on the accuracy of the powerstream code. Other compressor cavity cases, where the powerstream flows are in a more favorable range need to be simulated to ensure that the coupled execution procedure will work in the compressor section of a gas turbine engine.

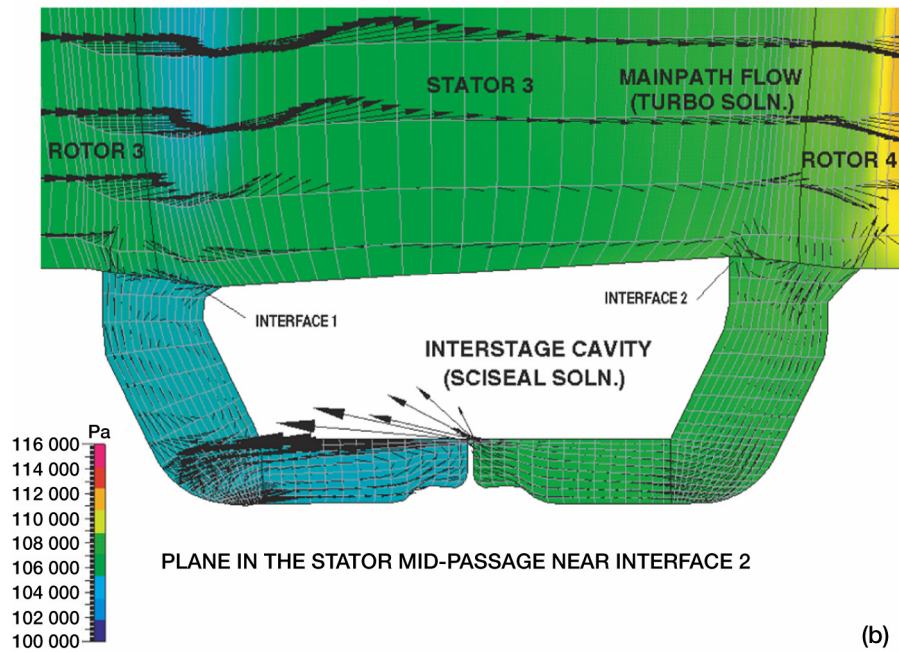
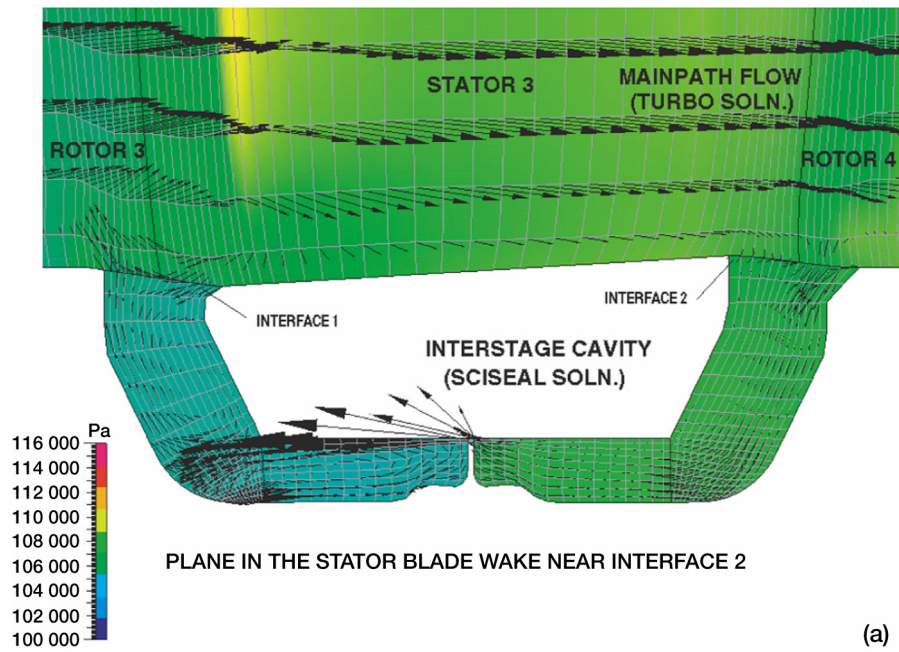


Figure 6-17.—Velocity and pressure field in the LSAC rig. Cutting planes as shown. (a) Cutting plane in stator blade wake. (b) Cutting plane in stator mid-wake region.

7. Summary and Recommendations for Future Work

With the drive for higher power and efficiencies from gas turbine engines, optimization of secondary flow systems has become important because of the potential for improvements. For successful optimization of the secondary/seals flows, details of the secondary system flow and thermal behavior, and its impact on the other flow systems in a gas turbine engine must be known. Present day numerical tools offer a way to provide such details, and the current work was focussed on two aspects: 1. To apply the present day advanced CFD tools to different real-life secondary flow applications from different original equipment manufacturer, to provide feedback and 2. Develop a computational methodology for coupled, time-accurate simulations of the powerstream and secondary flow, with focus on the disk-cavity and rim seal flows and interaction with the powerstream.

The preceding chapters of the report have presented the work performed on both areas of focus. Main objectives of the present work were completed successfully. The CFD code, SCISEAL, was used on three sets of problems. One was the validation study on flow and heat transfer in disk cavities, and the results with two different commonly used models were compared with very good correlation with published experimental data.

One of the OEM problems was the T56 engine turbine drum cavities from Allison Engine Company, Rolls Royce Aerospace Group (RRAE). Flow and conjugate heat transfer simulations on the inner disk cavities were performed and results compared with RRAE design data, again with good correlation. The results with conjugate heat transfer in the solid parts (rotors, seal supports) showed that additional thermal loads are placed on the cavity coolant flows by the conduction of heat in the solid parts. This additional load must be taken into account when designing and optimizing the secondary flow systems in the turbine sections. Additional parametric simulations also revealed interesting information on flow behavior in response to variations in coolant flow rates and seal clearances, which will be valuable in design process.

The second OEM problem was the aspirating face seal being developed by GE and Stein Seal Company. Initial 2-D CFD simulations provided results that were similar to those obtained from Stein Seals' design codes. However, at flow and geometrical conditions away from the design working conditions the predictions from the simpler design codes differed significantly. More importantly, the test seal showed unacceptable deviations from the design specifications. In this case the 3-D CFD simulations played a crucial role in analyzing this seal and coming up with the reasons for the observed behavior. The interaction of flow streams from two different parts of the seal (seal dam and bearing) at larger seal clearances (which could not be accounted for in the design codes) was identified as the main reason, and a fix suggested. The fix was first tested numerically using the 3-D model, and showed dramatic improvements in seal loads. The modification was then implemented on the GE test seal, and the seal performance was restored to the design specifications. The test seal design is currently being revised and additional simulations will be vital in ensuring that the new seal design will behave properly.

The second major objective, development of a coupled flow simulation capability was achieved by using two codes, MS-TURBO and SCISEAL for the powerstream and secondary flows, and coupling these with an interface algorithm. A number of issues such as interface placement, data exchange routines etc. were successfully resolved, and flux conservation across the interface was ensured. The coupling algorithm was completed, and tested on three different problems. The UTRC H.P. rig simulations matched the partial experimental data very well and currently the numerical results are being made available to UTRC for better instrumentation. Additional data from the rig, as it becomes available, will be valuable in validation of the current algorithm as well as others.

The coupling algorithm developed during this phase was important in linking the two selected codes to work together and provide proper physics during the data exchange. Another important aspect of this work is the methodology of the coupling itself. A number of issues were sorted out and proper solutions worked out. This experience will prove useful if similar coupling algorithms are to be developed for other applications.

7.1 Recommendations for Future Work

The work presented here is by no means complete and a number of future improvements and extensions can be made to further this work and to perhaps bring some of the numerical technology to the design stages of turbine secondary flow circuits. Some of the possible areas for future include, in brief:

1. Additional work on the 2-D simulations of the turbine drum cavities, including the conjugate heat transfer in the solid parts could prove valuable in better estimation of the coolant flow heat loads. One of the major problems is the lack of data from actual engines for code validation, and work in this area will also be very valuable.
2. The thermal fields in the solid portions of the secondary flow system can be used in a structures module to evaluate the thermal stresses and strains in these parts. Although the 2-D representation is not truly representative of the complex shaped solid parts in an actual engine, the thermal-structures calculation can provide some idea of the displacements and loads on the solid parts.
3. As remarked earlier, the coupled solutions were obtained with two separate codes, as this was the best alternative at the time of this project. In principle, the secondary flow code, SCISEAL, can be used in the powerstream if the sliding interface treatment were available in SCISEAL, and may provide better solution capabilities. Similar remarks may also be true in case of extending the powerstream code into the cavity region. Certainly this aspect should be explored further.
4. The coupled solution methodology should be tried out on more realistic flow cases, on actual engine conditions and geometries to evaluate the performance of the codes as well as to understand the coupled flow physics. To this end, additional simulations with flow and geometry variations on the H.P. rig would be useful, because the numerical solutions could be used for better rig designs and instrumentation.

8. References

1. Steinetz, B.M., and Hendricks, R.C., "Engine Seal Technology Requirements to Meet NASA's Advanced Subsonic Technology Program Goals," NASA-TM-106582, AIAA-94-2698, AIAA Joint Propulsion Conference, Indianapolis, IN, 1994.
2. Heidigger, N.J., Hall, E.J., and Denaley, R.A., "Parameterized Study of High-Speed Compressor Seal Cavity Flows," AIAA-96-2807, AIAA 32nd Joint Propulsion Conference, Lake Buena Vista, FL, July 1996.
3. Athavale, M.M., Przekwas, A.J., Hendricks, R.C., and Liang, A.D., "SCISEAL-A Three-Dimensional CFD Code for Accurate Analyses of Fluid Flows and Forces in Seals," Conference on Advanced Earth-to-Orbit Propulsion Technology, May 1992.
4. Athavale, M.M., Ho, Y.H., Forry, J.M., Munson, J.H., Hendricks, R.C., and Steinetz, B.M., "Simulation of Secondary Flow in Gas Turbine Disc Cavities and Interaction with the Main Flow Path," AIAA-95-2620, 31st AIAA Joint Propulsion Conference, San Diego, CA, July 1995.
5. Ho, Y.-H., Athavale, M.M., Forry, J.M., Hendricks, R.C., and Steinetz, B.M., "Simulation of Secondary Flow in Gas Turbine Disc Cavities, Including Conjugate Heat Transfer," ASME-96-GT-67, ASME International Gas Turbine and Aeroengine Congress and Exhibition, Birmingham, UK, June 1996.
6. Athavale, M.M., Ho, Y.-H., Forry, J.M., and Hendricks, R.C., "Simulation of Powerstream and Turbine Disc Cavity Flow Interaction Under Transient Conditions," AIAA-96-3305; AIAA 32nd Joint Propulsion Conference, Lake Buena Vista, FL July 1996.
7. Hwang, M-F., Shucktis, B., "Advanced Seals for Engine Secondary Flowpath," AIAA-95-2618, AIAA 31st Joint Propulsion Conference, San Diego, CA, July 1995.

8. Turnquist, N.A., Bagepalli, B.S., Reluzco, G., Wolfe, C.E., Tseng, T.W., McNickle, A.D., Dierkes, J.T., Athavale, M.M., and Steinetz, B.M., "Aspirating Seal Modeling and Full Scale Testing," AIAA-97-2631, 33rd AIAA Joint Propulsion Conference, Seattle, WA, July 1997.
9. Turnquist, N.A., Tseng, T.W., McNickle, A.D., Dierkes, J.T., Athavale, M.M., and Steinetz, B.M., "Analysis and Full Scale Testing of an Aspirating Face Seal with Improved Flow Isolation," AIAA-98-3285, AIAA 34th Joint Propulsion Conference, Cleveland, OH, July 1998.
10. Kilic, M., Gan, X., and Owen, J.M., "Turbulent Flow Between Two Disks Contrarotating at Different Speeds," *J. Turbomachinery*, Vol. 119, pp. 408-413, 1996.
11. Gan, X., Kilic, M., and Owen, J.M., "Flow Between Counterrotating Disks," *J. Turbomachinery*, Vol. 117, pp.298-305, 1995.
12. Northrop, A., and Owen, J.M., "Heat-Transfer Measurements in Rotating Disc Systems, Part 2: The Rotating Cavity with a Radial Outflow of Cooling Air," *Int. J. Heat and Fluid Flow*, Vol. 9, pp.27-36, 1988.
13. Athavale, M.M., Vaidya, N., Hendricks, R.C., and Steinetz, B.M., "A Computational Study of Turbulent Flow and Heat Transfer in a Rotating Disc Cavity, 7th International Symposium on Transport Phenomena and Dynamics of Rotating Machinery (ISROMAC-7), Honolulu, HI, 1998.
14. Janus, J.M., "Advanced 3-D CFD Algorithm for Turbomachinery," Ph.D. Thesis, Department of Aerospace Engineering, Mississippi State University, May 1989.
15. Janus, J.M., and Whitfield, D.L., "Counterrotating Prop-Fan Simulations which Feature a Relative Motion Multiblock Grid Decomposition Enabling Arbitrary Time-Steps, AIAA-90-687, AIAA Aerospace Sciences Meeting, Reno, NV, 1990.
16. Chen, J.P., "Unsteady Three-Dimensional Thin-Layer Navier-Stokes Solutions for Turbomachinery in Transonic Flows," Ph.D. Thesis, Department of Aerospace Engineering, Mississippi State University, Dec. 1991.
17. Janus, J.M., and Horstman, H.Z., "Unsteady Flow-Field Simulation of Ducted Prop-fan Configurations," AIAA-92-0521, AIAA Aerospace Sciences Meeting, Reno, NV, 1992.
18. Athavale, M.M., Przekwas, A.J., Hendricks, R.C, and Steinetz, B.M., "Development of a Coupled, Transient Simulations Methodology for Interaction Between Primary and Secondary Flowpaths in Gas Turbine Engines," AIAA-97-2727, AIAA 33rd Joint Propulsion Conference, Seattle, WA, July 1997.
19. Athavale, M.M., Przekwas, A.J., Hendricks, R.C., and Steinetz, B.M., "Coupled, Transient Simulations of the Interaction Between Power and Secondary Flowpaths in Gas Turbines," AIAA-98-3290, AIAA 34th Joint Propulsion Conference, Cleveland, OH, Jul 1998.
20. Wellborn, S.R., and Okiishi, T.H., "Effects of Shrouded Stator Cavity Flows on Multistage Axial Compressor Aerodynamic Performance," NASA CR 198536, October 1996.
21. Chien K.Y., "Prediction of Channel and Boundary-Layer Flows with a Low Reynolds Number Turbulence Model." *AIAA Journal* 20.1(1982): 33-38.

Appendix A

Selected Publications



AIAA-95-2620

**SIMULATION OF SECONDARY FLOW
IN GAS TURBINE DISC CAVITIES
AND INTERACTION WITH
THE MAIN FLOW PATH**

M.M. Athavale and Y.-H. Ho
CFD Research Corporation
Huntsville, AL

J.M. Forry and J.H. Munson
Allison Engine Company
Rolls Royce Aerospace Group
Indianapolis, IN

R.C. Hendricks and B.M. Steinetz
NASA Lewis Research Center
Cleveland, OH

**31st AIAA/ASME/SAE/ASEE
Joint Propulsion Conference and Exhibit
July 10-12, 1995/San Diego, CA**

For permission to copy or republish, contact the American Institute of Aeronautics and Astronautics
370 L'Enfant Promenade, S.W., Washington, D.C. 20024

SIMULATION OF SECONDARY FLOW IN GAS TURBINE DISC CAVITIES AND INTERACTION WITH THE MAIN FLOW PATH

M.M. Athavale and Y.-H. Ho
CFD Research Corporation, Huntsville, AL

J.M. Forry and J.H. Munson
Allison Engine Co., Rolls Royce Aerospace Group, Indianapolis, IN

R.C. Hendricks and B.M. Steinetz
NASA Lewis Research Center, Cleveland, OH.

ABSTRACT

This paper presents a numerical study of the flow and heat transfer processes in the interstage disc cavities, and associated rim and labyrinth seals in the turbine section of the Allison T-56 turboshaft engine. Calculations were performed using SCISEAL, an advanced 3-D CFD code for calculations of fluid flow and forces in turbomachinery seals and secondary flow elements. For fixed upstream main path gas flows the simulations included conjugate heat transfer in the interstage stator support to assess the effects of the main path and cavity flows. Computed gas flow rates and temperatures in the rim and labyrinth seal show a fair to good comparison with Allison T56/501D engine design calculations. The cavity flow and temperature fields were seen to be very sensitive to the interstage labyrinth seal clearance; e.g. flow reversal took place at the upstream rim seal with increase in the labyrinth seal clearance. The conjugate heat transfer analysis indicated temperature gradients in the stationary intercavity walls, mainly in the portion near the stator vanes, and this may lead to thermal distortion and possible changes in the rim and labyrinth seal clearances. The simulations show that the present day CFD codes can be valuable for performance predictions of the secondary flow systems, as well as aid in the design cycle.

INTRODUCTION

The demand for higher efficiencies in advanced gas turbine aero and aero derivative engines has driven the operating conditions to higher temperatures and pressures in compressor as well as turbine sections. With increasing severity of conditions, management of the secondary flow system, which provides component

cooling has become increasingly important. The coolant flow is essential to keep components temperatures to acceptable levels to achieve long life cycles. The compressed coolant air also represents a loss of engine efficiency, and hence has to be minimized. In the modern gas turbine engine secondary flow management is one of the most promising areas for engine efficiency increases, and hence there is drive to minimize the coolant losses. Optimization of the secondary coolant systems in a gas turbine engine thus is important, and a thorough understanding of the flow and heat transfer processes that take place in the disc cavities in the turbine as well as the compressor sections is essential. Effects of linking between the cavities and the main path must be taken into account when simulating these flows in the often interconnected disk cavities.

The flow and heat transfer processes in the single rim seal and disc cavity configurations has received a large amount of attention in the past. Early experimental and theoretical work considered simplified cavity and rim seal geometries to generate models for the performance of the cavities. Experimental and theoretical analysis of such configurations are given in References 1-3. A simple analytical model for disc cavity friction heating as well as main-path gas ingestion was given by, *e.g.*, Hasser *et.al.*⁴. These models were based on the integral momentum equations to treat the flow.

With the advent of the computational fluid dynamics (CFD) methodology, detailed analyses of the cavity flows were undertaken. Early CFD work was done on simplified geometries of a single disc cavity with the associated rim seal have been published. Laminar and

turbulent flows in such rotating cavities with inflow and outflow were presented by Chew^{5,6}. More recently, Ko and Rhode⁷ conducted studies on the heat transfer in a turbine disc with secondary cooling flows. Athavale *et.al.*⁸ also conducted a numerical study on a single cavity configuration, and variations in the cooling effectiveness in the cavity with purge flow and geometrical mismatches at rim seal were investigated.

The majority of these studies on rim seal and disc cavity flows have concentrated on the single cavity-seal configuration, with simplified cavity geometries. This approach provides a good first order analysis, but may not be satisfactory when applied to the flow problems in an actual engine. In an actual engine, the disc cavities have complex shapes, can have multiple connections with other cavities, and are connected to the main-path flow. The interaction of secondary flow elements with other secondary flows and main path can be quite strong, as illustrated in Hendricks *et.al.*⁹, and for this reason, the coupled intracavity and secondary-main path interaction needs to be explicitly included in the computations. This task has become easy with the current state-of-the-art multi-domain CFD codes, which allow the treatment of complicated shapes by domain splitting. A demonstration simulation of the interlinked cavities is given by Virr *et.al.*¹⁰. Recently, Athavale *et.al.*¹¹ presented a numerical study of the complete, complex secondary flow system in the UTRC Large Scale Rig, used to simulate the conditions in the space shuttle main engine high pressure fuel turbopump (SSME HPFTP). The flow domain included four multiply interconnected disc cavities, four main-path flows and rim seals, and three purge flow locations. Tracer gases were introduced in the experiments as well as simulations to find out the flow structure in this complex flow domain. The calculated flow rates as well as concentrations of tracer gas at several locations showed good agreement with the experimental data.

Secondary flow system management is important in the overall engine efficiency, and the leakage flows are typically controlled through tight seal clearances. In such cases, the understanding of the way flows in the cavities change with changing seal clearances, both rim and interstage seals is essential in the designing process. Another issue that needs to be considered is that the solid parts in a turbine often come into contact with gas streams with largely different temperatures. The thermal gradients set up in these parts need to be considered, as the resulting thermal strains can easily

alter the tight seal clearances to a point where the cavity flows may produce unacceptable patterns. Given the trend for tighter seal clearances and reduced purge rates, these two items deserve more attention in order to produce cavity designs that generate acceptable efficiencies as well as component life.

In the present study, baseline flow simulations were carried out on the turbine section of the Allison T-56 turboshaft engine to understand the flow and heat transfer processes that take place in the associated disc cavities. Three pairs of interstage cavities were modeled, and the last two of these included the conjugate heat transfer in the inter-cavity walls that exist under the stator vanes. These solid parts are in contact with the main-path hot gas on one side, and much cooler cavity gas on the other side. In addition, the walls also support the honeycomb rings that form stationary parts of the interstage labyrinth seals. In the present simulations the honeycombs were modeled as solid surfaces. The temperature information in these walls is important for estimating the thermal distortions at the rim seal locations as well as the changes in interstage seal clearances. Simulations on the first pair of the cavities did not involve the conjugate heat transfer analysis, but instead the simulations were carried out at two different labyrinth seal clearances to illustrate the effects of change in the clearance. In all cases, flow rates and gas temperatures at various seals were obtained and compared with design data from Allison.

DESCRIPTION OF THE FLOW SOLVER

The numerical simulations were carried out with an advanced 3-D CFD code SCISEAL, developed for the analysis of fluid flow and forces in turbomachinery seals under a NASA contract¹². The code has a finite-volume pressure-based formulation to integrate the flow and scalar equations in a sequential manner. A modified version of the SIMPLEC procedure is used to link the pressure and velocities. The code can handle incompressible as well as low and high speed compressible flows. An implicit multidomain capability is available, and is extremely important in the present simulations, where the complex shapes of the cavities makes single-block grid generation extremely difficult. The energy equation is capable of treating both fluid and solid regions and the conjugate surfaces, and this feature is also important in the disc cavity analyses. A variety of turbulence models,

including the standard and low-Re $k-\epsilon$ models and a 2-layer $k-\epsilon$ models are available. High order spatial (up to 3rd) and temporal (2nd) discretization schemes can be used for the convective and time derivatives. Other relevant capabilities include variable gas properties and inclusion of the viscous dissipation in the energy equation.

FLOW CONFIGURATION

The configuration considered in this study is the three interstage pairs of disc cavities and the interstage labyrinth seals in the turbine section of the T56/501D engine of Allison Engine Company, Rolls Royce Aerospace Group (Figure 1). These engines are currently installed on the C-130 military transport planes. The characteristics of the T56/501D engine are: a pressure ratio of 14.1, a mass flow rate 15.7 kg/s (34.6 lb/s), engine speed 14239 rpm. The engine delivers 5250 horse power at sea level takeoff conditions and the maximum turbine inlet temperature is 1364 K (1994 °F). The results presented in this paper are for the sea level takeoff condition. Flow information inside the cavities was generated by Allison with their design codes, and were made available for the comparison with numerical results. The data include static pressures inside the cavities, and the flow rates and total temperatures of the gas at the rim and labyrinth seals.

The complex geometry of the disk cavities was scanned directly from the engine drawings, and the outlines of the walls were generated, and fed into a grid generation package. Several critical geometric parameters, such as the labyrinth seal clearances, rim seal gaps, and the secondary flow injection areas were provided by Allison Engine Company. The simulations in the present study were assumed to be axisymmetric, and hence 2-dimensional, multi-domain grids were built for the three pairs of the interstage cavities. The Stage 1-2 cavities have a 34 domain grid, and two different grid sizes for the two labyrinth seal clearances considered here. The grid size for the 0.012 inch clearance was approximately 8800 cells, and for the 0.024 inch clearance it was 9500 cells. The energy solutions for the second and third pair of the cavities (Stage 2-3 and 3-4 cavities) included the central wall under the stator vanes in each of the pair. These walls were also gridded for heat conduction in the solid portions. The total number of domains in Stage 2-3 cavities were 37, and the Stage 3-4 cavities had a total of 44 domains. The Stage 2-3 and 3-4 cavities have larger physical dimensions, and

correspondingly larger grid sizes were used: approximately 45000 and 29000 cells in the Stage 2-3 and Stage 3-4 cavities respectively. For these demonstration calculations, a small initial effort was done to assess the grid independence of the solutions, and further efforts are planned.

FLOW AND BOUNDARY CONDITIONS

At the upstream boundaries of the main-paths (core flows) associated with the six rim seals, the inlet gas velocity and temperatures were specified, and constant static pressures were specified at the exit boundaries of each of these main paths. The inlet conditions change at each of the main-path section, and the values used here were established by the Allison design calculations. The mass flow rates and temperatures of the various purge flows were also known, and were imposed at the appropriate locations in all the cavities. In the Stage 2-3 and 3-4 cavities, the purge locations were concentrated in single locations within the corresponding interstage seals, while the Stage 1-2 cavity block had several points of injection. The computational grids on each of the cavity pairs and the interstage labyrinth seals as well as the locations of the purge flow injection are shown in Figures 2A-2C. Also shown in these figures are the boundary conditions that were used in the calculations.

The simulations in the Stage 1-2 cavities involved the change in flows due to labyrinth seal clearance changes. The energy equation in the stationary wall under the stator vanes was not included. Walls in the Stage 1-2 cavities were assumed adiabatic in the simulation. As outlined above, the stationary walls under the stator vanes in Stage 2-3 and 3-4 cavities were included in the energy equation computations. The surfaces of these walls are conjugate surfaces, and no explicit 'energy' boundary conditions are needed on these fluid-solid interfaces. The upper boundaries of these supports are in contact with the hot main-path gas, and these walls were assumed isothermal (Figures 2B and 2C). The convective heat transfer effects at the top walls were ignored and average values of the main path gas temperatures were applied at these walls. All the other walls were assumed adiabatic, which essentially include all rotor walls. In reality, the rotor walls are also conjugate surfaces in the overall turbine drum, and simulations for the overall configuration are planned to be completed in the near future. For the flow and momentum equations, all walls were no-slip walls, with appropriate tangential velocity conditions imposed

on the stationary and rotating walls.

The 2-dimensional, axisymmetric flow in the cavities and main-path was assumed compressible, with air as the working fluid. Sutherland's viscosity law was used to account for variations in the viscosity due to temperature. The central-differencing scheme was used for the convective fluxes in the momentum equations with a 10% damping (upwinding). The turbulence in the flow was treated with the standard k- ϵ turbulence model with wall functions. Effects of viscous dissipation were included in the energy equation. The computations on the three blocks of the cavities were done in separate, parallel runs since the solid portions of the rotors were not included in the energy equations for present calculations; these will be included in later computations.

RESULTS AND DISCUSSION

The numerical results presented here are the streamline and static pressure plots in each of the flow domains. The streamline plots are very useful in tracing the fluid motion and the static temperatures in the flow and solid parts are of obvious interest. Also presented below are the flow rates and temperatures at the rim and labyrinth seal locations, and a comparison with the design data.

Stage 1-2 Cavities

In the stage 1-2 cavities, the design flow is at a labyrinth seal clearance of 0.012 inches. There are several purge flow injection points, as well as a small exit path in the stator vanes as shown in Figure 2A. The streamlines are plotted in Figure 3 and show evidence of the injection points. The left cavity has a large central recirculation bubble, which pushes the coolant flow up along the rotor wall and down along the stator wall, where one of the purge flow stream mixes with the cavity flow. A portion of the overall purge flow discharges through the left rim seal and a part through the upper path in the stator vane (path 5 in Figure 2A). The remaining flow passes on through the labyrinth seal into the right cavity. This cavity also has a large recirculation bubble which entrains this coolant flow, and eventually is exhausted in the main path through the right rim seal. The flow patterns in both the rim seals indicate unidirectional flow out to the main stream, and no ingestion of the hot gas. This is reflected in the temperature plot, Figure 4, where the

bulk of the flow is relatively cool. The calculated mass fluxes and the gas temperatures through the seals are shown in Table 1A, and compared with the design data. As seen, a fair to good agreement is demonstrated for 1-2 labyrinth seal clearance of 0.012 inches.

Increasing the labyrinth seal clearance to 0.024 inches shows significant changes in the flow structure in the left cavity. The large bubble still exists, but is displaced away from the rim seal (Figure 5). This change is due to a recirculation bubble in the rim seal and under the vane platform, which now allows hot gas ingestion in the left cavity. The hot gas then passes along the top wall, and mixes with the cavity gas in the central bubble. This hot gas then passes through the labyrinth seal on into the right cavity, and eventually out through the right rim seal as before. The result of ingestion of the hot gas is an overall increase of approx. 150 K (270 °F) in the gas temperature in the left cavity, (with locally higher increases on the wall temperatures, see Figure 6) which is also reflected in the gas temperature in the labyrinth seal entrance, Table 1B. As seen in the table, the numerical results again show a fair-to-good correlation with the design data both in terms of the flow rates and the gas temperatures, including the ingestion in the left rim seal. The changes in the gas temperatures can also be expected to alter the thermal fields in the central wall, and conjugate heat transfer calculations are planned to investigate these effects.

Stage 2-3 and 3-4 cavities

Compared to the Stage 1-2 cavities, the stage 2-3 and 3-4 cavities have a much larger size as well as aspect ratios that are larger in the radial direction, and this alters the flow structure in these cavities. The left side cavities have a higher aspect ratio than the right cavities in both pairs (Figure 2B, C), and this changes the overall shapes of the recirculation patterns in the left and right cavities. In both pairs the coolant /purge flow was introduced at a point in between the interstage labyrinth seals. The labyrinth seal clearances were: 0.0146 and 0.0116 inches to the left and right of the purge injection location in the Stage 2-3 cavities, and 0.0051 and 0.0077 inches for the corresponding locations in Stage 3-4 cavities. The streamline (Figures 7 and 8) patterns in the two left cavities are similar, as are the patterns in the two right cavities. Flow patterns near the rim seals indicate that at baseline conditions, none of the rim seals ingest the mainstream

gas, and this is reflected in the temperatures that are seen in the four cavities (Figures 9 and 10), which are much below the main path gas temperatures. The temperatures in the right cavities in both the configurations are lower as compared to the left cavities, and one of the reasons for this is that the flow in the right cavities has overall higher velocities. The higher velocities generate a drop in gas temperatures as well as promote better mixing. In the left cavities the flow is nearly stagnant at the central stationary walls and this increases the gas temperatures in contact with the walls.

These cavities also included the conjugate heat transfer analyses in the central support walls, and the temperatures in the walls are also shown in Figures 9 and 10. In both cases, the region near the stator vanes show the highest temperatures, and it drops rather slowly as one moves radially inward. This reflects the much larger conductivity of the solid material as compared to the gas. These relatively high temperatures will generate thermal strains in these walls, and can result in changes in the interstage labyrinth seal clearances and alter the cavity flow fields.

The flow rates and gas temperatures through the rim seals are shown in Table 2. Also shown are the calculated static pressure values in the four cavities. These are compared with the design data for these parameters. The pressure values compare well with the design data. Computed values of gas temperatures in locations B and C show good correlation with the data; comparison at locations A and D shows some differences. The computed mass flow rates do not correlate as well with the design values, with differences of up to 30% on the Stage 2-3 cavities. In addition, the relative flow splits are not similar: computed results show higher flow rates through the right rim seals while the design data predicts the opposite. One of the reasons for the differences may be the location(s) and numbers of coolant injection points; computational grid refinement may also be needed. The calculations assumed a single injection point in each of the interstage labyrinth seals whereas there probably are multiple leakage paths. This matter is being investigated further.

SUMMARY

Flow and conjugate heat transfer computations were performed for multiple disc cavities in the turbine section of the Allison T56/501D engine using an

advanced CFD code, SCISEAL. The following remarks can be made based on the results:

1. The predicted results for the mass flows and gas temperatures at rim and labyrinth seals show a good to fair agreement with Allison T56/501D engine design calculations. The agreement was better in the Stage 1-2 cavities with better defined purge flow injection locations. Mass flow rates in the stage 2-3 and 3-4 cavities showed higher differences.
2. CFD cavity flow patterns were seen to be very sensitive to the interstage labyrinth seal clearances. In the stage 1-2 cavity, the upstream rim seal went from an egress of coolant flow to ingestion of the hot main path gas with an increase of seal clearance from 0.012 inches to 0.024 inches. Flow predictions under such different conditions can be of importance during the cavity designs as well as in experiment designs.
3. Two pairs of the cavities included the solid support walls in the heat-transfer calculations. The conjugate heat transfer analysis shows that due to the contact with the hot main stream gas these support walls are at higher temperatures than the surrounding gas in the cavities. This type of information can be useful in predictions of the thermal strains in the solid portions, which may affect the interstage seal clearances, cavity flow fields and longevity of the disc.
4. Additional analyses are clearly needed to include the stator walls in stage 1-2 cavities. In addition, the rotor walls in all stages need to be included in the heat-transfer calculations to present the overall picture of the complete turbine drum and the associated cavities. Such calculations are well within the capabilities of the CFD codes and will be undertaken in the near future. Calculations are also needed to assess the effects of thermal strains on the seal flows, coupling of the cavity flows with main path flow and the time dependent effects due to the blade wakes in the main path flow.

ACKNOWLEDGEMENTS

This work was supported by NASA Lewis Research Center under the contract NAS3-27392. This support is greatly appreciated.

REFERENCES

1. Owen, J.M., and Pincombe, J.R., "Velocity Measurements Inside a Rotating Cylindrical Cavity with a Radial Outflow of Fluid," *J. Fluid Mechanics*, Vol. 99, p. 111, 1980.
2. Owen, J.M., Pincombe, J.R., and Rogers, R.H., "Source-Sink Flow Inside a Rotating Cylindrical Cavity," *J. Fluid Mechanics*, Vol. 155, pp. 233-265, 1985.
3. Phadke, U.P., and Owen, J.M., "An Investigation for an Air-cooled Shrouded Rotating Disk System with Radial Clearance Seals," *Trans. ASME, J. of Engineering for Gas Turbine and Power*, Vol. 110, pp. 78-85, 1988.
4. Hasser, F., Jack, J., and McGreehan, W., "Windage Rise and Flowpath Gas Ingestion in Turbine Rim Cavities," *Trans. ASME, J. of Engineering for Gas Turbine and Power*, Vol. 110, pp. 78-85, 1988.
5. Chew J.W., "Predictions of Flow in Rotating Disk Systems Using the k-e Turbulence Model," ASME-88-GT-229, ASME Gas Turbine and Aeroengine Expo, Amsterdam, The Netherlands, 1988.
6. Chew, J.W., "A Theoretical Study of Ingress for Shrouded Rotating Disc Systems with Radial Outflow," ASME-89-GT-178, ASME Gas Turbine and Aeroengine Expo, Toronto, Canada, 1989.
7. Ko, S.H., and Rhode, D.L., "Thermal Details in a Rotor-Stator Cavity at Engine Conditions with a Mainstream," ASME-91-GT-275, ASME Gas Turbine and Aeroengine Expo, Orlando, FL, 1991.
8. Athavale, M.M., Przekwas, A.J., and Hendricks, R.C., "A Numerical Study of the Flow Field in Enclosed Turbine Disk Cavities in Gas Turbine Engines," 4th International Symposium on Transport Phenomena and Dynamics of Rotating Machinery (ISROMAC-4), Honolulu, HI, 1992.
9. Hendricks, R.C., Griffin, T.A., Kline, T.R., Csavina, K.R., Pancholi, A., Sood, D., "Relative Performance Comparison between Baseline Labyrinth and Dual-Brush Compressor Discharge seal in a T-700 Engine Test," Presented at the 39th International Gas Turbine and Aeroengine Conference, Netherlands, 1994.
10. Virr, G.P., Chew, J.W., and Coupland, J., "Application of Computational Fluid Dynamics to Turbine Disk Cavities," *Trans. ASME, J. of Turbomachinery*, Vol. 116, pp. 701-708, 1994.
11. Athavale, M.M., Przekwas, A.J., Hendricks, R.C., and Steinetz, B.M., "Numerical Analysis of Intra-Cavity and Power-Stream Flow Interaction in Multiple Gas-Turbine Disk-Cavities," ASME-95-GT-325, presented at the ASME Gas Turbine Congress and

Exposition, Houston, TX, 1995.

12. Athavale, M.M., Przekwas, A.J., Hendricks, R.C., and Liang, A., "SCISEAL - A Three-Dimensional CFD Code for Accurate Analyses of Fluid Flow and Forces in Seals," Presented at the Conference on Advances Earth-To-Orbit Technology, NASA MSFC, Huntsville, AL, May 1994.

Table 1 Comparison between the Design Data and the Prediction for Stage 1-2 Cavities (see Figure 2A for path No. notation).

(a) labyrinth seal clearance = 0.012 in.

Path No.	Design		Prediction	
	Massflow (lb/s)	Temp (°F)	Massflow (lb/s)	Temp (°F)
4	0.249	1058	0.308	1032
5	0.041	1058	0.030	1029
6	0.099	1058	0.095	1100

(b) labyrinth seal clearance = 0.024 in.

Path No.	Design		Prediction	
	Massflow (lb/s)	Temp (°F)	Massflow (lb/s)	Temp (°F)
4	0.510	1223	0.610	1315
5	0.038	1223	0.041	1148
6	-0.153	1691	-0.220	1830

Table 2 . Comparison between the Design Data and the Prediction for Stages 2-3 and 3-4 Cavities
(see Figures 2B and 2C for locations notation).

Locations	Design			Prediction		
	Mass (lb/s)	Pressure (psi)*	Temp. (°F)	Mass (lb/s)	Pressure (psi)*	Temp. (°F)
A	0.125	48	875	0.083	47.5	955
B	0.083	31	796	0.119	30.0	829
C	0.075	25	809	0.053	24.5	800
D	0.046	16	806	0.060	15.5	739

* Values at the center of the cavities.

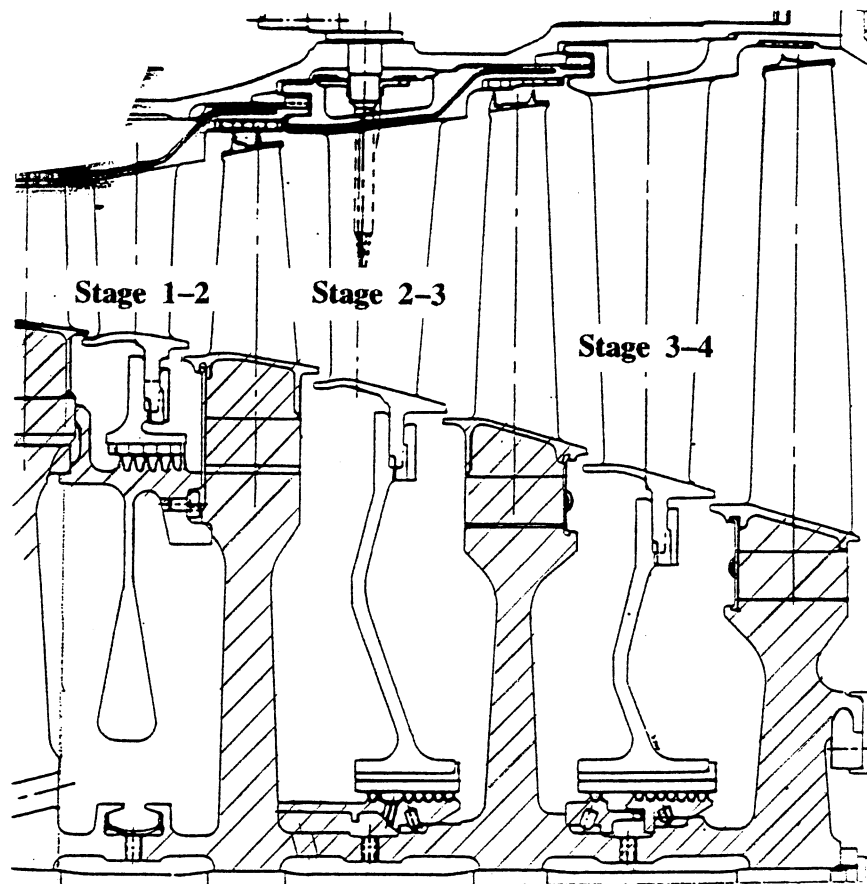


Figure 1. Schematic of the inner cavities of in the turbine drum of the Allison T56/501D engine.

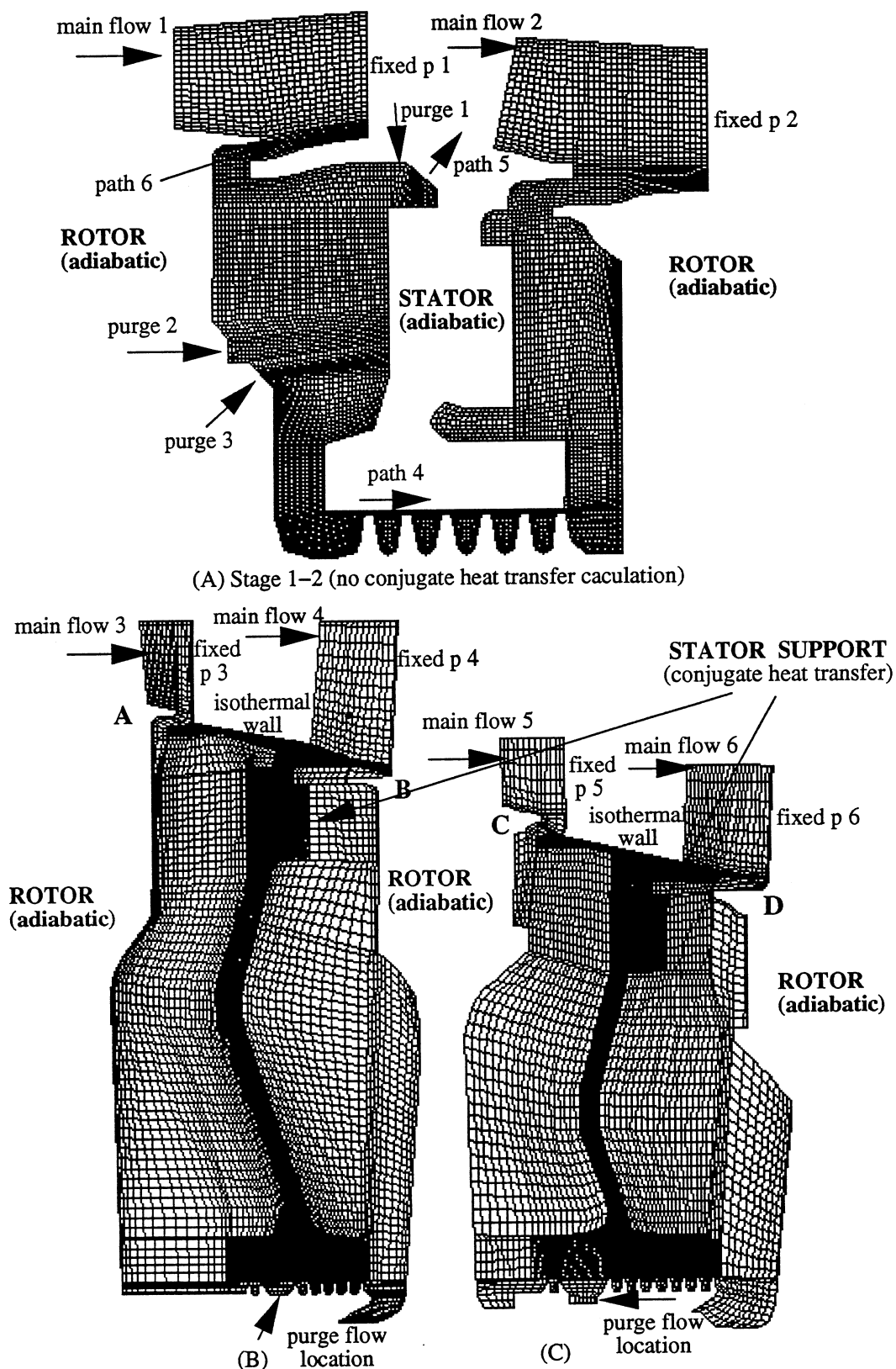


Figure 2 Computational Grids for the T-56 Turbine Cavities (stages 1-2 cavities are not the same scale as stages 2-3 and 3-4).

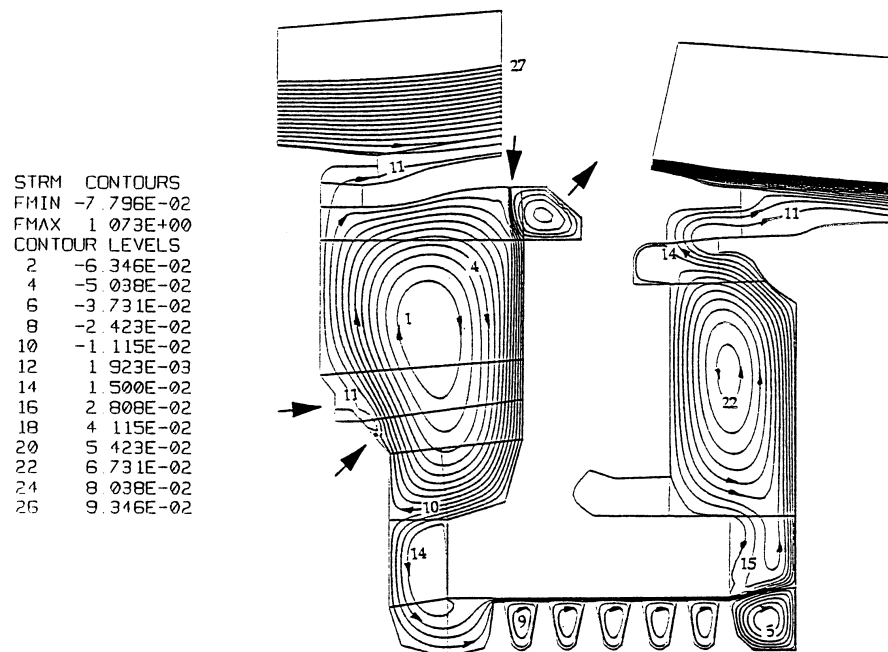


Figure 3. Streamline Plot for Stage 1-2 Cavities, Labyrinth Seal Clearance = 0.012 in
(Arrows indicate the locations of the purge flow injection)

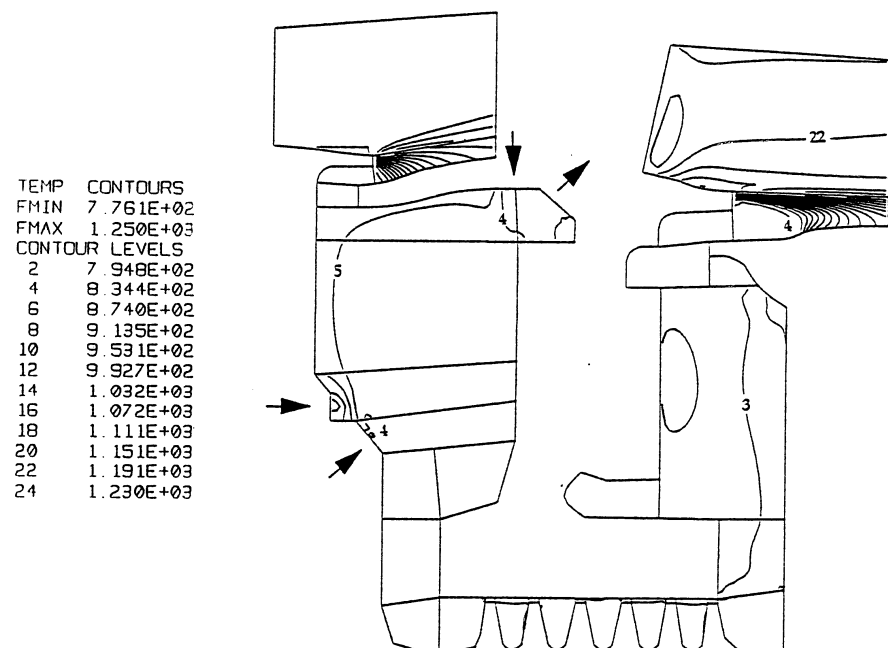


Figure 4. Temperature Contours for Stage 1-2 Cavities, Labyrinth Seal Clearance = 0.012 in.
(Arrows indicate the locations of the purge flow injection)

STRM	CONTOURS
FMIN	-5.329E-02
FMAX	1.097E+00
CONTOUR	LEVELS
2	-3.462E-02
4	-2.385E-02
6	-1.308E-02
8	-2.308E-03
10	8.462E-03
12	1.923E-02
14	3.000E-02
16	4.077E-02
18	5.154E-02
20	6.231E-02
22	7.308E-02
24	8.385E-02
26	9.462E-02

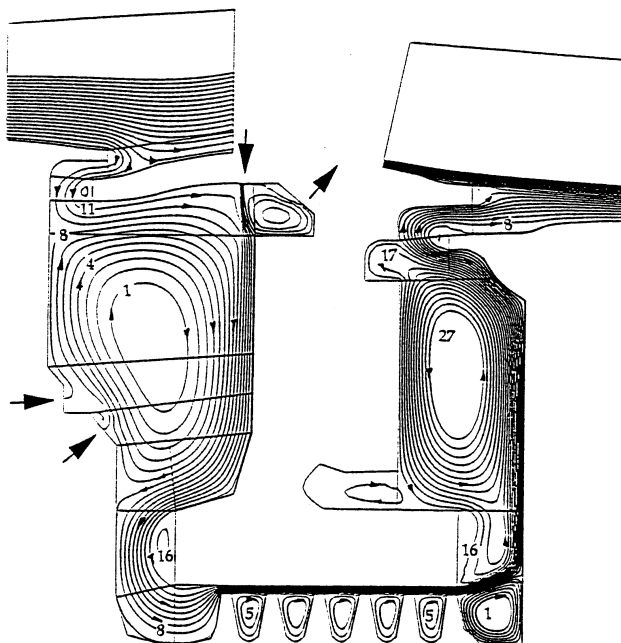


Figure 5. Streamline Plot for Stage 1-2 Cavities, Labyrinth Seal Clearance = 0.024 in.
(Arrows indicate the locations of the purge flow injection)

TEMP	CONTOURS
FMIN	7.768E+02
FMAX	1.251E+03
CONTOUR	LEVELS
2	7.988E+02
4	8.463E+02
6	8.938E+02
8	9.413E+02
10	9.888E+02
12	1.036E+03
14	1.084E+03
16	1.131E+03
18	1.179E+03
20	1.226E+03

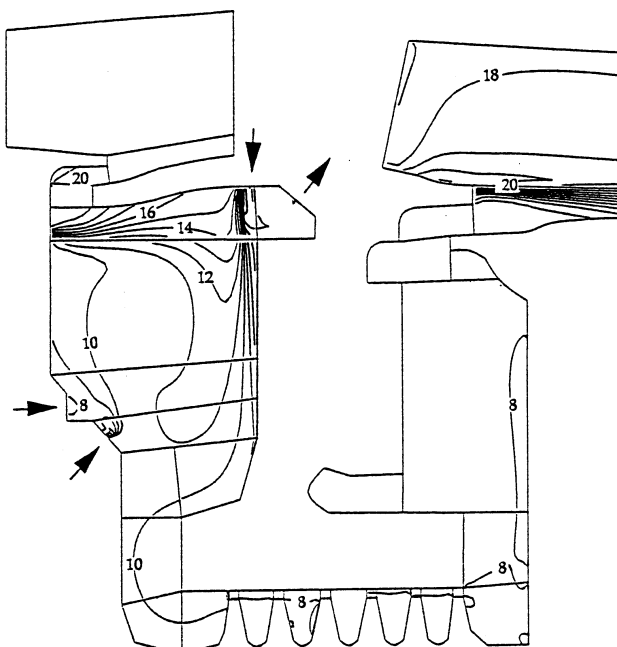


Figure 6. Temperature Contours for Stage 1-2 Cavities, Labyrinth Seal Clearance = 0.024 in.
(Arrows indicate the locations of the purge flow injection)

STRM CONTOURS
 FMIN -2.841E-02
 FMAX 1.544E+00
 CONTOUR LEVELS
 2 -1.650E-02
 4 -9.500E-03
 6 -2.500E-03
 8 4.500E-03
 10 1.150E-02
 12 1.850E-02
 14 2.550E-02
 16 3.250E-02
 18 3.950E-02
 20 4.650E-02

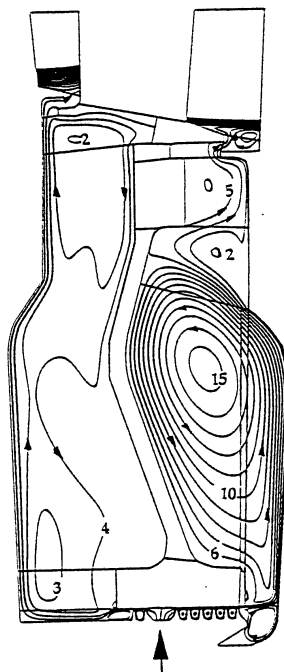


Figure 7. Streamline Plot for Stage 2-3 Cavities
 (Arrow indicates the location of the purge flow injection)

STRM CONTOURS
 FMIN -2.404E-02
 FMAX 5.761E-01
 CONTOUR LEVELS
 2 -1.650E-02
 4 -9.500E-03
 6 -2.500E-03
 8 4.500E-03
 10 1.150E-02
 12 1.850E-02
 14 2.550E-02
 16 3.250E-02
 18 3.950E-02
 20 4.650E-02

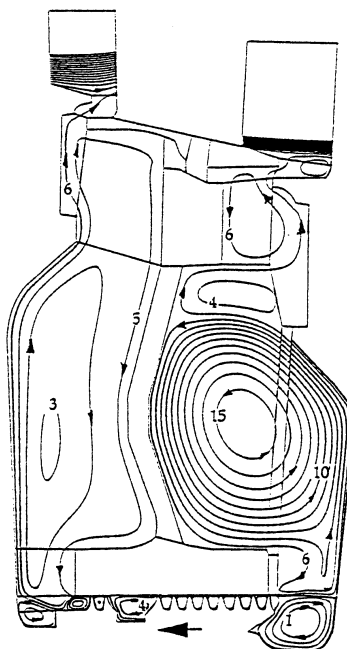


Figure 8. Streamline Plot for Stage 3-4 Cavities
 (Arrow indicates the location of the purge flow injection)

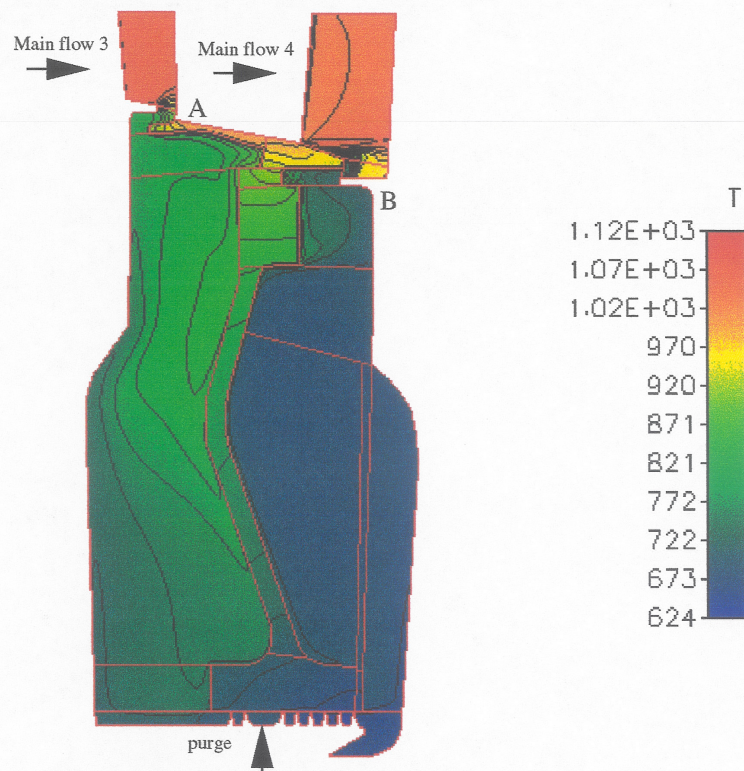


Figure 9. Temperatures in the Cavity Flowfield as well as the Central Support Wall of the Stage 2-3 Cavities

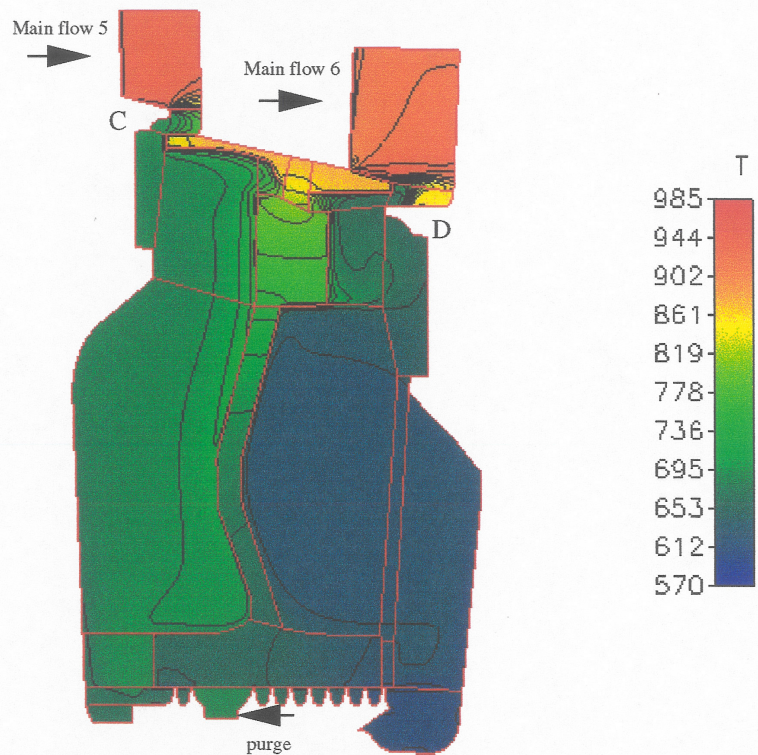


Figure 10. Temperatures in the Cavity Flowfield as well as the Central Support Wall of the Stage 3-4 Cavities



The Society shall not be responsible for statements or opinions advanced in papers or discussion at meetings of the Society or of its Divisions or Sections, or printed in its publications. Discussion is printed only if the paper is published in an ASME Journal. Authorization to photocopy material for internal or personal use under circumstance not falling within the fair use provisions of the Copyright Act is granted by ASME to libraries and other users registered with the Copyright Clearance Center (CCC) Transactional Reporting Service provided that the base fee of \$0.30 per page is paid directly to the CCC, 27 Congress Street, Salem MA 01970. Requests for special permission or bulk reproduction should be addressed to the ASME Technical Publishing Department.

Printed in U.S.A.

Presented at the ASME International Gas Turbine and Aeroengine Congress and Exhibition, Birmingham, UK, June 1996.

NUMERICAL SIMULATION OF SECONDARY FLOW IN GAS TURBINE DISC CAVITIES, INCLUDING CONJUGATE HEAT TRANSFER

Y.-H. Ho and M.M. Athavale
CFD Research Corporation, Huntsville, Alabama, USA

J.M. Forry
Allison Engine Co., Rolls Royce Aerospace Group,
Indianapolis, Indiana, USA

R.C. Hendricks and B.M. Steinetz
NASA Lewis Research Center,
Cleveland, Ohio, USA

ABSTRACT

A numerical study of the flow and heat transfer in secondary flow elements of the entire inner portion of the turbine section of the Allison T-56/501D engine is presented. The flow simulation included the interstage cavities, rim seals and associated main path flows, while the energy equation also included the solid parts of the turbine disc, rotor supports, and stator supports. Solutions of the energy equations in these problems usually face the difficulty in specifications of wall thermal boundary conditions. By solving the entire turbine section this difficulty is thus removed, and realistic thermal conditions are realized on all internal walls. The simulation was performed using SCISEAL, an advanced 2D/3D CFD code for predictions of fluid flows and forces in turbomachinery seals and secondary flow elements. The mass flow rates and gas temperatures at various seal locations were compared with the design data from Allison. Computed gas flow rates and temperatures in the rim and labyrinth seal show a fair to good comparison with the design calculations. The conjugate heat transfer analysis indicates temperature gradients in the stationary intercavity walls, as well as the rotating turbine discs. The thermal strains in the stationary wall may lead to altered interstage labyrinth seal clearances and affect the disc cavity flows. The temperature fields in the turbine discs also may lead to distortions that can alter the rim seal clearances. Such details of the flow and temperature fields are important in designs of the turbine sections to account for possible thermal distortions and their effects on the performance. The simulation shows that the present day CFD codes can provide the means to understand the complex flow field and thereby aid the design process.

INTRODUCTION

The demand for higher efficiencies in advanced gas turbine aero and aero-derivative engines has driven operating conditions to higher temperatures and pressures in compressor as well as in turbine sections. With increasing severity of conditions, management of the secondary flow system, which provides component cooling, has become increasingly important. The

coolant flow is essential to keep components temperatures to acceptable levels to achieve long life cycles. The compressed coolant air also represents a loss of engine efficiency, and hence has to be minimized. In the modern gas turbine engine, secondary flow management is one of the most promising areas for engine efficiency increases and, hence, there is drive to minimize the coolant losses. Optimization of the secondary coolant systems in a gas turbine engine is important, and a thorough understanding of the flow and heat transfer processes that take place in the disc cavities in the turbine as well as in the compressor sections is essential. Effects of linking between the cavities and the main path must be taken into account when simulating these flows in the often interconnected disk cavities.

The flow and heat transfer processes in the single rim seal and disc cavity configurations have received a large amount of attention in the past. Early experimental and theoretical work considered simplified cavity and rim seal geometries to generate models for the performance of the cavities. Experimental and theoretical analyses of such configurations are given in References 1-3. A simple analytical model for disc cavity friction heating as well as main path gas ingestion was given by, *e.g.*, Hasser *et al.*⁴. These models were based on the integral momentum equations to treat the flow.

With the advent of the computational fluid dynamics (CFD) methodology, detailed analyses of the cavity flows were undertaken. Early CFD work was done on simplified geometries of a single disc cavity with the associated rim seal. Laminar and turbulent flows in such rotating cavities with inflow and outflow were presented by Chew^{5,6}. More recently, Ko and Rhode⁷ conducted studies on the heat transfer in a turbine disc with secondary cooling flows. Athavale *et al.*⁸ also conducted a numerical study on a single cavity configuration, and variations in the cooling effectiveness in the cavity with purge flow and geometrical mismatches at the rim seal were investigated.

The majority of these studies on rim seal and disc cavity flows have concentrated on the single cavity-seal configuration with simplified cavity geometries. This approach provides a good first-order analysis, but it may not be satisfactory when applied to the

flow problems in an actual engine. In an actual engine, the disc cavities have complex shapes, can have multiple connections with other cavities, and are connected to the main path flow. The interaction of secondary flow elements with other secondary flows and the main path can be quite strong, as illustrated in Hendricks *et al.*⁹, and for this reason, the coupled intercavity and secondary-main path interaction needs to be explicitly included in the computations. This task has become easy with the current state-of-the-art multi-domain CFD codes, which allow the treatment of complicated shapes by domain splitting. A demonstration simulation of the interlinked cavities was given by Virr *et al.*¹⁰. Recently, Athavale *et al.*¹¹ presented a numerical study of the complete, complex secondary flow system in the UTRC Large Scale Rig.

The solid parts in a turbine often come into contact with gas streams with largely different temperatures. The thermal gradients set up in these parts need to be considered, as the resulting thermal strains can easily alter the tight seal clearances to a point where the cavity flows may produce unacceptable patterns. Given the trend for tighter seal clearances and reduced purge rates, these two items deserve more attention in order to produce cavity designs that generate acceptable efficiencies as well as component life. Recently, Athavale *et al.*¹² carried out the flow and conjugate heat transfer simulation of the Allison T-56 engine turbine disc cavities. They showed the effects of the labyrinth seal clearances on the flow characteristics as well as the possible thermal strains existing at the solid-fluid interfaces of the stator central support walls. In their predictions, three pairs of cavities were calculated separately. The flow simulation of the first pair of cavities did not include the conjugate heat transfer prediction and the rotor supports were not included in their study.

In this paper, a continuous and more thorough study was carried out on the turbine section of the Allison T-56 turboshaft engine to understand the flow and heat transfer processes that take place in the associated disc cavities. The entire turbine disc cavities, including three pairs of interstage cavities, were modeled. The conjugate heat transfer prediction included the inter-cavity walls that exist under the stator vanes and the rotor supports in between each pair of cavities. In addition, the walls that support the honeycomb rings that form stationary parts of the interstage labyrinth seals were also included in the simulation. In the present simulation the honeycombs were modeled as solid surfaces. The flow rates and gas temperatures at various seals were obtained and compared with the design data from Allison and the earlier prediction by Athavale *et al.*¹².

DESCRIPTION OF THE FLOW SOLVER

The numerical simulation was carried out with an advanced 2D/3D CFD code SCISEAL, developed for the analysis of fluid flows and forces in turbomachinery seals under a NASA contract¹³. Extensive validations of SCISEAL were performed over the past years. The flow fields inside look-through, stepped, planar labyrinth seals were computed and compared to the experimental data (Przekwas *et al.*¹⁴). The effects of purge flow and rim seal geometry on the ingestion of main-flow gas into a generic turbine disc cavity were studied and the results were compared to the experimental data (Athavale *et al.*¹⁵). A finite-volume, pressure-based formulation is used to integrate the flow and scalar equations in a sequential manner. A modified version of the SIMPLEC procedure is used to link the pressure and velocities. The code can handle incompressible as well as low and high-speed compressible flows. An implicit multidomain capability is available and is extremely important in the present simulation, where the complex shapes of

the cavities make single-block grid generation extremely difficult, if not impossible. The energy equation models both fluid and solid regions and the conjugate surfaces, and this feature is also important in the disc cavity analyses. A variety of turbulence models, including the standard and low-Re k - ϵ models and a two-layer k - ϵ models are available. High order spatial (up to 3rd) and temporal (2nd) discretization schemes can be used for the convective and time derivatives. Other relevant capabilities include variable gas properties and inclusion of the viscous dissipation in the energy equation.

FLOW CONFIGURATION

The configuration considered in this study consists of the three interstage pairs of disc cavities and the interstage labyrinth seals in the turbine section of the T56/501D engine of Allison Engine Company, Rolls Royce Aerospace Group. These engines are currently installed on the C-130 military transport planes. The characteristics of the T56/501D engine are: a pressure ratio of 14.1, a mass flow rate 15.7 kg/s, engine speed 14239 rpm. The engine delivers 5250 horse power at the sea level takeoff condition and the maximum turbine inlet temperature is 1364 K. The results presented in this paper are for the sea-level takeoff condition. Flow information inside the cavities was generated by Allison with their design codes and was made available for the comparison with the numerical results. The data include static pressures inside the cavities, and the flow rates and total temperatures of the gas at the rim and labyrinth seals. In this 2D, axisymmetric simulation, the ingestion effects due to rotor-stator interactions are neglected.

The complex geometry of the disk cavities was scanned directly from the engine drawings, and the outlines of the walls were generated and fed into a grid generation package. Several critical geometric parameters, such as the labyrinth seal clearances, the rim seal gaps, and the secondary flow injection areas were provided by Allison Engine Company. The flow field was assumed to be axisymmetric and, hence, a two-dimensional, multi-domain grid was built. The energy (temperature) solutions included the central walls under the stator vanes and the rotor supports between each pair of cavities. These walls and supports were also gridded for heat conduction in the solid portions. The total number of domains were 140, which had approximately 91,000 grid cells. For this calculation, a small initial effort was done to assess the grid independence of the solutions. It was found that no noticeable pressure changes were found compared to a coarser grid solution (Ref. 12). However, the effects of grid resolution on the flow details are still uncertain and require more grid dependency study. Further efforts are planned.

FLOW AND BOUNDARY CONDITIONS

At the upstream boundaries of the main paths (core flows) associated with the six rim seals, the inlet velocity and temperatures were specified, and constant static pressures were specified at the exit boundaries of each of these main paths. The inlet conditions differed at each of the main path section, and the values used here were established by the Allison design calculations. The mass flow rates and temperatures of the various purge flows were also known and were imposed at the appropriate locations in all the cavities. In the Stage 2-3 and 3-4 cavities, the purge flow locations were concentrated in double and single locations within the corresponding interstage seals, while the Stage 1-2 cavity block had several points of injection. The geometries of the turbine disc cavities and the interstage labyrinth seals as well as the locations of the purge flow injection are shown in Figure 1. Also shown in Figure 1 are the boundary conditions that were used in the

calculation.

In the simulation, walls on the left-hand side of the Stage 1-2 cavities as well as those underneath the Stage 1-2 cavities were assumed to be adiabatic due to a lack of temperature information at these locations. As mentioned above, the stationary walls under the stator vanes and the rotor supports were included in the energy equation computation. The surfaces of these walls were conjugate surfaces, and no explicit 'energy' boundary conditions were needed on these fluid-solid interfaces. The upper and lower boundaries of these supports were in contact with the hot main path gas and the cool secondary flows, and these walls were assumed isothermal (see Figure 1). The convective heat transfer effects at the top walls were ignored and average values of the main flow path gas temperatures were applied at these walls. All the other walls were also assumed isothermal, which essentially include all rotor walls. The temperatures of the cooling secondary flows were applied at these walls. For the momentum equations, all walls were no-slip walls, with appropriate tangential velocity conditions imposed on the stationary and rotating walls.

The two-dimensional, axisymmetric flow in the cavities and main path was assumed compressible with air as the working fluid. Sutherland's viscosity law was used to account for variations in the viscosity due to temperature. The central-differencing scheme (90%) was used for the convective fluxes in the momentum equations blending with a (10%) first-order upwinding damping. The turbulence in the flow was treated with the standard $k-\epsilon$ turbulence model with wall functions. Effects of viscous dissipation were included in the energy equation.

RESULTS AND DISCUSSION

The numerical results presented here are the streamline, static pressure and static temperature plots in each of the flow domains. The streamline plots are very useful in tracing the fluid motion; the static pressures contribute to a major portion of loading on solid surfaces; and, high static temperature gradients in the flow and solid parts may induce unacceptable thermal strains on the solid surfaces. Also presented below are the flow rates and temperatures at the rim and labyrinth seal locations, static pressure inside the Stages 2-3 and 3-4 cavities, and a comparison with the design data.

Stage 1-2 Cavities

In the stage 1-2 cavities, the design flow is at a labyrinth seal clearance of 0.3048 mm. There are several purge flow injection points, as well as a small exit path in the stator vanes as shown in Figure 1. The streamlines are plotted in Figure 2 and show evidence of the injection points. The left cavity has a large central recirculation bubble, which pushes the coolant flow up along the rotor wall and down along the stator wall, where one of the purge flow stream mixes with the cavity flow. A portion of the overall purge flow discharges through the left rim seal and a part through the upper path in the stator vane (path 5 in Figure 1). The remaining flow passes on through the labyrinth seal into the right cavity. This cavity also has a large recirculation bubble that entrains this coolant flow and eventually is exhausted into the main path through the right rim seal. The flow patterns in both the rim seals indicate unidirectional flow out to the main stream and no ingestion of the hot gas. This is reflected in the temperature plot, Figure 4, where the bulk of the flow is relatively cool. The conjugate heat transfer prediction shows that the stator part is heated up by the main stream gas. This process causes the temperature of the upper part of the stator support to be higher than the gas temperature inside the cavities. Therefore, temperature gradients across the conjugate surfaces may introduce thermal strains at these regions. The lower

part of the stator support is away from the main gas path and is at the same temperature level as the surrounding gas.

The static pressure distribution is shown in Figure 6 and the pressure can be seen to remain constant in each inner cavity. The pressure gradient across the cavity is the main mechanism to drive the secondary flow across the passage. The calculated mass fluxes and the gas temperatures through the seals are shown in Table 1 and are compared with the design data. A prediction without including the conjugate heat transfer for the stator support (Ref. 12) is also shown. As seen, a fair to good agreement is demonstrated and the effects of including the stator support in the temperature prediction are very significant. For example, at path no. 5, the temperature is increased by almost 157 K. Accordingly, the mass fluxes are also affected by the temperature changes.

Stage 2-3 and 3-4 Cavities

Compared to the Stage 1-2 cavities, the Stages 2-3 and 3-4 cavities have a much larger size as well as aspect ratios that are larger in the radial direction, and this alters the flow structures in these cavities. The left side cavities have a higher aspect ratio than the right cavities in both pairs (Figure 1), and this changes the overall shapes of the recirculation patterns in the left and right cavities. For the Stage 2-3 cavities, the cooling flow is introduced at two locations, while for the Stage 3-4 the coolant purge flow is introduced at a point between the interstage labyrinth seals. The labyrinth seal clearances are: 0.3708 and 0.2946 mm to the left and right of the purge injection location in the Stage 2-3 cavities, and 0.1295 and 0.1956 mm for the corresponding locations in the Stage 3-4 cavities. The streamline (Figure 3) patterns in the two left cavities are similar, as are the patterns in the two right cavities. The flow patterns near the rim seals indicate that, at the takeoff condition, none of the rim seals ingests the mainstream gas, and this effect is reflected in the temperatures that are seen in the four cavities (Figure 5), which are much below the main flow path gas temperatures. The temperatures in the right cavities in both the configurations are lower as compared to the left-hand cavities, and one of the reasons for this is that the flow in the right-hand cavities generally has higher velocities. The higher velocities generate a decrease in gas temperatures as well as promote better mixing. In the left-hand cavities the flow is nearly stagnant at the central stationary walls and thus increases the gas temperatures in contact with the walls.

The conjugate heat transfer analyses include the central support walls as well as the rotor support walls. The temperatures in the walls are also shown in Figure 5. In both cases, the region near the stator vanes show the highest temperatures, which decreases rather slowly as one moves radially inward. This decrease reflects the much larger conductivity of the solid material as compared to the gas. These relatively high temperatures will generate thermal strains in these walls and can result in changes in the interstage labyrinth seal clearances and alter the cavity flow fields. Similarly, the rotor support walls also have higher temperatures near the main gas path and the temperatures decrease as one moves radially inward. It is interesting to notice that the temperature in the rotor in between Stages 1-2 and 2-3 cavities decreases much faster than the one in between Stages 2-3 and 3-4. The main reason is that a low coolant flow temperature is specified at the lower left-hand side wall of the first rotor, while the same coolant flow temperature is only specified at the bottom of the second rotor support. The static pressure distributions for Stages 2-3 and 3-4 are shown in Figure 7. As for Stage 1-2, there is very little pressure gradient in each of the four cavities. Most pressure gradients are due to the pressure differences across the pairs of cavities and the higher pressure of the

coolant flow injected from the bottom of the cavities.

The flow rates and gas temperatures through the rim seals are shown in Table 2. The corresponding predicted results from Ref. 12 are also shown in Table 2 for a comparison. In Ref. 12, the Stages 2-3 and 3-4 cavities were computed separately without the inclusion of the rotor supports. Also shown are the calculated static pressure values in the four cavities. The pressure values compare well with the design data. The computed mass flow rates do not correlate as well with the design values, with differences of up to 30% on the Stage 2-3 cavities. In addition, the relative flow splits are not similar: computed results show higher flow rates through the right rim seals while the design data predict the opposite. One of the reasons for the differences may be the location(s) and numbers of coolant injection points; computational grid refinement may also be needed. Double and a single injection points are assumed for the Stages 2-3 and 3-4 cavities, whereas there probably are multiple leakage paths.

Comparing the results with those of Ref. 12, one can see that coupling solutions and including the rotor supports alter the flow characteristics near the rim seals. For example, the temperature at location B is increased by 78 K. However, the effects on the mass fluxes at the rim seals locations are minimal.

SUMMARY

Flow and conjugate heat transfer computations were performed for multiple disc cavities in the turbine section of the Allison T56/501D engine using an advanced CFD code, SCISEAL. The following remarks can be made based on the results:

1. The predicted results for the mass flows and gas temperatures at rim and labyrinth seals show fair agreement with Allison T56/501D engine design calculations. The agreement is better in the Stage 1-2 cavities with better defined purge flow injection locations. Mass flow rates in the stage 2-3 and 3-4 cavities show higher differences.
2. Both the stator and rotor support walls are included in the heat transfer calculation. The conjugate heat transfer analysis shows that, due to contact with the hot main stream gas, these support walls are at higher temperatures than the surrounding gas in the cavities. This type of information can be useful in the predictions of the thermal strains in the solid portions, which may affect the interstage seal clearances, cavity flow fields and longevity of the disc.
3. The inclusion of the rotors supports in the calculation shows that the flow temperatures near the rim seals are further increased (compared to a prediction without including the rotor supports) due to the contribution of the heat transfer in the rotor supports.

With the available flow information, calculations can be done in the future to assess the effects of thermal strains on the seal flows. Future efforts may also include coupling of the cavity flows with the main path flow and the time dependent effects due to the blade wakes in the main path flow.

ACKNOWLEDGEMENTS

This work was supported by NASA Lewis Research Center under the contract NAS3-27392. This support is greatly appreciated.

REFERENCES

Owen, J.M., and Pincombe, J.R., "Velocity Measurements Inside a Rotating Cylindrical Cavity with a Radial Outflow of Fluid," *J. Fluid Mechanics*, Vol. 99, p. 111, 1980.

Owen, J.M., Pincombe, J.R., and Rogers, R.H., "Source-Sink Flow Inside a Rotating Cylindrical Cavity," *J. Fluid Mechanics*, Vol. 155, pp. 233-265, 1985.

Phadke, U.P., and Owen, J.M., "An Investigation for an Air-cooled Shrouded Rotating Disk System with Radial Clearance Seals," *Trans. ASME, J. of Engineering for Gas Turbine and Power*, Vol. 110, pp. 78-85, 1988.

Hasser, F., Jack, J., and McGreehan, W., "Windage Rise and Flowpath Gas Ingestion in Turbine Rim Cavities," *Trans. ASME, J. of Engineering for Gas Turbine and Power*, Vol. 110, pp. 78-85, 1988.

Chew, J.W., "Predictions of Flow in Rotating Disk Systems Using the k- ϵ Turbulence Model," ASME-88-GT-229, ASME Gas Turbine and Aeroengine Expo, Amsterdam, The Netherlands, 1988.

Chew, J.W., "A Theoretical Study of Ingress for Shrouded Rotating Disc Systems with Radial Outflow," ASME-89-GT-178, ASME Gas Turbine and Aeroengine Expo, Toronto, Canada, 1989.

Ko, S.H., and Rhode, D.L., "Thermal Details in a Rotor-Stator Cavity at Engine Conditions with a Mainstream," ASME-91-GT-275, ASME Gas Turbine and Aeroengine Expo, Orlando, FL, 1991.

Athavale, M.M., Przekwas, A.J., and Hendricks, R.C., "A Numerical Study of the Flow Field in Enclosed Turbine Disk Cavities in Gas Turbine Engines," 4th International Symposium on Transport Phenomena and Dynamics of Rotating Machinery (ISROMAC-4), Honolulu, HI, 1992.

Hendricks, R.C., Griffin, T.A., Kline, T.R., Csavina, K.R., Pancholi, A., and Sood, D., "Relative Performance Comparison between Baseline Labyrinth and Dual-Brush Compressor Discharge seal in a T-700 Engine Test," Presented at the 39th International Gas Turbine and Aeroengine Conference, Netherlands, 1994.

Virr, G.P., Chew, J.W., and Coupland, J., "Application of Computational Fluid Dynamics to Turbine Disk Cavities," *Trans. ASME, J. of Turbomachinery*, Vol. 116, pp. 701-708, 1994.

Athavale, M.M., Przekwas, A.J., Hendricks, R.C., and Steinetz, B.M., "Numerical Analysis of Intra-Cavity and Power-Stream Flow Interaction in Multiple Gas-Turbine Disk-Cavities," ASME-95-GT-325, presented at the ASME Gas Turbine Congress and Exposition, Houston, TX, 1995.

Athavale, M.M., Ho, Y.-H., Forry, J.M., Munson, J.H., Hendricks, R.C., and Steinetz, B.M., "Simulation of Secondary Flow in Gas Turbine Disc Cavities and Interaction with the Main Flow Path," AIAA-95-2620, Presented at the 31st AIAA/ASME/SAE/ASEE Joint Propulsion Conference, San Diego, CA, July 10-12, 1995.

Athavale, M.M., Przekwas, A.J., Hendricks, R.C., and Liang, A., "SCISEAL - A Three-Dimensional CFD Code for Accurate Analyses of Fluid Flows and Forces in Seals," Presented at the Conference on Advances Earth-To-Orbit Technology, NASA MSFC, Huntsville, AL, May 1994.

Przekwas, A.J., Athavale, M.M., and Hendricks, R.C., "Progress in Advanced Modeling of Turbine Engine Seal Flows," AIAA Paper 94-2803, 1994.

Athavale, M.M., Przekwas, A.J., J.H., Hendricks, R.C., and Steinetz, B.M., "Numerical Analysis of Intra-Cavity and Power-Stream Flow Interaction in Multiple Gas-Turbine Disk-Cavities," ASME Paper 95-GT-325, 1995.

Table 1. Comparison between the Design Data and the Prediction for Stage 1-2 Cavities
(see Figure 1 for path no. notation).

Path No.	Design		Prediction (include conjugate heat transfer for solid parts)		Previous Prediction (without conjugate heat transfer for Stage 1-2 and rotors, Ref. 12)	
	Massflow(kg/s)	Temperature (K)	Massflow(kg/s)	Temperature (K)	Massflow (kg/s)	Temperature (K)
4	0.1129	843	0.1284	870	0.1397	829
5	0.0186	843	0.0249	984	0.0136	827
6	0.0449	843	0.0481	893	0.0431	866

Table 2 Comparison between the Design Data and the Prediction for Stages 2-3 and 3-4 Cavities
(see Figure 1 for locations notation).

Locations	Design			Prediction (include conjugate heat transfer for all solid parts)			Previous Prediction (without conjugate heat transfer for Stage 1-2 and rotors, Ref. 12)		
	Mass (kg/s)	Pressure (Pa)*x10 ⁵	Temperature (K)	Mass (kg/s)	Pressure (Pa)*x10 ⁵	Temperature (K)	Mass (kg/s)	Pressure (Pa)*x10 ⁵	Temperature (K)
A	0.0567	3.309	741	0.0390	3.282	790	0.0376	3.275	786
B	0.0376	2.137	698	0.0522	2.089	794	0.0540	2.068	716
C	0.0340	1.724	705	0.0249	1.682	769	0.0240	1.689	700
D	0.0209	1.103	703	0.0263	1.082	732	0.0272	1.069	666

* Values at the center of the cavities.

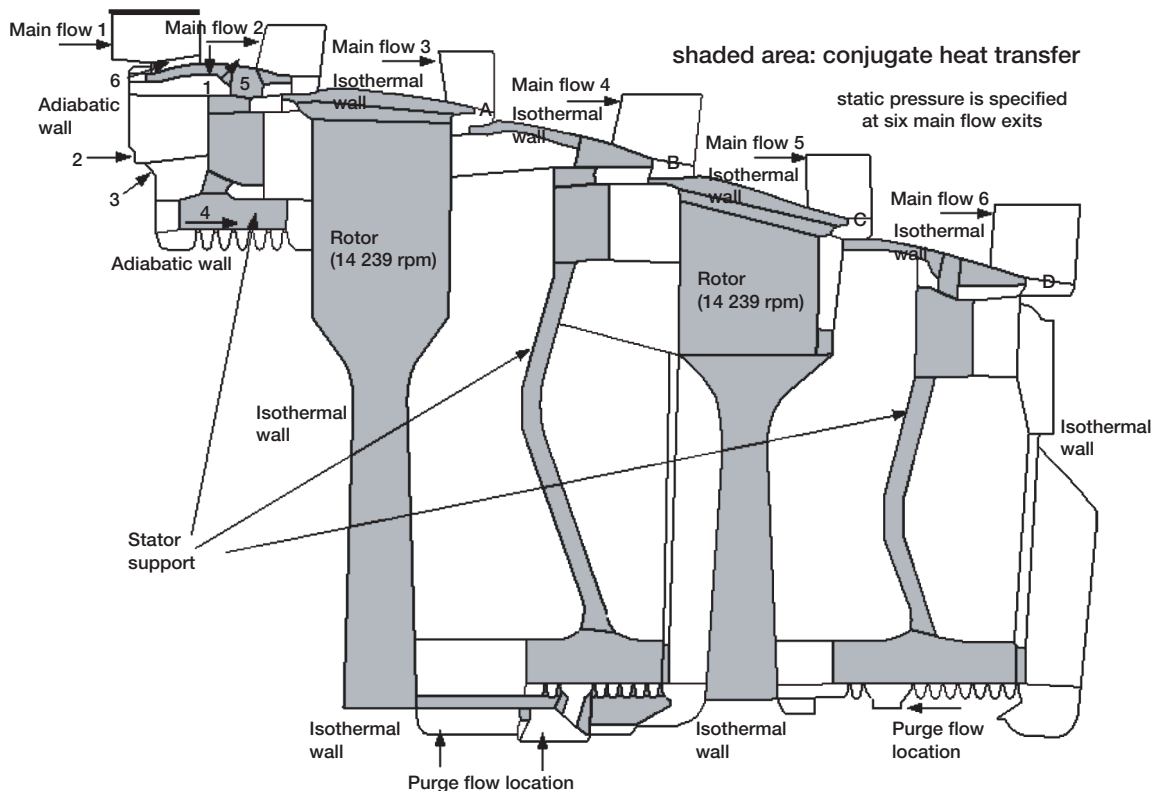


Figure 1. Flow Model for the Allison T-56/501D Turbine Cavities

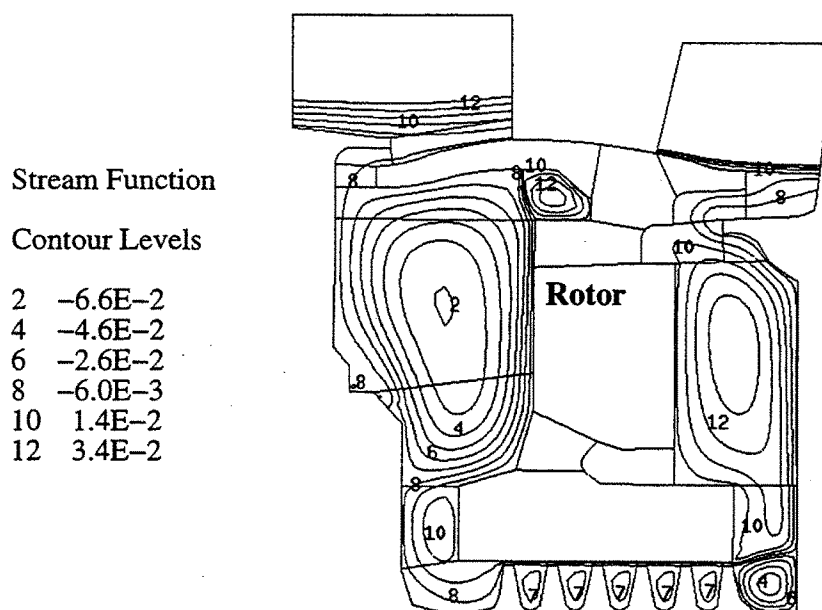


Figure 2 Stream Function Distribution inside the Stage 1-2 Cavities.

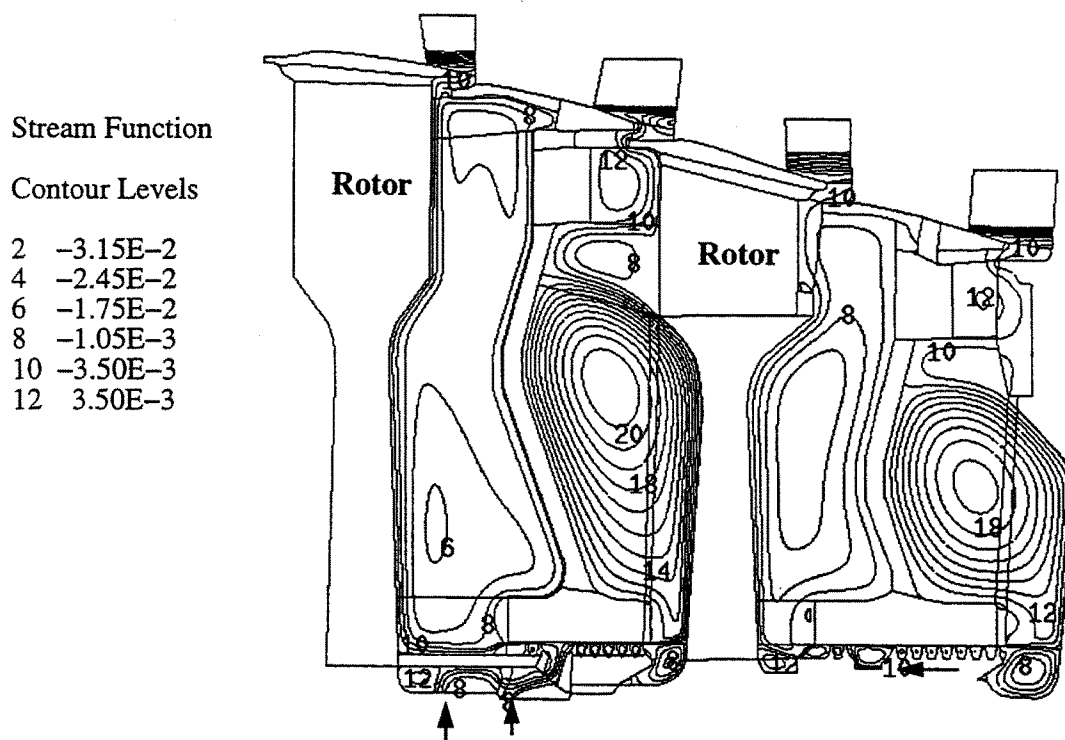


Figure 3 Stream Function Distribution inside the Stages 2-3 and 3-4 Cavities.

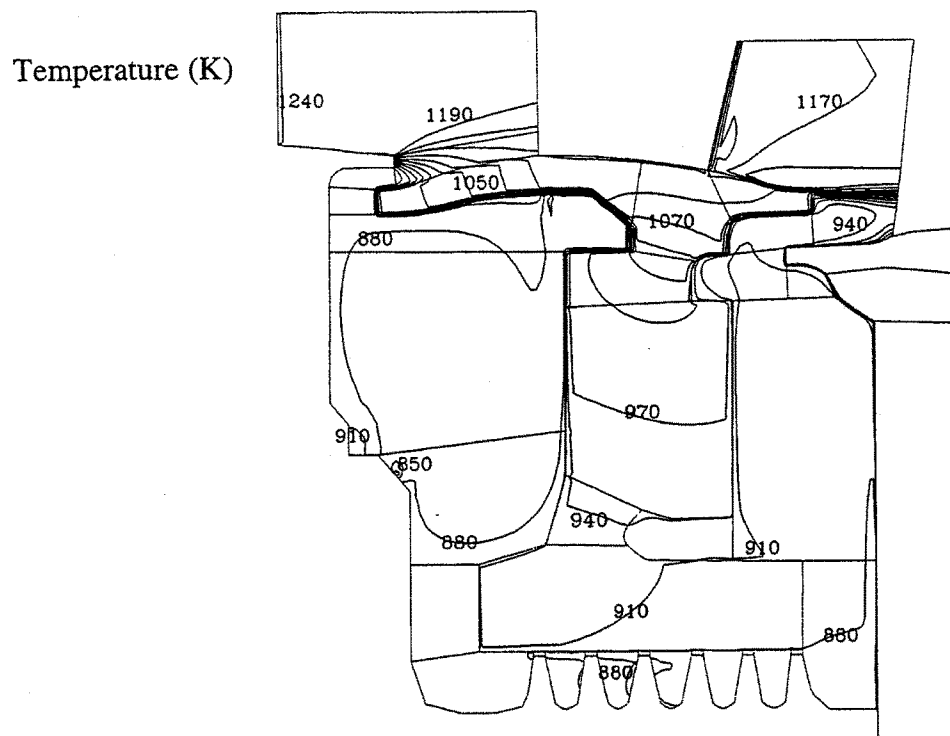


Figure 4 Static Temperature Distribution inside the Stage 1-2 Cavities and the Central Support Wall.

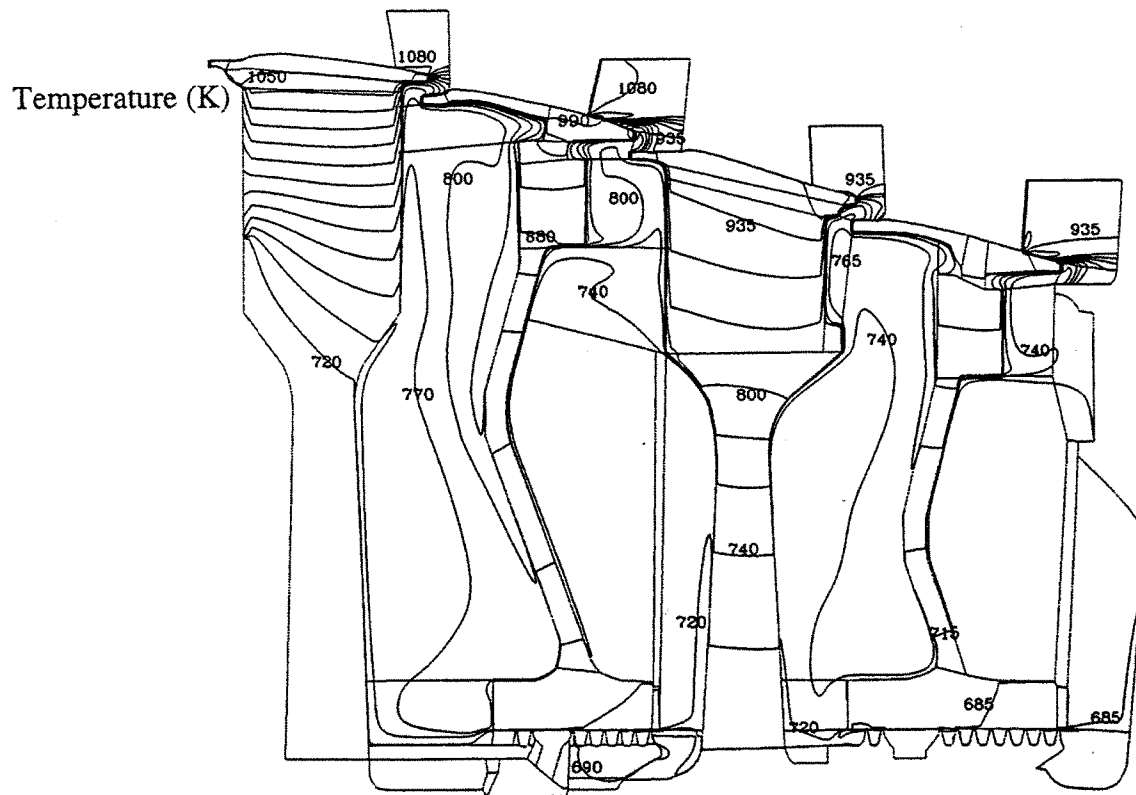


Figure 5 Static Temperature Distribution inside the Stages 2-3 and 3-4 Cavities , the Central Support Walls and the Rotors Support Walls.

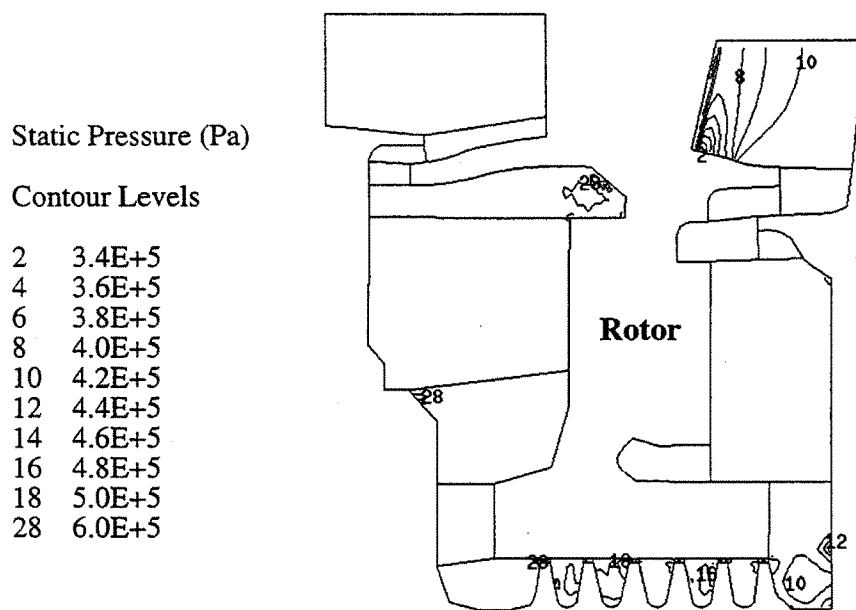


Figure 6 Static Pressure Distribution inside the Stage 1-2 Cavities.

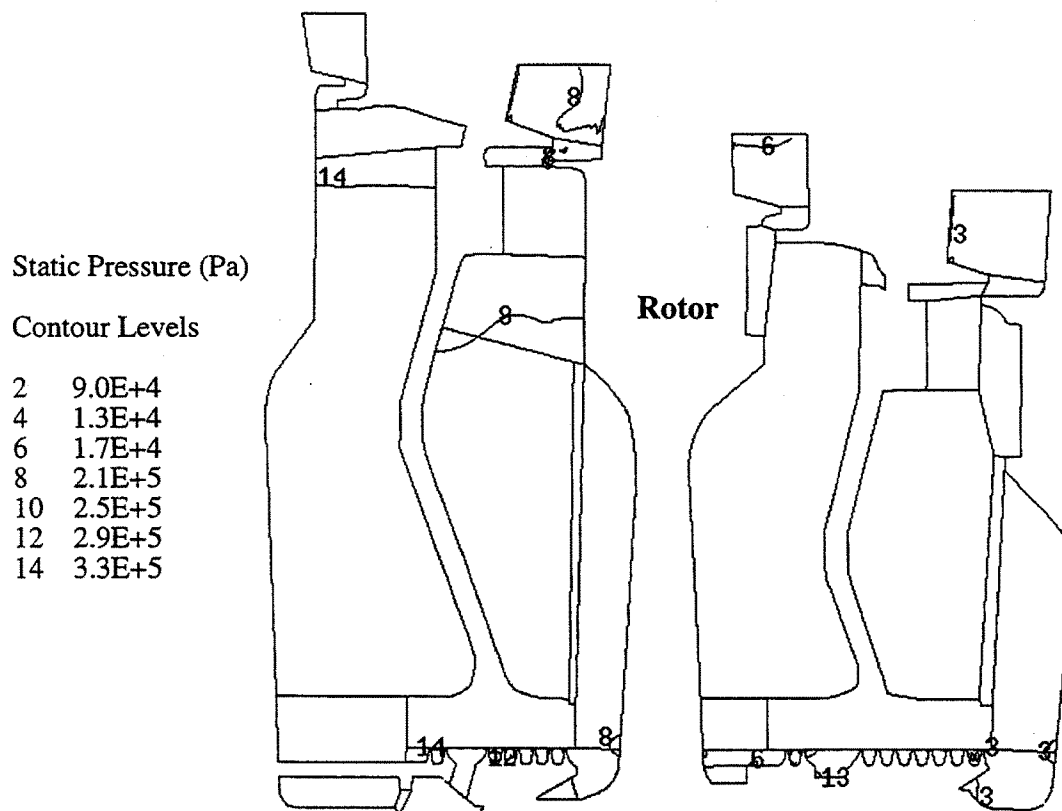


Figure 7 Static Pressure Distribution inside the Stages 2-3 and 3-4 Cavities.



AIAA-96-3305

**SIMULATION OF POWER-STREAM AND
TURBINE DISC CAVITY FLOW INTERACTION
UNDER TRANSIENT CONDITIONS**

M.M. Athavale and Y.-H. Ho
CFD Research Corporation
Huntsville, AL

J.M. Forry
Allison Engine Company
Rolls-Royce Aerospace Group
Indianapolis, IN

R.C. Hendricks
NASA Lewis Research Center
Cleveland, OH

**32nd AIAA/ASME/SAE/ASEE
Joint Propulsion Conference
July 1-3, 1996 / Lake Buena Vista, FL**

For permission to copy or republish, contact the American Institute of Aeronautics and Astronautics
1801 Alexander Bell Drive, Suite 500, Reston, VA 22091

SIMULATION OF POWER-STREAM AND TURBINE DISC CAVITY FLOW INTERACTION UNDER TRANSIENT CONDITIONS

M.M. Athavale and Y.-H. Ho
CFD Research Corporation, Huntsville, AL

J.M. Forry
Allison Engine Co., Rolls Royce Aerospace Group, Indianapolis, IN

R.C. Hendricks
NASA Lewis Research Center, Cleveland, OH

ABSTRACT

Flow in the powerstream of a multi-stage turbine is unsteady, due to rotating rows and changes in engine operating conditions. Effects of such transients on the turbine disc cavity flows should be considered when analyzing the coupled powerstream-cavity flows for coolant flow optimization. This paper presents details of numerical simulations done on interstage cavity and powerstream flow interaction under transient conditions that result from changes in operating conditions. The simulations were performed using SCISEAL, an advanced 2D/3D CFD code for predictions of flow and forces in turbomachinery seals and secondary flow elements. The transient involved changing flow conditions from high-speed ground idle (HSGI) to takeoff power. Steady-state solutions at both settings were obtained and showed good agreement with the design data from Allison. The transient simulations were done using HSGI solution as initial conditions. Solutions for step change as well as ramped change in boundary conditions were obtained. In both cases, the overall flow fields were seen to vary smoothly, with no ingress of the hot powerstream gases in the cavities. Similar time-dependent simulations with other operating point change conditions may need to be performed to ensure cooling performance when doing coolant flow optimization.

INTRODUCTION

The demand for higher efficiencies in gas turbine aero and aero derivative engines has driven the turbine operating conditions to higher temperatures and pressures. With increasing severity of conditions, management of the secondary flow system, which

provides component cooling has become increasingly important. The coolant flow is essential to keep component temperatures to acceptable levels for long life cycles, at the same time the coolant air represents a loss of efficiency, and needs to be kept to a minimum. In the modern gas turbine engine secondary flow is one of the most promising areas for engine efficiency increases, and hence there is drive to optimize the secondary flow circuit. A thorough understanding of the flow and heat transfer processes that take place in the disc cavities in the turbine sections is essential. Effects of linking between the cavities and the main path must be taken into account when simulating these flows in the often interconnected disk cavities.

The steady-state flow and heat transfer processes in the single rim seal and disc cavity configurations has received a large amount of attention in the past. Early experimental and theoretical work considered simplified cavity and rim seal geometries to generate models for the performance of the cavities¹⁻³. A simple analytical model for disc cavity friction heating as well as main-path gas ingestion was given by, *e.g.*, Hasser *et.al.*⁴.

Detailed steady-state analyses of the cavity flows have also been done using the computational fluid dynamics (CFD) techniques. The early CFD studies were done on simplified geometries of a single disc cavity with the associated rim seal. Laminar and turbulent flows in such rotating cavities with inflow and outflow were presented by Chew^{5,6}. More recently, Ko and Rhode⁷ conducted studies on the heat transfer in a turbine disc with secondary cooling flows. Athavale *et.al.*⁸ also conducted a numerical study on a single cavity configuration, and variations in the cooling effectiveness in the cavity with purge flow and

geometrical mismatches at rim seal were investigated. Some of the recent studies have also considered the actual engine environments where usually flows in multiple cavities with complex shapes interact with the powerstream and other cavities. A demonstration simulation of the interlinked cavities is given by Virr *et.al.*⁹. Other recent papers include a numerical study of the complete secondary flow system in the UTRC Large Scale Rig¹⁰, used to simulate the conditions in the space shuttle main engine high pressure fuel turbopump (SSME HPFTP). Steady state flow and heat transfer simulations in an actual engine were presented by Athavale *et.al*¹¹, where the interstage cavities in the turbine section of the Allison T56/501D engine were considered. Effects of labyrinth seal clearances on the flow and conjugate heat transfer on the internal supports were considered. In a recent paper by Ho *et.al*¹², the entire turbine section with conjugate heat transfer was simulated and temperature profiles in the flow as well as solid portions were presented.

Detailed steady-state results are very useful in performance assessment of the cooling system as well in estimating the temperatures in the solid portions for life predictions. However, the flow in a multi-row engine is inherently unsteady, due to a. blade wakes passing over the rim seals and b. changes in the flow due to changes in the operating condition change. Both of these effects disturb the averaged flow fields as predicted in the steady analyses and can generate local, temporary conditions that can lead to undesirable effects such as hot gas ingestion. Blade wake - passing can generate circumferential spots where there is local ingress even when in the average sense, there is a net egress of flow from the rim seal. As the engine is operated at different points during a typical flight, the operating conditions change and generate transients that also may lead to temporary hot gas ingress and affect the cooling performance in the cavities. Effects of blade wake-passing can lead to thermal cycling as the blades rotate, although the amplitude of the temperature variations may not be large. Changes in the operating conditions do not take place as often as the blade wakes, but if they lead to hot gas ingestion, the thermal variation can be large.

Simulating the transient effects in both cases is thus important, and with efforts towards optimizing coolant flow rates may become more important. The simulations for blade wake obviously require a 3-D grid with coupled main-path and cavity flow and is

computationally expensive. Effects of operating condition changes, however, can be potentially simulated using a 2-D axisymmetric problem and reduce the efforts involved. The present work is focussed on such a time-dependent simulation of the flow in a cavity-pair in the turbine section of an actual gas-turbine engine, under an operating condition change involved in going from the high-speed ground idle point to takeoff thrust at sea-level. Other possible pairs of operating points in normal operations, e.g. cruise power to cruise-idle conditions. One could also consider more drastic changes imposed on the engines in, e.g., a fighter plane where flight conditions can change much more rapidly.

DESCRIPTION OF THE FLOW SOLVER

The numerical simulations were carried out with an advanced 2-D/3-D CFD code SCISEAL, developed for the analysis of fluid flow and forces in turbomachinery seals under a NASA contract¹³. The code has a finite-volume pressure-based formulation to integrate the flow (Navier-Stokes) and scalar equations in a sequential manner. A modified version of the SIMPLEC procedure is used to link the pressure and velocities. The code can handle incompressible as well as low and high speed compressible flows. An implicit multidomain capability is available, and is extremely important in the present simulations, where the complex shapes of the cavities makes single-block grid generation extremely difficult. Both fluid and solid regions and the conjugate surfaces can be included in the energy transport, and this feature is also important in the disc cavity analyses. A variety of turbulence models, including the standard and low-Re $k-\epsilon$ models and a 2-layer $k-\epsilon$ models are available. High order spatial (up to 3rd) and temporal (2nd) discretization schemes can be used for the convective and time derivatives. Other relevant capabilities include variable gas properties and inclusion of the viscous dissipation in the energy equation.

FLOW CONFIGURATION

The configuration considered in this study was the first interstage pair of disc cavities (Stage 1-2 cavities) and the interstage labyrinth seal in the turbine section of the T56/501D engine of Allison Engine Company, Rolls Royce Aerospace Group (Figure 1). These engines are currently

installed on the C-130 military transport planes. The characteristics of the T56/501D engine are: a pressure ratio of 14.1, a mass flow rate 15.7 kg/s (34.6 lb/s), engine speed 14239 rpm. The engine delivers 5250 horse power at sea level takeoff conditions and the maximum turbine inlet temperature is 1364 K (1994 °F).

The results presented here consider two steady-state operating points and the transient that occurs when the conditions change from one point to the next. One set of steady-state conditions corresponds to high-speed ground idle (HSGI) at sea-level, which is taken as the engine condition just prior to takeoff. The second operating point corresponds to the seal-level takeoff conditions. The transient from the first operating point to the second then corresponds to the increase of engine throttle from the idle to takeoff power. The solutions presented here consider all three cases.

Flow information inside the cavities for the two steady-state operating conditions was generated by Allison with their design codes, and were made available for the comparison with numerical results. The data include static pressures inside the cavities, and the flow rates and total temperatures of the gas at the rim and labyrinth seals at both steady-state operating points. The transition time for the change from HSGI conditions to takeoff conditions was estimated by Allison engineers at 5 seconds. However, exactly how the boundary conditions change over this period is unknown. In the present simulations, two cases were considered:

- a. A step change: Start with the steady-state solution at HSGI, change all boundary conditions to the takeoff values, and compute the evolution of the flow in the cavities and powerstreams.
- b. Ramped boundary change: Use the HSGI and takeoff conditions as the starting and ending points of a 5 second ramp, and vary all conditions linearly over this period.

It is clear that neither of the two fit the actual processes that go on in the engine. Case A is clearly a drastic process, and is not expected to be realistic, but it provides one extreme. Case B may be somewhat more realistic. The actual process

probably involves an initial exponential change from the conditions, and an asymptotic approach to the takeoff conditions. Using both cases A and B, we may, however, be able to approximate the probable response in a "piecewise" fashion.

The geometry of the disk cavities was scanned from the engine drawings and the outlines were fed into a grid generation package. Several critical geometric parameters, such as the labyrinth seal clearances, rim seal gaps, and the secondary flow injection areas were provided by Allison Engine Company. The flow was assumed to be axisymmetric. A multi-domain grid with 34 domains and approx. 8800 cells was built for the cavity pair. The interstage labyrinth seal clearance was 300 microns (0.012 inches). A small effort was spent on grid refinement studies on the time-accurate solution runs and additional efforts may be needed later. For the present set of results the solid parts were not modeled in the energy equation. Steady-state solutions with conjugate heat transfer were reported in Ref. 12, and showed that the gas temperatures increases from 30 to 150K in some of the leakage paths. The effects of heat transfer in the solid parts need to be included in future.

FLOW AND BOUNDARY CONDITIONS

At the upstream boundaries of the main-paths (core flows) associated with the two rim seals, the inlet gas velocity (all components) and temperatures were specified, and constant static pressures were specified at the exit boundaries of the two main paths. The inlet conditions change at each of the main-path section, and the values used here were established by the Allison design calculations. The mass flow rates and temperatures of the various purge flows were also known, and were imposed at the appropriate locations. In the present case, there were three main points of flow injection. The computational grid used in the cavities and the interstage labyrinth seals as well as the locations of the purge flow injection are shown in Figures 2. Also shown in these figures are the boundary conditions that were used in the calculations. For the flow and momentum equations, all walls were no-slip walls, with appropriate tangential velocity conditions imposed on the stationary and

rotating walls. The walls were assumed adiabatic for the energy equation solutions. The rotation speed is 14239 rpm for the takeoff and 13500 rpm. for the HSGI point; in the present calculations it was taken as 14239 rpm for both steady-state cases as well as the transient calculations.

The 2-dimensional, axisymmetric flow in the cavities and main-path was assumed compressible, with air as the working fluid. Sutherland's viscosity law was used to account for variations in the viscosity due to temperature. The central-differencing scheme was used for the convective fluxes in the momentum equations with a 10% damping (upwinding). The turbulence in the flow was treated with the standard $k-\epsilon$ turbulence model with wall functions. Effects of viscous dissipation were included in the energy equation. The time-dependent simulations were done using the Crank-Nicholson scheme in time for second-order time accuracy. A constant time step of 0.1 seconds was used in the ramped boundary condition simulations. For the step boundary change, the time step was kept 0.0025 seconds for the first 0.1 second, 0.01 seconds for the next 0.3 seconds.

RESULTS AND DISCUSSION

The numerical results presented here are the streamline and temperature plots in each of the flow domains. Also presented below in tabular form are the flow rates and temperatures at the rim and labyrinth seal locations, and comparison with the design data.

Steady-State Simulations

Steady-state flow was simulated at the HSGI and takeoff points. The results of the mass flow rates and temperatures of the flow through the rim and labyrinth seals as well as a purge are given in Tables 1 and 2. Also included in the tables are the values of these parameters from Allison design calculations, and a good agreement is seen between the corresponding sets of computed results. The streamlines for the two flow conditions are plotted in Figures 3a and 3b. As seen from these figures, both the rim seals show egress of the coolant. Effective cooling of the

cavities is seen from Figures 4a and 4b where the gas temperature contours in the cavities are shown. These figures and Table 1 indicate that although the temperature values in the two data sets differ by a large amount, in terms of the purge flow rates and the overall flow features, the two cases are very similar, and this plays some role in the transient simulations described next.

Time-Accurate Flow Simulations

As described earlier, the time-accurate simulations were done using two time-functional forms. Results for these are described below.

A. Step change: Results for this case are shown in Figures 5 and 7. Changes in the massflow rates through the rim seal I (path 6 in Fig. 2) and interstage labyrinth seal as a function of time are shown in Figure 5. Some initial oscillations in the flow rates are seen, which quickly settle down to the steady-state values. The temperature fields at several times in the early transient are shown in Figure 7 and the contours near the rim seal (path 6) show the effects of the flow oscillations. The cavity flow field has relatively small inertia and as a result achieves the steady state solutions very quickly, within about 40-50 milliseconds. A look at the streamlines (not shown here) indicated that although the rim seal flow rates fluctuate to some extent, the flow structures in the cavity and main flow remain relatively unchanged.

B. Ramped Change: The estimated time for the change in flow conditions is about 5 seconds, and in this case the flow parameters were assumed to vary linearly with time over 5 seconds. One point to be noted here is that all the variables were changed in a linear fashion, including the purge flow velocities. This may generate a purge flow rate variation that is not linear with time, since the mass flow rate involved the velocities as well as the gas density. This point may need to be addressed if the mass flow rates are to be varied linearly.

The mass flow rates through rim seal I and labyrinth seal are shown in Figure 6, and show a gradual change in the flow rates, as expected. Temperature fields during the first 2.5 seconds of

the transient are shown in Figure 8, and show a gradual, smooth change in the overall temperature values. The streamline plots (not shown) also indicate a smooth change from one time-step to next, without the generation of any recirculation patterns etc., that would disrupt the flow.

In both the time-histories, the flow was seen to behave smoothly, and without any indication of disruption. A comparison of purge rates in Tables 1A and 1B indicates that in spite of the large changes in the gas temperatures, the mass flow rates are very close to each other at the two different points. In addition, the pressure levels (not shown here) for the two cases are also similar, and these two factors are seen to generate time-varying boundary conditions that are fairly benign, even when a step change is considered.

SUMMARY

Flow and heat transfer computations were performed for the Stage 1-2 disc cavities in the turbine section of the Allison T56/501D engine using an advanced CFD code, SCISEAL. Two steady-state conditions, corresponding to the high-speed ground idle and the takeoff points, were simulated. Next, time-accurate simulations of the flow-field as the boundary conditions changed from HSGI to takeoff point were calculated assuming two different time-functions. The following remarks can be made based on the results:

1. The predicted steady-state results for the HSGI and takeoff conditions, in terms of the mass flows and gas temperatures key points show good agreement with Allison engine design calculations. The simulations did not include a leakage path through the labyrinth seal support, and this leakage flow added to the labyrinth seal flow. This is the reason for higher predicted flow rates in path 4.
2. Time-transients were calculated using two different time-histories, a step change and a linearly ramped change. In both cases, the flow changes were found to be smooth, with no evidence of hot gas ingestion in the cavities through the rim seals. The flow patterns in both

time-transients were seen to maintain their basic overall characteristics which were similar to the steady-state points.

3. The time-variation of boundary conditions used in the simulations do not exactly represent the actual case. More accurate time-histories are needed, and should include the variation of the gas properties as well as the purge flow rates.
4. The flow fields did not show a dramatic change, perhaps because the starting and ending point of the time-transient have similar purge mass flows, and pressures; only temperatures showed significant changes, and were not sufficient to disrupt the cavity flows. Similar studies should still be carried out for two reasons: there may be other condition changes more drastic than considered here. Also, with smaller, optimized coolant flow rates, the safety margins in the flow rates may become too small to prevent ingestion even with smaller operating point changes.

REFERENCES

1. Owen, J.M., and Pincombe, J.R., "Velocity Measurements Inside a Rotating Cylindrical Cavity with a Radial Outflow of Fluid," *J. Fluid Mechanics*, Vol. 99, p. 111, 1980.
2. Owen, J.M., Pincombe, J.R., and Rogers, R.H., "Source-Sink Flow Inside a Rotating Cylindrical Cavity," *J. Fluid Mechanics*, Vol. 155, pp. 233-265, 1985.
3. Phadke, U.P., and Owen, J.M., "An Investigation for an Air-cooled Shrouded Rotating Disk System with Radial Clearance Seals," *Trans. ASME, J. of Engineering for Gas Turbine and Power*, Vol. 110, pp. 78-85, 1988.
4. Hasser, F., Jack, J., and McGreehan, W., "Windage Rise and Flowpath Gas Ingestion in Turbine Rim Cavities," *Trans. ASME, J. of Engineering for Gas Turbine and Power*, Vol. 110, pp. 78-85, 1988.
5. Chew J.W., "Predictions of Flow in Rotating Disk Systems Using the k- ϵ Turbulence Model," ASME-88-GT-229, ASME Gas Turbine and Aeroengine Expo, Amsterdam, The Netherlands, 1988.
6. Chew, J.W., "A Theoretical Study of Ingress for Shrouded Rotating Disc Systems with

- Radial Outflow," ASME-89-GT-178, ASME Gas Turbine and Aeroengine Expo, Toronto, Canada, 1989.
7. Ko, S.H., and Rhode, D.L., Thermal Details in a Rotor-Stator Cavity at Engine Conditions with a Mainstream," ASME-91-GT-275, ASME Gas Turbine and Aeroengine Expo, Orlando, FL, 1991.
 8. Athavale, M.M., Przekwas, A.J., and Hendricks, R.C., "A Numerical Study of the Flow Field in Enclosed Turbine Disk Cavities in Gas Turbine Engines," 4th International Symposium on Transport Phenomena and Dynamics of Rotating Machinery (ISROMAC-4), Honolulu, HI, 1992.
 9. Virr, G.P., Chew, J.W., and Coupland, J., "Application of Computational Fluid Dynamics to Turbine Disk Cavities," *Trans. ASME, J. of Turbomachinery*, Vol. 116, pp. 701-708, 1994.
 10. Athavale, M.M., Przekwas, A.J., Hendricks, R.C., and Steinetz, B.M., "Numerical Analysis of Intra-Cavity and Power-Stream Flow Interaction in Multiple Gas-Turbine Disk-Cavities," ASME-95-GT-325, ASME Gas Turbine Congress and Exposition, Houston, TX, 1995.
 11. Athavale, M.M., Ho, Y.-H., Forry, J.M., Munson, J.H., Hendricks, R.C., and Steinetz, B.M., "Simulation of Secondary Flow in Gas Turbine Disc Cavities and Interaction with the Main Flow Path," AIAA-95-2620, 31st Joint Propulsion Conference, San Diego, CA, July 1995.
 12. Ho, Y.-H., Athavale, M.M., Forry, J.M., Hendricks, R.C., and Steinetz, B.M., "Numerical Simulation of Secondary Flow in Gas Turbine Disc Cavities, Including Conjugate Heat Transfer," ASME-96-GT-67, ASME Gas Turbine Congress and Exposition, Birmingham, UK, June 1996.
 13. Athavale, M.M., Przekwas, A.J., Hendricks, R.C., and Liang, A., "SCISEAL - A Three-Dimensional CFD Code for Accurate Analyses of Fluid Flow and Forces in Seals," Conference on Advances Earth-To-Orbit Technology, NASA MSFC, Huntsville, AL, May 1994.

Table 1. Comparison between the Design and the Prediction for Takeoff Condition
(see Figure 2 for Path No. Notation)

Path No.	Design		Prediction	
	Massflow (kg/s)	Temperature (K)	Massflow (kg/s)	Temperature (K)
4	0.1129	843	0.1404	827
5	0.0186	843	0.0165	830
6	0.0449	843	0.0428	864

Table 2. Comparison between the Design and the Prediction for High-Speed Ground Idle Condition
(see Figure 2 for Path No. Notation)

Path No.	Design		Prediction	
	Massflow (kg/s)	Temperature (K)	Massflow (kg/s)	Temperature (K)
4	0.0980	718	0.1184	717
5	0.0159	718	0.0182	725
6	0.0459	736	0.0441	721

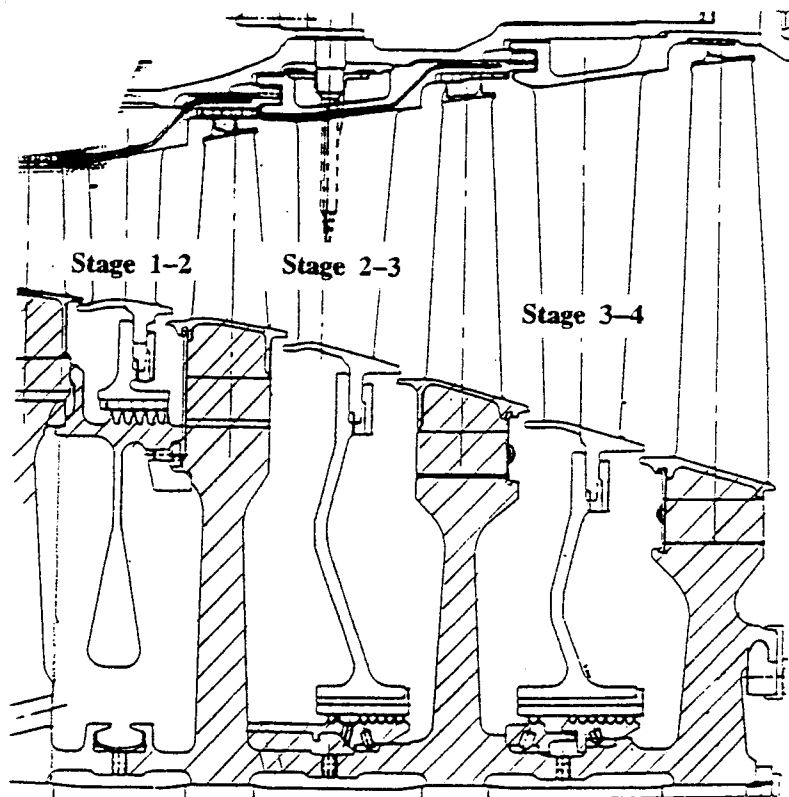


Figure 1 Schematic of the Inner Cavities in the Turbine Drum of the Allison T56/501D Engine

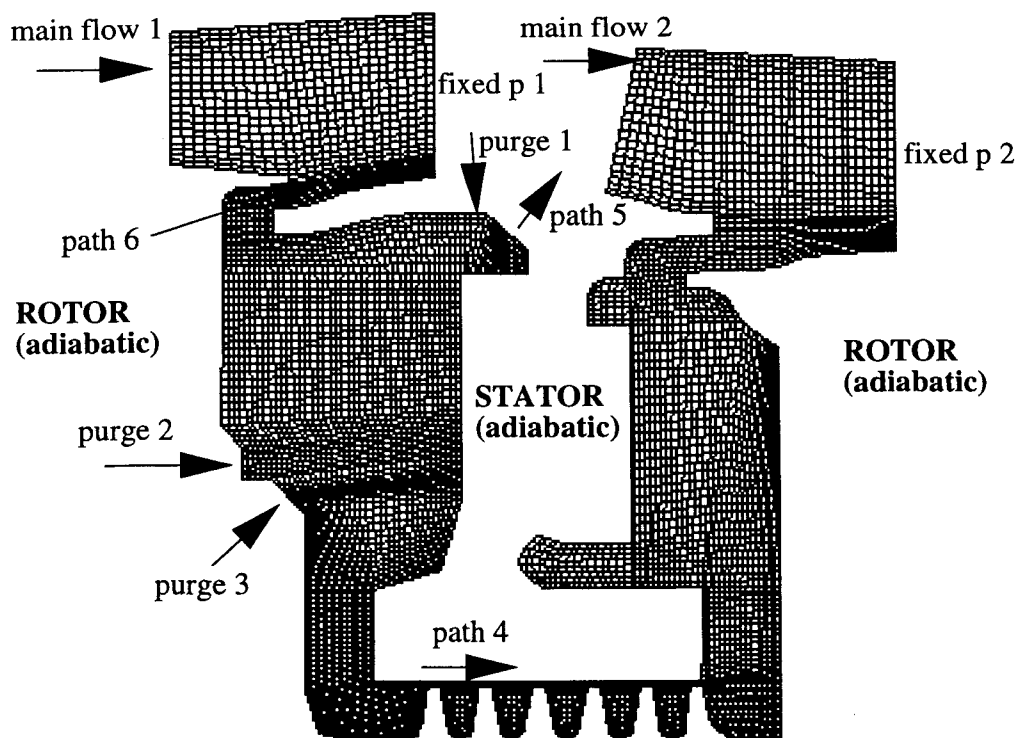


Figure 2 Computational Grids for the T-56 Turbine Stage 1-2 Cavities.

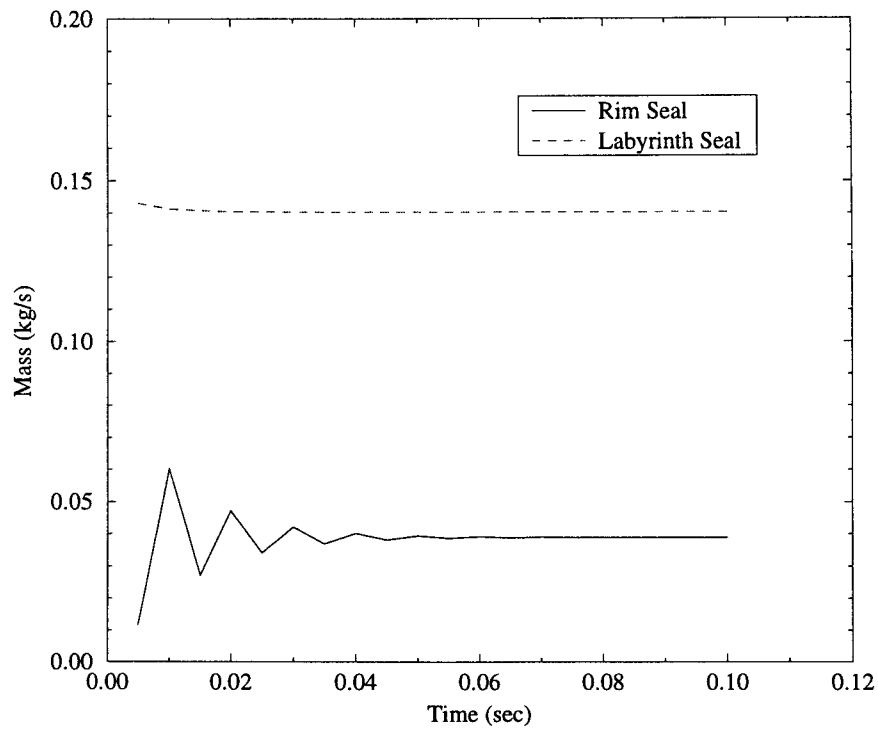


Figure 5. Time History of the Mass Flow Rates at the Rim Seal and the Labyrinth Seal with a Simple Step Jump Approach from High-Speed Ground Idle to Takeoff Conditions

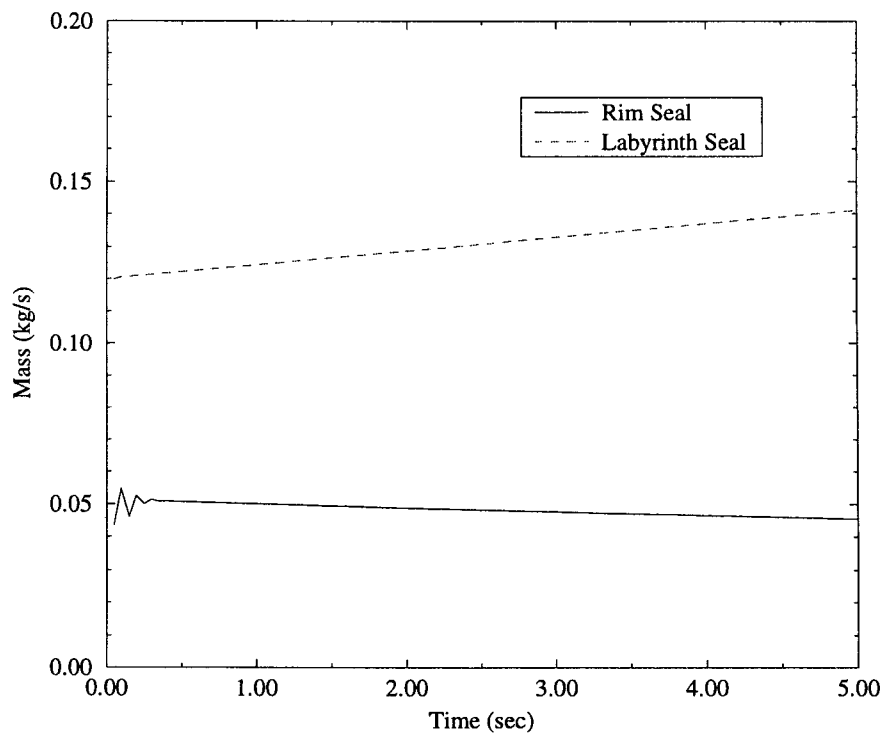


Figure 6. Time History of the Mass Flow Rates at the Rim Seal and the Labyrinth Seal with a Linear Ramping Approach from High-Speed Ground Idle to Takeoff Conditions.



AIAA 97-2727

Development of a Coupled, Transient Simulation Methodology for Interaction Between Primary and Secondary Flowpaths in Gas Turbine Engines

Mahesh M. Athavale and Andrzej J. Przekwas
CFD Research Corporation
Huntsville, AL

and
R.C. Hendricks and B. Steinetz
NASAS Lewis Research Center, OH

**33rd AIAA/ASME/SAE/ASEE Joint Propulsion
Conference & Exhibit**
July 6–9, 1997 / Seattle, WA

For permission to copy or republish, contact the American Institute of Aeronautics and Astronautics
1801 Alexander Bell Drive, Suite 500, Reston, VA 22091

Development of a Coupled, Transient Simulation Methodology for Interaction Between Primary and Secondary Flowpaths in Gas Turbine Engines

M. M. Athavale* and A.J. Przekwas†
CFD Research Corp., Huntsville, AL

R.C. Hendricks and B.M. Steinetz
NASA Lewis Research Center, Cleveland, OH

ABSTRACT

Optimization of secondary flows in gas turbine engines promises significant, efficiency increases. Effects of such optimization on the interaction with the mainpath flows need to be thoroughly investigated. The inherent unsteadiness of flow in the mainpath of a multi-stage engine coupled with reduced secondary flow rates may lead to local hot gas ingestion in the turbine disc cavities, with adverse effects on component life. A time-accurate simulation methodology is being developed to provide detailed knowledge of these flow-fields. The method involves use of two codes specially developed for the two flowpaths, coupled through an interface for data exchange. The multi-stage transient power stream flow is handled by the MS-TURBO code with a deforming/clicking grid algorithm, while the turbulent flow heat-transfer in the secondary path is handled by the SCISEAL code using an unstructured/Cartesian adaptive grid. Results of adaptive grid algorithm on a typical turbine disc cavity are shown, and a description of the methodology and current status of the coupling algorithm is presented.

INTRODUCTION

Demand for higher performance from gas turbine engines has led to higher operating temperatures and pressures. Adequate cooling of components, especially in the turbine section, becomes vital under these conditions for acceptable component life. Cooling is usually achieved by coolant air bled from the compressor section. This air, although necessary, represents a loss, and is a prime candidate for optimization in the drive to increase the engine efficiency through secondary flow management. Under these conflicting requirements, a detailed knowledge of the flow and heat-transfer pro-

cesses in the secondary flow systems such as disc cavities, and their interaction with the main path flows becomes critical at the design stage to ensure adequate component life.

Flow and heat transfer processes in rotating cavities formed between two rotor disks as well as the cavities formed in rotor-stator disks have received considerable attention in the past. Early work on the rotating cavity flow and heat transfer includes experimental [1-3] as well as analytical [4,5] studies. Work on the rotor-stator configuration with a rim seal includes experimental [6,7] and analytical [e.g. Ref. 8] studies done on simplified geometries. Analytical models for the cavity flows typically used integral flow equations and often did not include the interaction with mainpath flow. Such models are inadequate for generating the flow details that may be needed for future designs.

Computational fluid dynamics (CFD) techniques are being increasingly used to provide detailed flow-field information that the analytical methods could not generate. Several studies, dealing with single cavity configuration with simplified geometry are available in the literature [9-12]. Ko and Rhode [10] and Athavale et al. [11,12] presented 2-D axisymmetric flow and heat transfer results in generic turbine disc cavities. The cavities considered were of the rotor-stator type with a rim seal and some measure of interaction with a mainpath flow was provided. Results for different coolant flow rates, and geometry changes in the rim seal were presented in these studies.

A recent study by Heidegger, et al. [13] presented simultaneous, 3-D solutions of the powerstream and seal cavity flow interaction in a typical multistage compressor. Their results show that the leakage flow out of the seal cavities can affect the powerstream significantly, mainly by altering the inlet flow near the stator blade root area, and can potentially affect the performance of the overall compressor.

* Group Leader / Research

† Vice President / Research

In an actual engine, the turbine or compressor has multiple disc cavities, with intra-cavity connections and multiple mainpath flow conditions, and the shapes of the cavities are far more complicated than those considered in these works. More recently, several studies have been performed with CFD to take into account the complex cavity shapes as well as multiple cavity configurations [14-17]. Virr et al. [15] presented a demonstration case for a multiple cavity turbine drum configuration. Athavale et al. [16] studied the multiply-connected disc cavities and interaction with main-path for the UTRC Large Scale Rig. Studies on an actual turbine drum geometry were presented for the Allison T-56 turbine drum inner disc cavities in refs. 14 and 17. The studies included the interaction of disc cavity flows with main stream, interstage labyrinth seals as well as the conjugate heat transfer between the flow and the solid parts (rotor and stator disks) of the turbine drum to generate a comprehensive flow and heat transfer picture of the turbine section.

The majority of the CFD work done so far was based on the 2-D axisymmetric model and did not account for the circumferential variations that are typically present in a multi-stage turbine machine. The flow in the mainpath contains blade wakes that move with the rotor blades, and generate a time-periodic flow-field in the circumferential direction. The blade wakes, as they pass over the rim seals at the blade platforms, generate local flow variations that may lead to local flow features that may differ considerably from the averaged, 2-D solutions. Information on these local, time-varying features becomes more important during the design stages, as this can lead to performance degradation in the compressor section, and, perhaps local ingestion of hot mainpath gas in turbine disc cavities that will affect component life.

The present paper describes a new computational methodology that is being developed by NASA to treat the complex, 3-D, time-dependent flow field that exists in the turbine mainpath flow and couple it with the secondary flow-fields that exist in the sub-platform regions of the secondary flow system (See Figure 1). The flow characteristics in the two flow streams differ significantly. The mainpath flow is typically compressible, transonic, and the geometries involved are usually simpler, mainly annulus base. The sub-platform flows are typically low-subsonic, dominated by recirculating, turbulent flows and the domain geometries are complex shaped, and usually contain narrow passages relating to the seals. In addition, the secondary flow calculations also need to consider conjugate heat transfer to the solid parts from the flow. In view of these different require

ments, it was decided to use two different codes for the two different flow paths, such that each code was developed especially for one flow path. Thus, each of the codes took into account of the requirements of the corresponding flow stream and physics. The following sections give a brief outline of the two codes that are being used, a description of the interface algorithm and issues that are involved in coupling the codes. Some examples of grid-adaptation for the cavity flows using the secondary path code are also presented

DESCRIPTION OF THE CODES

The two codes that were selected are the MS-TURBO code [18,19] that was developed for the high speed mainpath flows in multi-stage turbomachines. The secondary flow will be treated using SCISEAL [20], a code developed for the secondary and turbomachinery seal flows. Both of the codes were developed under separate NASA contracts. A brief description of the codes follows:

MS-TURBO code [18,19]

This code uses the 3-D unsteady Euler/N-S form of the flow equations. The code was developed for the multi-row turbomachinery transient mainpath flows that result from the relative motion between successive blade rows. Each blade row is separated in radial zones if needed, and treated one at a time. The in-core storage requirement is for one blade row at a time only, which reduces the working memory size and allows any number of blade rows. Information at the blade row boundary faces is stored in separate arrays which are used to provide the linking between successive blade rows. The flow equations are written in the generalized form and the convective fluxes are discretized using the flux-difference splitting methods with third-order accuracy achieved using the Osher-Chakravarthy method. The first-rate convective fluxes, e.g., at a cell face are written as:

$$\tilde{F}_{i+\frac{1}{2}} = \frac{1}{2} \left[\tilde{F}_i + \tilde{F}_{i+1} - \Delta \tilde{F}_{i+\frac{1}{2}}^+ + \Delta \tilde{F}_{i+\frac{1}{2}}^- \right] \Delta \tilde{F}_{i+\frac{1}{2}}^\pm \quad (1)$$

where are the flux differences along right and left running characteristics. Higher order accuracies are achieved by adding corrective flux difference terms to this expression. The diffusive terms are discretized using the central-differencing method. Flux near sharp gradients is limited using a Van Leer flux limiting scheme. The code used the thin-layer N-S equations

where the diffusive terms in the flow-wise direction are neglected. The code has an eddy-viscosity based turbulence model to treat turbulent flows. The boundary conditions are set to fit a typical turbomachine problem, and are relatively easy to set up.

Structured grids are used in each of the blade rows. When the blade rows move with respect to each other, the flow is resolved in time unlike a class of solvers that use circumferential averaging. This time resolution is important for the present application as was outlined in an earlier section. The interface between a moving row and a stationary row consists of an interface zone that is allowed to deform as one blade row moves past the next. A clicking algorithm is used in conjunction with the deformation which allows a cell to 'click' to the next cell after a certain amount of deformation. When the grid on the end faces of the deformation zone is known, the grid inside the deformation zone is calculated using linear interpolation. This ensures reasonably good grid quality in the deformation zone at any time during the simulations. Grid distortion and clicking implies moving grids, and motion of the grid is included in the time derivative of the flow variables through a transformation. The flow domain that will be used for the present application will have an interface boundary on the hub surface of the blade rows, at the place where the rim seal is present.

SCISEAL code [20,21]

This code was developed at CFDRC for simulations of flows in the secondary flow elements and turbomachinery seals. The released version of the code uses a pressure based finite volume methodology to integrate the Navier-Stokes equations on structured, multi-block grids. The pressure-based solution scheme allows treatment of slow and recirculating flows. The code has a variety of turbulence models including standard k-e and Low-Re k-e models, a comprehensive set of boundary condition types, and high-order spatial and temporal discretization schemes. A detailed description of the code capabilities is given in Ref. 20.

As remarked earlier, the shapes of the disc cavities are in general very complex and contain large cross-sectional areas meeting small gap areas e.g. a labyrinth seal. Generation of a structured multiblock grid on such problem can become cumbersome and time consuming. In addition, grid refinements/adjustments may be needed to resolve flow features that may not be obvious beforehand. Part of the current work is focussed on making grid generation and problem setup/running as easy to the

user as possible. The items that are under consideration are

1. **Adaptation/incorporation** of the unstructured/adaptive Cartesian grid solution methodology [21] in SCISEAL: Use of unstructured grids in the complex shapes of the disc cavities will simplify the grid generation procedure, and facilitate ease of use when coupling the flow solutions with conjugate heat transfer and structural mechanics in the solid parts. Using the triangular cells in 2-D or tetrahedra in 3-D is easiest for grid generation, but can lead to accuracy loss and more computational time. To avoid this, the code can handle a variety of cell/cell-face types including triangle, quads and polygons in 2-D and tetrahedrons, pyramids, bricks, and prisms with arbitrary polygonal cross-sections in 3-D.
2. **Grid Adaptor:** To further simplify the grid generation and solution process, the code is coupled with a grid adaptor to adapt the grids to the local flow conditions for optimum use of the grids. Starting with a baseline coarse grid, the adaptor can be used to add cells (by splitting) in areas of high gradients, or coarsen it as needed; success of this process depends a great deal on the adaptation criterion used. At present, the adaptor uses a combined 'deviation' function outlined below as a criterion to split cells:

$$\text{Deviation} = C_1 \nabla \times (\bar{\Omega} \times \bar{V}) + C_2 \nabla p + C_3 \nabla T \quad (2)$$

where c_1 , c_2 , c_3 are the weights specified by the user such that $c_1 + c_2 + c_3 = 1$. The deviation function is a vector, and this allows directional splitting of cells as against isotropic splitting. The deviation functions such as ∇p are generated by SCISEAL at the end of each run which are then fed to the adaptor for the next refinement. The grid can be refined or coarsened by specifying a maximum number of cells desired in the adapted grid. Coarsening of the grid can be done at best up to the original coarse or root grid.

To illustrate the use of the adaptor and the grid refinement/clustering process, a pair of turbine disc cavities from the Allison T-56 engine was considered (see Ref. 14) The problem definition and the boundary conditions are shown in Figure 2. The startup grid for the problem is shown in Figure 3a. This grid has approximately 1200 cells. An earlier structured grid solu-

tions[14] used about 8000 cells for this 2-D geometry. Using the above defined error vector with c1 and c3 as the two major contributors, the original grid was successively refined. This involved running SCISEAL on a new grid to partially converge the solution, obtaining the error distribution, and then adapting and refining the grid based on this error distribution. The demonstration calculation was arbitrarily stopped at a grid size of 5000 cells. The initial and final grids as well as two intermediate grid are shown in Figures 3a-3d. The resulting temperature and streamline field on the finest grid are shown in Figure 4a and 4b. These results are in qualitative agreement with the structured grid solutions obtained in [13]; quantitative comparisons will be done by integration of flow quantities at selected locations, using an appropriate post-processor.

As seen in Figures 3a-3d, the grid refinement takes place in the areas with high gradients of the flow quantities specified in the Error function. Form of this error function as well as the actual variables used in its definition can change depending on the problem type and flow physics encountered. The present error function may not be the best suited for this problem and may need to be modified to include gradients of other flow variables, e.g. density, mach number, which are relevant to compressible flows.

COUPLING INTERFACE METHODOLOGY

During a typical run the two codes will be running on one or more machines, while an additional set of routines has been developed that will perform the interfacing of the two codes for the coupling of primary and secondary streams. The overall execution flow chart for the parallel, coupled execution is shown in Figure 5. As seen, the interfacing routines need to perform several functions outlined below:

1. Initial data preparation in each of the two codes for exchange with the other code. This preparation includes information of the grids, flow variables and fluxes.
2. During the solution process, the interface routine checks for the execution status of each of the codes to assess whether the two codes are at appropriate stage to exchange data.
3. Preparation of the data in both codes for interpolation and exchange. This involves storing appropriate type of data from appropriate grid locations in each of the codes.
4. Interpolation of the data from grids in one code to the grids in the other code. The grid data are exchanged and prepared in format needed for inter-

polarization routines. The grid topology and type (structured, unstructured) are taken into account during the interpolation.

5. Actual exchange of the interface data: this is done at present through disk file that are written out from each of the codes. Writing of the data is keyed to some flag files that indicate whether the earlier data sets have been used by the other code or not. If not the interpolation routine waits till the other code is ready. The data transfer can be done through direct exchange of data through message passing rather than through disk files.
6. Check of the data that has been read in each code, and placing the data from temporary locations to the appropriate storage locations for use by the code in the next iteration. This part becomes important during boundary condition implementation in each of the codes where the interfaces are placed

The interface itself consists of three separate units: A set of routines associated with MS-TURBO that assemble the grids and interface variable information, a set with SCISEAL to perform the same function in SCISEAL, and a separate code that is used to perform interpolation of variables/fluxes from one code to the other in item 4 above, and which is called from both codes.

Formulation of Interface Methodology

Several issues needed to be resolved during the formulation of the interfacing routines. Some of these are discussed below, together with the current formulations that have been used.

1. Differences in code formulations: This is by far the most important issue one faces when coupling two codes. Some of the differences to be noted are:
 - A. The TURBO code is a density-based code with an implicit, coupled equation solution method. The SCISEAL code is pressure-based, and uses a sequential equation solution method.
 - B. Cell face convective fluxes in TURBO are based on the flux-difference splitting method, while the fluxes in SCISEAL are calculated as a product of the convection multiplied by an appropriate flow variable.
 - C. Subiterations in each of the time step is a necessary requirement for the SCISEAL code due to the sequential equation method. TURBO code, on the other hand, can be used to directly march in time without subiterations. The code,

though, has subiterations to improve time accuracy.

Given these differences, it is obvious that the data exchange had to be in such a way as to avoid conflicting demands from the two codes, e.g. insisting that the cell face fluxes at the interface be calculated independently from the two codes and somehow be reconciled. It is essential, however, to ensure that the interface flux conservation is maintained at all times. To achieve this the current interface formulation does following exchange:

- a. Variable values from SCISEAL at the cell layer next to the interface are interpolated from the SCISEAL grid to the TURBO grid. These variables are used by the TURBO code in a phantom layer to calculate the fluxes at the boundary.
 - b. The fluxes calculated by the TURBO code then are interpolated to the SCISEAL grid and passed back to SCISEAL where they are imposed directly on the boundary cell faces as flux boundary conditions. Thus, the fluxes at the interfaces are always balanced, without any conflicts.
 - c. SCISEAL needs face fluxes of the turbulence quantities k and ϵ when there is flow from the TURBO code to SCISEAL code. These are not available from the TURBO code and need to be calculated locally in SCISEAL. This is done using the convective fluxes from TURBO code and extrapolated values of k and ϵ from SCISEAL.
2. Level of linking of the data sets: This refers to the level at which the two codes exchange data. One possibility is at the end of each time-step. This is a fairly loose coupling and may not be sufficient. At present the data exchange is planned to be done after every subiteration during the time stepping procedure. With a sufficiently large number of subiterations in each code, this coupling is expected to be sufficiently implicit to provide a stable algorithm and maintain accuracy.
 3. Matching of the execution times: This is a result of different methodologies and different grid sizes that are expected to be employed. The readiness of each code to receive and write data to the other code is keyed on existence of several flag and data files.
 4. Interpolation algorithm: At each data exchange, the data from one code have to be interpolated to the

grid from the other code, and an accurate, robust interpolation algorithm is needed. At present the algorithm in place uses local cell center values and gradients to interpolate data from one grid to another. Global flux conservation is not implicit in the algorithm and has to be ensured after the fluxes from TURBO have been interpolated. This procedure will be replaced with an algorithm based on a conservative scheme where one grid is projected onto the other and actual area intersections are found to facilitate interpolation. This algorithm conserves fluxes implicitly.

PRESENT STATUS AND PLANS

At present all of the coding is completed and debugging runs are in progress. The completed module will be validated using steady and unsteady data from the UTRC high-pressure turbine stage rig which is being tested at UTRC. A schematic of the overall rig is shown in Figure 6. The arrangement of the rotor and starter rows and the associated disc cavity and rim and labyrinth seals in the rig is shown in Figure 7. This rig will provide high quality experimental data for the time-transient interaction of the mainpath and cavity flows. The interaction will be simulated using the coupled code and compared with the experiments. Additional cases for validation will be sought and used as available. Near future plans also include development of a graphical user interface (GUI) that will provide capabilities of easy grid generation and problem setup. The GUI will also provide controls during code execution and provide the capability of code coupling through direct information exchange rather than through disc files.

SUMMARY

A method to perform parallel, coupled time-accurate simulations of the secondary and primary flowpaths has been proposed and currently being developed. The methodology involves use of two different codes, developed specially for the two different flowstreams, will be used to treat the flows in the respective streams. The mainpath flow will be treated using MS-TURBO, which uses a deforming/clicking grid zone to couple multiple blade rows and provide time-accurate solutions of the mainpath. The secondary flow stream will be treated by SCISEAL, a code developed for the turbulent flow and heat transfer in this stream. The code has unstructured/adaptive Cartesian grid capability which will be particularly useful in treatment of complex cavity shapes. A grid adaptor has been developed for grid refinement/redistribution for optimal grid usage in the secondary path. An interpolation algorithm has been developed to

couple the two codes during execution and to provide the coupling between the two flowpaths. This is the first time such a comprehensive methodology has been proposed for primary and secondary flow coupling, and with the drive for ever increasing power and efficiency from modern gas turbine engines, the developed codes can be expected to become very useful in the design and performance evaluation process of modern gas turbines.

ACKNOWLEDGMENTS

This work was supported under NASA Contract NAS3-27392, with R.C. Hendricks and B.M. Steinetz as the Program Monitors. This support is greatly appreciated. Thanks are due to Drs. Jayent Sabnis and R. Johnston of UTRC for providing the UTRC rig figures.

REFERENCES

- Owen, J.M., and Pincombe, J.R., "Velocity Measurements Inside a Rotating Cylindrical Cavity with a Radial Outflow of Fluid," *J. Fluid Mechanics*, Vol. 99, p. 111, 1980.
- Gan, X., Kilic, M., and Owen, J.M., "Flow Between Counterrotating Disks," *J. Turbomachinery*, Vol. 117, pp.298-305, 1995.
- Northrop, A., and Owen, J.M., "Heat-Transfer Measurements in Rotating Disc Systems, Part 2: The Rotating Cavity with a Radial Outflow of Cooling Air," *Int. J. Heat and Fluid Flow*, Vol.9, pp.27-36, 1988.
- Owen, J.M., Pincombe, J.R., and Rogers, R.H., "Source-Sink Flow Inside a Rotating Cylindrical Cavity," *J. Fluid Mechanics*, Vol. 156, pp.233-265, 1985.
- Chew, J.W., and Rogers, R.H., "An Integral Method for the Calculation of Turbulent Forced Convection in a Rotating Cavity with Radial Outflow," *Int. J. Heat and Fluid Flow*, Vol. 9, pp.37, 1988.
- Johnson, B.V., Daniels, W.A., Kaweki, E.J., and Martin, R.J., "Compressor Drum Aerodynamic Experiments with Coolant Injected at Selected Locations," *J. Turbomachinery*, Vol. 113, pp.272-280, 1991.
- Graber, D.J., Daniels, W.A., and Johnson, B.V., "Disk Pumping Test," AFWAL-TR-87-2050, 1987.
- Chew, J.W., "A Theoretical Study of Ingress for Shrouded Disc Systems with Radial Outflow," ASME-89-GT-178, ASME Gas Turbine and Aeroengine Expo., Toronto, Canada, 1989.
- Chew, J.W., "Predictions of Flow in Rotating Disk Systems Using the k- ϵ Turbulence Model," ASME-88-GT-229, ASME Gas Turbine and Aeroengine Expo., Amsterdam, The Netherlands, 1988.
- Ko, S.H., and Rhode, D.L., "Thermal Details in a Rotor-Stator Cavity at Engine Conditions with a Mainstream," ASME-91-GT-275, ASME Gas Turbine and Aeroengine Expo., Orlando, FL, 1991.
- Athavale, M.M., Przekwas, A.J., and Hendricks, R.C., "A Numerical Study of the Flow-Field in Enclosed Turbine Disk-Cavities in Gas Turbine Engines," ISROMAC-4, Honolulu, HI, 1992.
- Przekwas, A.J., Athavale, M.M., and Hendricks, R.C., "Progress in Advanced Modeling of Turbine Engine Seal Flows," AIAA-94-2803, AIAA Joint Propulsion Conference, Indianapolis, IN, 1994.
- Heidegger, N.J., Hall, E.J., and Delaney, R.A., "Parameterized Study of High-Speed Compressor Seal Cavity Flow," AIAA-96-2807, 32nd AIAA Joint Propulsion Conference, Lake Buena Vista, FL, 1996.
- Athavale, M.M., Ho, Y.H., Forry, J.M., Munson, J.H., Hendricks, R.C., and Steinetz, B.M., "Simulation of Secondary Flow in Gas Turbine Disc Cavities and Interaction with Main Flow Path," AIAA-95-2620, AIAA Joint Propulsion Conference, July 1995, San Diego, CA.
- Virr, G.P., Chew, J.W., and Coupland, J., "Application of Computational Fluid Dynamics to Turbine Disc Cavities," *J. Turbomachinery*, Vol.116, pp.701-708, 1994.
- Athavale M.M., Przekwas, A.J., Hendricks, R.C., and Steinetz, B.M., "Numerical Analysis of Intra-Cavity and Power-Stream Flow Interaction in Multiple Gas-Turbine Disk-Cavities," ASME-95-GT-325, ASME Gas Turbine and Aeroengine Expo., Houston, TX, 1995.
- Ho, Y.H., Athavale, M.M., Forry, J.M., Hendricks, R.C., and Steinetz, B.M., "Numerical Simulation of Secondary Flow in Gas Turbine Disc Cavities, Including Conjugate Heat Transfer," ASME Paper 96-GT-67, ASME Gas Turbine and Aeroengine Expo., June 1996, Birmingham, UK.
- Janus, J.M., and Horstman, H.Z., "Unsteady Flow-field Simulation of Ducted Prop-fan Configurations," AIAA-92-0521, AIAA Aerospace Sciences Meeting, Reno, NV, 1992.
- Janus, J.M., and Whitfield, D.L., "Counterrotating Prop-Fan Simulations Which Feature a Relative-Motion Multiblock Grid Decomposition Enabling Arbitrary Time-Steps," AIAA-90-687, AIAA Aerospace Sciences Meeting, Reno, NV, 1990.
- Athavale M.M., Przekwas, A.J., Hendricks, R.C., and Liang, A., "SCISEAL-A Three-Dimensional CFD Code for Accurate Analyses of Fluid Flows and Forces in Seals," Conference on Advanced Earth-to-Orbit Propulsion Technology, May 1992.

21. Athavale, M.M., Jiang, Y., and Przekwas, A.J.,
“Application of an Unstructured Grid Solution
Methodology to Turbomachinery Flows,” AIAA-

95-0174, AIAA Aerospace Sciences Meeting,
Reno, NV, 1995.

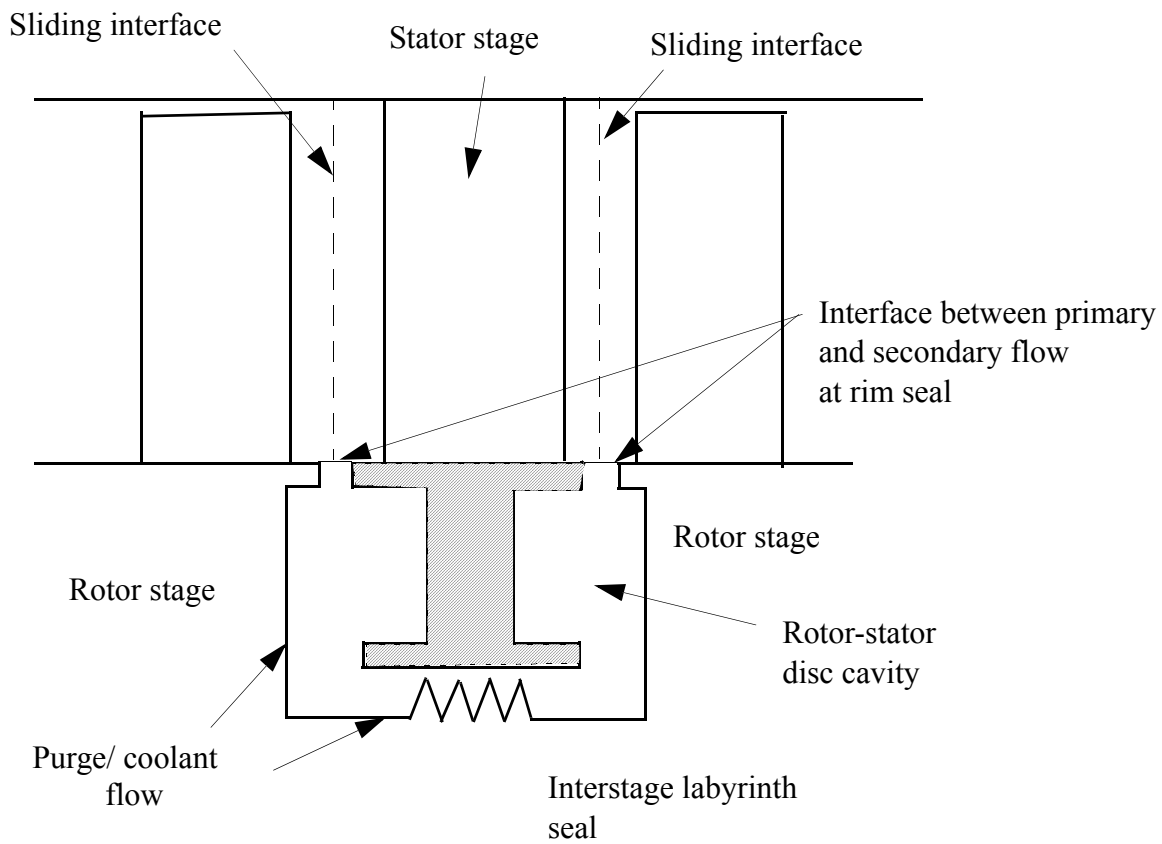


Figure 1 Schematic of a Typical Interstage Cavity in a Turbine Section with Interfaces of Interest

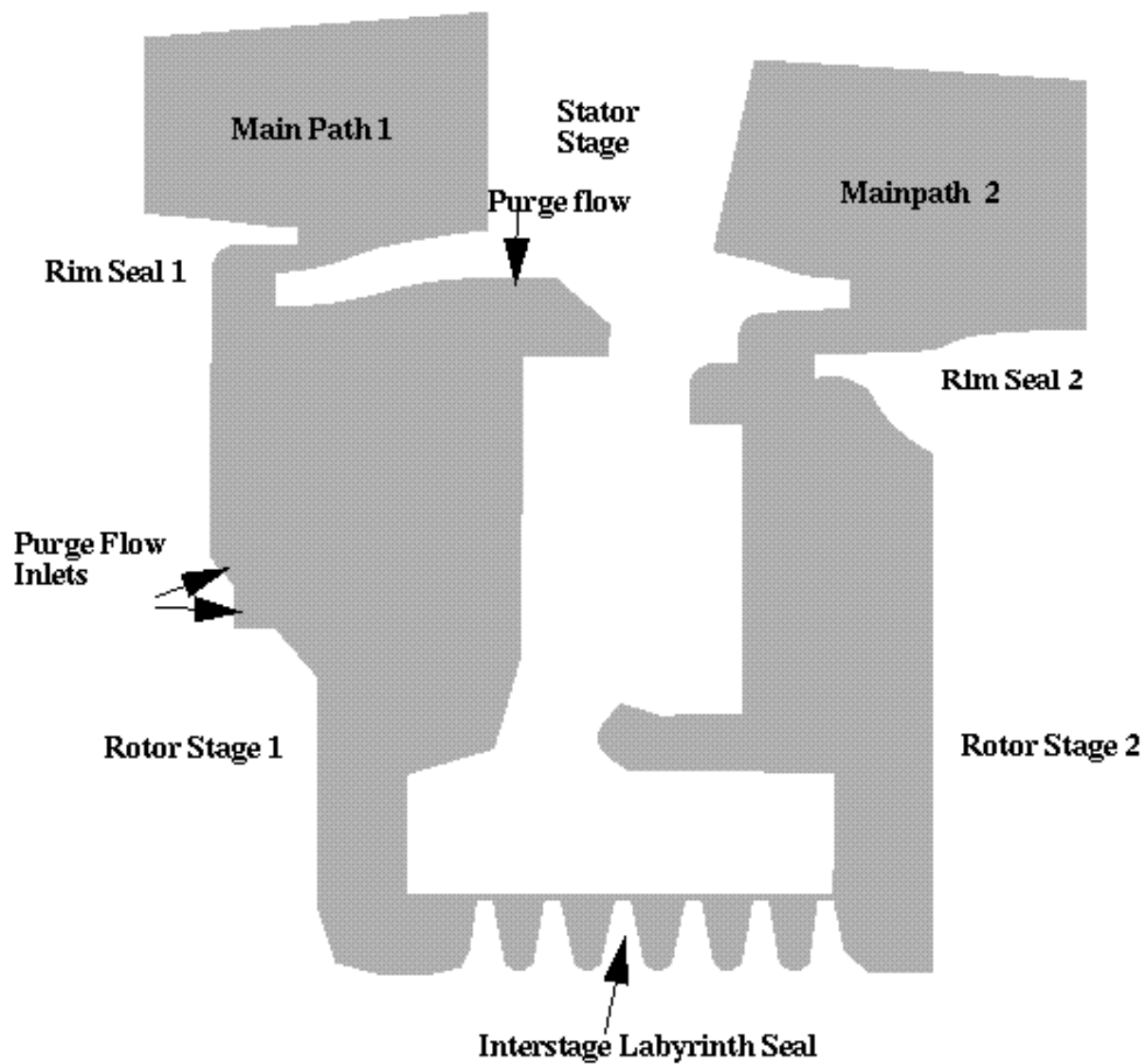
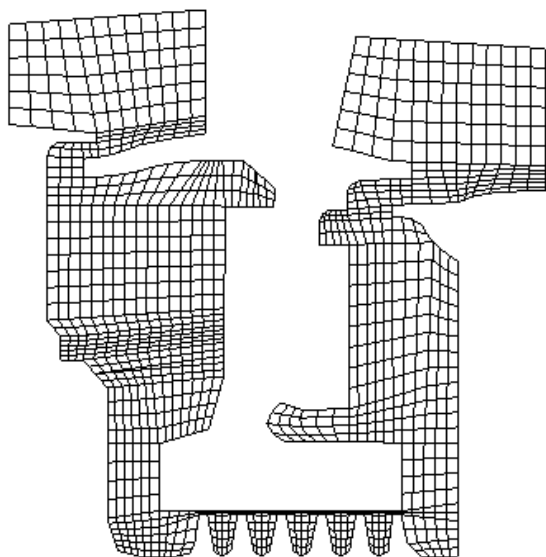
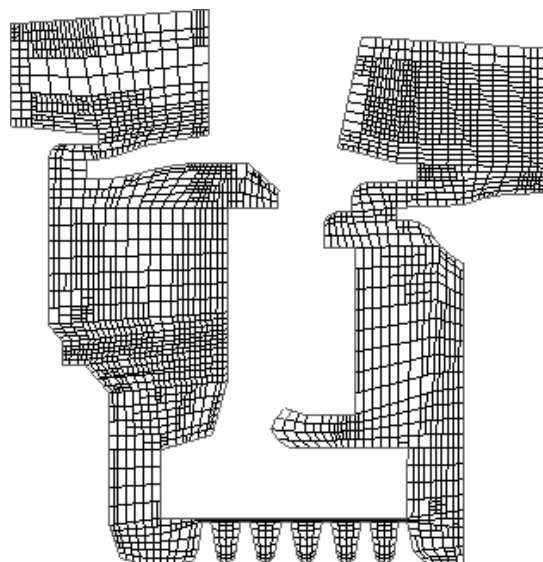


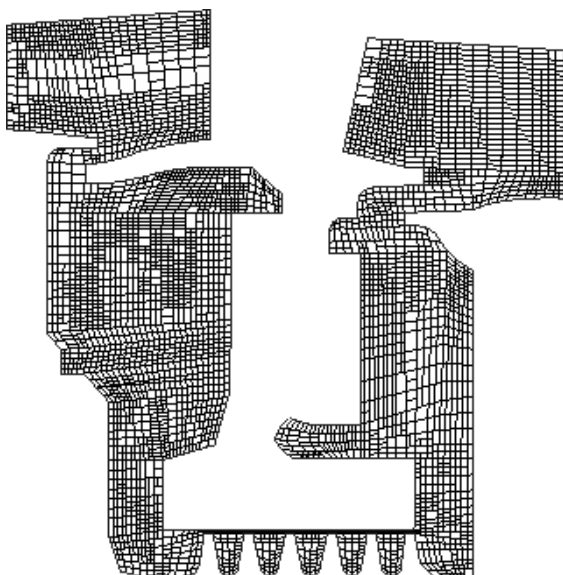
Figure 2. Flow Domain and Conditions for the Allison T56 Stage 1-2 Disc Cavity with Interstage Labyrinth Seal



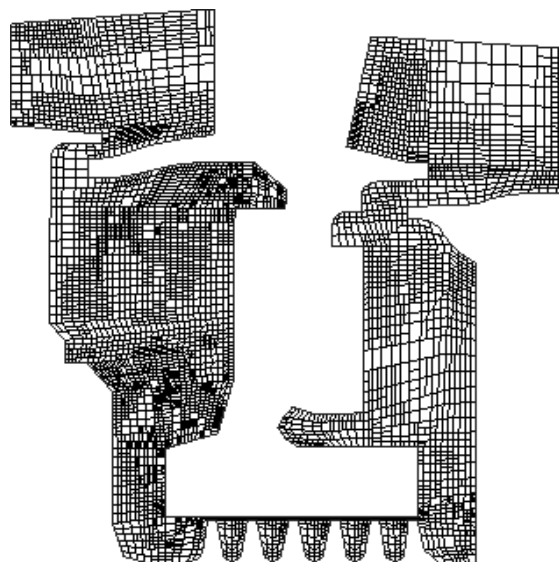
(a) Root Grid, 1180 Cells



(b) Adapted Grid, 2500 Cells

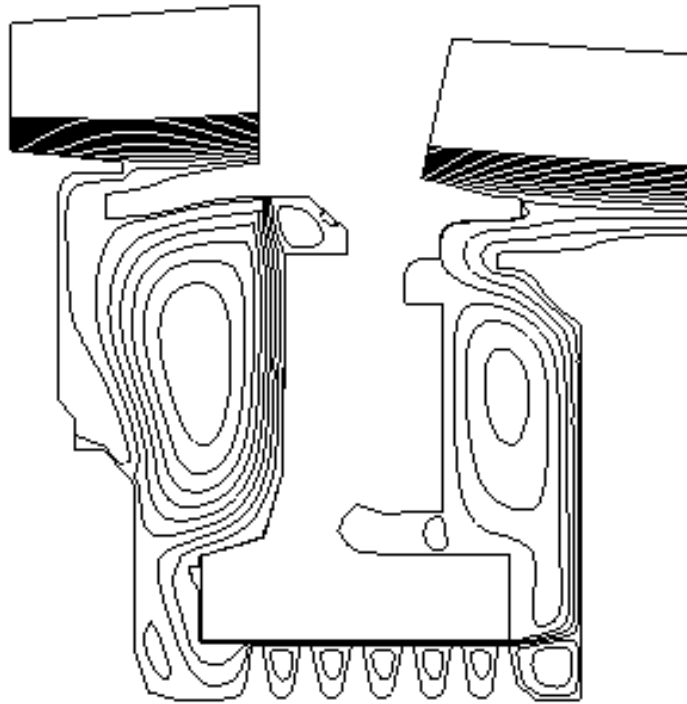


(c) Adapted Grid, 4000 Cells

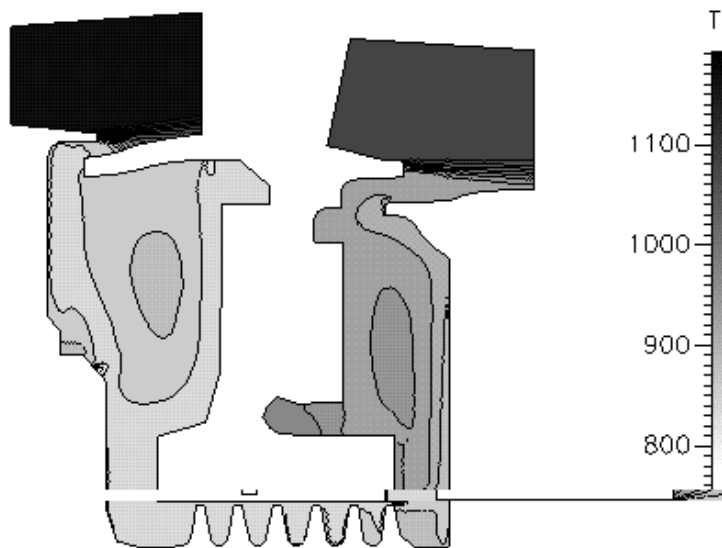


(d) Adapted Grid, 5000 Cells

Figure 3. Computational Grids for the Cavity Problem at Various Levels of Refinement



(a) Streamline Plot (Lines in the Mainpath Have Been Supressed). Note Outgoing Flow in Both Rim Seals



(b) Temperature Field in the Cavity

Figure 4. Cavity Solutions on the 5000 Cell Grid

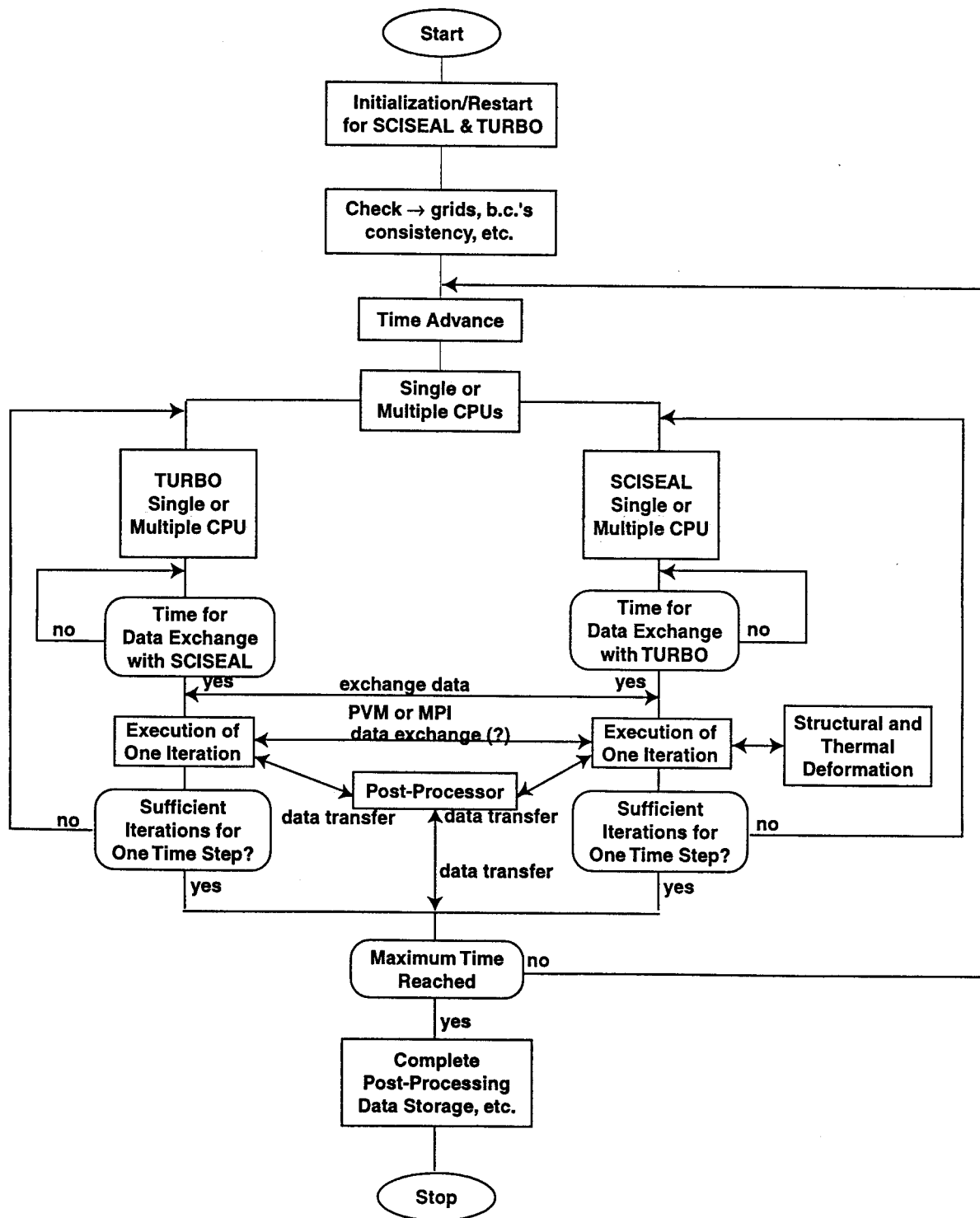


Figure 5. Flowchart for the Coupled Execution of SCISEAL and MS-TVRBO Codes

CROSS-SECTION OF RIM SEAL INGESTION RIG

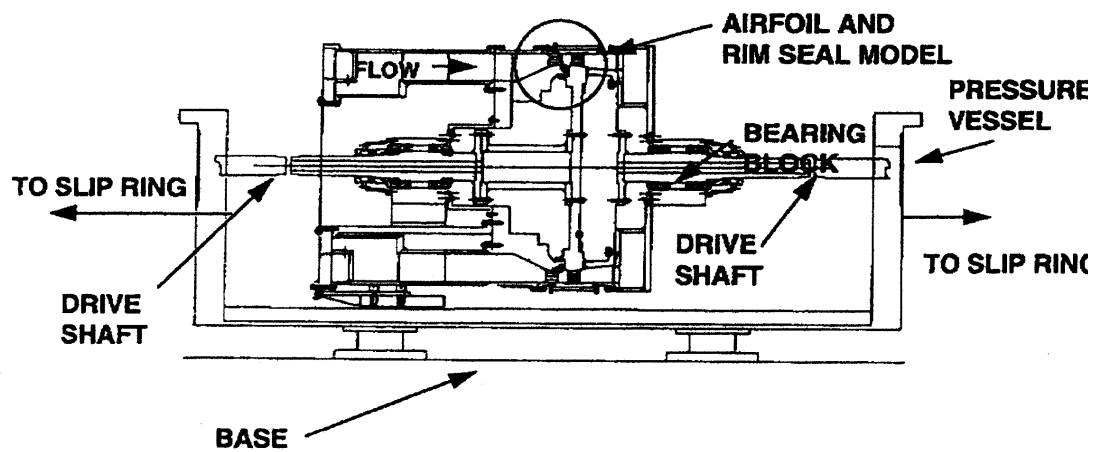


Figure 6. Cross Section of the Rim Seal Ingestion Rig

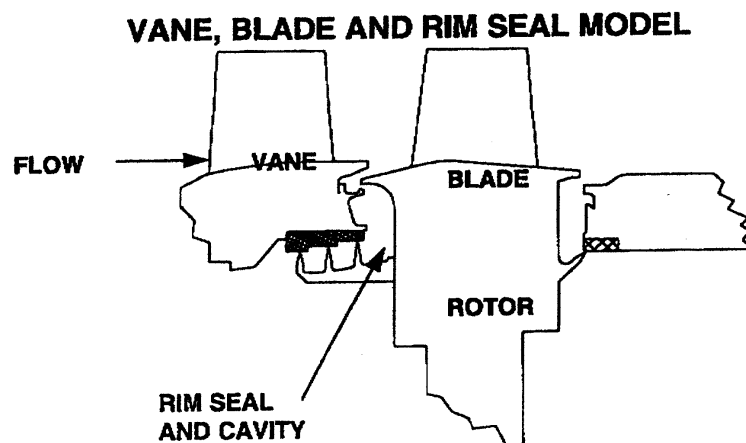


Figure 7. Details of the Stator and Rotor with Associated Cavity, Rim and Labyrinth Seals



AIAA-98-3285

Analysis and Full Scale Testing of an Aspirating Face Seal with Improved Flow Isolation

N.A. Turnquist
General Electric Corporate Research and Development
Niskayuna, NY

T.W. Tseng
General Electric Aircraft Engines
Cincinnati, OH

A.D. McNickle, J.T. Dierkes
Stein Seal Co
Kulpsville, PA

M. Athavale
CFD Research Corporation
Huntsville, AL

B.M. Steinetz
NASA Lewis Research Center
Cleveland, OH

**34th AIAA/ASME/SAE/ASEE
Joint Propulsion Conference
July 13-15, 1998 / Cleveland, OH**

For permission to copy or publish, contact the American Institute of Aeronautics and Astronautics
1801 Alexander Bell Drive, Suite 500, Reston, VA 22091

ANALYSIS AND FULL SCALE TESTING OF AN ASPIRATING FACE SEAL WITH IMPROVED FLOW ISOLATION

Norman A. Turnquist
General Electric Corporate Research and Development
Niskayuna, NY

Alan McNickle, Joan Dierkes
Stein Seal Co.
Kulpsville, PA

Tom Tseng
General Electric Aircraft Engines
Cincinnati, OH

Mahesh Athavale
CFD Research Corporation
Huntsville, AL

Bruce Steinetz
NASA Lewis Research Center
Cleveland, OH

Abstract

An enhanced aspirating face seal is being evaluated as a possible replacement for labyrinth seals in aircraft engines for reduced leakage and improved engine efficiency. A 36" diameter aspirating seal, designed to fit in the GE90 engine, has undergone dynamic testing in a rig designed to mimic the pressure, rotor speed, rotor runout, and seal tilt conditions expected in actual service. Seal/rotor axial clearances, as well as leakage rates, are monitored during testing. To date, tests have been conducted at pressures as high as 100 psid and rotor speeds of up to 2400 RPM, with a rotor axial runout as great as 0.010" TIR. Results indicate that by isolating the seal air dam flow from the hydrostatic bearing flow, a 0.0015"-0.003" seal/rotor air gap is formed, with consistently low leakage rates. The results of 3-D Computational Fluid Dynamics (CFD) analyses support the test results, and underscore the importance of flow isolation with respect to seal performance. This paper covers the following: the full scale test facility, the test plan, test results for the original seal, analytical results, test

results for the enhanced seal, and future plans.

Introduction

Conventional labyrinth seals are typically designed with a rotor radial clearance that increases proportionally with diameter¹. Aspirating face seals, as described by Hwang², are non-contacting seals that are designed to establish an equilibrium position within close proximity (typically 0.0015"-0.003") of the rotor surface regardless of the seal diameter. As such, they have a potentially significant performance advantage over conventional labyrinth seals, particularly at large diameters. In addition, aspirating seals are inherently not prone to wear, owing to their non-contacting nature, so their performance is not expected to degrade over time. A 36" diameter aspirating seal, for application to the GE90 low pressure aft outer seal location, was designed and fabricated by the Stein Seal Company^{2,3}. A cross-section of the seal design, enhanced by the presence of a flow deflector on the rotor face, is shown in Fig. 1, and major seal components are listed in Table 1. A test plan has been

established to evaluate seal performance under a variety of conditions that the seal would be subjected to in the GE90 aircraft engine application. The tests are being executed on a full scale rotary test rig, and analyses have been performed using 3-D Computational Fluid Dynamics (CFD) in order to validate test results. This paper focuses on test results for the original seal design, analytical validation of the test results and use of CFD analysis to evaluate an enhanced design, and test results for the enhanced seal/rotor configuration.

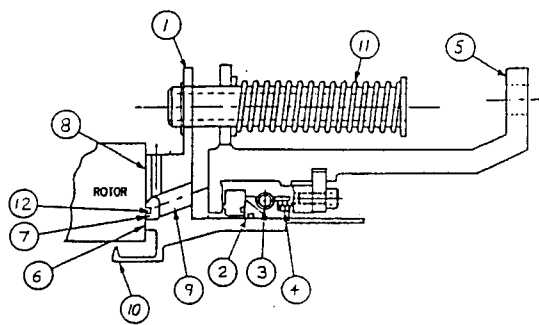


Figure 1 Cross section of the enhanced 36" diameter aspirating face seal

1	Primary face seal ring
2	Secondary piston ring
3	Radial garter spring
4	Axial compression springs
5	Seal housing
6	Primary seal dam
7	Vent Groove
8	Hydrostatic gas bearing surface
9	Vent slots
10	Aspirator tooth
11	Retraction coil springs
12	Flow Deflector (enhanced seal only)

Table 1 Aspirating face seal components

The Test Facility

The full scale test rig was originally designed for testing 50" diameter brush seals and has been modified to test the 36" diameter aspirating seal. The assembled rig cross-section with the installed aspirating seal consists primarily of a pressure vessel built around a 36" diameter rotor, as shown in Fig 2. In order to balance thrust forces on the rotor, a 36" diameter brush seal is used on the side of the rotor opposite the aspirating seal. The rig configuration is such that air enters radially inward of both seals, and exits radially outward to an exhaust plenum that is common to both seals. The rig is capable of testing at pressures up to 100 psid, and speeds up to 2400 RPM.

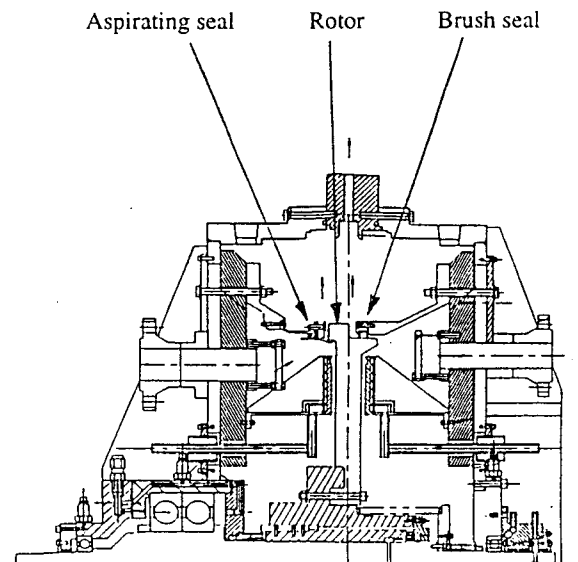


Figure 2 The Full Scale Test Rig

At pressures less than 15 psig, the rotor thrust force is reduced sufficiently to enable static testing with the brush seal half of the pressure vessel completely removed. With this arrangement, seal movement during closure can be visually observed, air gap measurements can be

taken with feeler gauges, and the seal can be manually perturbed from its equilibrium position. Static tests run at low pressures with this configuration have proven to be good indicators of seal behavior at elevated pressures with rotation.

In order to monitor the seal/rotor clearance during closed vessel testing, two axial proximity probes have been mounted to the seal, approximately 90 degrees apart. The probes provide a direct measurement of the air gap between the face of the aspirating seal and the adjacent rotor sealing surface. Also, in order to ensure that the seal is operating reliably and repeatably prior to rotation, the aspirating seal has been electrically isolated from the rig and equipped with six electrical contact probes, equally spaced around the perimeter of the seal. These probes, like the axial proximity probes, are mounted to the outer flange of the aspirating seal itself. The probe tips are set to contact the rotor when the aspirating seal face is <0.001 " from the rotor surface, and trigger an audible alarm when contact occurs.

To evaluate seal performance in the presence of a 1/rev. axial rotor runout, the rotor face itself is machined with the desired runout of 0.000", 0.005" or 0.010".

Finally, the rig can be configured with the aspirating seal mounted on a tilting mechanism that provides angular seal misalignment up to ± 0.27 degrees. The entire seal assembly is tilted relative to the rotor, mimicking the relative seal/rotor orientation during maneuvering.

The Test Plan

The complete test plan is designed to evaluate the aspirating seal's performance

while subjected to the effects that it will be exposed to during operation in the GE90 engine. These include ground idle, take-off, cruise with and without rotor runout, and hard maneuvers that induce relative seal/rotor tilt. The complete test plan is described by Wolfe *et al*¹. All tests, with the exception of the dust ingestion test, are performed on the full scale prototype seal. Briefly, the test program consists of the following: a.) Dust ingestion test, performed on a 14.7" diameter seal to evaluate the effect of dust particles on seal leakage; b.) Static leakage test, to measure leakage at pressure differentials as high as 100 psid; c.) Tracking test, to evaluate the seal's ability to track the rotor during axial excursions; d.) Dynamic leakage test, to evaluate seal performance under rotation, at speeds up to 2400 RPM; e.) Rotor runout test, to determine the effect of axial rotor runouts of 0.000", 0.005", and 0.010"; f.) Seal tilt test, to evaluate the seal's ability to track the rotor as it is tilted 0.27 degrees, with and without rotation.

Test Results for the Original Seal/Rotor Configuration

Results of the dust ingestion test, as well as the static leakage and tracking tests on the original seal, are described by Wolfe *et al*¹. The dust ingestion test was conducted by the Stein Seal Company, and completed on a 14.7" diameter seal. In its original configuration, the seal/rotor geometry is as shown in Fig. 3. Note the absence of any obstructions to radial flow between the seal dam and the air bearing.

A seal/rotor rub incident during full scale dynamic leakage testing resulted in a "wiped" seal and rotor. Subsequent testing of the reworked seal revealed the behavior described by Turnquist *et al*⁴. Seal closure occurred at a pressure differential

of 2-3 psid. Seal/rotor clearance was 0.016", with a leakage rate of 1.37 lbm/s at a pressure differential of only 10.3 psid. Open vessel tests were conducted at low pressures to visually observe seal behavior and manually check seal clearances around its circumference. During these tests, the seal was manually pulled closer to the rotor and pushed further away. In both cases, the seal returned to its equilibrium position, re-establishing a uniform, 0.016" equilibrium clearance with the rotor.

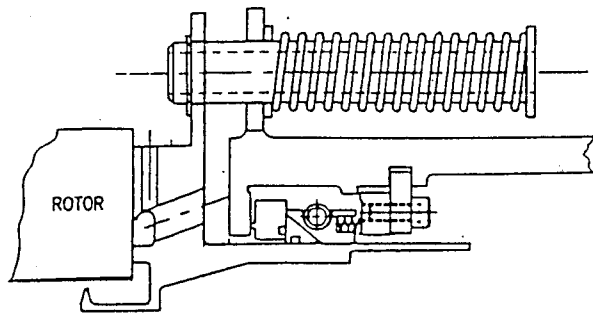


Figure 3 Original Seal/Rotor geometry

A number of seal parameters were varied in an effort to determine the cause of the large air gap, including the number of open orifice holes in the seal face, the axial travel distance to closure, the number and stiffness of the return springs, and the labyrinth tooth clearance. It was shown that varying the travel to closure from 0.125" to 0.020" has no significant effect on seal behavior, while the return springs' primary function is to ensure uniform seal movement rather than affect the seal's equilibrium position. However, the number of open orifice holes and the total differential pressure across the seal were shown to significantly affect seal equilibrium position and leakage rate, as shown in Figs. 4 and 5. Additionally,

reducing the clearance between the labyrinth tooth and the rotor from 0.085" to 0.050" moves the seal's equilibrium position 0.004" closer to the rotor, to 0.012". This effect was investigated further by reducing the labyrinth tooth clearance to 0.035". In this configuration, the design air gap of 0.0015" was achieved at limited pressure differentials of up to 38 psid, with a corresponding leakage rate of 0.40 lbm/s. However, beyond this pressure differential the seal's equilibrium position shifts sharply to 0.012", with a corresponding increase in leakage. The implication is that the reduced labyrinth seal clearance limits flow to the aspirating seal face, shifting the point at which the seal operates properly to a higher pressure differential. However, relying on a reduced tooth clearance as a means of achieving proper seal operation is unacceptable, since the labyrinth tooth clearance must be sufficient to accommodate expected relative rotor/stator radial movements in the engine.

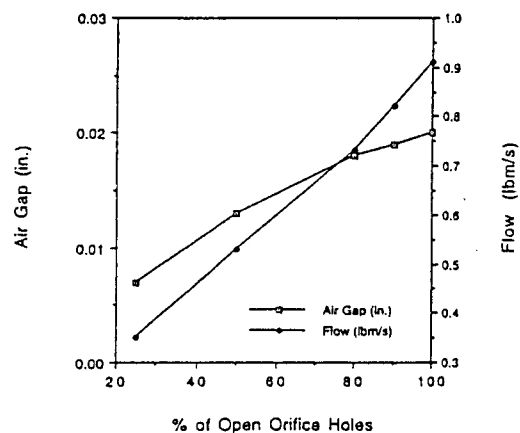


Figure 4 Original Seal/Rotor Air Gap and Leakage vs. % of Open Orifice Holes at 5 psid

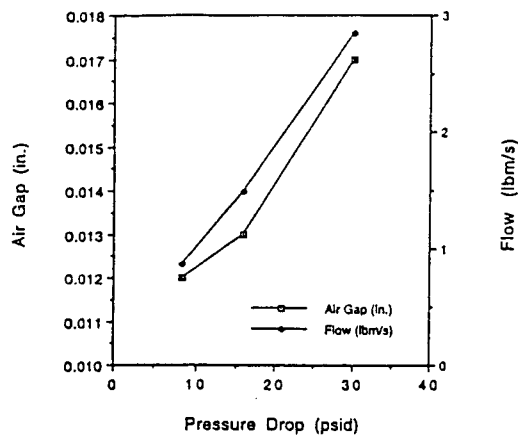


Figure 5 Original Seal/Rotor Air Gap and Leakage vs. Seal Differential Pressure with 50% of Orifice Holes Blocked

Finally, the effect of rotation on the leakage performance of the aspirating seal in its original configuration was investigated. 50% of the seal orifice holes were blocked in an effort to bring the seal reasonably close to the rotor. Rotor speed was gradually increased from 0 RPM to 2400 RPM with the pressure difference across the seal held at 15 psid. Throughout the speed range, the seal/rotor air gap was approximately 0.012"-0.014", indicating that for this magnitude of air gap, rotation has little or no effect on seal behavior, as shown in Fig 6.

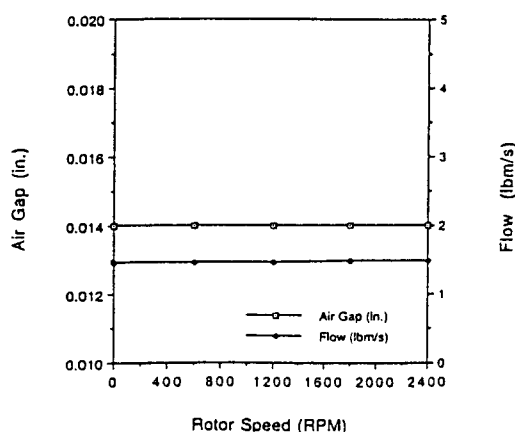


Figure 6 Original Seal/Rotor Air Gap and Leakage vs. Rotational Speed for 15 psid with 50% of Orifice Holes Blocked

The conclusion from this series of tests is that with the seal in its original configuration, flow through the seal generates a pressure force on the seal face in excess of the force required to achieve a 0.001"-0.003" air gap, and limiting the flow through the seal tends to limit these pressure forces.

Analytical Results

An axisymmetric multi-body model of the aspirating seal, described by Bagepalli *et al*⁵, was created in order to analyze the forces acting on the original seal during various steady state and transient operating conditions. This model shows that the seal's equilibrium position is established when the back pressure force pushing the seal toward the rotor is balanced by the film forces at the air bearing and air dam regions, the spring force, and any friction forces. The open vessel tests revealed that the seal's equilibrium position is quite independent of friction, since the seal consistently returned to the same position when it was manually perturbed from equilibrium. Additionally, variation in the stiffness and number of retaining springs resulted in only slight changes in the air gap thickness. Thus, the axisymmetric model supports the conclusion that the equilibrium position of the aspirating seal is primarily influenced by the pressure forces generated at the air bearing face and the air dam.

In order to evaluate the pressure forces created at the air bearing and air dam regions of the seal while capturing the effects of discrete orifice holes in the seal face, 3-D Computational Fluid Dynamics (CFD) analyses were performed for the original seal/rotor geometry. A wire frame of the 3-D model, representing the exact seal geometry as tested, is shown in

Fig. 7. The model includes the discrete orifice hole and axial slot geometry over a 2.5 degree sector of the seal, as well as the effects of compressibility, turbulence, and viscosity.

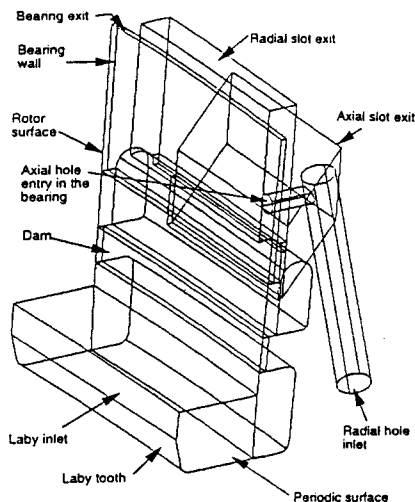


Figure 7 The 3-D CFD model

The seal was analyzed at the measured test conditions of 0.016" clearance and a pressure differential of 7.1 psid, and the forces acting on the seal were shown to be balanced to within 2%. The calculated flow rate of 0.97 lbm/s agrees very well with the measured value of 1.03 lbm/s. Viewing the flow axially, as in Fig. 8, reveals a very limited region in which the flow from the air bearing holes is influential. This flow pattern surrounding the orifice is consistent with that observed on the seal after testing. Note that over the entire arc, there is mixing of the flows from the dam and air bearing regions of the seal, and the strong radial component originating at the dam hinders the formation of a hydrostatic film at the air bearing. The radial flow from the dam slows upon entering the hydrostatic bearing region, resulting in increased pressure at the bearing face as shown in Fig. 9. This increased pressure inhibits the seal's ability to close.

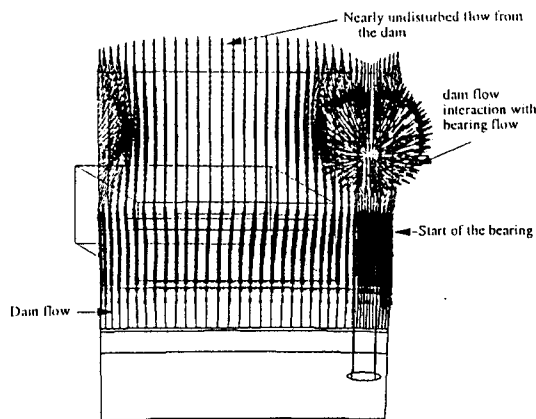


Figure 8 Original Seal/Rotor flow field viewed in the axial direction for 0.016" axial clearance

The analytical results indicate that in its original configuration, the force balance generated at a 0.016" axial clearance will not allow the seal to continue moving closer to the rotor. Flow from the air dam is intended to exit the seal via the seal vent slots. However, the introduction of flow from the dam into the air bearing region of the seal raises the pressure at the air bearing face, limiting seal closure.

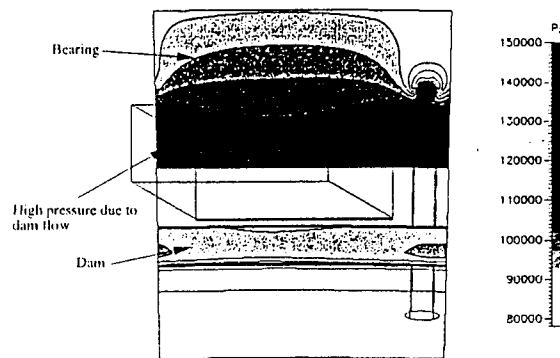


Figure 9 Original Seal/Rotor pressure distribution viewed in the axial direction for 0.016" axial clearance

Please see pages 23 to 26 for better representations of the above figures.

The CFD model was modified to include a “virtual” axial wall extending from the rotor face in the cavity between the air dam and air bearing regions of the seal. This wall, or flow deflector, effectively prevents radial flow leaving the air dam region from entering the air bearing region. Instead, flow from the air dam is forced to exit the seal via the vent slots, and is prevented from influencing the flow from the orifice holes in the air bearing. Fig. 10 shows the flow field for the enhanced seal/rotor configuration, again for a clearance of 0.016” and a pressure differential of 7.1 psid. Note that the flows from the air dam and air bearing regions are completely isolated, with all of the air dam flow exhausting the seal before reaching the air bearing. More importantly, Fig. 11 illustrates the pressure distribution for the case where the flow deflector is present, and reveals reduced pressures acting on the air bearing face in comparison to the original configuration. Integrating the pressure forces for the two configurations shows that the net pressure acting on the air bearing face is increased by >10% when the air dam flow is allowed to influence the air bearing region.

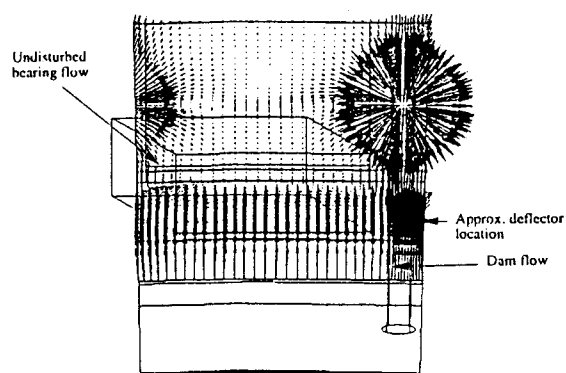


Figure 10 Enhanced Seal/Rotor flow field viewed in the axial direction for 0.016" axial clearance

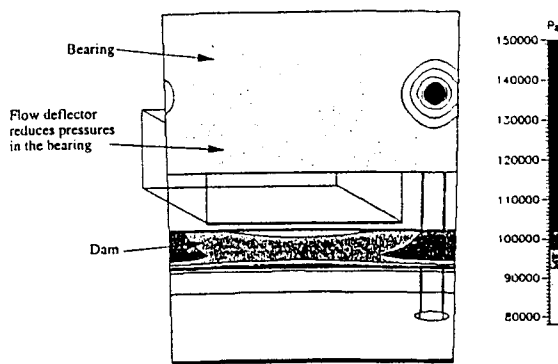


Figure 11 Enhanced Seal/Rotor pressure distribution viewed in the axial direction for 0.016" axial clearance

Based on the CFD results, it is apparent that preventing the air dam radial flow from entering the air bearing region reduces the total pressure within the air bearing, allowing the net force on the seal to draw it closer to the rotor. This can be achieved by modifying the rotor geometry to include an axial protrusion in the region between the air dam and air bearing.

Test Results for the Enhanced Seal/Rotor Configuration

The enhancement modeled in the CFD analysis was put to practice by modifying the existing 36" test rotor. The flow deflector was machined directly onto the rotor face, as shown in Fig. 12. The following is a description of the results of static and dynamic leakage tests for the aspirating seal/rotor configuration employing the flow deflector modification. Before permanently machining the rotor, trial static tests were run at limited pressures, with a temporary flow deflector attached to the rotor face. Only after promising results were obtained

Please see pages 23 to 26 for better representations of the above figures.

from these trials did rotor modification proceed.

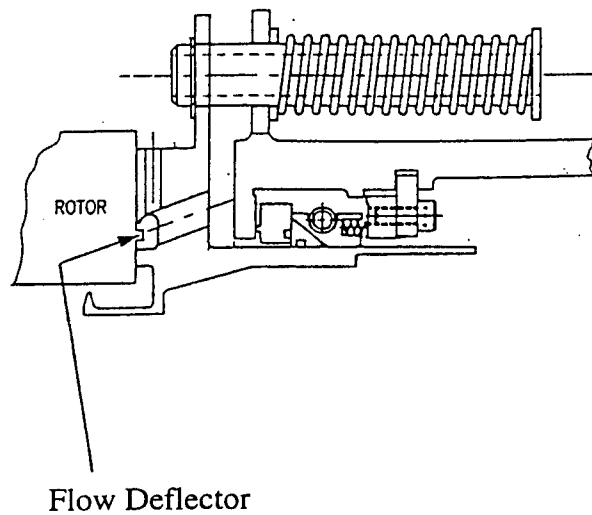


Figure 12 Enhanced Seal/Rotor geometry, showing Radial Flow Deflector

1. 0.000" TIR Rotor Axial Runout:

With an axial rotor runout of 0.000" TIR, leakage data was obtained for the enhanced seal/rotor configuration both statically and with rotation. As with the original configuration, seal closure occurred at a seal differential pressure of 2-3 psid, and seal behavior was reliable and repeatable. Fig. 13 shows leakage as a function of pressure differential both with and without rotation. Fig. 14 shows only the dynamic leakage, along with the speeds at which the data was collected. Note that the rotor speed is increased as the pressure differential is increased, in order to simulate actual engine conditions. Seal/rotor air gap was measured to be 0.001"-0.0015" throughout this test. Post-test inspection of the seal and rotor revealed no evidence of rubbing contact between the two.

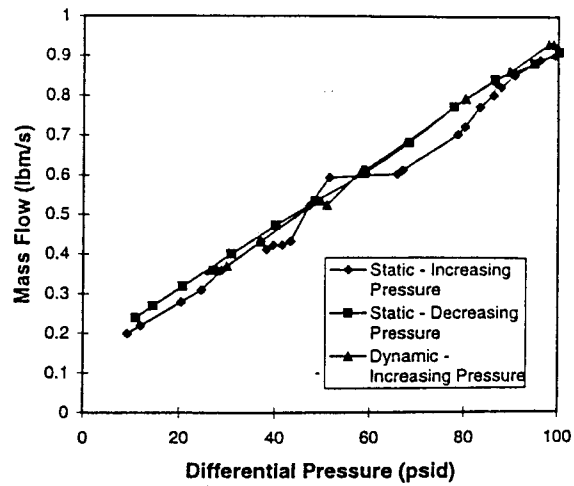


Figure 13 Enhanced Seal/Rotor Static and Dynamic Leakage vs. Pressure Differential with 0.000" TIR

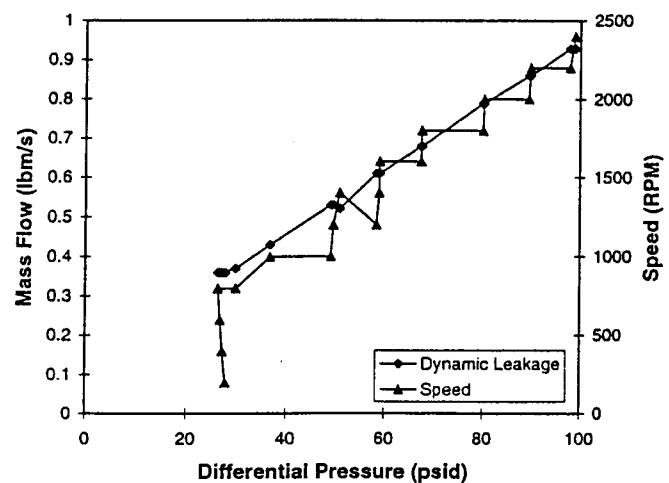


Figure 14 Enhanced seal/rotor Dynamic Leakage and Rotor Speed vs. Pressure Differential with 0.000" TIR

2. 0.005" TIR Rotor Axial Runout:

The test rotor was modified to incorporate a 0.005" TIR axial runout in the rotor face, with the flow deflector modification retained. Again, seal closure occurred at 2-3 psid, and leakage data was obtained both with and without rotation. With the 0.005" runout, leakage is approximately 17% greater than with the 0.000" runout at full pressure and speed, indicating that the waviness of the rotor increases the total leakage area. Fig. 15 shows static leakage as a function of pressure differential, while

Figs. 16 and 17 show dynamic leakage for both increasing and decreasing pressure differentials, respectively.

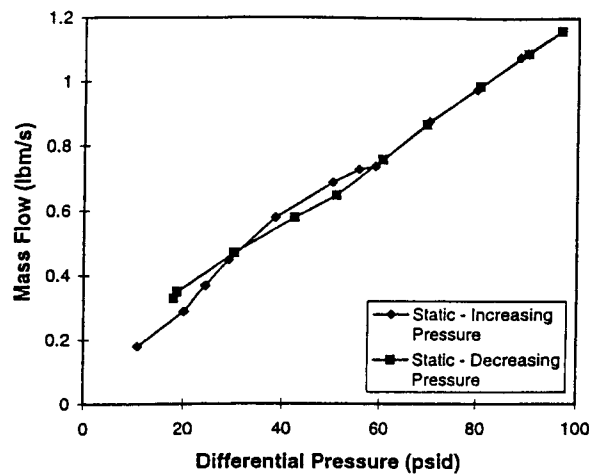


Figure 15 Enhanced Seal/Rotor Static Leakage vs. Pressure Differential with 0.005" TIR

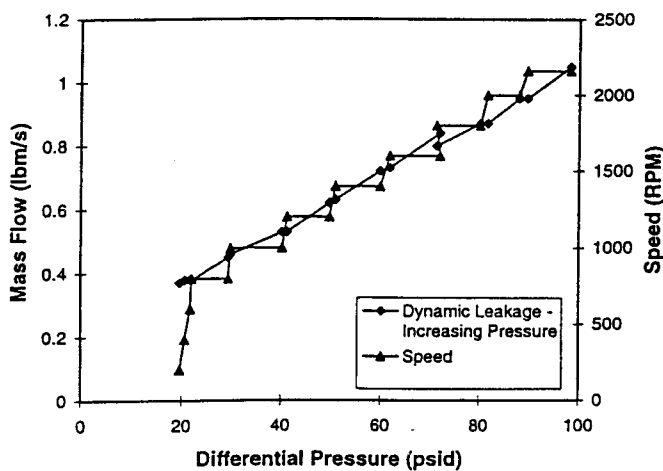


Figure 16 Enhanced Seal/Rotor Dynamic Leakage and Rotor Speed vs. Pressure Differential for increasing Pressure Differential with 0.005" TIR

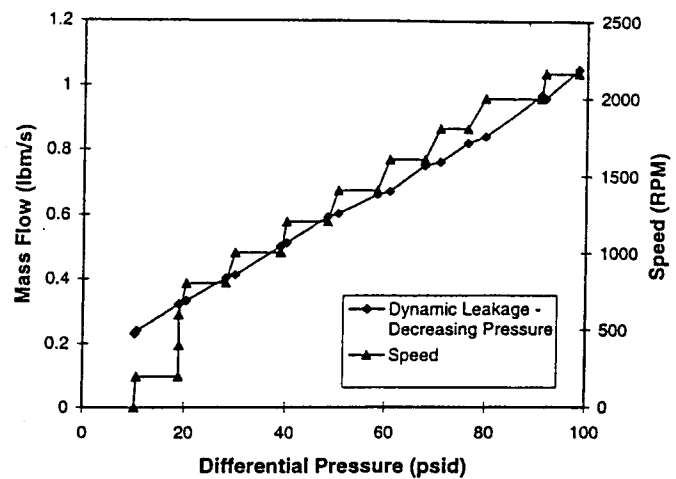


Figure 17 Enhanced Seal/Rotor Dynamic Leakage and Rotor Speed vs. Pressure Differential for Decreasing Pressure Differential with 0.005" TIR

3. 0.010" TIR Rotor Axial Runout:

The 36" test rotor underwent further modification to include a 0.010" TIR axial runout, again retaining the flow deflector between the air dam and air bearing regions of the seal. Static leakage data for this configuration is shown in Fig. 18.

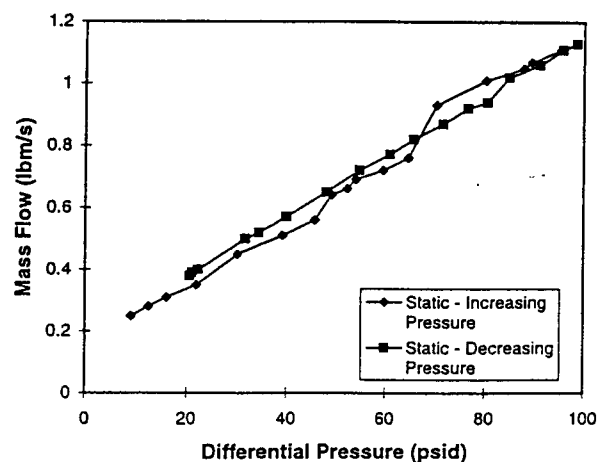


Figure 18 Enhanced Seal/Rotor Static Leakage vs. Pressure Differential with 0.010" TIR

Again, seal closure occurred at 2-3 psid, and seal behavior was repeatable. For the 0.010" runout configuration, Figs. 19 and 20 show dynamic leakage and rotor speed for the cases of increasing and decreasing pressures, respectively.

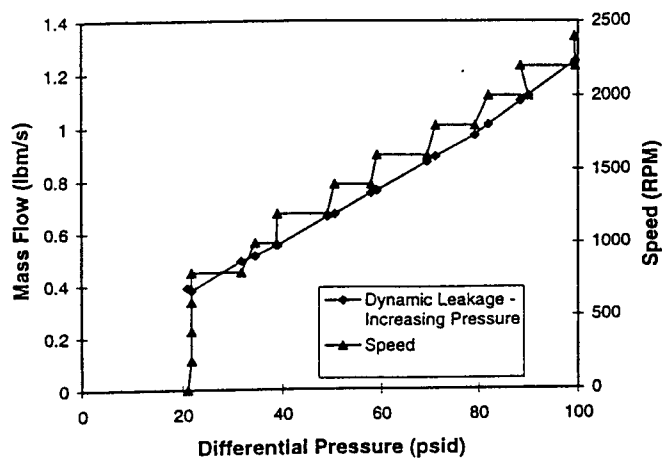


Figure 19 Enhanced Seal/Rotor Dynamic Leakage and Rotor Speed vs. Pressure Differential for increasing Pressure Differential with 0.010" TIR

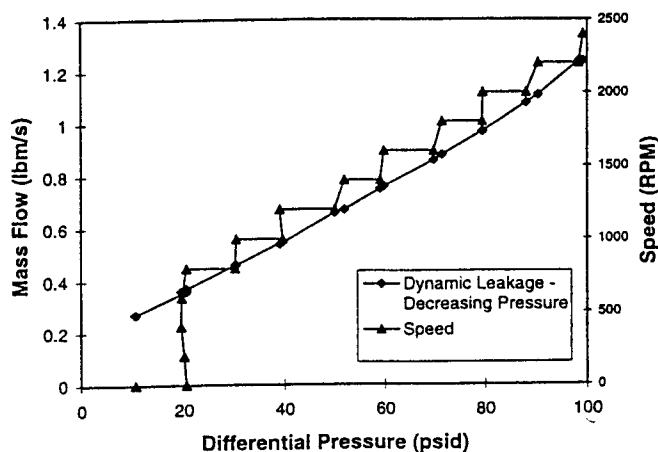


Figure 20 Enhanced Seal/Rotor Dynamic Leakage and Rotor Speed vs. Pressure Differential for decreasing Pressure Differential with 0.010" TIR

Note that with the additional rotor waviness, leakage at full pressure and speed is approximately 33% greater than the 0.000" runout configuration. Fig. 21 summarizes dynamic leakage data for the cases of 0.000", 0.005", and 0.010" TIR rotor runout, respectively, including data obtained both increasing and decreasing the differential pressure across the seal.

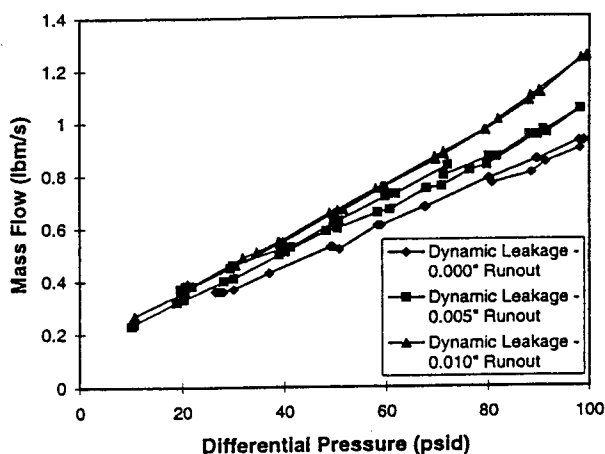


Figure 21 Dynamic Leakage vs. Pressure Differential for 0.000", 0.005", and 0.010" Rotor TIR

Future Plans

Modifications to the full scale test rig are currently underway to permit testing with seal tilt. In the actual engine, the seal remains stationary while the rotor deflects up to $\pm 0.27^\circ$ during maneuvering. However, tests will be conducted for the same relative tilt by pivoting the seal and seal holder, while the rotor axis of rotation remains fixed. This test will be conducted on the seal/rotor configuration with the flow deflector enhancement, with a rotor runout of 0.000" TIR.

In parallel with the testing, CFD analyses are being conducted to evaluate seal

design options that would eliminate the need for the flow deflector. It is hoped that an acceptably robust design can be achieved that does not require the rotor modification associated with the flow deflector. Once an acceptable design is reached, a prototype seal will be fabricated and the test sequence will be repeated for the improved design.

Conclusions

Based on the tests that have been completed to date, along with the analytical work that has been performed using CFD, the following conclusions can be drawn:

1. Mixing of flows from the air dam and air bearing regions of the seal produces excessive pressure within the air bearing region, thereby hindering the formation of a hydrostatic film and limiting seal closure. Isolation of these two flows is crucial to seal performance.
2. As originally designed, the 36" aspirating seal has been shown experimentally to seek an equilibrium clearance of approximately 0.016" to the adjacent rotor surface, and leakage rates are consistent with this clearance.
3. The presence of a flow deflector between the air dam and air bearing regions of the seal effectively forces radial flow from the air dam to exit via the vent slots, allowing a hydrostatic film to form at the air bearing and resulting in a seal/rotor clearance of 0.001"-0.0015", with correspondingly low leakage rates.
4. With the air dam and air bearing flows isolated, the seal performs effectively with rotor runouts as great as 0.010" TIR. When compared to data obtained with 0.000" TIR, the effect of runout is to

increase seal leakage by 15% for 0.005" TIR, and 33% for 0.010" TIR.

5. The 36" aspirating seal shows promise as a potential replacement for labyrinth type seals in aircraft engine applications.

References

1. Wolfe, C.E., Bagepalli, B., Turnquist, N.A., Tseng, T.W., McNickle, A.D., Hwang, M.F., & Steinetz, B.M., "Full Scale Testing and Analytical Validation of an Aspirating Face Seal," AIAA/ASME/SAE/ASEE 32nd Joint Propulsion Conference, Lake Buena Vista, Florida, July 1996.
2. Hwang, M.F., Pope, A.N. & Shucktis, B., "Advanced Seals for Engine Secondary Flowpath," AIAA/ASME/SAE/ASEE 31st Joint Propulsion Conference, San Diego, California, July 1995.
3. Pope, A.N., U.S. Patent No. 5284347, "Gas Bearing Sealing Means," issued February 8, 1994.
4. Turnquist, N.A., Bagepalli, B., Reluzco, G., Wolfe, C.E., Tseng, T.W., McNickle, A.D., Dierkes, J.T., Athavale, M., & Steinetz, B.M., "Aspirating Face Seal Modeling and Full Scale Testing," AIAA/ASME/SAE/ASEE 33rd Joint Propulsion Conference, Seattle, Washington, July, 1997.
5. Bagepalli, B., Imam, I., Wolfe, C.E., Tseng, T., Shapiro, W. & Steinetz, B., "Dynamic Analysis of an Aspirating Seal for Aircraft Engine Application," AIAA/ASME/SAE/ASEE 32nd Joint Propulsion Conference, Lake Buena Vista, Florida, July 1996.

A Computational Study of Turbulent Flow and Heat Transfer in Rotating Disc Cavities

Mahesh M Athavale
N. Vaidya

CFD Research Corporation
3325 Triana Blvd.
Huntsville, AL 35805

Robert C. Hendricks
Bruce M. Steinetz

NASA Lewis Research Center
21000 Brookpark Rd.
Cleveland, OH. 44135

ABSTRACT

The present paper describes the results of a computational study performed to examine turbulent flows in rotating disc cavities with radial throughflow. The problems considered are: turbulent flow in a contra-rotating cavity and turbulent flow and heat transfer in a co-rotating cavity. The standard k- ϵ model with wall functions and the low Reynolds number model of Chien have been used to generate a comparative set of results for specified values of the inlet mass flow rate, rotational Reynolds number, and imposed surface and inlet temperature distributions. The comparisons provided include radial and angular velocity profiles in the case of the co-rotating cavity, and radial variation of the local Nusselt number in the case of the contra-rotating cavity. The present predictions from the different turbulence models compare well with each other and also with the available experimental data, thereby, indicating that any of these models may be applied to simulate rotating cavity flows with reasonable confidence.

Keywords: Rotating cavity flow, Computational Fluid Dynamics, Turbine disc cavity, Turbulence models, Flow and heat transfer

1. INTRODUCTION

Disc cavities are present in turbine and compressor sections of a typical gas turbine engine. These may be formed by a stator-rotor combination, e.g. cavities at the rotor disks and just under the blade platforms, as well as rotor-rotor combination that exist between two rotor discs, underneath the rotor-stator cavities. In general the rotating cavities have axial throughflow near the axis (e.g. compressor section) or a radial throughflow that eventually enters the rotor-stator system for cooling and sealing purposes. Coolant flow distributions become quite important in the turbine section where the air is used to cool the discs and blades and thus affects the life of the components. The coolant air flow represents a loss in engine performance, and represents a quantity for optimization in the drive for better engine performance and efficiency. With reduced coolant flow rates, detailed and accurate information on flow/heat transfer occurring in the cavities becomes critical to ensure adequate cooling of the hot components at varying engine operating conditions.

A large number of studies on flows in stator-rotor systems as well as rotating cavity flows are available in the literature. A number of early studies deal with experiments on simplified geometry cavity systems and empirical correlations for flow and heat-transfer processes [1-3].

Several studies involved development of simplified analytical models for the cavity flows, typically based on the boundary layer equations at the walls which were linked with an inviscid core in the cavity center [3-5]. Such techniques were useful and accurate for simplified cavity geometries and flows, however, accuracy of such models can be expected to suffer when dealing with the complicated shapes of a typical disc cavity

and when interaction with the powerstream is present.

Several recent studies have used the computational fluid dynamics (CFD) techniques to the cavity problems. Treatment of single, simplified systems [7-9] as well as multiple cavities with multiple intracavity as well as cavity-powerstream interactions [10-12]. These studies involved treatment of the flow as well as heat transfer and coupled flow and conjugate heat transfer in the gas and the solid components. These analyses have provided means of achieving detailed flow and heat transfer results and on complex cavity shapes that were usually not amenable to simplified treatments. Additionally some efforts have also been made towards working these problem in a time-dependent mode and with accounting for the interaction with the non-axisymmetric flows generated by the powerstream blades. The list of references cited here is by no means exhaustive, and represents only a small fraction of the work that has been done on the cavity problems.

The success of such computations depends on the employed numerical schemes as well as the physical models. The flows that occur in the cavities are almost always turbulent, and the selection of the appropriate turbulence model is one of the important issues when the physical modeling is concerned. A number of turbulence models have been developed and employed including the simpler models such as Baldwin-Lomax and more detailed ones based on the turbulence energy and dissipation, for example, the standard k- ϵ model, multiple scale k- ϵ model, and various low Reynolds number models. The focus of the present paper is to compare results obtained from two different, commonly used models on a prototypical cavity problem and compare the results with experimental data. The choice of the models that are used and the appropriateness of any one particular model to a particular problem is always a point of contention. In the present work, rather than justifying the use of a given model, the focus is on the accuracy of the models that are commonly and routinely used and are available in a number of general purpose CFD codes, and in particular in SCISEAL [13]. Undoubtedly, there are other turbulence models available which may prove to be more “accurate” for the class of problems considered herein.

2. DESCRIPTION OF THE CFD CODE

The simulations presented here were performed using SCISEAL, an advanced 3-D CFD code developed under a NASA contract for the fluid flow and force analyses of turbomachinery seals and secondary flow systems [13]. The current version of the code uses a finite-volume, pressure-based scheme to integrate Navier-Stokes equations. The code uses a SIMPLEC type of scheme for pressure-velocity coupling and can treat compressible and incompressible flows. A full set of boundary conditions types and high order spatial and temporal differencing schemes are available. The code has treatment for: conjugate heat transfer, rotating and stationary frame, 2-D/3-D modeling, rotordynamics coefficient calculation procedures, and a variety of turbulence models, including the ones used in the present study, namely standard k- ϵ model and the low Reynolds number (low-Re) model of Chien [14].

Patel et al. [15] evaluated the performance of several low-Re turbulence models for favorable and adverse pressure gradients in boundary layers. The comparisons presented by them for the skin friction coefficient C_f in the flat plate boundary layer case showed that the good agreement to data is obtained by the models of Chien [14] and Wilcox and Rubesin [16], while those of Launder and Sharma [17] and Lam and Bremhorst [18] under- and overpredicted the value, respectively. For the same case, the Lam and Bremhorst model was able to capture the turbulent kinetic energy profile relatively very well. The C_f comparisons for favorable pressure gradient flows involving relaminarization showed that the Launder and Sharma model provided relatively better predictions. The overall conclusion of the study of Patel et al. [14] was that the above models provide comparable results and that they all need further refinement to be used with confidence.

With respect to the ease of implementation of the models for general complicated geometries, the Launder and Sharma model has the distinct advantage in that the damping functions are not dependent explicitly on the distance from the wall. However, the dissipation equation in this model has a complicated extra term that is a function of the square of the second derivative of the velocity.

3. MODEL EQUATIONS

The turbulence models used in the present study are the high Reynolds number standard k- ϵ model of

Launder and Spalding and the low Reynolds number model of Chien. The k-ε system of equations in the Chien model can be expressed as below:

$$\begin{aligned}\nabla \cdot (\rho \mathbf{VK}) &= \nabla \cdot \left[\left(\mu + \frac{\mu_t}{\sigma_k} \right) \nabla k \right] + P - \rho \epsilon \\ \nabla \cdot (\rho V \tilde{\epsilon}) &= \nabla \cdot \left[\left(\mu + \frac{\mu_t}{\sigma_\epsilon} \right) \nabla \tilde{\epsilon} \right] + \frac{\tilde{\epsilon}}{k} [f_1 C_{\epsilon 1} P - f_2 C_{\epsilon 2} \rho \tilde{\epsilon}] + E\end{aligned}$$

where the dissipation ε is related to the quantity $\tilde{\epsilon}$ by

$$\epsilon = \epsilon_0 + \tilde{\epsilon}$$

with ϵ_0 being the value of ε at the wall.

The production term P is defined as

$$P = \tau_t : \nabla \mathbf{V}$$

where the turbulent stress tensor is modeled using Bousinessq's eddy viscosity concept as

$$\tau_t = \mu_t \left[\nabla \mathbf{V} + (\nabla \mathbf{V})^T \right] - \frac{2}{3} \mu_t (\nabla \cdot \mathbf{V}) \mathbf{I} - \frac{2}{3} \rho k \mathbf{I}$$

The eddy viscosity is defined as

$$\mu_t = f_\mu C_\mu \rho \frac{k^2}{\tilde{\epsilon}}$$

The expressions used in the Chien model for the empirical damping functions f_μ , f_1 and f_2 , and the values of the empirical constants are summarized in Table 1.

Table 1. Damping Functions and Empirical Constants Used in Chien's Low Reynolds Number Turbulence Model

f_μ	$1 - e^{-0.0115y^+}$	$c_{\epsilon 1}$	1.35
f_1	1	$c_{\epsilon 2}$	1.80
f_2	$1 - 0.22 e^{-(Re_T / 6)^2}$	c_μ	0.09
ϵ_0	$2 \mu k / y^2$	σ_k	1.0
E	$-\frac{2 \mu \tilde{\epsilon}}{\rho y^2} e^{-0.5 y^+}$	σ_ϵ	1.3

The nondimensional parameters Re_T , R_y and y^+ are defined as:

$$Re_T = \frac{\rho k^2}{\tilde{\epsilon} \mu}, \quad R_y = \frac{\rho k^{1/2} y}{\mu}, \quad y^+ = \frac{\rho U_\tau y}{\mu}$$

In the above relations, 'y' is the distance to the wall and U_τ is the friction velocity. The boundary condition for k at the no-slip wall is $k = 0$. The boundary condition for ε is built into the $\tilde{\epsilon}$ -equation by the inclusion of the factor ϵ_0 . The effective thermal conductivity in the case of heat transfer problems is calculated as

$$\lambda_{eff} = C_p \left[\frac{\mu}{Pr} + \frac{\mu_t}{Pr_t} \right]$$

where C_p is the specific heat, Pr and Pr_t are the laminar and turbulent Prandtl numbers with Pr_t taken as equal to 0.9.

4. DESCRIPTION OF THE FLOW PROBLEMS

The two different types of rotating cavity configuration considered in the present study are:

1. Flow in a cavity formed between two contra-rotating discs with a radial throughflow. This type of flow has been studied in Refs. 16-18 and disc cavities of this type may be encountered in turbine engines with proposed contra-rotating turbine sections [19-21].
2. Flow and heat transfer in a co-rotating cavity [22], which is a much more common type of disc cavity and that which is usually found in the turbine section where the radial throughflow is used as coolant and sealing air for the rotor-stator type of disc cavities.

Following are details of the geometry, flow conditions and results of the simulations.

1. CONTRA-ROTATING CAVITY FLOW

A. Geometry and flow conditions

A schematic of this cavity is shown in Figure 1 and is based on the description provided in [19,20]. Using the notation and details provided in [20], the geometry is described by the following aspect ratios: the gap ratio $G = s/b = 0.12$, the shroud-clearance ratio $G_c = s_c/b = 0.016$, and the inner to outer radius ratio $a/b = 0.128$, where the outer radius b of the cavity is 391 mm. The rotational speeds of the left and right disc are equal and opposite ($\Gamma = -1$). The important flow parameters in this problem are the nondimensional inlet mass flow rate C_w and the rotational Reynolds number Re_ϕ . In the experiments in [19], the throughflow entered through an axial hole in the left disc and then was introduced in the cavity radially through a pair of rotating gauze tubes of 50 mm radius to provide a nearly uniform radial velocity distribution. Experimental measurements include those of the radial and tangential velocity components along the axial direction at several radial stations.

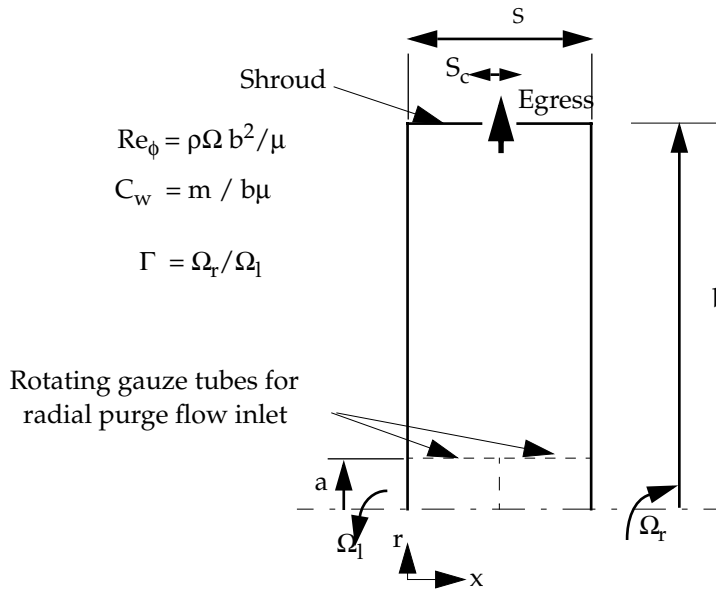


Fig. 1. Schematic diagram of the contra-rotating cavity.

The computational domain considered in the present study is enclosed by the two discs in the axial direction, and by the shroud at the outer radius and the gauze tube at the inner radius (Figure 1). A 2-D grid with 95 cells in the radial direction and 67 cells in the axial direction was generated with appropriate clustering near the walls to yield proper near-wall distances needed in the low-Re model. For the standard $k-\epsilon$ model with the wall functions the grid size was reduced to 47 cells in the axial and 88 cells in the radial direction. The reduction is needed to keep the near wall distance large enough to be acceptable for the wall

functions. A limited amount of grid-independence study was performed to ensure that the solutions were nearly insensitive to further grid refinement. It should be noted here that the 95×67 grid resolution employed here is comparable in the radial direction and nearly half as small in the axial direction as the 113×65 grid employed in [20] wherein the symmetry of the flow about the axial midplane was invoked. Thus, the present results will serve as a good indicator of the minimum resolution required for reasonable accuracy in the computed results.

B. Computational Results and Discussion

Two-dimensional, axi-symmetric, swirling flow simulations were carried out at three different values of the nondimensional flow rate $C_w = 2310, 6320$ and 9280 , corresponding to $Re_\phi = 6.66 \times 10^5, 7.08 \times 10^5$, and 6.84×10^5 , respectively. In each case, the disc speed was fixed to achieve the appropriate value of Re_ϕ .

Air at 297 K was used as the working fluid, and at the low speeds involved, it was assumed to be incompressible and to have constant properties. Central differencing scheme with 10% damping was used for the convective fluxes. The simulations were carried out using the standard k- ϵ model with wall functions and the low-Re model of Chien.

An inlet boundary was specified at the gauze tube (i.e. at inner radius a) with a uniform radial velocity to yield the correct volume flow rate (see Figure 1). The disc and shroud walls were specified as no-slip walls with the appropriate angular velocities. At the clearance between the shrouds where the flow exits, a constant pressure boundary was specified.

The computed streamlines using the low-Re model of Chien are shown in Figure 2 for $C_w = 2310$ and 6320 . As was described in [20], the following characteristic regions exist in this problem: a source region extending radially outward from the inlet where the radial velocity is everywhere positive, an axial midplane core region with radial inflow, boundary layers on the discs with radial outflow, and contra-rotating cells between the boundary layers and the core. With reference to Figure 4, the present predictions for $C_w = 2310$ show the existence of two secondary contra-rotating cells close to the inlet apart from the two primary ones near the core. Though the rotations of the secondary and primary cells on the same side of the axial midplane were found to be in opposite direction, these cells are sufficiently separated radially by a region in which rotational effects are nearly absent. At the higher value of $C_w = 6320$, the source region penetrates comparatively farther into the core, and only a primary system of contra-rotating cells can be discerned.

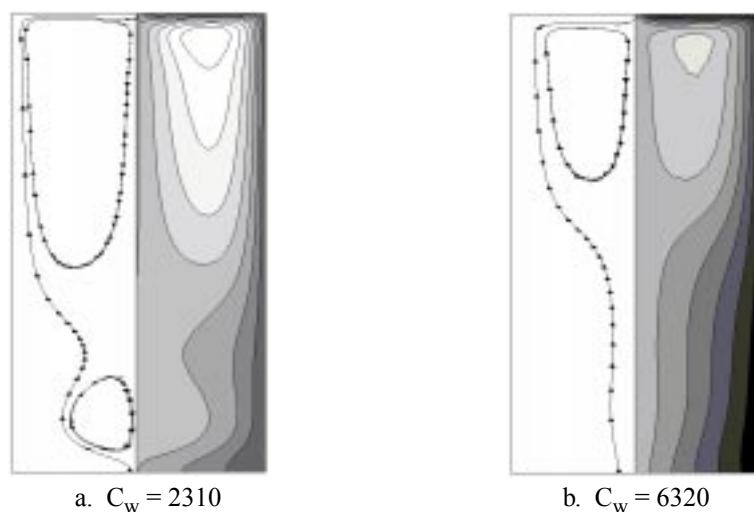


Fig. 2. Computed streamlines for contra-rotating cavity.

Experimental data [20] for this case are in terms of axial distribution of tangential and radial velocity components at different radial locations. Although the simulations were carried out at three different coolant flow rates C_w , results for one flow rate are shown here, specifically, for $C_w = 6320$. The radial and tangential velocity distributions at $r/b = 0.6, 0.7, 0.8$ and 0.85 are plotted in Figures 3-6. The velocities have been

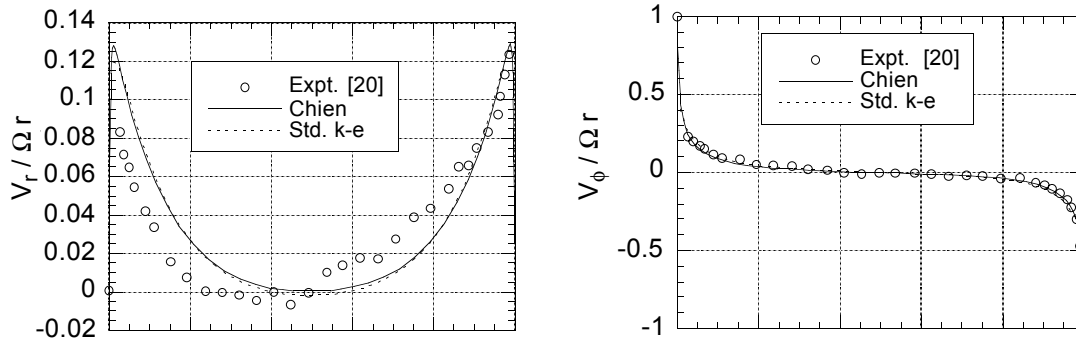


Fig. 3. Radial and tangential velocity distributions at $r/b = 0.6$.

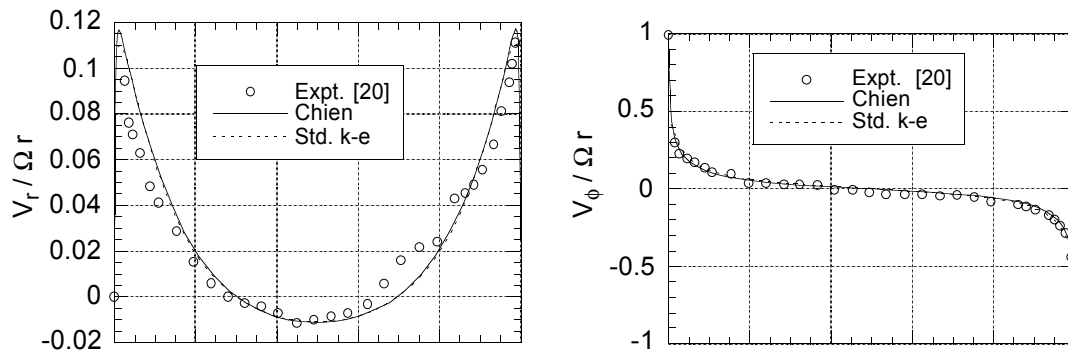


Fig. 4. Radial and tangential velocity distribution at $r/b = 0.7$.

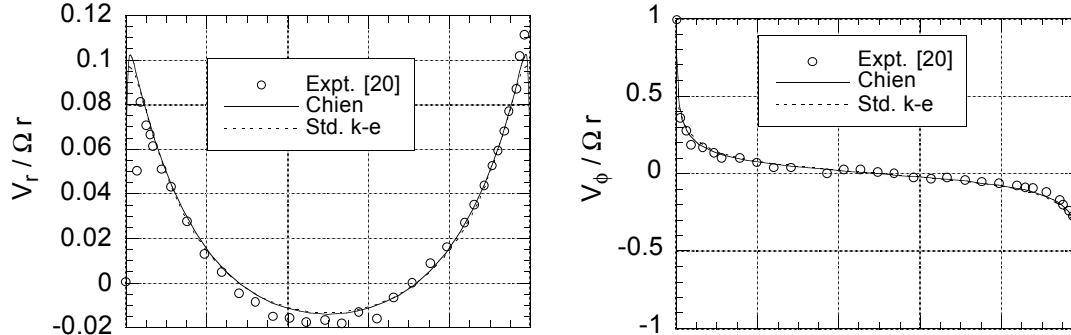


Fig. 5. Radial and tangential velocity distribution at $r/b = 0.8$.

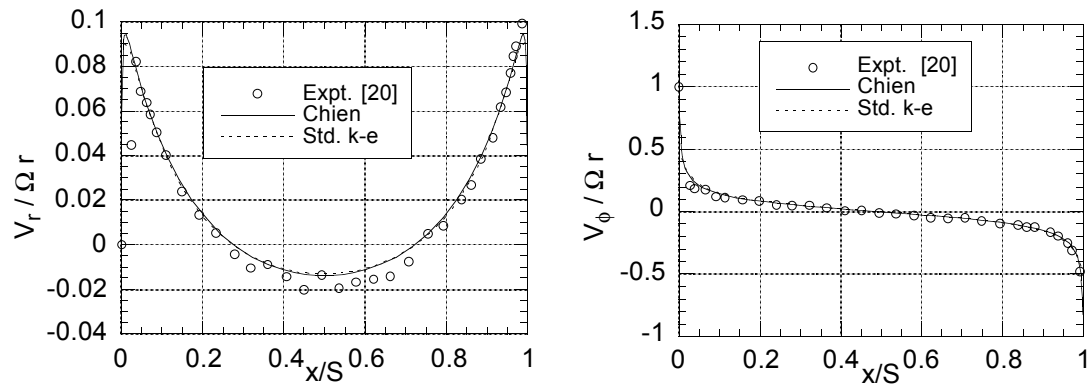


Fig. 6. Radial and tangential velocity distribution at $r/b = 0.85$.

scaled with the local wall tangential velocity which is equal to Ωr . Data points from measurements are represented by symbols in these figures and the curves represent results from the simulations using the two different turbulent models. In general the agreement between the two model predictions and with the data is good to very good in the case of the tangential velocities at all radial locations. Radial velocity plots also compare well with the experimental data near the shroud. At the lower radius, the experimental data shows higher radial velocities near the downstream disc wall ($x/S = 1$). This is a result of the axial entry of the coolant flow in the experimental setup. Although not shown here, this skewness in the radial velocity plots gets more pronounced with increasing coolant flow rates.

2. CO-ROTATING CAVITY FLOW AND HEAT TRANSFER

A. Geometry and flow conditions

The co-rotating cavity was formed with two discs joined at the outer radius with a single shroud [22]. The configuration is similar to that of the contra-rotating cavity but with the discs now rotating in the same direction, (Figure 1) i.e., $\Gamma = 1$. The values of the geometric ratios are the same as those used in [22]: gap ratio $G = 0.138$, radius ratio $a/b = 0.104$, with the outer radius $b = 428$ mm. Coolant flow was introduced into the cavity through an axial hole in the ‘upstream’ disk and the flow exited through the shroud holes. The discs were instrumented for temperature and wall heat flux measurements and had embedded electric heaters for heat addition. Radial distribution of wall heat fluxes were measured at different coolant flow rates, rotational speeds and wall temperature distributions. Three different wall temperature distributions were considered: constant, decreasing with radius, and increasing with radius.

The flow domain considered is similar in shape to the one shown earlier for the contra-rotating cavity (see Figure 1). The coolant was assumed to enter the cavity radially. The grid used for the low Reynolds number model had 84 cells in the axial direction and 136 in the radial direction. The grid for the standard k- ϵ model had 52 and 94 cells in the axial and radial directions, respectively. As before, this reduction was needed to keep the near wall distances in the proper y^+ range. This reduction is also one of the reasons why the standard k- ϵ model becomes economical and hence attractive in complex simulations.

B. Computational Results and Discussion

The working fluid was taken as air. As before, central differencing scheme with 10% damping was used for the convective fluxes. Boundary condition at the inlet (inner radius) was a specified inlet flow rate corresponding to specified values of C_w and inlet temperature (see Figure 1). A constant pressure exit boundary was specified at the slot in the shroud. In actuality this is a set of discrete holes; in the 2-d axis-symmetric simulations a slot with equivalent flow area was used. No-slip walls with appropriate angular velocities were assumed on disc and shroud surfaces.

Two choices were available for the specification of the energy equation boundary conditions at the disc walls: 1) use the measured temperature profiles as imposed boundary values, and 2) model the disc as a solid piece with embedded heaters and solve a conjugate heat transfer problem that would give both the flux and temperatures as solutions. In the absence of sufficient details of heater construction and operation, the first choice was used in the computations as was also done in [22]. Three different types of profiles were generated in the experiments: radially constant, increasing and decreasing temperatures. A typical set of these profiles is shown in Figure 7. These experimental temperature profiles were imposed on the upstream and downstream disc walls for the energy equation.

For a constant nondimensional coolant flow rate C_w of 7000, and a rotational Reynolds number Re_ϕ of 2×10^6 , parametric simulations were performed by imposing the wall temperatures as described above. The computed temperature distributions were post-processed to obtain the radial variation of the local Nusselt number on the ‘upstream’ and ‘downstream’ discs.

The predicted radial Nusselt number profiles from the two turbulence models are compared with the experimental data [22] in Figures 8a-c. In these plots the computed values are represented by curves and the data by symbols. Again, the comparison with the experimental data both in terms of the general trend as well as local magnitudes is good. As was found in the experiments [22], the present predictions show that the local Nusselt number becomes negative (Figure 8b) as the shroud is approached. Since the imposed surface temperature is greater than the inlet temperature, i.e., $T_S - T_I > 0$, a negative value of Nu, by

definition, implies that the local heat flux is negative, i.e., heat is transferred from the fluid to the wall. This indicates that the heat gained by the fluid from the disc near the inlet region is returned to the disc at larger radius. As in the previous case, predictions from the two turbulence models show little differences. These comparisons provide confidence in the utilization of the standard k- ϵ model with a relatively much coarser grid to simulate cavity heat transfer problems.

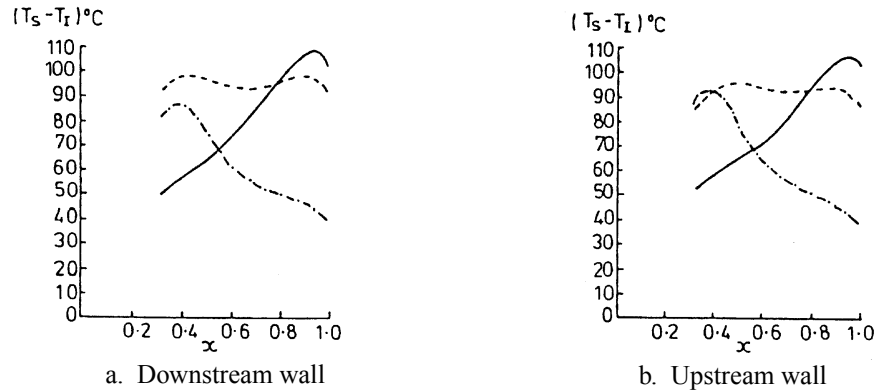


Fig. 7. Imposed disc surface temperature distributions.

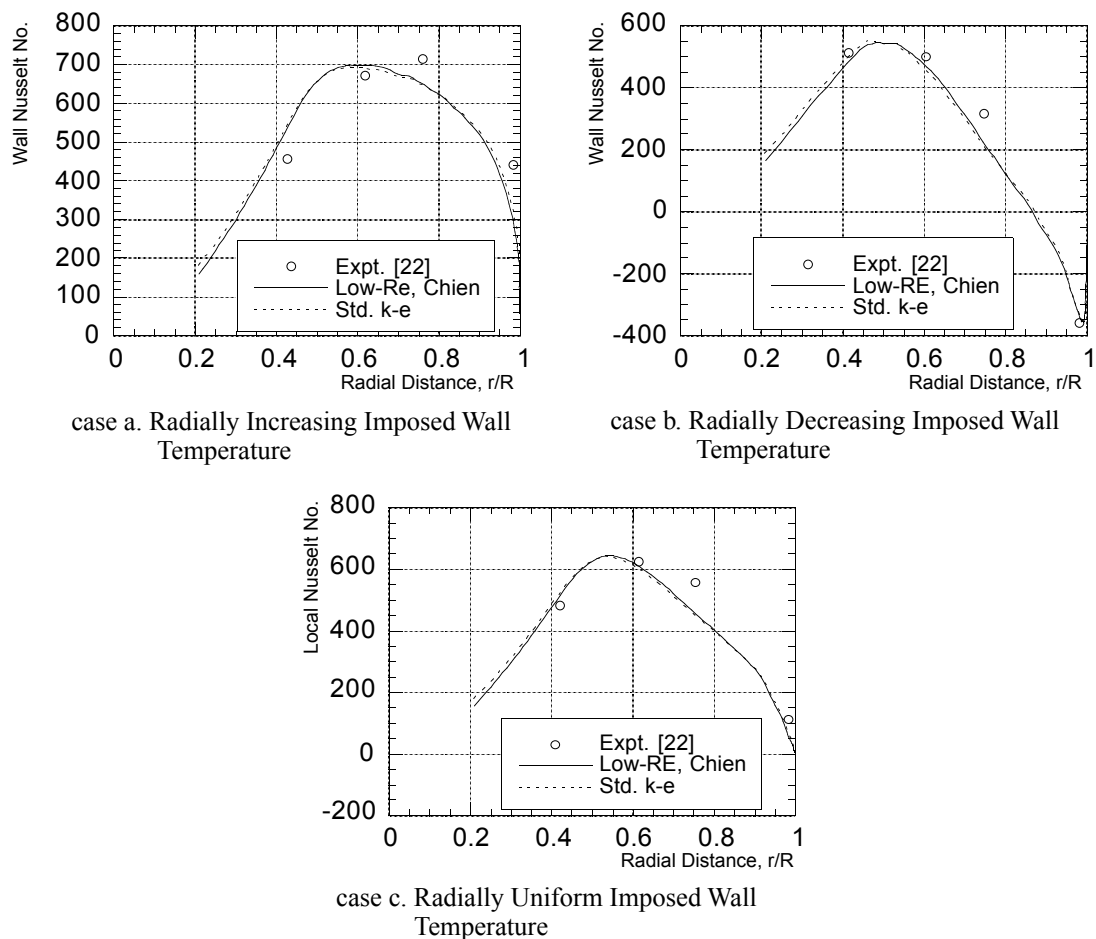


Fig. 8. Radial variation of local Nusselt number for various imposed disc wall temperatures.

SUMMARY

An advanced 3-D CFD code, SCISEAL was applied to simulate flow and heat transfer in two different rotating cavity configurations. The turbulence models employed were the standard k- ϵ model with wall functions and the low Reynolds number model of Chien. This exercise was undertaken to validate the numerics and physical models in SCISEAL by comparison with experiments, and to assess the performance of the turbulence models on this class of problems. It is recognized that there are several other turbulence models that are available and are being used. One can claim that these have better predictive capabilities; however, the intent of this work was to test the accuracy of the more widely used models that were available in the code.

The model predictions were compared with the available data for velocity profiles in the contra-rotating cavity configuration, and for local Nusselt number in the co-rotating cavity configuration. The overall results show that both models produce results that are very similar to each other, and show a good correlation with the experimental data. The good agreement between the standard k- ϵ model and the low-Re model of Chien is possibly due to the fairly high Reynolds numbers investigated in the present study. As expected, however, the models show discrepancies near the walls where the viscous effects become predominant and where the Chien model is expected to be more accurate. The correlation of the results with the experimental data serves to validate the accuracy of the SCISEAL predictions. Based on this set of results, both models employed in this study are seen to do an adequate job of dealing with the flows in disc cavities provided proper care is taken in the mesh generation and boundary condition specifications to match the restrictions and range of validity of each model.

REFERENCES

1. Owen, J.M., Air-Cooled Gas Turbine Discs: A Review of Recent Research, *Int. J. Heat and Fluid Flow*, Vol. 9, No. 4 (1988) pp.354-365.
2. Bayley, F.J., Owen, J.M., The Fluid Dynamics of a Shrouded Disk System With a Radial Outflow of Coolant, *J. Engg. for Power* (1970) pp.335-341.
3. Phadke, U.P., Owen, J.M., An Investigation of Ingress for an Air-Cooled Shrouded Rotating Disk System With Radial-Clearance Seals, *J. Engg. for Power*, Vol. 105 (1983) pp. 178-183.
4. Chew, J.W., and Rogers, R.H., An Integral Method for the Calculation of Turbulent Forced Convection in a Rotating Cavity with Radial Outflow, *Int. J. Heat and Fluid Flow*, Vol.9 (1988) pp.37.
5. Chew, J.W., A Theoretical Study of Ingress for Shrouded Disc Systems with Radial Outflow, ASME-89-GT-178, ASME Gas Turbine and Aeroengine Expo, Toronto, Canada (1989).
6. Johnson, B.V., Daniels, W.A., Kaweki, E.J., and Martin, R.J., Compressor Drum Aerodynamic Experiments and Analysis With Coolant Injected at Selected Locations, *J. Turbomachinery*, Vol.113 (1991) pp.272-280.
7. Chew, J.W., Predictions of Flow in Rotating Disk Systems Using the k- ϵ Turbulence Model, ASME-88-GT-229, ASME Gas Turbine and Aeroengine Expo, Amsterdam, The Netherlands (1988).
8. Ko, S.H., and Rhode, D.L., Thermal Details in a Rotor-Stator Cavity at Engine Conditions with a Mainstream, ASME-91-GT-275, ASME Gas Turbine and Aeroengine Expo, Orlando, FL (1991).
9. Athavale, M.M., Przekwas, A.J., Hendricks, R.C., A Numerical Study of the Flow-Field in Enclosed Turbine Disk-Cavities in Gas Turbine Engines, ISROMAC-4, Honolulu, HI (1992).
10. Virr, G.P., Chew, J.W., and Coupland, J., Application of Computational Fluid Dynamics to Turbine Disk Cavities, *J. Turbomachinery*, Vol. 116 (1994) pp.701-708.
11. Athavale, M.M., Przekwas, A.J., Hendricks, R.C., and Steinetz, B.M., Numerical Analysis of Intra-Cavity and Power-Stream Flow Interaction in Multiple Gas-Turbine Disk-Cavities, ASME-95-325, ASME Gas Turbine and Aeroengine Expo, Houston, TX (1995).
12. Ho, Y.H., Athavale, M.M., Przekwas, A.J., Forry, J.M., and Steinetz, B.M., Numerical Simulation of Secondary Flow Gas Turbine Disc Cavities Including Conjugate Heat Transfer, ASME-96-67, ASME Gas Turbine and Aeroengine Expo, Birmingham, U.K. (1996).
13. Athavale, M.M., Przekwas, A.J., Hendricks, R.C., and Liang, A., SCISEAL- A Three-Dimensional CFD Code for Accurate Analyses of Fluid Flow and Forces in Seals, Proceedings of the Advanced E.T.O. Technology, NASA MSFC, Huntsville, AL (1994).

14. Chien, K.-Y., Predictions of Channel and Boundary Layer Flows with a Low-Reynolds-Number Turbulence Model, *AIAA Journal*, Vol. 20 (1982) pp. 33-38.
15. Patel, V.C., Rodi, W., and Scheurer, G., Turbulence Models for Near-Wall and Low-Reynolds Number Flows: A Review, *AIAA Journal*, Vol. 23 (1984) pp. 1308-1319.
16. Wilcox, D.C. and Rubesin, W.M., Progress in Turbulence Modeling for Complex Flow Fields Including Effects of Compressibility, NASA Tech. Paper 1517 (1980).
17. Launder, B.E. and Sharma, B.I., "Application of the Energy-Dissipation Model of Turbulence to the Calculation of Flow Near a Spinning Disc," *Letters in Heat and Mass Transfer*, Vol. 1 (1974) pp. 131-138.
18. Lam, C.K.G. and Bremhorst, K.A., Modified Form of the k- ϵ Model for Predicting Wall Turbulence, *Journal of Fluids Engineering*, Vol. 103 (1981) pp. 456-460.
19. Gan, X. Kilic, M., and Owen, J.M., Superposed FLOW Between Two Discs Contrarotating at Differential Speeds, *Int. J. Heat and Fluid Flow*, Vol. 15, No. 6 (1994) pp.438-446.
20. Gan, X., Kilic, M., and Owen, J.M., Flow Between Contrarotating Disks, *J. Turbomachinery*, Vol. 117 (1995) pp. 298,305.
21. Kilic, M., Gan, X., and Owen, J.M., Turbulent Flow Between Two Disks Contrarotating at Different Speeds, *J. Turbomachinery*, Vol. 118 (1996) pp. 408-413.
22. Northrop, A., and Owen, J.M., Heat Transfer Measurements in Rotating Disc Systems, Part 2: The Rotating Cavity with a Radial Outflow of Cooling Air, *Int. J. Heat and Fluid Flow*, Vol.9, No.1 (1988) pp. 27-36.

NOMENCLATURE

A = Area, m²

b = outer radius of cavity, m

C_w = Nondimensional coolant flow, q/vR

K = turbulence kinetic energy, m²/s²

k = thermal conductivity, W/m-K

L = Characteristic length, m

Nu = Nusselt Number, qr/(T_S-T_I)

q = heat flux, W/m²

R = outer radius

Re_φ = Rotational Reynolds number, ΩR²/ν

r = radial coordinate, m

T = Temperature, K

x,y,z = Cartesian coordinate directions, distances, m

y⁺ = Nondimensional friction distance

Greek

ρ = density, kg/m³

ν = kinematic viscosity, m²/s

μ = dynamic viscosity, Pa-S

ω = disc rotation speed, rad/s

τ = stress, Pa

ε = turbulence dissipation rate

Subscripts

S = wall

I = inlet

Appendix B
An Algorithm for Interpolation Between Computational
Interfaces With Arbitrary Grid Matching

B.1 Introduction

A robust interpolation algorithm was developed for the data exchange between SCISEAC and MS-TURBO across interfaces. The interpolation algorithm had to treat interfaces that had only partial overlaps, stressed grids on cylindrical surfaces, structured and unstructured grid topologies and different grid face counts in the two interfacing grids. The interpolation methodology that was developed and used here involves the following steps:

- (1) Interpolate values of the current variable from face centers to nodes on side 1 of the interface;
- (2) Use the nodal values of the current variable to calculate the gradient of the current variable at face centers on side 1 of the interface; and
- (3) Use values and gradients of the current variable at face centers on side 1 of the interface to calculate values of the current variable at face centers on side 2 of the interface.

Details of each of these steps are given in the following subsections.

B.2 Methods

B.2.1 ‘Face center’ values vs. ‘cell center’ values.—The interface interpolation method described below is a discussion on how to interpolate from face center values on one side of the interface to face center values on the other side. This method therefore necessarily assumes that the face center values for a given variable are available along the interface. In the practical implementation of the algorithm, the CFD code which supplies the face center values can use as accurate a technique as desired for the extrapolation of this values from the cell center.

B.2.2 Necessary input for the interpolation algorithm.—The complete list of information necessary for interpolation from a local interface boundary to a remote boundary is as follows:

- (1) Face-node list describing the nodes which surround a given face along the interface [local].
- (2) Total number of faces, total number of nodes, and a list containing the number of nodes per face (the current algorithm is designed for the most general case of polynodal faces) [local].
- (3) Nodal coordinates (x,y,z) along the interface [local]
- (4) “ordered_nodes” parameter which is true if the nodes are arranged sequentially (clockwise or counter-clockwise) around the face centroid in the face-node list or false if the nodes are not ordered [local]
- (5) Face centroids (sctr, yctr, zctr) for the remote interface [remote].
- (6) Face center data (u,v,w,P,etc) [local]

The code is capable of handling faces with any number of nodes and it is not necessary to order the face node list in any particular format.

B.2.3 Face Normal Vectors.—The interpolation algorithm requires a normal vector for each face. This normal vector is uniquely defined for a three noded ‘tri’ face, but for the general case of polynodal faces, all of the nodes will not necessarily lie in the same plane. In this case, the face normal is calculated by averaging the ‘sub-face’ normals (figure B.1). The sub-face normals are calculated by taking a cross product of the vectors from the face centroid to two face nodes. The expression for the average face normal is therefore given by:

$$\overrightarrow{face_normal} = \sum_{i=1}^{num_nodes_per_face} \frac{\vec{n}_{sub_face,i}}{|\vec{n}_{sub_face,i}|} \quad (B.1)$$

where

$$\vec{n}_{sub_face,i} = \vec{r}_{ctr-node,i} \times \vec{r}_{ctr-node,i+1} \quad (B.2)$$

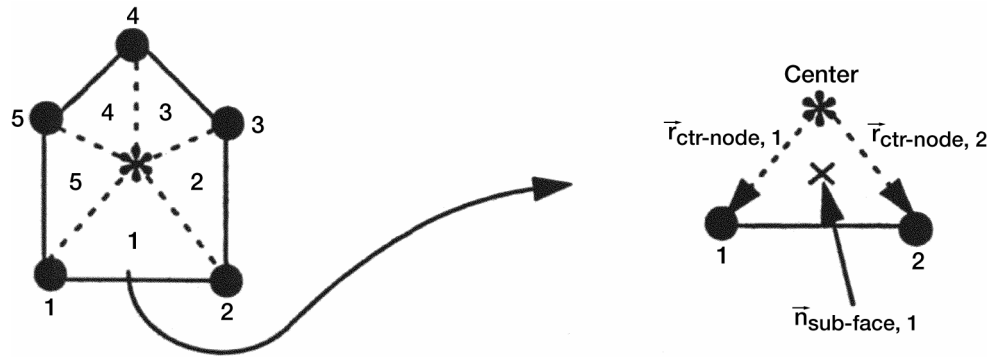


Figure B-1.—Face normals are calculated as the average of all of the subface normals.

This method for computing the face normals requires that the nodes be oriented in order (clock-wise or counter-clockwise) around the face centroid. If the nodes are not in order, the current doing will order the nodes before calculating the face normal. This ordering process is done as follows. A normalized baseline vector is established from the face centroid to the first node in the node list.

The dot product between this baseline vector and the normalized vectors from the face center to all other nodes is evaluated. The node which yields the maximum dot product is established as the second node in the list.

Next, the dot product and cross product between the second vector and all remaining center to node vectors are evaluated. In addition, the dot product of the first sub-face normal and the calculated cross products from the remaining nodes is evaluated. The node which produces the maximum dot product with the second node vector AND has a positive dot product between the old sub-face and the evaluated cross products is assigned to be the next node in the list.

This process is repeated for the remaining nodes.

The second dot product evaluation between the sub-face normal and the other subface normals is designed to be consistent for face geometries like that shown in figure B.2d. On this face, the dot product between the normalized vectors from the center to node 3 and the center to node 4 is larger than the dot product between the normalized vectors from the center to node 3 and the center to node 5. However, node 5 is the next node seen as this face is traversed clockwise. The constraint that the dot product between the previous sub-face normal and the current sub-face normal must be positive causes node 5 to be chosen as the next node rather than node 4.

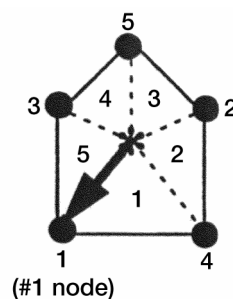


Figure B-2a.—Normalizes baseline vector from face centroid to first node in the node list.

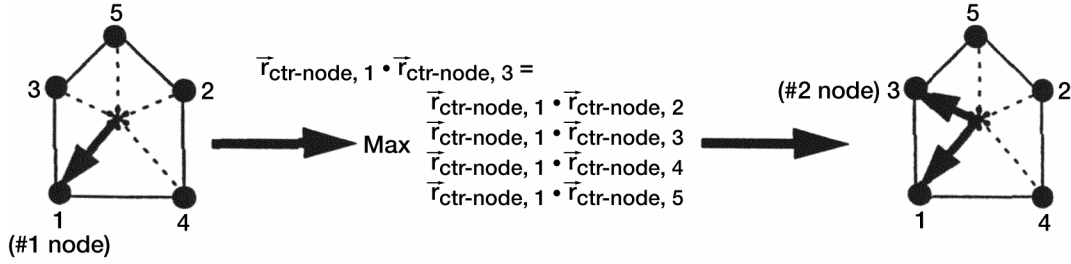


Figure B-2b.—The normal for the sub-face between the first and second nodes is then evaluated.

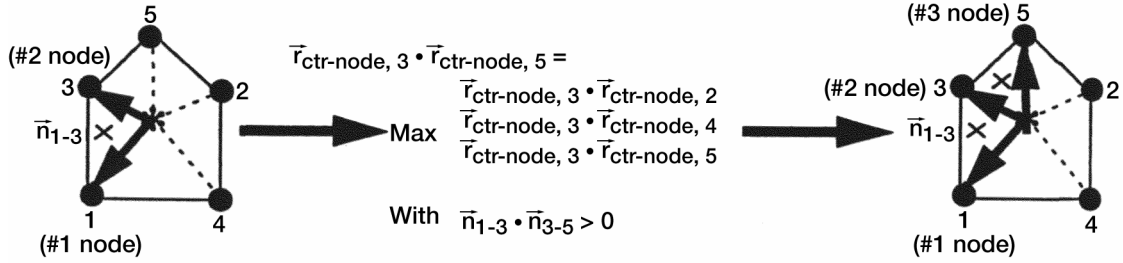


Figure B-2c.—The third node is chosen as the node which yields maximum dot product with the previous node to center vector AND has a dot product between the new subface normal and the old subface normal which is greater than zero.

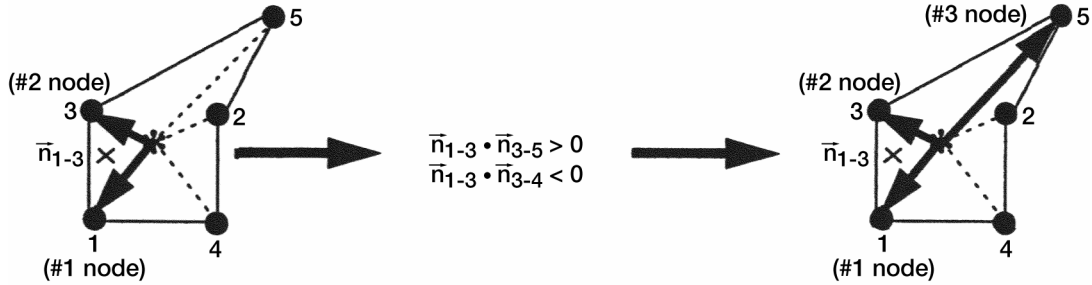


Figure B-2d.—Node 5 is chosen to be the third node even with a highly skewed face geometry.

B.2.4 Cell center to nodal interpolation.—The cell center to nodal interpolation is accomplished using Laplacian interpolation algorithms described in references 1 (three-dimensional) and 2 (two-dimensional). The Laplacian interpolation algorithm is designed to be 100 percent accurate in the interpolation of linear function form face centers to interior nodes. In summary, a nodal value, q_0 , can be obtained as a weighted average of cell center values (q_1, q_2, \dots, q_n) (figure B.3):

$$q_0 = \frac{\sum_{i=1}^n w_i q_i}{\sum_{i=1}^n w_i} \quad (\text{B.3})$$

With the following definitions:

$$w_i = \lambda_x(x_i - x_0) + \lambda_y(y_i - y_0) + \lambda_z(z_i - z_0) \quad (\text{B.4})$$

$$\lambda_x = \frac{\left[-R_x(I_{yy}I_{zz} - I_{yz}^2) + R_y(I_{xy}I_{zz} - I_{xz}I_{yz}) - R_z(I_{xy}I_{yz} - I_{yy}I_{xz}) \right]}{D} \quad (\text{B.5})$$

$$\lambda_y = \frac{\left[R_x(I_{xy}I_{zz} - I_{xz}I_{yz}) + R_y(I_{xx}I_{zz} - I_{xz}^2) + R_z(I_{xx}I_{yz} - I_{xy}I_{xz}) \right]}{D} \quad (\text{B.6})$$

$$\lambda_z = \frac{\left[-R_x(I_{xy}I_{yz} - I_{yy}I_{xz}) + R_y(I_{xx}I_{yz} - I_{xy}I_{xz}) - R_z(I_{xx}I_{yy} - I_{xy}^2) \right]}{D} \quad (\text{B.7})$$

$$D = I_{xx}(I_{yy}I_{zz} - I_{yz}^2) - I_{xy}(I_{xy}I_{zz} - I_{xz}I_{yz}) + I_{xz}(I_{xy}I_{yz} - I_{yy}I_{xz}) \quad (\text{B.8})$$

$$R_x = \sum_{i=1}^n (x_i - x_0) \quad (\text{B.9})$$

$$R_y = \sum_{i=1}^n (y_i - y_0) \quad (\text{B.10})$$

$$R_z = \sum_{i=1}^n (z_i - z_0) \quad (\text{B.11})$$

$$I_{xx} = \sum_{i=1}^n (x_i - x_0)^2 \quad (\text{B.12})$$

$$I_{yy} = \sum_{i=1}^n (y_i - y_0)^2 \quad (\text{B.13})$$

$$I_{zz} = \sum_{i=1}^n (z_i - z_0)^2 \quad (\text{B.14})$$

$$I_{xy} = \sum_{i=1}^n (x_i - x_0)(y_i - y_0) \quad (\text{B.15})$$

$$I_{xz} = \sum_{i=1}^n (x_i - x_0)(z_i - z_0) \quad (\text{B.16})$$

$$I_{yz} = \sum_{i=1}^n (y_i - y_0)(z_i - z_0) \quad (\text{B.17})$$

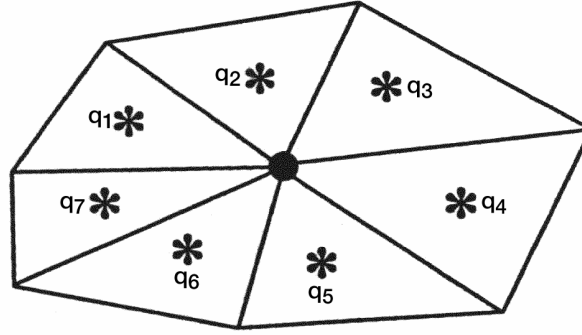


Figure B-3.—The nodal value of the variable 'q' is obtained as a weighted average of the surrounding face center values.

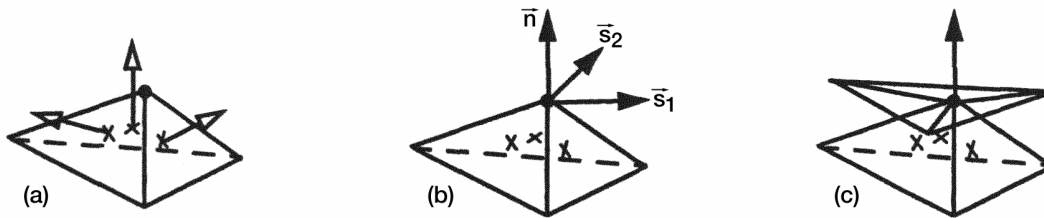


Figure B-4.—Face normal vectors surrounding a node (a) are average to generate a "node_normal" unit vector, n, and two in-plane unit vectors, s1 and s2 (b). All calculations involving the face centroid coordinates are carried out in the projected normal plane (c).

In practice this three-dimensional interpolation method fails under certain conditions such as when the contributing faces are coplanar. The current coding checks for these failure conditions and reverts to the two-dimensional Laplacian interpolation in the case of failure of the three-dimensional algorithm. Likewise the two-dimensional Laplacian fails under certain conditions (such as when the contributing faces are colinear). In this case the coding reverts to a distance based weighting:

$$w_i = \frac{1}{r_{i \rightarrow \text{node}}} \quad (\text{B.18})$$

where $r_{i \rightarrow \text{node}}$ is the distance between face center i and the node 0. This means that for linear function, the interpolation (or extrapolation) of values to the boundary nodes will not necessarily be exact.

The one difficulty with reverting from the 3-D Laplacian to the 2-D Laplacian interpolation is the choice of which two directions (i.e., x and y ?; x and z ?; y and z ?) to use in the 2-D Laplacian. This problem is avoided in the current coding by projecting all face center cartesian coordinates (x, y, z) into the average normal plane (s_1, s_2, n) of the node (figure B.4):

$$\overrightarrow{\text{node_normal}}_i = \sum_{j=1}^{\text{num_faces_per_node}, i} \frac{\overrightarrow{\text{face_normal}}_j}{\left| \overrightarrow{\text{face_normal}}_j \right|} \quad (\text{B.19})$$

Therefore the 3-D Laplacian uses the coordinates s_1, s_2 , and n while the 2-D Laplacian uses only s_1 and s_2 . It should be noted that the in-lane unit vectors s_1 and s_2 can be chosen arbitrarily using the node as the origin and the node_normal vector as the normal for the projection plane.

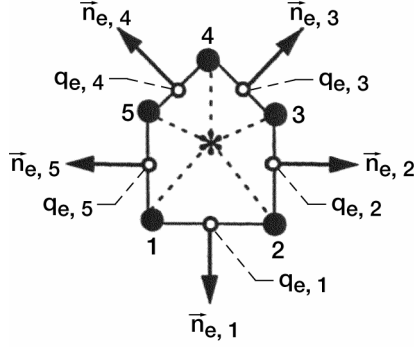


Figure B-5.—Edge normal vectors for an example face.

B.2.5 Calculation of Gradients.—Nodal values are used to calculate the face center gradient based upon a version of Green’s Theorem. Green’s theorem is given by

$$\nabla q = \frac{\int_{\Gamma} q_e \vec{n} d\Gamma}{\mathcal{V}} \quad (\text{B.20})$$

where q_e is the value of q on the boundary (Γ), \vec{n} is the normal along the boundary, and \mathcal{V} is the cell volume. On a 2-D face, eq. (B.20) becomes

$$\nabla q = \frac{\sum_{i=1}^{\text{number of edges}} q_{e,i} \vec{n}_{e,i} A_{e,i}}{\mathcal{V}} \quad (\text{B.21})$$

where \vec{n}_e is the normal vector at each edge, A_e is the edge ‘area’ (actually edge length), and \mathcal{V} is the face ‘volume’ (face area figure B.5).

$$\mathcal{V} = \sum_{i=1}^{\text{number of subfaces}} \mathcal{V}_{\text{subface},i} \quad (\text{B.22})$$

$$\mathcal{V}_{\text{subface},1} = \frac{1}{2} \vec{r}_{\text{ctr-node},1} \times \vec{r}_{\text{ctr-node},2} \quad (\text{B.23})$$

$$A_{e,1} = \sqrt{(x_2 - x_1)^2 + (y_2 - y_1)^2} \quad (\text{B.24})$$

$$q_{e,1} = \frac{1}{2} (q_1 + q_2) \quad (\text{B.25})$$

The face volume is calculated by summing all of the sub-face volumes (eq. (B.22)), and each sub-face volume is calculated as one-half of the magnitude of the cross product between the vectors from the face center to the first node and the face center to the first node and the face center to the second node (eq. (B.23)). Note that the quantity q_e is simply the average of the value of q at the two nodes of a given edge (eq. (B.25)). The variable “edge_normal” in the interpolation coding is the quantity:

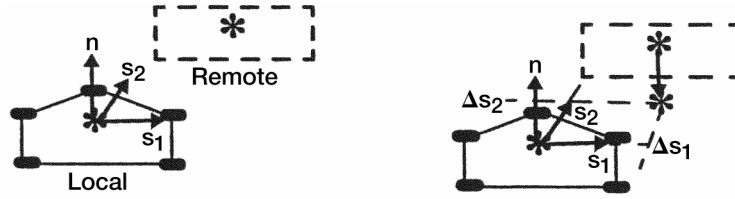


Figure B-6.—Values are assigned to the remote face by finding the closest local centroid to the remote centroid, projecting the remote centroid into the local face normal plane, and using the local value of the variable and the local gradient to determine the remote value.

$$edge_normal = \frac{\bar{n}_{e,i} A_{e,i}}{V} \quad (B.26)$$

All of the above calculations are with the assumptions that the face lies in a 2-D plane. For the current algorithm, this is not necessarily the case. Therefore, before calculating the gradient, all nodes are projected in the average face normal plane (defined by the face center as the origin and the face_normal vector).

B.2.6 Interpolation across the interface.—Interpolation across the interface is achieved by first finding the closest face centroid on the local interface to the remote face. Next, the remote face centroid is projected into the face-normal plane of the closest local centroid. Finally, a value of the variable of interest is assigned to the remote face based upon the value of the local face, the projected distance from the local face centroid to the opposing face centroid, and the gradient of the variable on the local face (figure B.6 and eq. (B.27)):

$$q_{remote} = q_{local} + \nabla a \bullet \{\Delta s_1, \Delta s_2\} \quad (B.27)$$

B.5 References

1. Frink N.T. (1994). “Recent Progress Toward a Three-Dimensional Unstructured Navier-Stokes Flow Solver,” Presented at the 32nd Aerospace Sciences Meeting in Reno, Nevada. AIAA Paper No. 94-0061.
2. Rausch R.D., Vatina J.T., Yang H.T.Y. (1991). “Spatial Adaptation procedures on Unstructured meshes for Accurate Unsteady Aerodynamic Flow Computation,” Presented at the AIAA/ASME/ASCE/AHS/ASC 32nd Structures, Structural Dynamics, and materials Conference, Baltimore, Maryland. AIAA paper No. 91-1106.

Appendix C

Users' Manual for Coupled, Time-Accurate, Three-Dimensional Computations of Primary-Secondary Flow Interactions at Rim Seals With SCISEAL-MS—TURBO Codes

Mahesh M. Athavale
CFD Research Corporation
Huntsville, Alabama 35805

Summary

This document provides a methodology for coupling of two different flow solvers for flows across a moving interface, such as occurs in rotating machinery. Herein the coupling is between a flow code called MS-TURBO that will represent the behavior of the primary flow and SCISEAL that will be used to represent the secondary flow fields. For a typical turbomachine the primary flow is bounded between the casing or shrouds and the blade-vane platforms and drums. The secondary stream is sub-platform and represents the fluid that provides cooling and stability for seals, bearings, and cavities as well as the drums and several components of the primary flow, such as turbine blades. While coupling of the codes is described elsewhere in published documents, this report describes the basics for operating the codes singularly or as coupled codes and as such assumes that these codes are already part of the user's computational system.

Athavale, Mahesh M.: Users' Manual for Coupled, Time-Accurate, Three-Dimensional Computations of Primary-Secondary Flow Interactions at Rim Seals With SCISEAL-MS—TURBO Codes. NASA/CR—2004-212983/VOL1, 2004.

Available from the NASA Center for Aerospace Information.

REPORT DOCUMENTATION PAGE			Form Approved OMB No. 0704-0188	
Public reporting burden for this collection of information is estimated to average 1 hour per response, including the time for reviewing instructions, searching existing data sources, gathering and maintaining the data needed, and completing and reviewing the collection of information. Send comments regarding this burden estimate or any other aspect of this collection of information, including suggestions for reducing this burden, to Washington Headquarters Services, Directorate for Information Operations and Reports, 1215 Jefferson Davis Highway, Suite 1204, Arlington, VA 22202-4302, and to the Office of Management and Budget, Paperwork Reduction Project (0704-0188), Washington, DC 20503.				
1. AGENCY USE ONLY (Leave blank)		2. REPORT DATE November 2005		3. REPORT TYPE AND DATES COVERED Final Contractor Report
4. TITLE AND SUBTITLE Analysis of Coupled Seals, Secondary and Powerstream Flow Fields in Aircraft and Aerospace Turbomachines			5. FUNDING NUMBERS Cost Center 2250000013 NAS3-27392	
6. AUTHOR(S) M.M. Athavale, Y.H. Ho, and A.J. Przekwas				
7. PERFORMING ORGANIZATION NAME(S) AND ADDRESS(ES) CFD Research Corporation 215 Wynn Drive Huntsville, Alabama 35805			8. PERFORMING ORGANIZATION REPORT NUMBER E-14240	
9. SPONSORING/MONITORING AGENCY NAME(S) AND ADDRESS(ES) National Aeronautics and Space Administration Washington, DC 20546-0001			10. SPONSORING/MONITORING AGENCY REPORT NUMBER NASA CR-2005-212716 CFDRC 4117/1	
11. SUPPLEMENTARY NOTES Project Manager, Robert C. Hendricks, Research and Technology Directorate, NASA Glenn Research Center, organization code R, 216-977-7507.				
12a. DISTRIBUTION/AVAILABILITY STATEMENT Unclassified - Unlimited Subject Categories: 01, 07, 20, and 37 Available electronically at http://gltrs.grc.nasa.gov This publication is available from the NASA Center for AeroSpace Information, 301-621-0390.			12b. DISTRIBUTION CODE	
13. ABSTRACT (Maximum 200 words) Higher power, high efficiency gas turbine engines require optimization of the seals and secondary flow systems as well as their impact on the powerstream. This work focuses on two aspects: 1. To apply the present day CFD tools (SCISEAL) to different real-life secondary flow applications from different original equipment manufacturers (OEM's) to provide feedback data and 2. Develop a computational methodology for coupled time-accurate simulation of the powerstream and secondary flow with emphasis on the interaction between the disk-cavity and rim seals flows with the powerstream (SCISEAL-MS-TURBO). One OEM simulation was of the Allison Engine Company T-56 turbine drum cavities including conjugate heat transfer with good agreement with data and provided design feedback information. Another was the GE aspirating seal where the 3-D CFD simulations played a major role in analysis and modification of that seal configuration. The second major objective, development of a coupled flow simulation capability was achieved by using two codes MS-TURBO for the powerstream and SCISEAL for the secondary flows with an interface coupling algorithm. The coupled code was tested against data from three differed configurations: 1. bladeless-rotor-stator-cavity turbine test rig, 2. UTRC high pressure turbine test rig, and, 3. the NASA Low-Speed-Air Compressor rig (LSAC) with results and limitations discussed herein.				
14. SUBJECT TERMS Turbomachine seals; Secondary flow; Design; Numerical analysis			15. NUMBER OF PAGES 153	
			16. PRICE CODE	
17. SECURITY CLASSIFICATION OF REPORT Unclassified	18. SECURITY CLASSIFICATION OF THIS PAGE Unclassified	19. SECURITY CLASSIFICATION OF ABSTRACT Unclassified	20. LIMITATION OF ABSTRACT	

